Analysis Automation and Evaluation of Space Angle for the D3 Stress Estimation Method

by

Haoran Sun

Submitted in partial fulfillment of the requirements
for the degree of Master of Applied Science

at

Dalhousie University
Halifax, Nova Scotia
July 2021

TABLE OF CONTENTS

LIST OF TABLES

LIST OF FIGURES

ABSTRACT

The importance of underground in-situ stress determination has been well established in the area of mining and petroleum engineering. In 2016, Dr. Lin and Zou proposed a displacement-based back analysis method to evaluate the complete 3D in-situ stress state underground. This method requires obtaining the diametrical displacement data from three non-parallel cross-sections of multi-branch or a directional well, and subsequently, calculates the in-situ stress through five mathematical models using excel spreadsheets. The objectives of my research include 1) developing independent desktop applications based on the back analysis method to facilitate calculation, 2) exploring the relationship between the accuracy of the results of back analysis and the orientations of measurement wellbores to provide guidance in field applications.

In this research, two stand-alone MFC applications based on the back analysis method for 2D and 3D stress estimation were developed, respectively. There are six functions in the applications: “Save the input data file,” “load the input data file,” “Compute,” “Display the distribution of measurements,” “Export the calculation result,” and “Exit.” To obtain the results of the in-situ stresses, users can simply enter the required input data in the graphical user interface of the applications and the data are processed by the built-in functions in the applications.

Simulated test examples are applied to the applications to perform error assessment and statistical analysis. The results showed that the stress estimation method provides the most accurate results of in-situ stress as the orientations of the three cross-sections are perpendicular to each other. The space angle between the orientation of each two cross-sections is suggested to be at least 50°. The accuracy of the back-analyzed in-situ stresses is compared with the assumed stresses with further discussions on their relationships.

LIST OF ABBREVIATIONS AND SYMBOLS USED

Below is the list of abbreviations and symbols used in this thesis.

Abbreviations

CSIRO	Commonwealth Scientific and Industrial Research Organisation
CSIR	Council for Scientific and Industrial Research
USBM	US Bureau of Mine cell
VS	Visual Studio
MFC	Microsoft Foundation Class

Symbols

σ_x , σ_y, σ_z	Normal stress in the x-y-z coordinate system
τ_{xy}, τ_{yz}, τ_{xz}	Shear stress in the x-y-z coordinate system
σ_1 , σ_2, σ_3	Principal stresses in the global coordinate system
σ_{Hmax}	Maximum horizontal in-situ stress
σ_{Hmin}	Minimum horizontal in-situ stress
$[M]$	Coefficient matrix
$[M_{com}]$	Convergence coefficient matrix
$[M_m]$	Coefficient matrix for mud pressure
$[M_p]$	Coefficient matrix for pore pressure
P_m	Mud pressure
P_P	Pore pressure
I	Inclination angle
β	Bearing angle
N	Total number of measurements in a measurement plane
u	Diametrical convergence
φ	Porosity

E	Young's modulus
ν	Poisson's ratio
α	Biot's coeffient
S	Skempton's coefficient

ACKNOWLEDGEMENTS

I would like to express my deepest appreciation to my supervisor Prof. Steve D.H. Zou, for giving me the opportunity to do the research and providing invaluable guidance during my MASc study and research.

I would like to extend my deepest gratitude to my internal committee member - Dr. Cui. Lin for her continuous supervision and insightful suggestions in my research work. I also appreciate my external committee member – Dr. Yi. Liu, for reading the thesis and giving valuable input.

Finally, I am extremely grateful to my family for their love, understanding, and continuous support in completing this research work.

CHAPTER 1 INTRODUCTION

1.1 RESEARCH BACKGROUND

In-situ stress is the natural stress confined below the ground surface of the undisturbed rock mass. It results from the weight of the overlying strata and the stress generated from tectonic events. The three-dimensional stress state at a point within a rock mass is represented by three normal stress components $\{\sigma_x, \sigma_y, \sigma_z\}$ and six shear stresses $\{\tau_{xy}, \tau_{yx}, \tau_{yz}, \tau_{zy}, \tau_{xz}, \tau_{zx}\}$, as displayed in Figure 1.1 (Lin and Zou 2019). Shear stresses have three pairs of equal components: $\tau_{xy} = \tau_{yx}$; $\tau_{yz} = \tau_{zy}$; $\tau_{xz} = \tau_{zx}$. Therefore, six independent stress components $\{\sigma_x, \sigma_y, \sigma_z\ \tau_{xy}, \tau_{yz}, \tau_{xz}\}$ can represent the complete 3D stresses. Upon the conversion of an x-y-z coordinate system to a specific orientation for which the shear stresses equal zero, the 3D stress state can be denoted by three principal stress components $\{\sigma_1, \sigma_2, \sigma_3\}$ and their orientations.

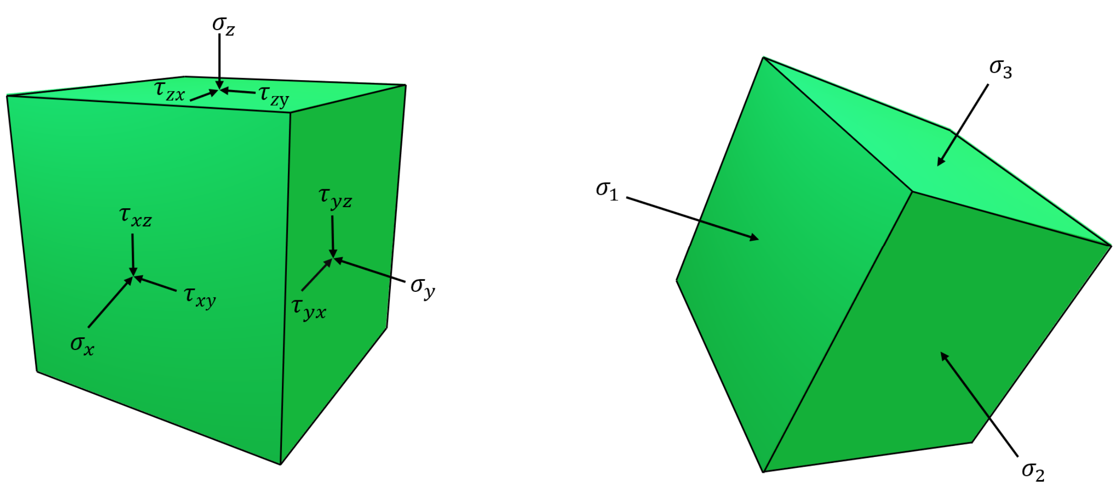

Figure 1.1 Three dimensional in-situ stress

In-situ stress is an important parameter in underground engineering projects. Mine excavation and petroleum drilling generally disturb the underground stress field due to the removal of stressed rock masses. Consequently, stress around the opening or wellbore will be redistributed. If the induced stress exceeds the strength of the surrounding rock masses, it may lead to rock failure and wellbore collapse. Therefore, in-situ stress field estimation is of paramount importance to develop a pre-excavation design and drilling plan while ensuring safety control.

Up to now, various researchers have proposed over 20 methods for in-situ stress determination (e.g., Fairhurst 2003 and Gaines et al. 2012). However, the majority of the methods are expensive and may not be able to provide accurate results. Overcoring is the only method to determine the complete 3D in situ stresses. To address these issues, Drs. Lin and Zou developed a more applicable stress measurement method – displacement-based back analysis method – in 2016 (Lin and Zou 2016). This method can help estimate 2D in-situ stress in the cross-section perpendicular to the wellbore and the complete 3D in-situ stress field using the borehole deformation. The 2D in-situ stress analysis requires the borehole deformation data measured from the cross-section of a wellbore. On the other hand, the 3D in-situ stress analysis, which is named as the D3 stress estimation method, needs the deformation data from at least three non-parallel cross-sections (Lin and Zou 2021). With varying field conditions of permeability, pore pressure, and mud pressure in the petroleum field, they developed five comprehensive models for both 2D and 3D analyses. Dr. Lin's research demonstrated that the estimation of 2D stresses using back analysis always converges to the real solution, even with the addition of 20% input errors to the simulated accurate deformation data. However, the results of 3D stress estimation using back analysis have relatively large errors in some cases, and the accuracy of these results is affected by the orientations and correlations of the three measurement wellbores.

1.2 RESEARCH OBJECTIVES

As a follow-up to Dr. Lin's study, my research is aimed at 1) developing independent desktop applications to realize the automated analysis of the stress estimation method. 2) exploring the relationship between the accuracy of the back analysed results and the orientations of measurement wellbores to provide guidance in field applications.

The first step of this study is to develop two console applications as the prototype of the desktop applications. These applications are programs with a text-only computer interface. In comparison to the Windows applications with GUI (Graphical User Interface), these applications can be developed in a shorter period. Consequently, the potential bugs and basic logic of the source code of these applications can be efficiently rectified and improved. Furthermore, we need to design the GUI and develop two MFC applications (Microsoft Foundation Class-based Windows application) for 2D and 3D analyses, respectively. These MFC applications are expected to process the input data, show the results of the back analysis on the GUI, and allow users to export the data to a text file. The applications will then be used to test and analyze the simulated borehole deformation data based on various wellbore orientations. Error assessment and statistical analysis should also be performed with the tested results. Based on the results of these analyses, the reasonable range of the orientations of three wellbores will be determined.

A flow chart outlining my research is displayed in Figure 1.2.

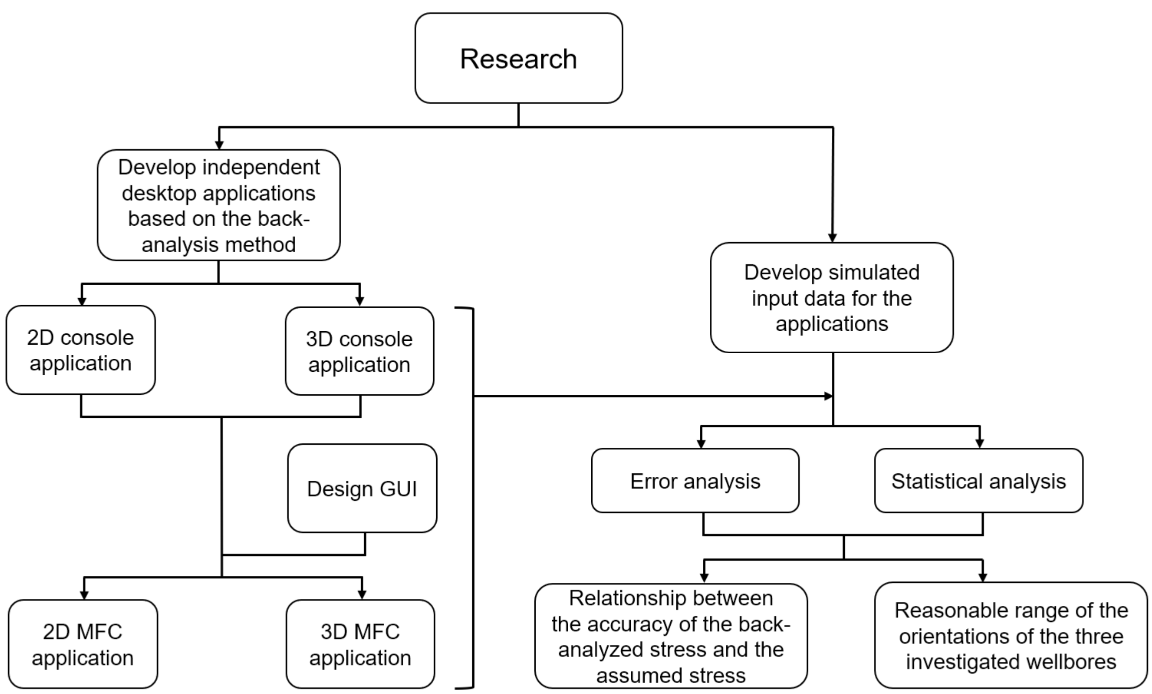

Figure 1.2 Outline of research

CHAPTER 2 LITERATURE REVIEW

In the mining and petroleum industry, high-stress relief will cause many problems on wellbore stability and excavation safety. Therefore, the understanding of underground in-situ stress has great importance in designing strategic drilling plans and maintaining wellbore stability. In the past, more than 20 stress measurement methods have already been developed. According to different measurement principles, those methods can be grouped into the borehole-based method, drill core-based method, geophysical method, methods performed on rock surfaces, and geological observation method (Figure 2.1).

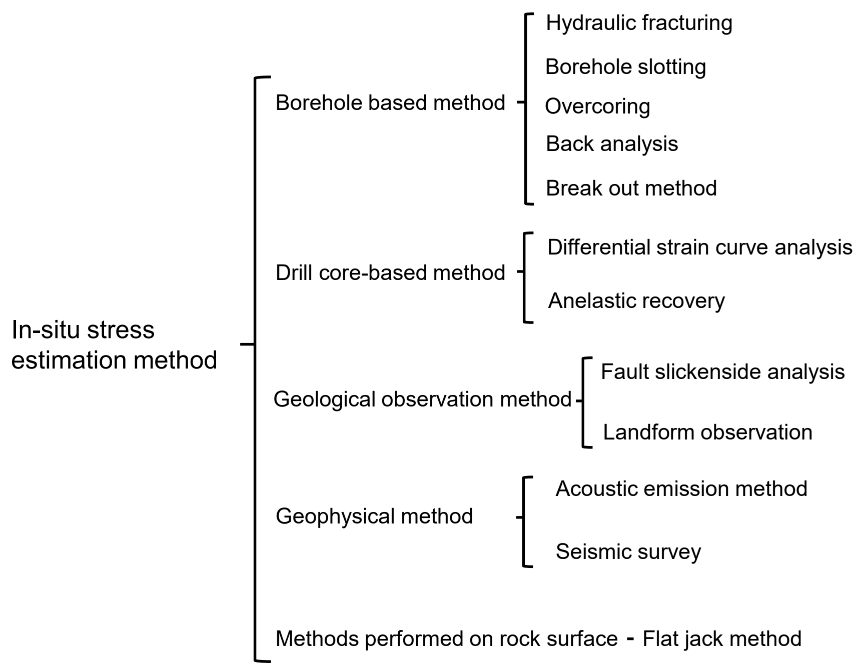

Figure 2.1 In-situ stress estimation method

In the following, eight prevalent stress estimation methods will be reviewed. They include the hydraulic fracturing method, acoustic emission method, break out method, flat jack method, overcoring method, borehole slotting method, geological method, and back analysis method. They are the typical and widely-used methods in the domain of the mining and petroleum industry. Moreover, the new back analysis method developed by Dr. Lin under the guide of Dr. Zou will also be introduced.

2.1 HYDRAULIC FRACTURING METHOD

In the past few decades, the hydraulic fracturing method becomes a crucial tool for the pre-excavation design of large underground projects, such as tunnels, waste disposal galleries, hydraulic powerhouses, energy storage caverns, and hot dry rock projects (Abé et al. 1992). In petroleum and mining engineering, hydraulic fracturing is the most prevalent in-situ stress measurement method. This method utilizes the shut-in pressure and the re-opening pressure during the hydraulic fracturing process to assess the 2D underground in-situ stress state in the plane perpendicular to the test borehole.

At the first step of the hydraulic fracturing works, a pair of packers are installed in the desired depth to isolate the target layer. Then, high-pressure fluids will be injected into the isolation layer driven by the surface pump. Figure 2.2 is the sketch of the hydraulic fracturing process, where the blue arrow indicates the fluid's flow direction. The pressure of the space between the packers is going to rise rapidly (typically 0.1-1.0 MPa/s) until the surrounding rocks get ruptured. As the fractures are expanded, the surface pump needs to be stopped. The fluids will continue invading into the gap between the induced fractures accompanied by the decay of downhole pressure. When the down-hole pressure tends to be steady, record the shut-in pressure P_f. The magnitude of the minimum horizontal stress σ_h can be determined directly from P_f:

$$\sigma_h = P_f \tag{2.1}$$

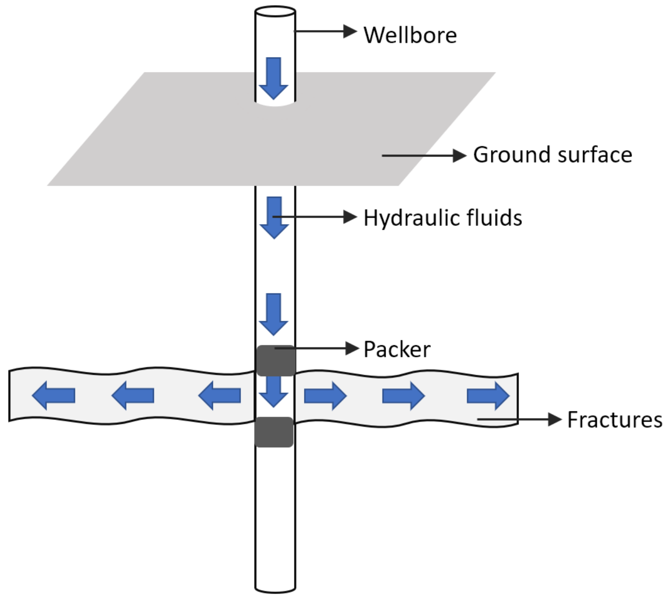

Figure 2.2 Hydraulic fracturing process

The wellbore pressure is released in the next step with the well's re-opening, and the induced fractures are thus be closed. The following repressurize process is going to re-open those fractures. Assumed the orientations of the principal stress are vertical and horizontal and the rock mass is isotropic and linear-elastic, the maximum horizontal stress σ_H could be calculated by the re-opening pressure P_r and the shut-in pressure P_f through Equation (2.2).

$$\sigma_H = 3\sigma_h - P_r \tag{2.2}$$

Furthermore, the orientation of the maximum horizontal stress coincides with the fracture's extension direction. A geologic radar or the down-hole camera makes it possible to observe the propagating directions of the underground fractures around the wellbore in a macroscopical way.

The hydraulic fracturing method could estimate the magnitude and directions of the stress state in a measurement plane under certain assumptions. However, the measurement of the downhole pressure may give rise to errors and further influence the estimation of in-situ stress (Hayashi et al., 1997). Most of the fluids tend to chase the tip of expanding fractures at the shut-in stage, but part of the fluids seep into the circumferential rocks driven by the pressure difference. The fluid loss will affect the following downhole pressure measurement and further influence the reliability of the in-situ stress determined by this method. Considering the fracturing fluid invades to ambient rocks, Haimson proposed Equation (2.3) to correctify the calculation of σ_H by hydraulic fracturing method (Haimson 1968) :

$$\sigma_H = 3\sigma_h + s_t - 2P_r + \alpha \frac{1-2\nu}{1-\nu}(P_r - P_P) \tag{2.3}$$

Where: P_r is the formation fracture pressure. s_t is the tensile strength of the formation. α is the Biot's coefficient. ν is the Poisson's ratio. P_P is the pore pressure.

Limited by the premise that the orientations of the principal stress are vertical and horizontal, the hydraulic fracturing method can only determine a 2D stress state. At present, many scholars are still working on developing a more accurate stress analysis model based on it, and this method is still the most prevalent underground stress state estimation method in mining and petroleum engineering.

2.2 ACOUSTIC EMISSION METHOD

The acoustic emission method is the method utilizing the Kaiser effect to track the original underground stress. In 1959, Kaiser indicated that, during the process of compression, the acoustic emission of rock samples intensified when the value of loading pressure reaches the maximum value that the rock mass has experienced in history (Kaiser 1996). It is generally assumed that the acoustic emission phenomenon comes from the micro-fracture inside the rock. In the microscopic perspective, when the loading pressure exceeds the sample's ancient confining pressure, the microfractures and weak joints inside the rock mass will extend and generates acoustic signals. The point that the acoustic emission effect intensified is named as "Kaiser point." Based on the Kaiser effect, the acoustic emission method makes it possible to determine in-situ stress through lab experiments (Lehtonen and Cosgrove 2012).

In practice, rock samples from a vertical well should be gathered. Figure 2.3 displays the distribution of the four desired rock samples in a vertical well. Specifically, a vertical core sample and three radial core samples should be drilled from the wellbore's surrounding rock, and the angle between each radial sample is 45 degrees. Acoustic detection equipment needs to be attached to the test sample's cylinder surface during the subsequent uniaxial test to monitor the acoustic signals in real-time and find the sample's Kaiser point. The in-situ stress could be calculated by the Equation(2.4) according to DR Hughson's research in 1986 (Hughson and Crawford 1986) :

$$\sigma_v = \sigma_A + \alpha P_P \tag{2.4a}$$

$$\sigma_H = \frac{\sigma_B+\sigma_C}{2} + \frac{\sigma_B-\sigma_C}{2}(1+t\,an^2(2\theta))^{\frac{1}{2}} + aP_P \tag{2.4b}$$

$$\sigma_h = \frac{\sigma_B+\sigma_C}{2} - \frac{\sigma_B-\sigma_C}{2}(1+t\,an^2(2\theta))^{\frac{1}{2}} + aP_P \tag{2.4c}$$

$$t\,an\,(2\theta) = \frac{\sigma_B+\sigma_D-2\sigma_C}{\sigma_B+\sigma_D} \tag{2.4d}$$

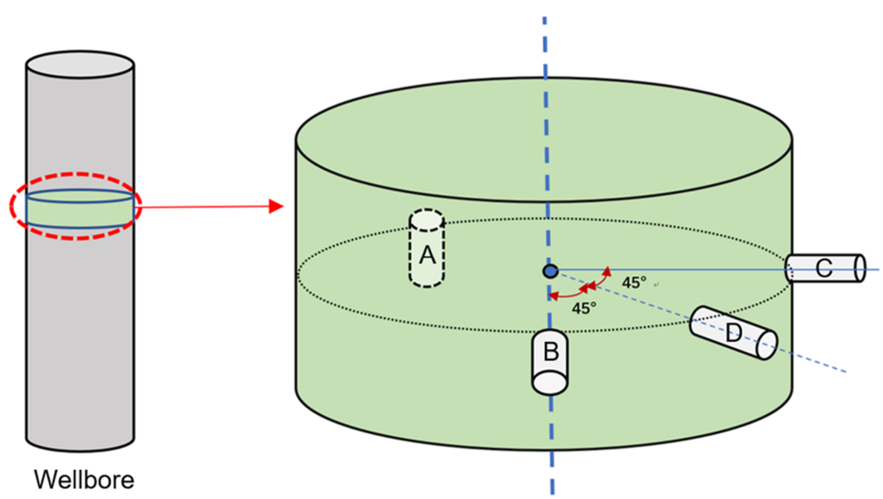

Figure 2.3 Directional coring

Where σ_v is vertical stress, α is the effective stress coefficient and P_P is pore pressure. σ_A is the pressure loaded to sample A at its Kaiser point and the same for other samples. θ is the direction of maximum in-situ stress.

If the orientation of one principle stress is assumed consistent with the vertical direction, the result of σ_v, σ_H and σ_h could be approximate to the three principal stress components in the field stress state.

The crucial procedure of the acoustic emission method is the determination of the Kaiser point. However, except for a few types of rock, scholars do not have a consensus of opinion about how to determine the Kaiser point scientifically (Li and Norlund 1993). Some scholars adopt the turning point at the acoustic signal-time period curve as the Kaiser point, whereas someone believes the Kaiser point shows up at the turning point on the curve of acoustic signal versus strain change, etc. On the other hand, the ancient maximum pressure experienced by the test sample sometimes cannot represent its field stress state at present. Thus, many researchers only introduce the stress analysis result from the acoustic emission method to their study as a reference.

Although many factors weaken the accuracy of the in-situ stress determined by the acoustic emission method, it still carved out a new way for the underground in-situ stress estimation.

2.3 BREAKOUT METHOD

The “Breakout” is to describe the spalling region on the surface of the wellbore. During the drilling process, stressed rock masses are removed by the drill bits, and the circulating drilling mud provides temporary support to the wellbore. If the pressure difference between the confining pressure and the mud pressure exceeds the ambient rock’s compressive strength, it may lead to crushing failure on the wellbore surface. The induced spalling zone can be observed by downhole cameras in the well-logging process. In 1982, a study (Bell and Gough 1982) performed on the caliper-logging data of a well in Colorado’s oilfield showed that the orientation and dimension of the spalling area tend to be consistent. Zoback and Moos supported the former perspective and summarized that the spalling domains on each side of the wellbore are likely to be centered along the minimum horizontal stress direction (Zoback and Moos 1985). They further indicated that the field stress state could be estimated from the orientation and area of the breakout region.

With the emerge of the image logging technique, the downhole crushing failure could be investigated visually. Figure 2.4 is a sketch of the plane view of two breakout areas on both sides of a well.

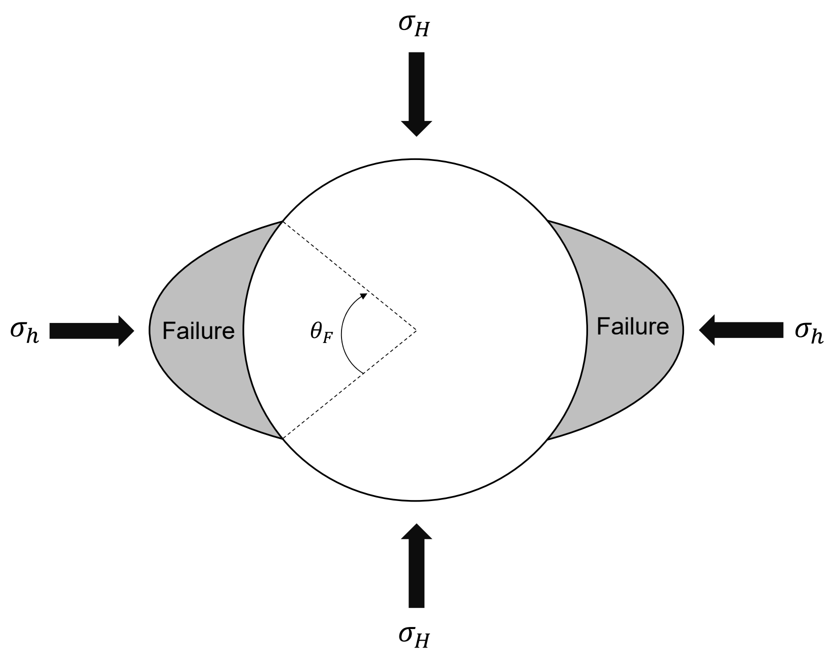

Figure 2.4 Crushing failure in the wellbore

σ_H and σ_h is the maximum and minimum horizontal principal stress, respectively. The area of the failure zone and the corresponding angle θ_F can be determined by image logging technology. The magnitude of maximum horizontal stress in a vertical well can be calculated by Equation 2.5, according to Barton's research in 1988 (Braton and Zoback 1988).

$$\sigma_H = \frac{(c+2P_P+\Delta P)-\sigma_h(1+2\cdot cos(\pi-\theta_F))}{1-2\cdot cos(\pi-\theta_F)} \tag{2.5}$$

Where: P_P is the pore pressure. ΔP is the pressure difference between the pore pressure and mud pressure. C is the compressive strength of the surrounding rock.

It should be noted that the independent evaluation for compressive strength and minimum horizontal stress is required for this method. Furthermore, the limitations of this method are obvious: The mud cake layer on the wellbore's surface may obscure the breakout region. Followed by the completion of drilling works, the extension of the failure zone due to the drilling fluid invasion also exerts some influence on the precision of measurement. Consequently, the breakout method is still needed to be improved in future studies.

2.4 GEOLOGICAL METHOD

The tectonic events on the earth are generated from the natural underground in-situ stress. Geological information extracted from those events can be used to trace the orientation of the in-situ stress. On the rock surface of natural faults, fault slickenside recorded the activity of tectonic events. According to the field measurement data from the Neogene formation in Greece, Angelia illustrated a geological method to estimate the field stress state by investigating fault slickenside (Angelia 1979).

In practice, hundreds groups of fault slip data, including fault azimuth, fault dip, and the pitch of slickensides, are required to be measured in a field site such as a cliff or trench. Assumed that each fault is driven by an independent stress tensor, and their slippage orientation is governed by the shear stress components applied on the fault surface. The orientation of the three principal stress can thus be estimated by Equation (2.6) through the least square minimization procedure.

$$\overrightarrow{M_1} = \Sigma\left(\overrightarrow{S_k}, \overrightarrow{f_\kappa}\right)^2 \tag{2.6a}$$

$$\overrightarrow{M_2} = \frac{1}{4}\Sigma\left|\overrightarrow{S_k} - \frac{\overrightarrow{f_k}}{|\overrightarrow{f_k}|}\right|^2 \tag{2.6b}$$

$$\overrightarrow{M_3} = \Sigma\, mi\, n\left[tg^2\left(\overrightarrow{S_k}, \overrightarrow{f_k}\right), 1\right] \tag{2.6c}$$

Where $\overrightarrow{M_1}$, $\overrightarrow{M_2}$, and $\overrightarrow{M_3}$ indicate the orientation of the three principal stress. The subscript k denotes the serial number for each fault. $\overrightarrow{S_k}$ is the unit vector along the slippage direction. $\overrightarrow{f_k}$ is the shear stress vector. Since the reconstruction of the in-situ stress orientation through slickenside investigation is a non-linear problem, a further iterative process will be involved in the analysis.

Apart from the fault slickenside, some particular landforms, such as the volcano, can also give clues for estimating the direction of underground stress. For the poly-genetic volcanos, many radial dikes can be observed from their flank site. Those radial dikes are formated by the magmas come from the flank eruption in ancient time. Governed by the compression stress, those magmas have a trend to distribute parallel with the orientation of the maximum in-situ stress; thus, the radial dikes are also likely to elongate in the same direction (Nakamura 1977).

Generally, the geological method can be applied in the unfrequented region, where some clear evidence of tectonic events is available. The method's major limitation is that it can only estimate the direction of underground in-situ stress; the magnitude of the principal stress cannot be determined in this way.

2.5 OVERCORING METHOD

In1958, Hust stated his underground stress analysis result according to the measurement data from the piezomagnetic gauge in Lasiwall and Scandinavia (Hust 1958). That arouses the interest of geologists around the world. Scholars began to work on estimating underground stress through the overcoring technique. Overcoring method utilizes the induced strain or deformation change from a core sample during the overcoring process to backtrack the complete 3D stress state through mathematical formulations.

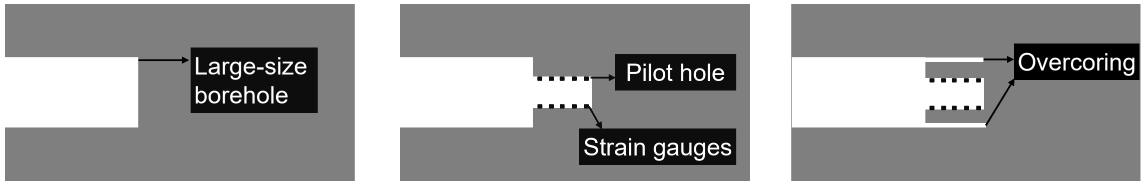

Figure 2.5 Overcoring method

Overcoring process can completely relieve the confining pressure restricting the desired core sample through the removal of its ambient stressed rock mass. Figure 2.5 displays the procedures of the overcoring method (Cui Lin et al. 2019). In the initial process, a large-diameter borehole is drilled into the target rock formation. At the bottom of the large borehole, a smaller coaxial pilot hole will be drilled subsequently. Meanwhile, several groups of strain or deformation sensors are glued on the cylinder surface of the pilot hole. After that, the big hole will be overcored until it covers the domains of the sensors in the pilot hole, and during which the strain/deformation change will be monitored and recorded persistently. Assuming the rock properties are isotropic and homogeneous, the in-situ stress field in 3D could be calculated by the strain/deformation data using the linear elastic formula.

The measurement of strain/deformation change plays a key role in this method, and they adopt different measuring tools. In terms of the deformation measurements, the USBM and ISR gauge developed by the US Bureau of Mine and Sigra Pty., Ltd, respectively, are widely used in field stress measurement (Merrill 1967). In essence, the mechanical structure for both gauges is similar. The gauge consists of 3 pairs of cantilever transducers, which are placed 60 degrees apart, and thus can measure the diametrical deformation change in 3 directions (As displayed in Figure 2.6).

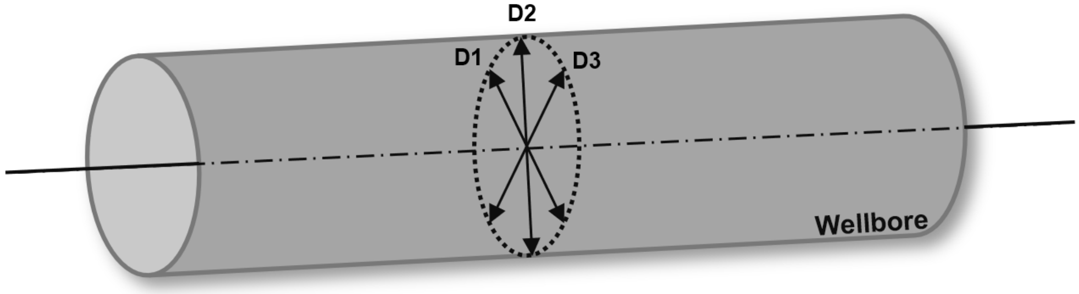

Figure 2.6 USBM measurement orientations

Assumed that a borehole is drilled along the Y direction, and the diametrical deformation data are obtained from the stress relief process (overcoring). The stress components in the X-Z plane could be calculated by the following equation:

$$\begin{pmatrix} \sigma_x \\ \sigma_y \\ \tau_y \end{pmatrix} = \begin{bmatrix} 3d\frac{1-v^2}{E} + \frac{dv^2}{E} & -d\frac{1-v^2}{E} + \frac{dv^2}{E} & 0 \\ \frac{dv^2}{E} & 2\,d\frac{1-v^2}{E} + \frac{dv^2}{E} & 2\sqrt{3}\,d\frac{1-v^2}{E} \\ \frac{dv^2}{E} & 2\,d\frac{1-v^2}{E} + \frac{dv^2}{E} & -2\sqrt{3}\,d\frac{1-v^2}{E} \end{bmatrix}^{-1} \begin{bmatrix} D_1 + \frac{d_v}{E}\sigma_y \\ D_2 + \frac{d_v}{E}\sigma_y \\ D_3 + \frac{d_v}{E}\sigma_y \end{bmatrix} \tag{2.7}$$

Where D_1 , D_2 and D_3 represent the measured displacement in three different orientations, respectively.

There are six unknown stress components included in three dimensions, and only three of six could be calculated from the measurements in one borehole according to Equation (2.7). Subsequently, obtaining the deformation data from at least two non-perpendicular and non-parallel boreholes could fulfill the requirements of determining the complete 3D stress state.

As for the strain gauge, the CSIRO cell developed by the University of Queensland in 1984 (Leahy 1984) and the CSIR cell invented by Leeman in 1969 (Leeman 1969) are very prevalent in practice. The principle for both cells is similar, whereas the CSIRO cell is entirely reusable in comparison with the one-off CSIR cell. In conventional form, the CSIRO cell consists of 3 groups of strain gauges bonded to the wellbore wall by cement.

The angle between each group is 120 degrees, and each group contains 3~4 sub-gauges aiming at different orientations. For each sub-gauge, their measured orientation could be denoted as θ and η (Figure 2.7).

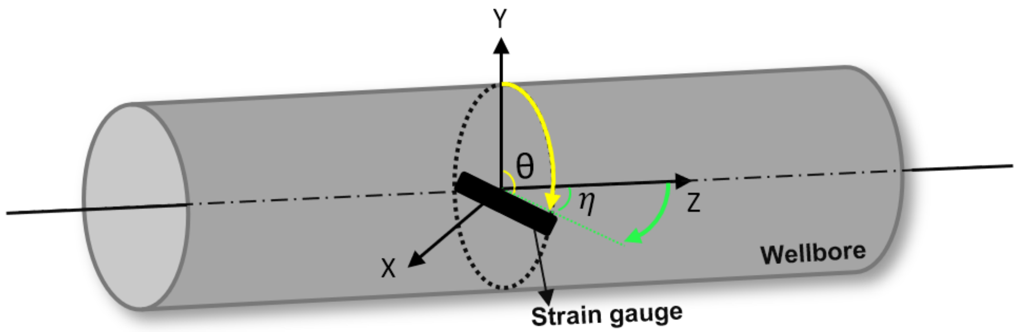

Figure 2.7 CSIRO measurement orientations

According to the linear-elastic principle, the six in-situ stress components could be calculated by the strain change data measured in one wellbore through Equation (2.8):

$$\varepsilon_\eta = [c]\left[\sigma_x\ \sigma_y\ \sigma_z\ \tau_{xy}\ \tau_{yz}\ \tau_{xz}\right] \tag{2.8}$$

Where matrix contains all the strain change measured by each gauge; $[c]$ is the coefficient matrix related to the rock properties and the orientation for each sub-gauge.

Both strain and deformation sensors are widely applied in the overcoring method. Compared with the deformation measurement, only one borehole is required to be drilled for the strain measurement. Hence, compared with USBM, the CSIRO cell will be more cost-efficient. The USBM cell is reliable when the influence of underground temperature is considered. USBM cell uses a full-bridge circuit, which prevents the effection of the temperature change (Cai and Blackwood 1987). In contrast, the CSIRO cell adopts the quarter-bridge circuit, and an extra dummy gauge is required to be installed with it as a temperature compensation instrument.

Overcoring is a borehole-based stress estimation method in the mining area that can determine the complete 3D stress state. It is very costly because of the requirement for overcoring equipment and labor. The infeasibility of performing overcoring works in deep wells prevented its application in petroleum engineering.

2.6 BOREHOLE SLOTTING METHOD

Borehole slotting is a 2D stress estimation method according to the principle of local stress relief in a borehole. In practice, a slot will be cut on the surface of a vertical wellbore by a diamond-impregnated blade driving through an air turbine (Figure 2.8 and 2.9). The depth of the slot should exceed 16 millimeters to relieve the tangential pressure around the slots completely, and the direction of it should be parallel with the borehole axis (Li and Peng 2018). During the cutting process, a strain sensor adjacent to the slot will persistently record the tangential strain change on the surface of the borehole.

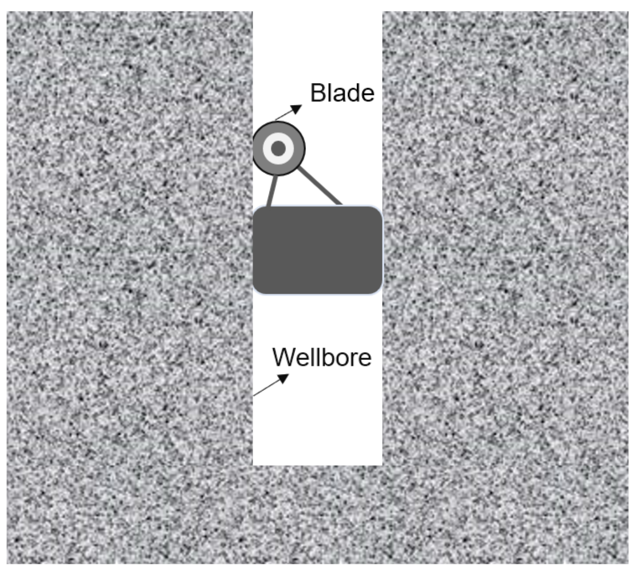

Figure 2.8 Borehole slotting

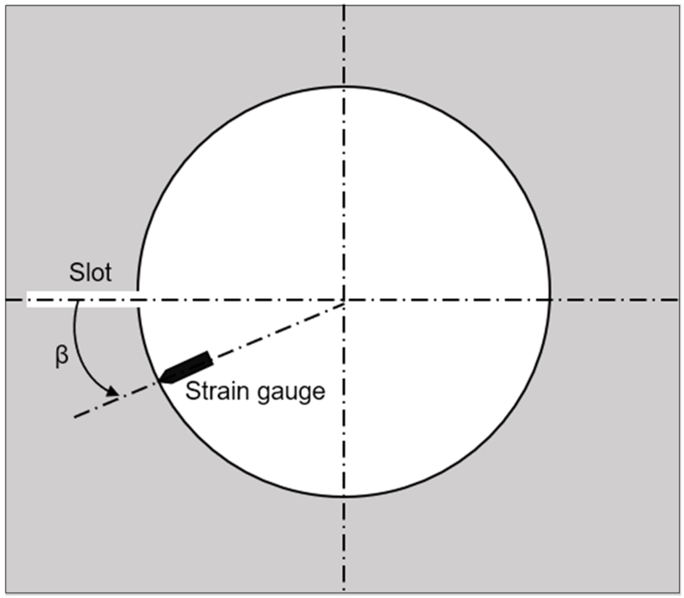

Figure 2.9 Plane-view of the slotting

Assumed that the surrounding rock is isotropic and linear elastic, the 2D field stress state on the measurement plane perpendicular to the slot can be calculated by Equation (2.9).

$$\varepsilon_\theta = \frac{1-\nu^2}{E}[1 - 2\cos(2\beta) \;\; 1 + 2\cos(2\beta) \;\; -4\sin(2\beta)]\{\sigma_x \; \sigma_y \; \tau_{xy}\} \tag{2.9}$$

Where ε_θ is the recorded strain change in different directions.

Theoretically, the stress state in a 2D plane could be calculated by the tangential strain change from three slots orientated in different horizontal directions due to the three unknown stress factors. So in most practice cases, three slots, which are 120 degrees apart from each other, will be cut at the desired depth (Bock and Foruria 1983).

Compared with other borehole-based methods such as overcoring, the borehole slotting method is more cost-effective since no additional drilling or coring works are needed. Nevertheless, the borehole slotting cannot determine a complete 3D state.

2.7 FLAT JACK METHOD

The flat jack method, which is also called the rock mass surface stress relief method, is an old and widely-used direct stress estimation method. It was first proposed by Tincelin in 1951 (Tincelin 1951). This method requires cutting a slot on the surface of rock mass in order to relieve the stress nearby the slot. Resulted displacement of the ambient rock is recorded by reference pins or displacement transducers on both sides of the slot, as shown in Figure 2.10.

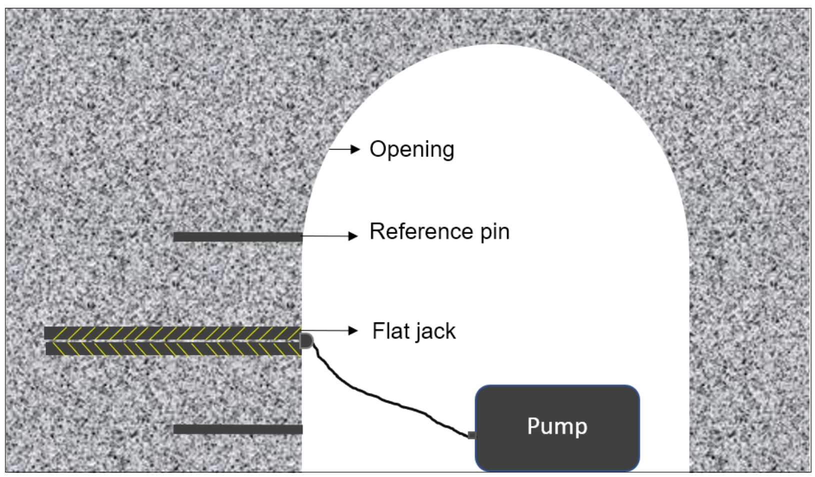

Figure 2.10 Flat jack process

When the deformation readings are completed, which generally takes three to four days (Hoskins 1966), a rectangular flat jack is mounted into the slot. The support pressure inside the flat jack will rise up gradually until the deformation caused by the stress relief is recovered. According to the measurement data, the compressive stress applied perpendicularly on the slot could be calculated by Equation (2.10) (Pawel 2000):

$$\sigma_m = K_m K_a p \tag{2.10}$$

The Km is the calibration factor, which is generally provided by the manufacturer of the flat jack. Ka is the ratio of the measured area of the flat jack to the average measured area of the slot. The p is the output pressure of the flat jack.

However, the traditional flat jack test always cannot yield satisfactory result since the measurement area is so small that is likely to be disturbed by previous excavations. To address these issues, the large flat jack test method (LFJ test) is developed (Bruno 2010). Unlike the small-size flat jack in the traditional way, LFJ adopts a large-size flat jack of which the test zone could exceed ten square meters, as depicted in Figure 2.11. The principle of compressive stress calculation is consistent with the traditional method, but the results generated from the LFJ test are believed to be more reliable because the disturbance of excavation decays in a large-scale test zone.

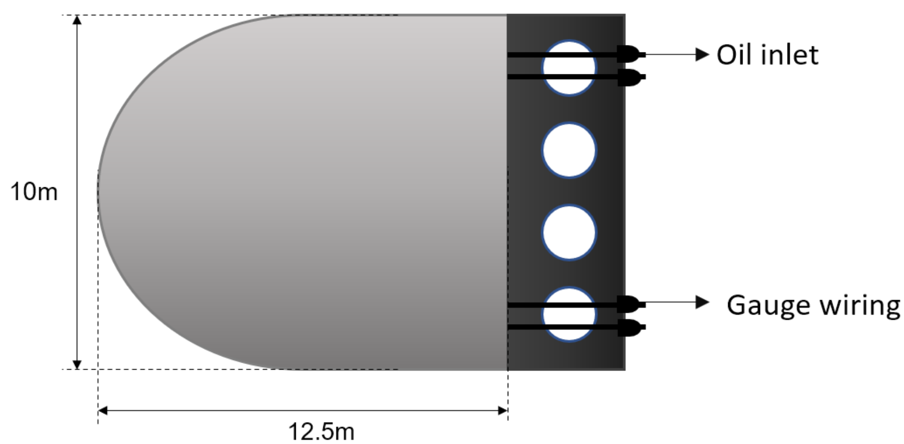

Figure 2.11 Large flat jack

Overall, the analysis result of the flat jack method is limited in the compressive stress in a small region. Neither the two-dimensional in-situ stress nor the complete 3D field stress state can be estimated in this way. Furthermore, the testing zone is restricted in the region adjacent to the surface of rock mass, where the equipment can get access to, such as the wall of a tunnel or large opening.

2.8 BACK ANALYSIS METHOD

2.8.1 Back analysis method in mining excavation

The back analysis is a method that utilized the induced displacement or stress change to backtrack the virgin in-situ stress field. More specifically, during the excavation process, the in-situ stress field around a borehole or opening will be disturbed, so if the induced displacement or stress change can be measured, the original in-situ stress field may be possible to be back analyzed. In 1990, Zou and Kaiser presented a back analysis method, which utilizing the recorded displacement change during the excavation process of a tunnel to estimate the stress field in two dimensions (Kaiser and Zou 1990).

When an opening is excavated, the opening will deform under the affection of the underground stress. The induced deformation can be monitored through relative movement measurement and convergence measurement shown in Figure 2.11. In practice, the former is performed with the multiple anchor extensometer. The extensometer is inserted in the rock formation adjacent to the target excavation zone. It will record the displacements of its multiple sensors in real-time during the followed excavation works. In terms of the latter, convergence is the distance between each pair of points located on the opening's excavation boundary. The variation of convergence indicates the deformation of the surrounding rock mass during the excavation process.

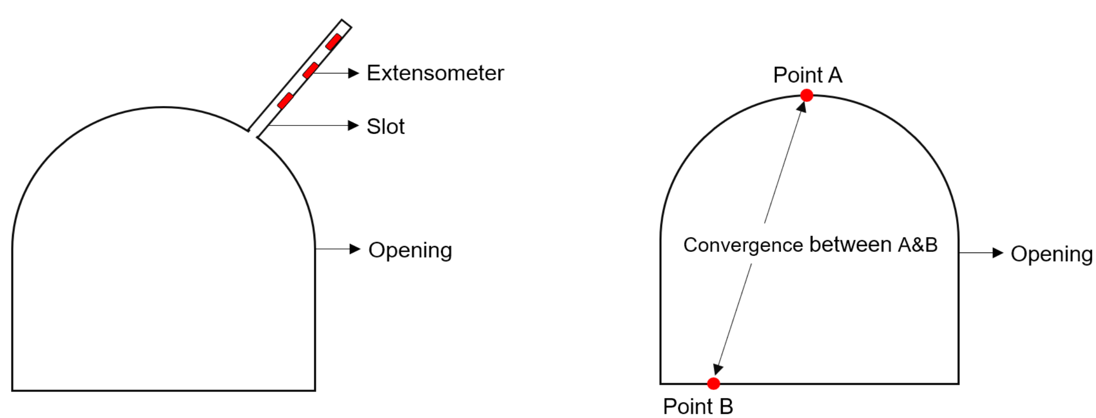

Figure 2.12 Deformation measurement in tunnels

According to the linear-elastic theory, the simplified overall relationship between the deformation and in-situ stress could be written as:

$$\{u\} = [M] \cdot \{\sigma\} \tag{2.11}$$

where, $\{u\}$ is the matrix of displacement, $\{\sigma\}$ contains the in-situ stress components and $[M]$ is the coefficient matrix that represents the geometry of the excavation boundary, ambient rock properties, and the location of the measurement points. The in-situ stress components can thus be solved through the least square method as shown in Equation (2.12):

$$\{\sigma\} = ([M]^T \cdot [M])^{-1} \cdot [M]^T \cdot \{u\} \tag{2.12}$$

It should be noted that only when the value of the determinant of $[M]^T \cdot [M]$ is non-zero, would Equation 2.12 have a unique solution for stress components.

Compared with some traditional stress analysis methods such as overscoring, the back analysis method is simple to operate and cost-effective. Furthermore, this method is feasible to be applied in the deep and stress-concentrated regions (Martin and Kaiser 2003).

2.8.2 Back analysis method in petroleum drilling

Enlightened by the principle of the back analysis method, Dr. Lin and Zou developed a practical method to determine the field stress state from the wellbore deformation data in the petroleum field (Lin and Zou 2016). During the well-drilling process, stressed rock masses are removed and carried out through the drilling mud. The drilling mud is an oil-based or water-based fluid used to aid drilling and support wellbore. Since the mud pressure is not always balanced with the confining pressure, the wellbore tends to be deformed under the effect of drilling induces stress redistribution.

2.8.2.1 Borehole convergence measurement in the petroleum field

The measurement of the borehole diametrical deformation can be achieved by the caliper-logging. Generally, the well-logging works are performed during or following the drilling process, which utilized specialized down-hole tools to measure the geological properties of the formation around the wellbore. The drilling-induced wellbore deformation could be measured by a particular tool - caliper. A caliper consists of multiple metallic arms, a center shaft, and a specialized downhole cable. Figure 2.13 displays the classic four-arm caliper designed by Schlumberger (Paul. B 2002):

Figure 2.13 Four arm well-logging caliper

At the caliper-logging process, the caliper needs to be put down to the bottom of the well and open the metallic arms tightly against the borehole wall. In the subsequent lifting process, its displacement sensor will keep recording the diametrical distance between the tip of the arms and the central shaft, as illustrated in Figure 2.14. The downhole cable would transmit the information of measurement data to the ground through electrical signals so that the variation of borehole size can be monitored in real-time. The caliper is probably the most reliable and practical tool for borehole-dimension measurement in the petroleum industry.

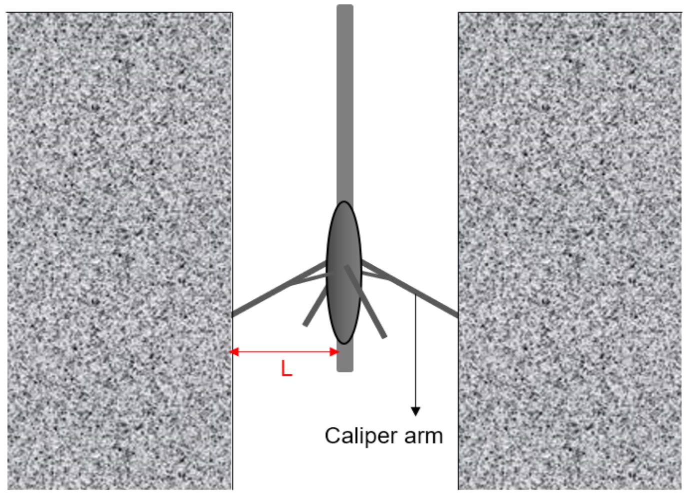

Figure 2.14 Caliper log works

Based on the borehole convergence data measured by caliper, the back-analysis method can calculate the in-situ stress underground through mathematic formulations.

2.8.2.2 In-situ stress estimation in 2D

The method can help estimate 2D in-situ stress in the cross-section perpendicular to the wellbore. In-situ stress in a 2D plane contains three independent stress components $\{\sigma_x, \sigma_y, \tau_{xy}\}$. Those components can be further converted to the maximum horizontal stress σ_H and minimum horizontal stress σ_h through mathematical equations.

In practice, the 2D stress analysis method can be applied in an oil well orientated to any direction. During the drilling process, a cross-section of the well tends to deform under the effect of in-situ stress (Figure 2.15).

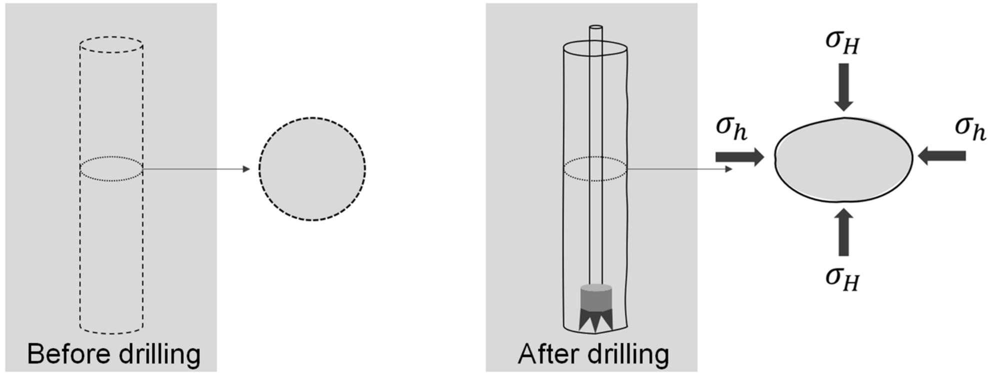

Figure 2.15 Wellbore deformation during the drilling process

According to Dr. Lin's formulation (Lin and Zou 2021), the stress components in the plane of the cross-section could be calculated by solving Equation (2.13):

$$[M]\{\sigma\} - [M_m]P_m - [M_P]P_P = \{\mathrm{u}\} \tag{2.13}$$

Where: $[M_m]$, $[M_P]$ and $[M]$ are the matrix corresponding to rock properties and measurement location. P_m is the drilling mud pressure, and P_P is the pore pressure. $\{\sigma\}$ contains the three stress components σ_x, σ_y, and τ_{xy}. $\{u\}$ represents the convergence data measured by the caliper in the cross-section towards different directions.

2.8.2.3 In-situ stress estimation in 3D

In the actual field, the in-situ stresses underground are in a three-dimensional state. Some issues encountered in mining and petroleum engineering cannot be simply dealt with as a 2D stress condition. In order to determine the 3D in-situ stress by the back-analysis method, caliper-logging data from at least three parallel wells should be gathered according to Lin's models. Drilling three wells for determining the 3D in-situ stress is not practical in the oil field due to the high cost. In another way, the caliper-logging data could be measured from three different cross-sections in a directional well or a branch well

(Figure 2.16).

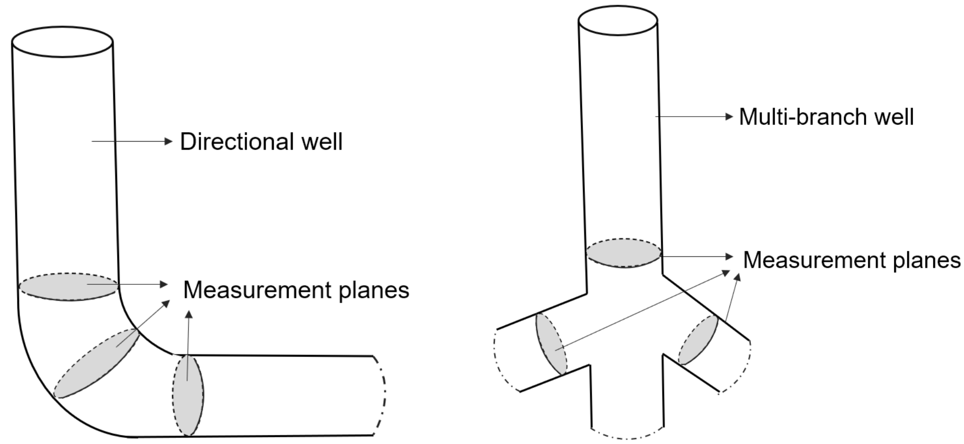

Figure 2.16 Measurement planes from a directional well/ multi-branch well

It should be noted that the caliper-logging data from each cross-section are required to be in the same layer of the rock formation. The in-situ stress components in three dimensions can be calculated by solving Equation (2.14) (Lin 2019)

$$[M_1]\{\sigma_1\} - [M_{m1}]P_{m1} - [M_{P1}]P_{P1} = \{u_1\} \tag{2.14a}$$

$$[M_2]\{\sigma_2\} - [M_{m2}]P_{m2} - [M_{P2}]P_{P2} = \{u_2\} \tag{2.14b}$$

$$[M_3]\{\sigma_3\} - [M_{m3}]P_{m3} - [M_{P3}]P_{P3} = \{u_3\} \tag{2.14c}$$

Where $\{u_1\}$ is the borehole convergence data obtained from the cross-section of the first well, and so for $\{u_2\}$, $\{u_3\}$. In the calculation process, $\{\sigma_1\}$, $\{\sigma_2\}$, $\{\sigma_3\}$ are converted by stress transformation into $\{\sigma\}$, which consists of the six unknown in-situ stress components σ_x, σ_y, σ_z, τ_{xy}, τ_{yz} and τ_{xz}. Matrices $[M_{m1}]$, $[M_{m2}]$, $[M_{m3}]$ have been converted to a common x-y-z coordinate system through stress transformation and are going to be combined into a single matrix $[M_{mcon}]$, and so for the $[M_{pcon}]$, $[M_{con}]$. Equation (2.14) can thus be written as:

$$[M_{con}]\{\boldsymbol{\sigma}\}-[M_{conm}]P_m - [M_{conp}]P_P = \{u_{con}\} \tag{2.15}$$

The $[M_{con}]$, $[M_{conm}]$, $[M_{conp}]$ are the matrix related to rock properties, downhole pressures, and the location of the cross-sections.

In petroleum drilling, drilling mud is injected into the well to control underground pressure, lubricate drill bits and suspend cuttings. The underground formation nearby the oil or gas reservoir can be seen as the porous media saturated with stressed fluids. As the drilling mud intrudes into the formation driven by the pressure difference between mud and pore fluid, part of the solid mud particles will be filtered by the porous media and format a mud-cake layer sticking tightly on the wellbore surface. The mud cake layer is easy to be formed in high permeability rock formation and can prevent drilling fluid loss. This will affect the stress around the wellbore.

Considering different properties of the mud cake and rock mass, Dr. Lin developed five comprehensive models for both 2D and 3D analyses: 1) non-porous rock, 2) high permeability rock & permeable mud cake, 3) high permeability & non-permeable mud cake, 4) low permeability rock & permeable mud cake, 5) low permeability rock & non-permeable mud cake (Cui Lin and Steve Zou 2019). For those five models, the detailed equations for the calculation of $[M_{conm}]$($[M_m]$), $[M_{conp}]$ ($[M_p]$), $[M_{con}]$ ($[M]$) are also different.

In conclusion, there is now a back-analysis method for determining the 3D in-situ stresses in petroleum engineering – the D3 stress estimation method. Compared with other methods, it is more practical and cost-effective since most of the desired data can be obtained through the necessary well-logging works.

CHAPTER 3 AUTOMATION OF ANALYSIS FOR THE BACK-ANALYSIS METHOD OF IN-SITU STRESS ESTIMATION

In order to realize the automated analysis and visualization of the above-stated back-analysis method, two independent Windows applications for the 2D and 3D stress analyzes need to be developed, respectively. The applications are expected to process the input data, complete calculations, display the back-analyzed stress results on the screen, and allow users to export the data to a text file. In the first step, two C++ based-console applications are developed to accomplish the calculation task. The console application is a computer program with a text-only interface. In comparison to the Windows applications with GUI (Graphical User Interface), console applications can be developed in a shorter period. Consequently, the potential bugs and basic logic of the source code of these applications can be efficiently rectified and improved.

Followed by the development of two console applications, two independent MFC applications with graphic user-interface are designed. The console applications can be deemed as the prototype of MFC applications, and the source codes of the former are fully implanted into the latter.

3.1 CONSOLE APPLICATION FOR 2D IN-SITU STRESS ESTIMATION

In order to develop the console application for the 2D in-situ stress analysis model (2D console application for short), the C++ language is selected as the programming language. C++ is an object-oriented language that encompasses concepts such as classes, inheritance, and data abstraction that make its code reusable and reliable (Seban 1994). Besides, it is also compatible with various computer operating systems, for example, Linux and Windows.

Dev C++ is selected as a developing tool for the console application. It is a full-featured integrated development environment (IDE) and equipped with the most prevalent C++ compiler – GCC, which is distributed under the GNU General Public License. The compiler is necessary for the development of applications, which is responsible for translating the source code into objective code for programming. The source code is the human-readable instructions written by programmers. It is the fundamental component of a computer application, and the entire source code for the console applications is written in C++ language. The source code is not functional until it is translated into the computer-executable code by the compiler. The interface of Dev C++ is concise and clear (as displayed in Figure 3.1), and it is also easy to get started, especially for beginners.

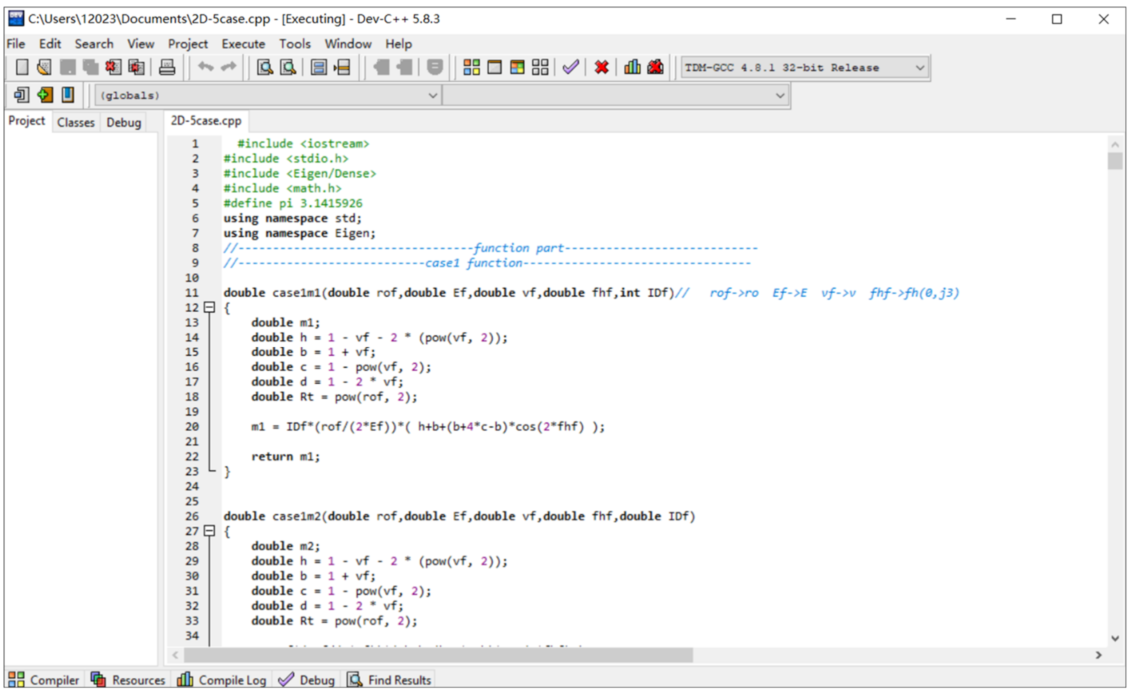

Figure 3.1 Interface of Dev C++

The development of the console application starts with the CPP file, which is the file that contains all of the source codes written by the programmer. When the CPP file is debugged and prepared, the Dev C++ will be used to compile the CPP file and create an executable file (exe file). The exe file is a computer file that runs a program. When it is opened, the source code instructions will be executed.

The source code of the 2D console application can be divided into four sections: pre-processing, input, calculation, and output.

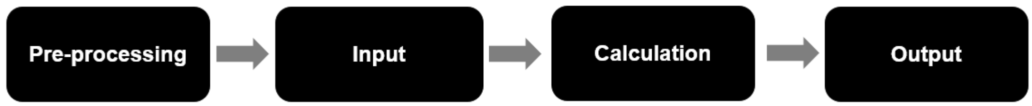

Figure 3.2 Four sections of the source code

At the initial section of pre-processing, all the library functions and related source files are defined and processed by the pre-processor, which is a stand-alone program of the compiler. Since many matrix calculations are involved in the in-situ stress estimation, a template library – Eigen is invoked in this part to facilitate calculation. Eigen is a free template library for linear algebra based on C++ language, and it does not contain any dependencies or links to any binary library.

In the input section, the program will automatically open an external input file and read data from it. The input file is a text file that stores the input data. These data are restricted by a standardized format, and users are required to type the value of desired parameters into the file through a keyboard. It should be noted that the format of the characters typed in must follow the sample file; otherwise, the program can not recognize any datum from it.

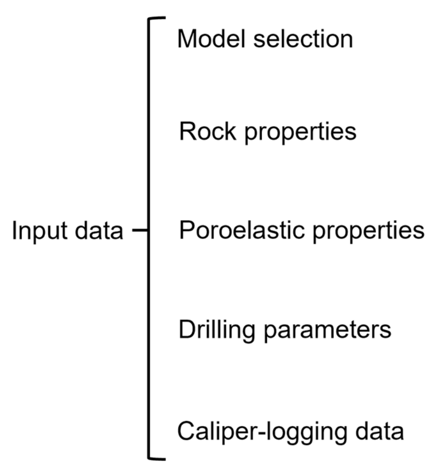

Figure 3.3 Input data of the console application

The input data can be divided into five parts: model selection, rock properties, poroelastic properties, drilling parameters, and caliper-logging data (Figure 3.3). As mentioned in the literature review, the back-analysis method includes five comprehensive models considering the different field conditions of permeability, pore pressure, and mud pressure in the petroleum field. Consequently, in the model selection part of the input data, model numbers 1, 2, 3, 4, 5 denote the condition of non-porous rock, high permeability rock and permeable mud cake, high permeability rock and non-permeable mud cake, low permeability rock, and permeable mud cake, low permeability rock, and non-permeable mud cake, respectively. The rock properties parameters include Young's modulus, Poisson's ratio, and poroelastic properties contain Biot's coefficient, porosity and Skempton's coefficient. Drilling parameters include well radius, pore pressure, and mud pressure. Caliper-logging data consist of the measured borehole diameters and the orientations for the measurement points. It should be noted that at least four groups of borehole diameters must be typed into the input file of the 2D console application, according to Dr.Lin (Lin and Zou 2016).

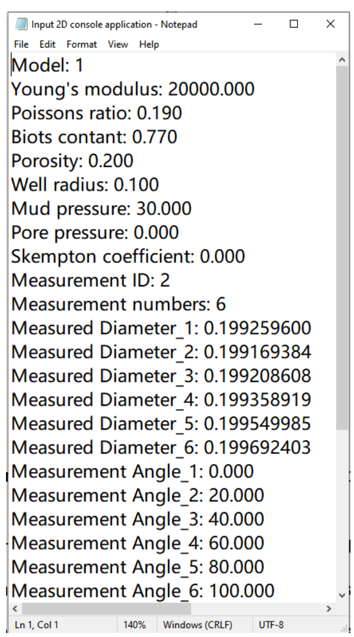

Model: 1
Young's modulus: 20000.000
Poissons ratio: 0.190
Biots contant: 0.770
Porosity: 0.200
Well radius: 0.100
Mud pressure: 30.000
Pore pressure: 0.000
Skempton coefficient: 0.000
Measurement ID: 2
Measurement numbers: 6
Measured Diameter_1: 0.199259600
Measured Diameter_2: 0.199169384
Measured Diameter_3: 0.199208608
Measured Diameter_4: 0.199358919
Measured Diameter_5: 0.199549985
Measured Diameter_6: 0.199692403
Measurement Angle_1: 0.000
Measurement Angle_2: 20.000
Measurement Angle_3: 40.000
Measurement Angle_4: 60.000
Measurement Angle_5: 80.000
Measurement Angle_6: 100.000

Figure 3.4 Input text file of 2D console application

The data obtained from the input file (Figure 3.4) are assigned to the related variables which are pre-defined in the program. In the following calculation section, the program will check the reasonability of each variable and calculate the in-situ stress components based on them.

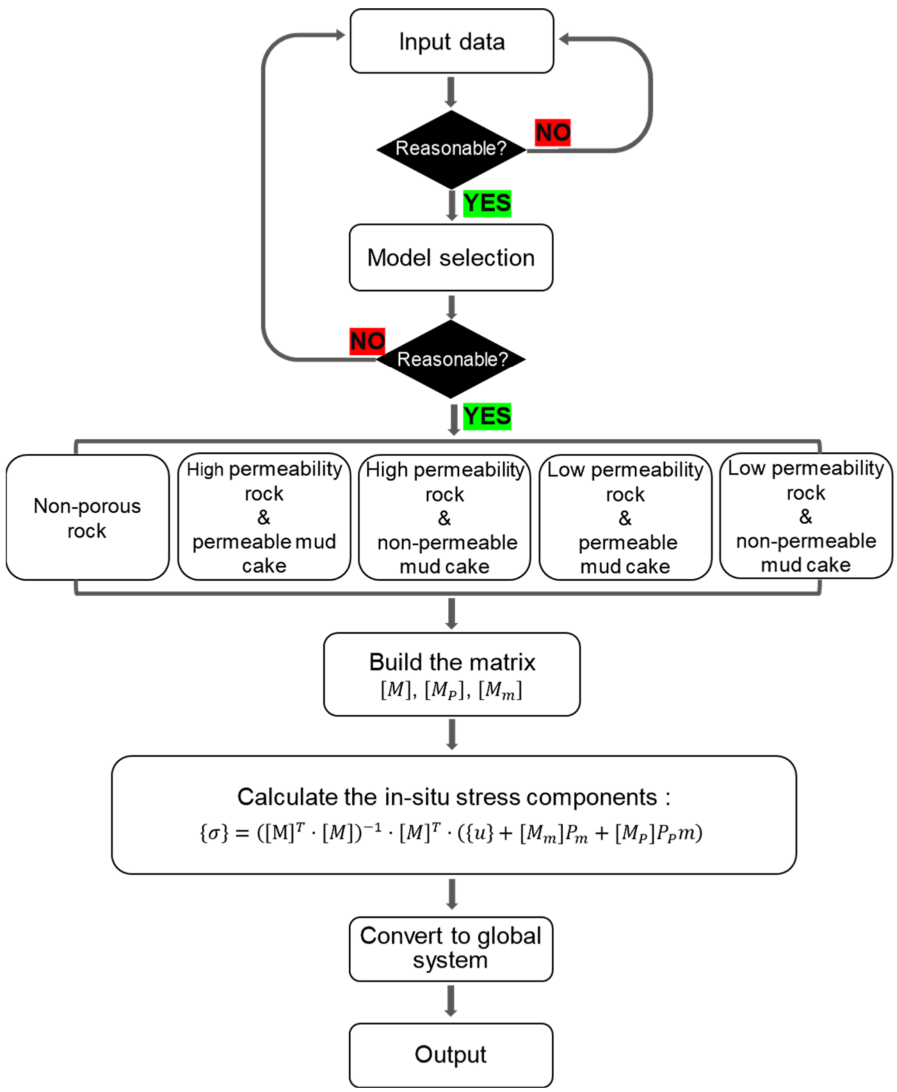

Figure 3.5 Flow chart of the 2D application's calculation part

Figure 3.5 shows the flow chart of the calculation sequence. The program invokes the input data at the beginning. Then, it will process the information of model selection and pick up one of the five comprehensive models. According to the source code of formulas in the selected model, each row of the matrix $[M]$, $[M_m]$, $[M_P]$ are calculated separately and combined together. Subsequently, the program will forward to solve the 2D in-situ stress components ($\{\sigma\}$) through the least square method with Equation (3.1):

$$\{\sigma\} = ([M]^T \cdot [M])^{-1} \cdot [M]^T \cdot (\{u\} + [M_m]P_m + [M_P]P_Pm) \tag{3.1}$$

Since the stress components σ_x, σ_y, τ_{xy} encompassed in $\{\sigma\}$ are the in-situ stresses in a local coordinate system, the program will further convert them into the global coordinate system, for which the shear stress τ_{xy} equals zero. In the research, a horizontal measurement plane in a vertical wellbore is investigated, and the North-East coordinate system is selected as the global coordinate system. Thus the stress state of the investigated plane can be described by the maximum horizontal component σ_H and the minimum horizontal component σ_h. In the last stage of the calculation part, the program will export the $\{\sigma_x, \sigma_y, \tau_{xy}\}$, $\{\sigma_H, \sigma_h\}$, and the orientation of the σ_H to a particular output text file automatically.

Aiming at preventing human errors when users typing the input data and guaranteeing the program can obtain all of the necessary parameters, the instructions of reasonability judgments are assigned to the following conditions:

1) Whether the value of each input datum is in an acceptable range.

2) Whether the input data match the model selection.

3) Whether the size of each matrix is reasonable.

4) Whether the program obtains sufficient data from the input text file.

Once the program detects the conditions mentioned above as unreasonable, a warning dialogue will pop out to remind users to check and retype the input data. For example, Figure 3.6 illustrates the source code related to the input of Young's modulus, which is represented by the letter “E.”

```
while (fscanf(fp, "Young's modulus: %lf", &E))
{
    if (E > 0) break;
    cout << "Not in reasonable range (E>0), please check!" << endl;
    fprintf(fpw, "Not in reasonable range (E>0), please check!");
    return 0;
}
```

Figure 3.6 Young's modulus reasonability judgment

It can be seen that an "if" conditional instruction is included in a "While" loop, and only when the value of Young's modulus is positive, the program will break out of the loop to process the following statements. Otherwise, the program will be interrupted to remind the user to make a correction through a warning dialogue, as displayed in Figure 3. 7.

```
C:\Users\12023\Documents\2D-5case.exe
Not in reasonable range (E>0), please check!
--------------------------------
Process exited after 1.066 seconds with return value 0
```

Figure 3.7 Warning dialogue

In the final output section of the source code, the calculated in-situ stress result will be exported to an output text file, as shown in Figure 3.8. It displays the magnitude of the in-situ stress components in the local coordinate system (σ_x, σ_y, τ_{xy}), the stress components in the global coordinate system (σ_{Max}, σ_{Min}), and the direction of the σ_{Max}. The letter "σ" is replaced by the "Sigma" in the text file due to the conflicts between the source code and the special Greek letter. Furthermore, if the program is interrupted due to unreasonable input data, the corresponding prompt information will also be recorded in the output file.

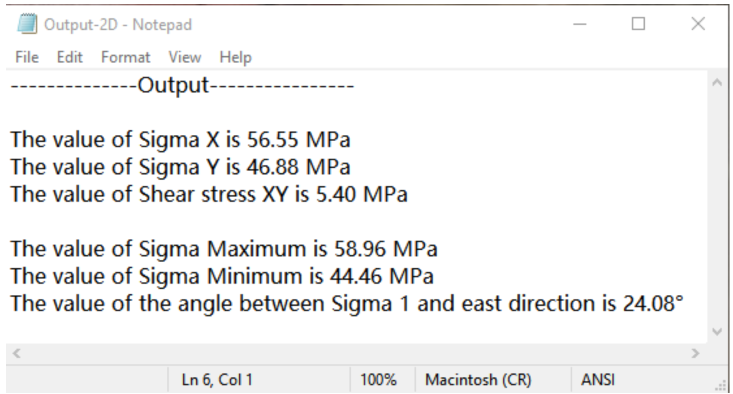

Figure 3.8 Output text file of 2D console application

The four basic sections of the 2D console application's source code have been illustrated above. After the source code is compiled and run successfully, the executable file (exe file) of the console application is generated at the same file path as the CPP file. It is a stand-alone program with a small volume of merely 2.2 megabits (Figure 3.9), which means users can download the application package conveniently.

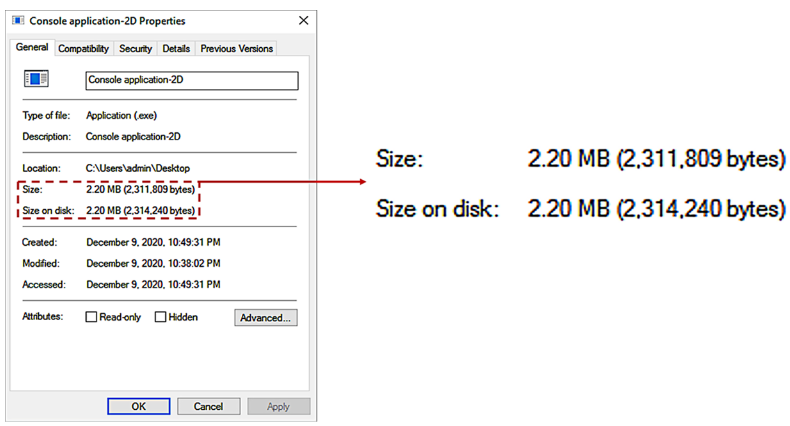

Figure 3.9 Properties page of the 2D console application's executable file

Since the content in the input text file must follow a standard format, a sample input file is packaged together with the executable file.

3.2 OPERATION PROCEDURES OF THE 2D CONSOLE APPLICATION

The operation procedure of the 2D console application is straightforward, which contains three concise steps:

a) Download and decompress

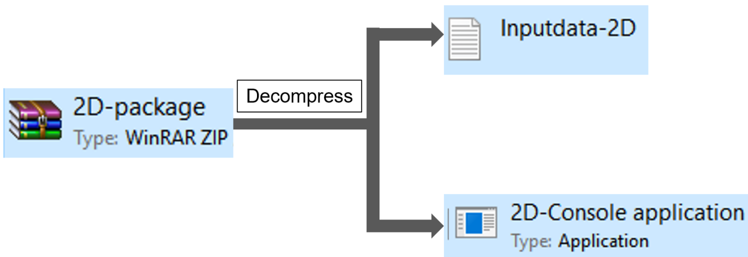

b) Open the text file and input the required data

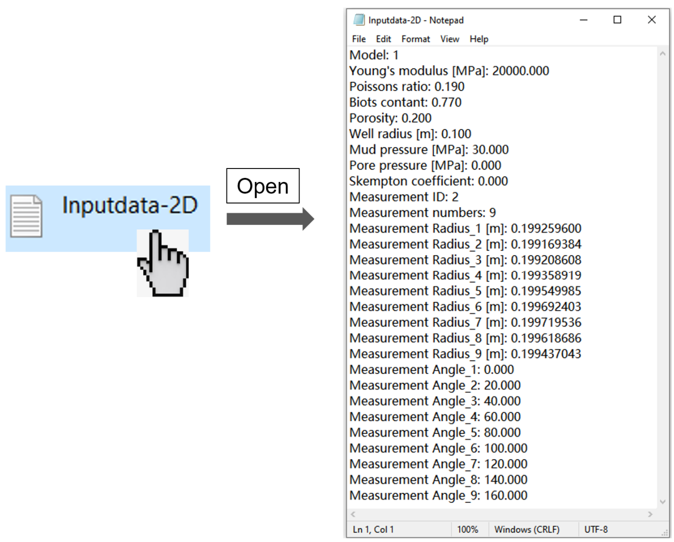

c) Click the executable file to generate the output text file

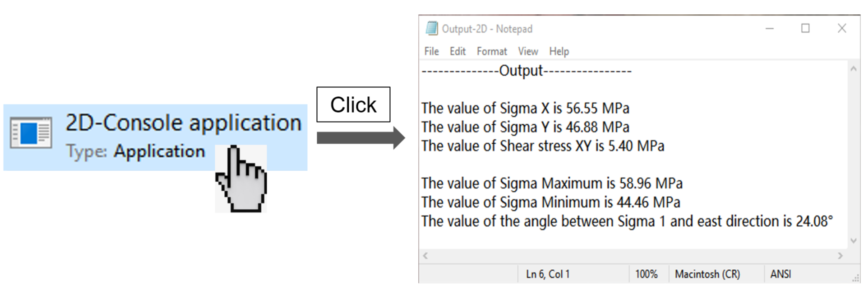

The users should download and decompress the application package to their computer.

Then, the desired data of caliper-logging, rock properties, drilling parameters, and model selection should be typed into the input text file according to the format of the sample file. When all the required data are typed in the input text file and saved, the users can double click the icon of the executable file of the 2D console application to run the program. The calculation and back analysis process only take a few seconds, and an output text file will be generated automatically, where the final analysis results are shown in.

3.3 CONSOLE APPLICATION FOR 3D IN-SITU STRESS ESTIMATION

The 3D console application is also a C++-based program and developed through Dev C++. The structure of the 3D console application's source code is similar to the 2D application, which can be divided into pre-processing part, input part, calculation part and output part. The pre-processing part is exactly the same for both applications, whereas the input part for these two applications differs in the required parameters. Compared with the 2D application, the 3D application requires obtaining the drilling parameters, rock properties, and convergence data from three non-parallel wells or measurement planes. A sample input text file for the 3D console application is shown in Figure 3.10. This sample file is also attached to the application package so that users can directly modify the value of input parameters in it.

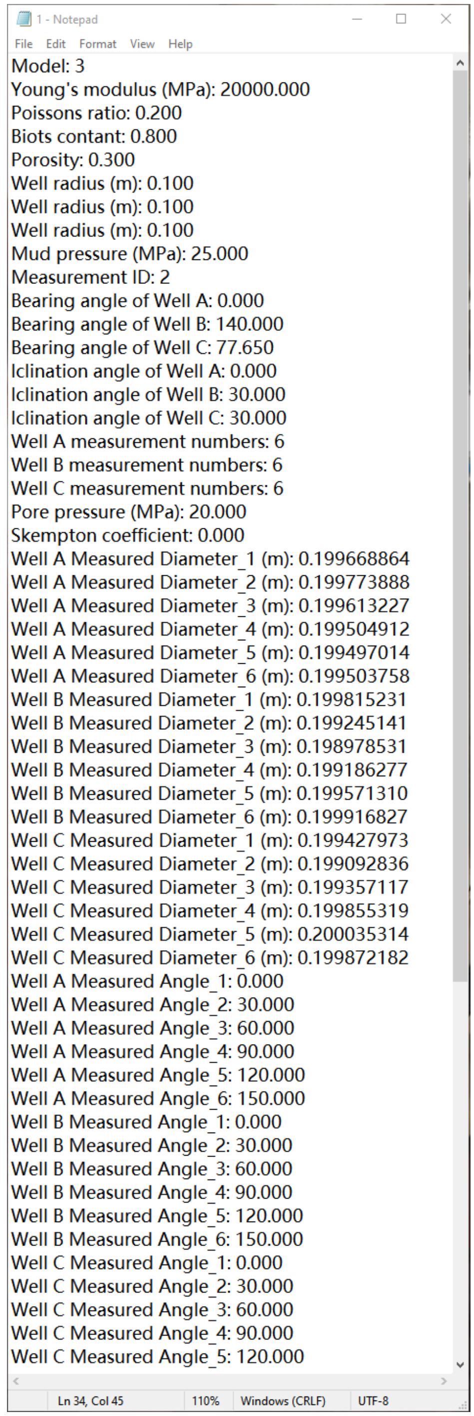

1 - Notepad
File Edit Format View Help
Model: 3
Young's modulus (MPa): 20000.000
Poissons ratio: 0.200
Biots contant: 0.800
Porosity: 0.300
Well radius (m): 0.100
Well radius (m): 0.100
Well radius (m): 0.100
Mud pressure (MPa): 25.000
Measurement ID: 2
Bearing angle of Well A: 0.000
Bearing angle of Well B: 140.000
Bearing angle of Well C: 77.650
Iclination angle of Well A: 0.000
Iclination angle of Well B: 30.000
Iclination angle of Well C: 30.000
Well A measurement numbers: 6
Well B measurement numbers: 6
Well C measurement numbers: 6
Pore pressure (MPa): 20.000
Skempton coefficient: 0.000
Well A Measured Diameter_1 (m): 0.199668864
Well A Measured Diameter_2 (m): 0.199773888
Well A Measured Diameter_3 (m): 0.199613227
Well A Measured Diameter_4 (m): 0.199504912
Well A Measured Diameter_5 (m): 0.199497014
Well A Measured Diameter_6 (m): 0.199503758
Well B Measured Diameter_1 (m): 0.199815231
Well B Measured Diameter_2 (m): 0.199245141
Well B Measured Diameter_3 (m): 0.198978531
Well B Measured Diameter_4 (m): 0.199186277
Well B Measured Diameter_5 (m): 0.199571310
Well B Measured Diameter_6 (m): 0.199916827
Well C Measured Diameter_1 (m): 0.199427973
Well C Measured Diameter_2 (m): 0.199092836
Well C Measured Diameter_3 (m): 0.199357117
Well C Measured Diameter_4 (m): 0.199855319
Well C Measured Diameter_5 (m): 0.200035314
Well C Measured Diameter_6 (m): 0.199872182
Well A Measured Angle_1: 0.000
Well A Measured Angle_2: 30.000
Well A Measured Angle_3: 60.000
Well A Measured Angle_4: 90.000
Well A Measured Angle_5: 120.000
Well A Measured Angle_6: 150.000
Well B Measured Angle_1: 0.000
Well B Measured Angle_2: 30.000
Well B Measured Angle_3: 60.000
Well B Measured Angle_4: 90.000
Well B Measured Angle_5: 120.000
Well B Measured Angle_6: 150.000
Well C Measured Angle_1: 0.000
Well C Measured Angle_2: 30.000
Well C Measured Angle_3: 60.000
Well C Measured Angle_4: 90.000
Well C Measured Angle_5: 120.000
Ln 34, Col 45 110% Windows (CRLF) UTF-8

Figure 3.10 Input text file of 3D console application

It should be noted that at least four groups of caliper-logging data are required to be gathered from each wellbore (12 groups in total) and typed into the input file, according to Dr. Lin's theory (Lin and Zou 2019).

The program structure for the calculation part of the two applications are comparable: Similar reasonability judgments are assigned for the input section, five comprehensive models are involved, the least squared method is applied to solve the in-situ stress, and the in-situ stress components are further converted from local to the global coordinate system. The detailed equations for the calculation part are referred from Dr.Lin (Lin and Zou 2019). Furthermore, the Eigen library is also invoked in the 3D application to facilitate the matrix operations.

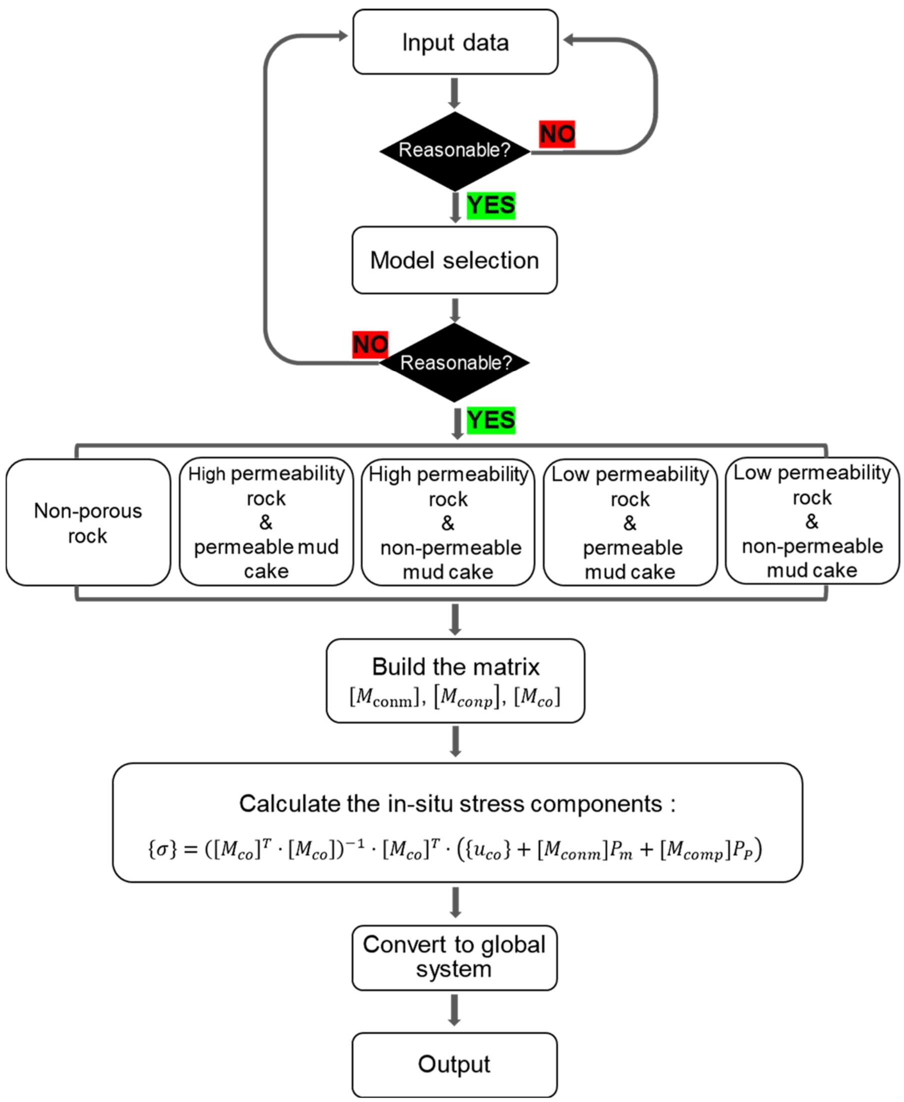

Figure 3.11 Flow chart of the 3D console application's calculation part

After the input data are processed and the calculation is complete, the analysis results will also be displayed automatically and saved in an output text file.

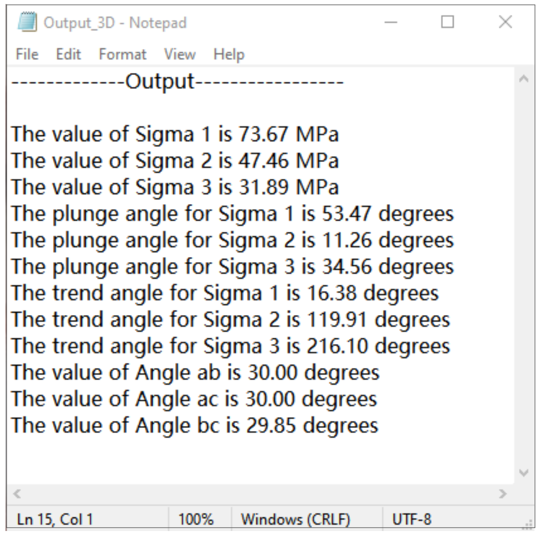
Output_3D - Notepad
File Edit Format View Help
-------------Output-----------------

The value of Sigma 1 is 73.67 MPa
The value of Sigma 2 is 47.46 MPa
The value of Sigma 3 is 31.89 MPa
The plunge angle for Sigma 1 is 53.47 degrees
The plunge angle for Sigma 2 is 11.26 degrees
The plunge angle for Sigma 3 is 34.56 degrees
The trend angle for Sigma 1 is 16.38 degrees
The trend angle for Sigma 2 is 119.91 degrees
The trend angle for Sigma 3 is 216.10 degrees
The value of Angle ab is 30.00 degrees
The value of Angle ac is 30.00 degrees
The value of Angle bc is 29.85 degrees

Ln 15, Col 1 | 100% | Windows (CRLF) | UTF-8

Figure 3.12 The output text file of the 3D console application

As can be seen from Figure 3.12, the output file illustrates the magnitude and orientations of the three principal stress components. The orientations are indicated by the plunge angle and trend angle. Specifically, the plunge angle is the angle in a vertical plane between the stress vector and the horizontal plane, which varies between 0 degrees to 90 degrees, as displayed in Figure 3.13.

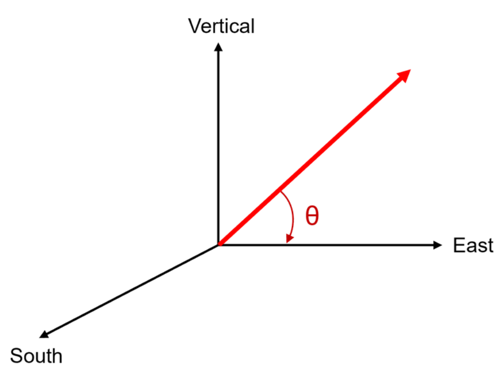

Figure 3.13 The plunge angle

The trend angle is the angle between the direction of the horizontal components of the stress vector and the direction of the North axis, positive clockwise. As can be seen from Figure 3.14, the angle is counted in a clockwise way from the direction of the North axis.

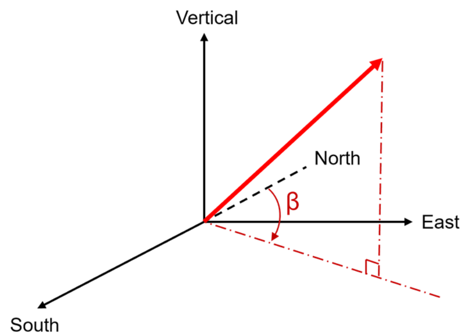

Figure 3.14 The trend angle

In addition, the space angles between the orientations of each two wellbores are also displayed in the output file. The “Angle ab” represents the space angle between the orientations of well A and well B, “Angle bc” is for well B and well C, and “Angle ac”.is for well A and well C.

The application’s executable file is generated when its source code file is compiled. Figure 3.15 is the properties page of the executable file, and its size is 2.26 megabits, which is only 0.06 megabits bigger than the 2D console application.

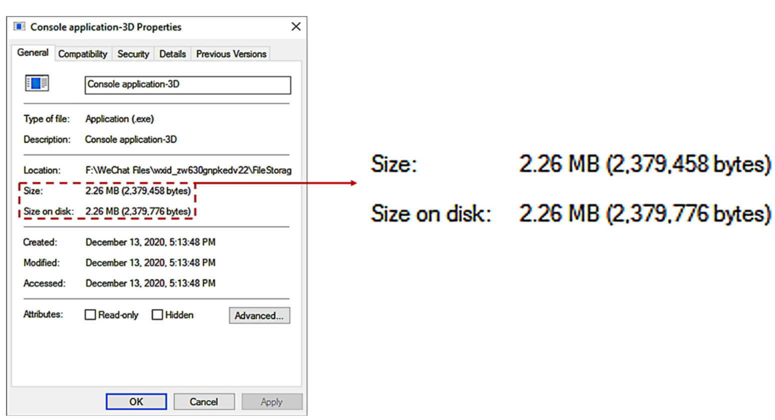

Figure 3.15 Properties page of the 3D console application’s executable file

3.4 OPERATION PROCEDURES OF THE 3D CONSOLE APPLICATION

The operation procedures for the 3D console application are similar to the 2D application, which include three steps:

a) Download and decompress

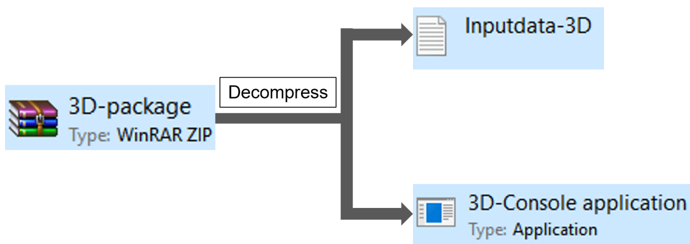

c) Open the text file and input the required data

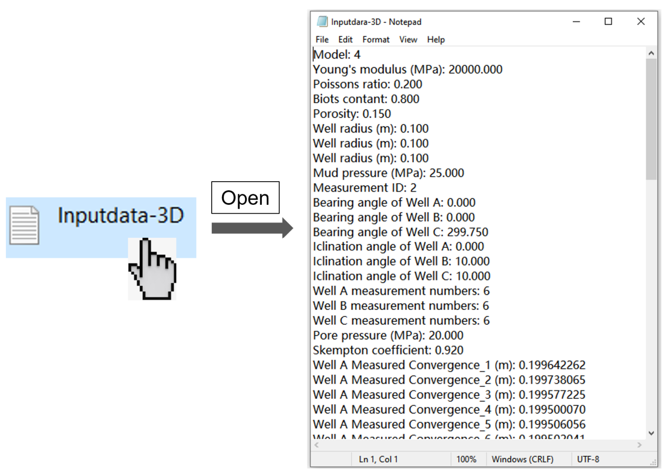

b) Click the executable file to generate the output text file

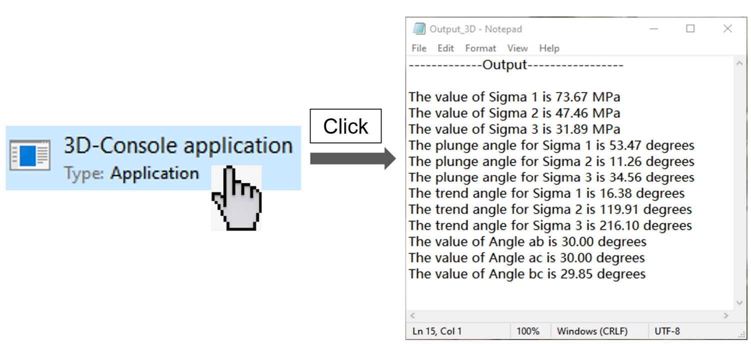

The two applications' development process, structure of the source code, and instruction of the user operation have already been illustrated.

The overall framework of the 3D console application is similar to that of the 2D application. They are developed by the same compiler, and the logic construction of their source code is consistent. Both applications have a small file size, which guarantees users' convenience during the uploading and downloading process. The drawbacks of the console application are also evident:

1) There is no graphic user interface for both console applications.
2) The strict restriction of the input text file format greatly impacts the user experience. As mentioned above, users must follow the format of the sample file when they are compiling the input data. Once an extra space or letter is deleted or add carelessly, the input data will not be read by the application, and it is tough to find where the problem is when going back to check a text file with approximately 60 rows.
3) The input file is limited to stay in the same path as the executable file. There is no option for the user to load the input file in other paths from their storage disk. In order to improve the application according to these shortcomings, Windows applications with graphic user interfaces and necessary ancillary functions need to be developed. Consequently, two MFC applications based on the two console applications are designed and created in the subsequent studies.

3.5 MFC APPLICATION FOR 2D IN-SITU STRESS ESTIMATION

In the design of the MFC application, the developing tool is switched from Dev C++ to VS 2013 (Visual Studio 2013). The VS 2013 is a more powerful and multifunctional IDE (integrated development environment) provided by Microsoft, and its Microsoft Foundation Class Library (MFC), which is a C++ object-oriented library, can help to develop an independent desktop application – MFC application.

Since the MFC applications are developed based on the console applications and belong to C++-based programs, the source code of the console application's calculation part can be fully implanted into the MFC applications. After figuring out the calculation part, the remaining required part to be designed is the arrangement of the GUI and the necessary functions. Under the guide of Dr.Zou and Dr.Lin, the MFC application based on the 2D in-situ stress model (2D application for short) is developed.

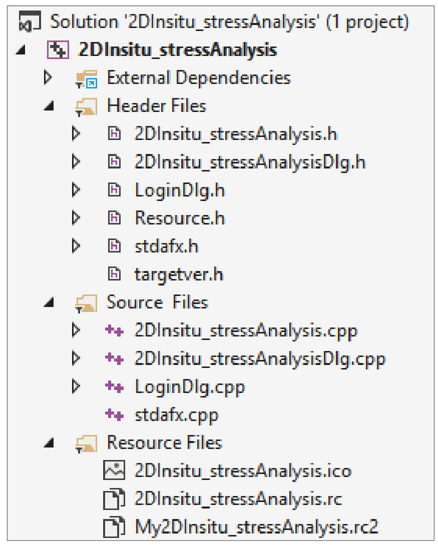

Figure 3.16 The solution of the 2D MFC application

Figure 3.16 shows the solution of the 2D MFC application in Visual Studio 2013. The solution is a "container" that contains all the necessary tools and project files to accomplish the development of the applications. The basic parts of the solution for 2D MFC application consist of the following modules:

1) Header files

   The header files include the project headers and declaration of the project class.

2) Source files

   Source files encompass the source code for implementing the basic function of the application and processing the data analysis. It is also the place where the source code from the console application is implanted in.

3) Resource files

   From the suffix ".rc" located in the resource files, programmers could create and design the user interface's properties, styles, and layout.

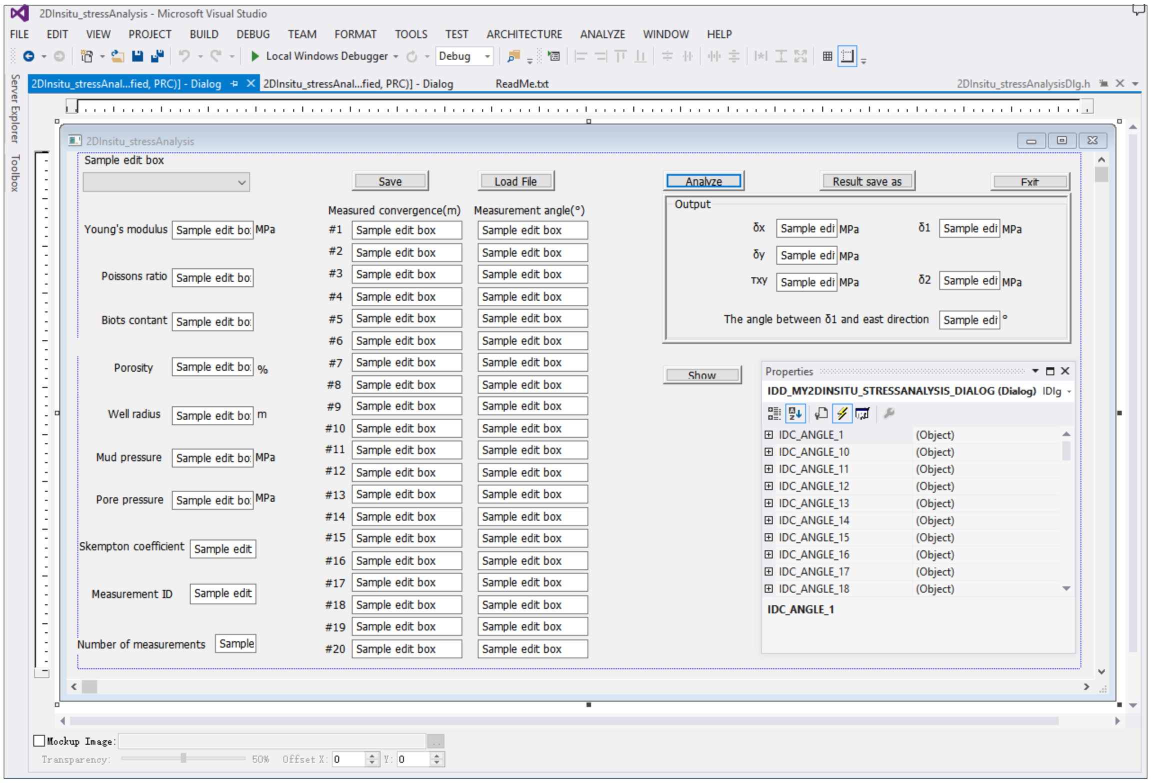

Figure 3.17 Resource view mode of the 2D MFC application

As the file “2DInsitu_stressanalysis.rc” is opened, the resource view dialogue of the UI will show up, as displayed in Figure 3.17. In this mode, the controls, such as the button control, edit box control, and scroll bar control, could be added from the side toolbox, and their properties could be defined from the properties dialogue.

4) External dependencies

The files which are not explicitly added to the header files folder but are nonetheless included using the #include directive are assigned to the external dependencies folder

When all the project files in the solution are prepared, the “Local Windows Debugger” button can be clicked to generate the executable file of the MFC application. Figure 3.18 depicts the properties page of the executable file. It can be seen that the volume of the executable file is merely 9.34 megabits, so the 2D MFC application is a small volume application.

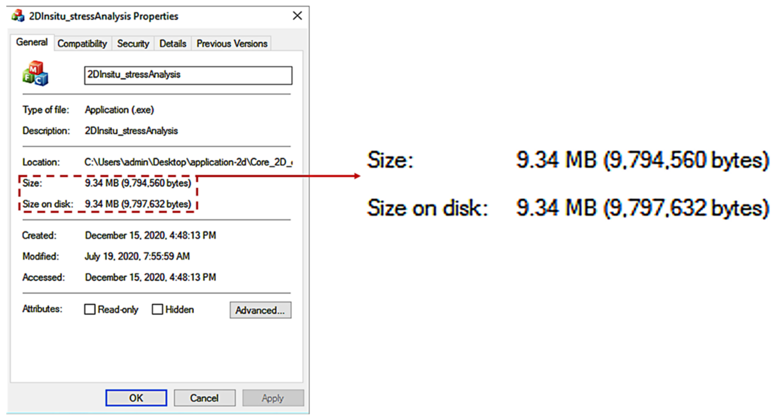

Figure 3.18 The properties page of the 2D MFC application

This MFC application contains two graphic interfaces, which are the log-in interface and the user interface. The log-in interface will pop out once the executable file is double-clicked, from where the users are required to type in the valid combination of the account name and password. All the combinations are pre-defined in the source code part by the programmer.

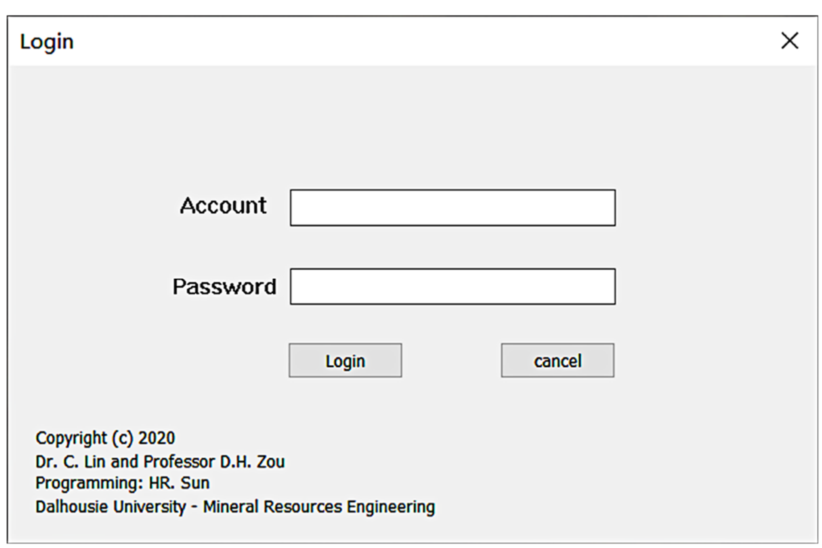

Figure 3.19 Log-in interface of the 2D MFC application

Figure 3.19 depicts the log-in interface of the application. As the program recognizes the valid combination of the account name and the password, the user interface will pop out immediately.

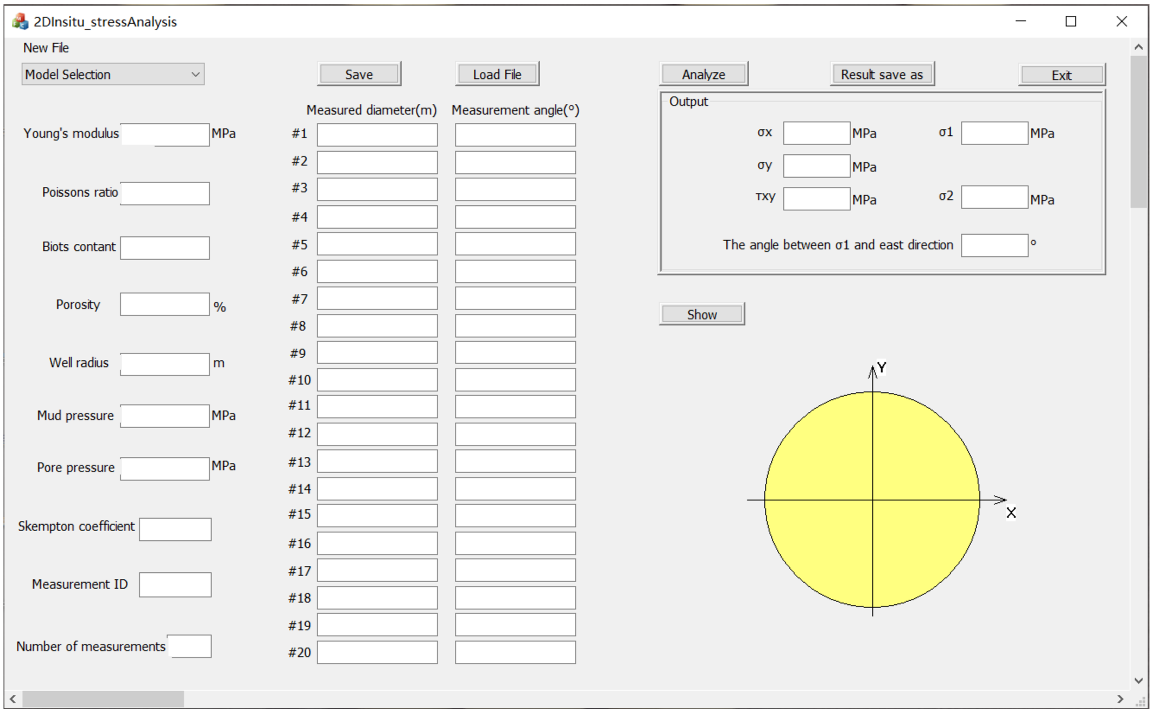

Figure 3.20 User interface of the 2D MFC application

Figure 3.20 displays the user interface of the 2D in-situ stress analysis application. It encompasses a scroll bar, a text label, six buttons, fifty static texts, fifty input edit boxes, six output boxes and a graphics area.

The scroll bar is the square control named “Model selection” located in the interface’s upper left. When it is clicked, the bar will be unfolded to show the five options of the calculation model, as displayed in Figure 3.21.

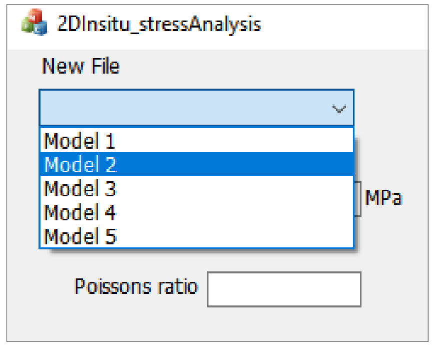

Figure 3.21 Model selection bar

The static texts can not be modified or selected by users, such as the name of the input parameter and the serial number of the borehole convergence data. For each text indicating the name of the input parameters, an edit box is put adjacently to let users type in. Only numerals are allowed to be typed into the edit box.

The parameters required to be input by the users include Young's modulus, Poisson's ratio, Biot's coefficient, porosity, mud pressure, pore pressure, Skempton's coefficient, well radius, number of measurements, measured convergence, measurement angle, and the measurement ID. The "number of measurements" parameter indicates how many measurements are taken by the well-logging caliper. It controls the number of measured convergence and angle data read by the application. For example, If the number of measurements is 7, the application will only read the data of convergence and angle from group 1 to group 7. The measurement ID indicates the measuring mode of the caliper. If the caliper adopts diameter measurement, the measurement ID is 1, and the radius measurement is represented by 2.

The six buttons located in the interface, which are "save," "load file," "analyze," "result save as," "show," and "exit," are used to realize six primary functions as the figure shown below.

Functions

- Save the input data file
- Load the input data file
- Compute
- Display the distribution of measurements
- Export the calculation result
- Exit

Figure 3.22 Functions of the 2D MFC application

During the input process, the users can save the data whenever necessary by clicking the save button, and the datum in each input box will be recorded and saved in a standard text file. It should be noted that the format of the file's content is consistent with the console application's input file. Furthermore, those text files can be edited and re-written to the input boxes by clicking the "load file" button, and the file's name is displayed in the top left corner of the interface.

The graphic area is designed to observe the distribution of the measurement points visually. Since the shape of the borehole is a round circle, a yellow circle with a black outline is drawn at the lower right of the interface to represent the measured cross-section inside the well. An x-y coordinate system is drawn inside the circle to indicate the orientations. When the caliper-logging data are typed into the related edit boxes, the "show" button can be clicked to display the distribution of the measurement point in the graphic area (Figure 3.23). Those points marked with a serial number indicate the location of the caliper's touchpoint around the borehole wall. The serial number of each point refers to the group number of the input convergence data.

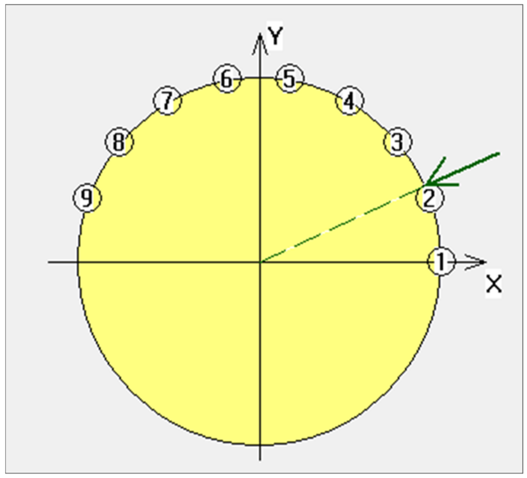

Figure 3.23 Display of the measurement points

The "analyze" button is responsible for processing the input data and performs the calculation section. If the value of some parameters cannot match their reasonable range during the calculation process, a prompt dialogue will pop out to remind the users to recheck the related parameter and reinput (Figure 3.24).

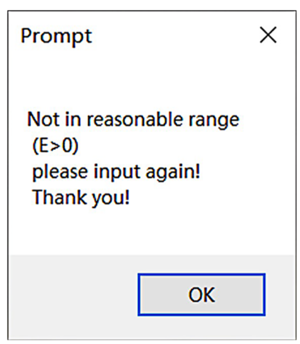

Figure 3.24 Prompt dialogue

The calculated results are displayed in the output area located in the upper right of the user interface. It encompasses the value of σ_x, σ_y, τ_{xy}, σ_1, σ_2, the angle between σ_1 and positive direction of the X axis. To be specific, the σ_x, σ_y, and τ_{xy} are the 2D in-situ stress components in the local coordinates system. The σ_1 (maximum horizontal in-situ stress) and σ_2 (minimum horizontal in-situ stress) are the 2D in-situ stress components in the global system.

The “Result save as” button is designed for the export function. When the button is clicked, a “save as” dialogue will show up, from where users could export the output data as a text file and save it in a hard disk drive (Figure 3.25).

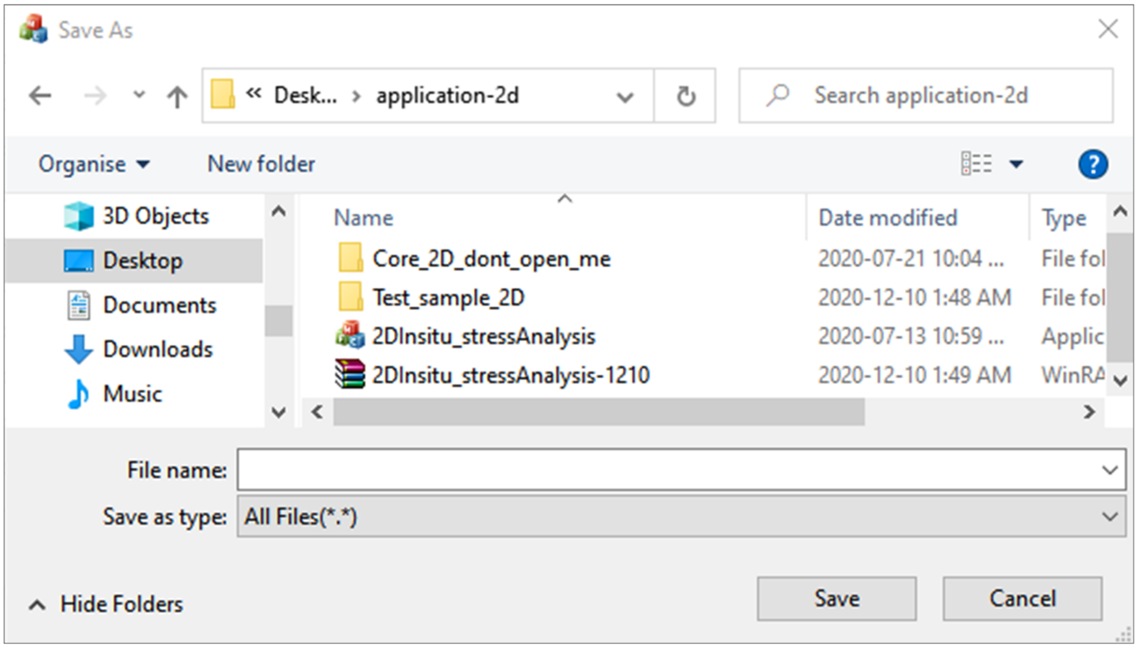

Figure 3.25 “Save as” dialogue

In this exported text file, all the input and output data are recorded. This file can be loaded to the user interface again through the “Load” button. Figure 3.26 shows a sample of the output text file exported from the application.

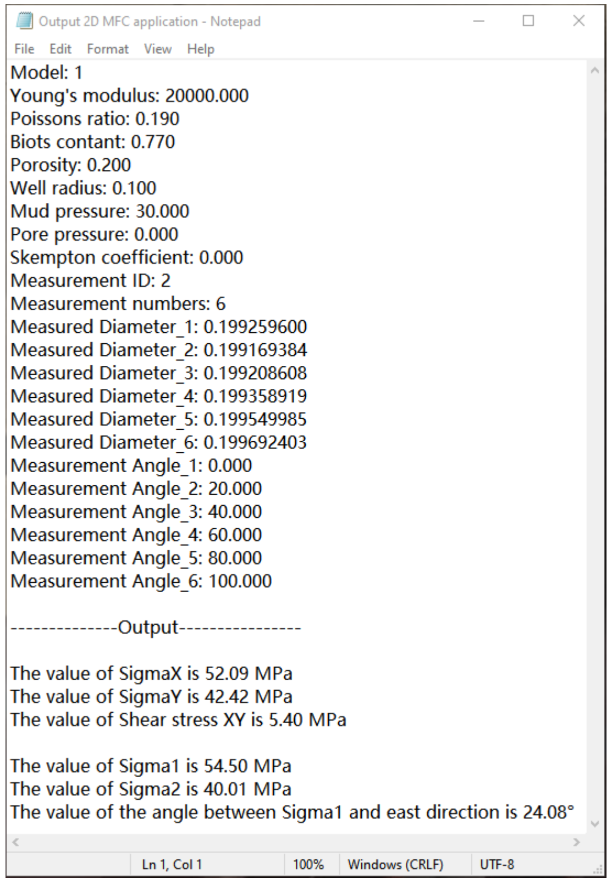

Figure 3.26 Output text file of the 2D MFC application

In the top right of the interface, the “exit” button is used to exit the program. As it is clicked and if the data in the interface are not saved, a prompt dialogue will pop out to remind users to save the file (Figure 3.27). The three options in the dialogue, which are “Yes,” “No,” and “Cancel,” allow users to save the data into a text file, exit the application directly, or go back to the interface.

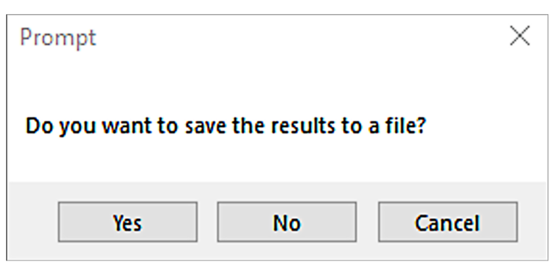

Figure 3.27 Exit prompt dialogue

3.6 OPERATION PROCEDURES OF THE 2D MFC APPLICATION

The user operation procedures for the 2D MFC application can be summarized into the following steps:

a) Download & Decompress

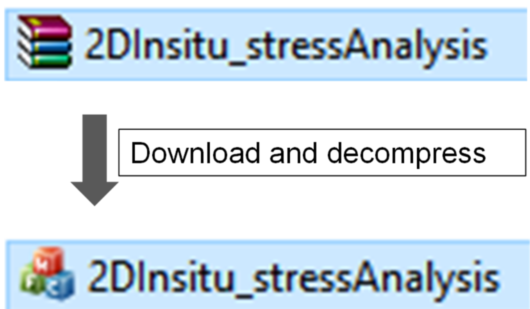

b) Input the required data to the user-interface

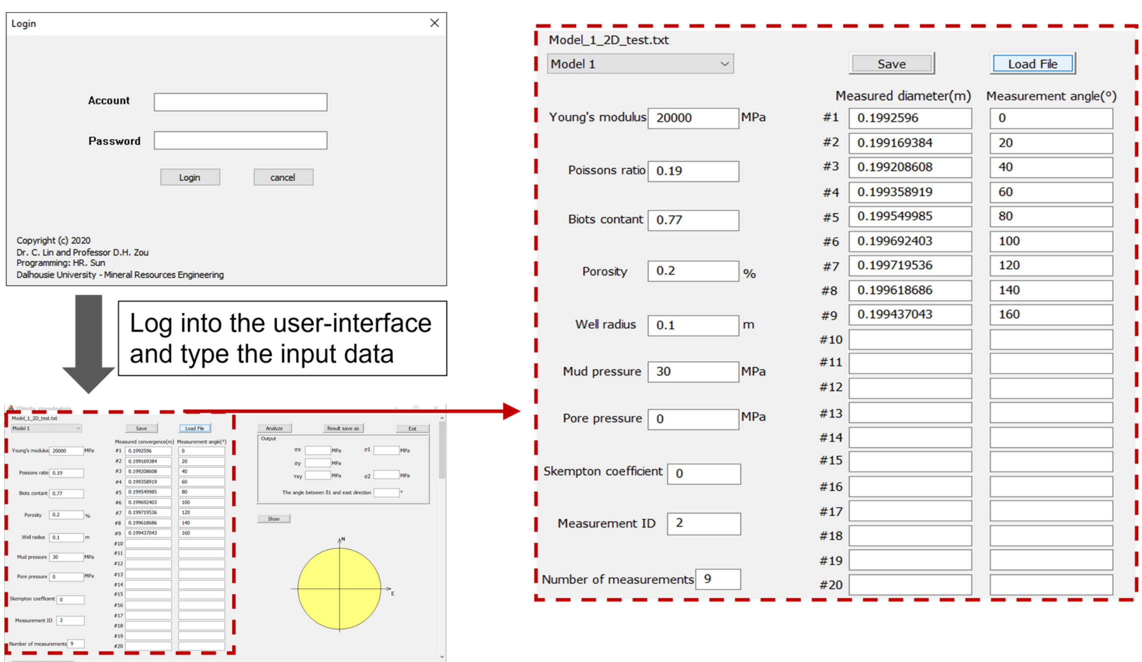

c) Run the application to compute the input data

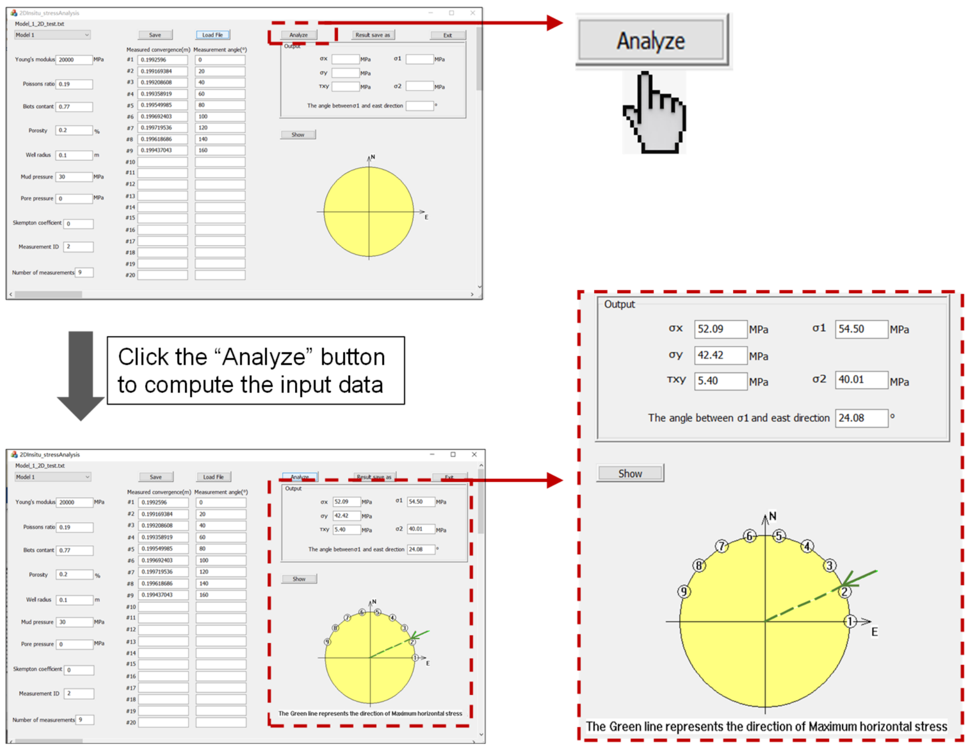

d) Output the results

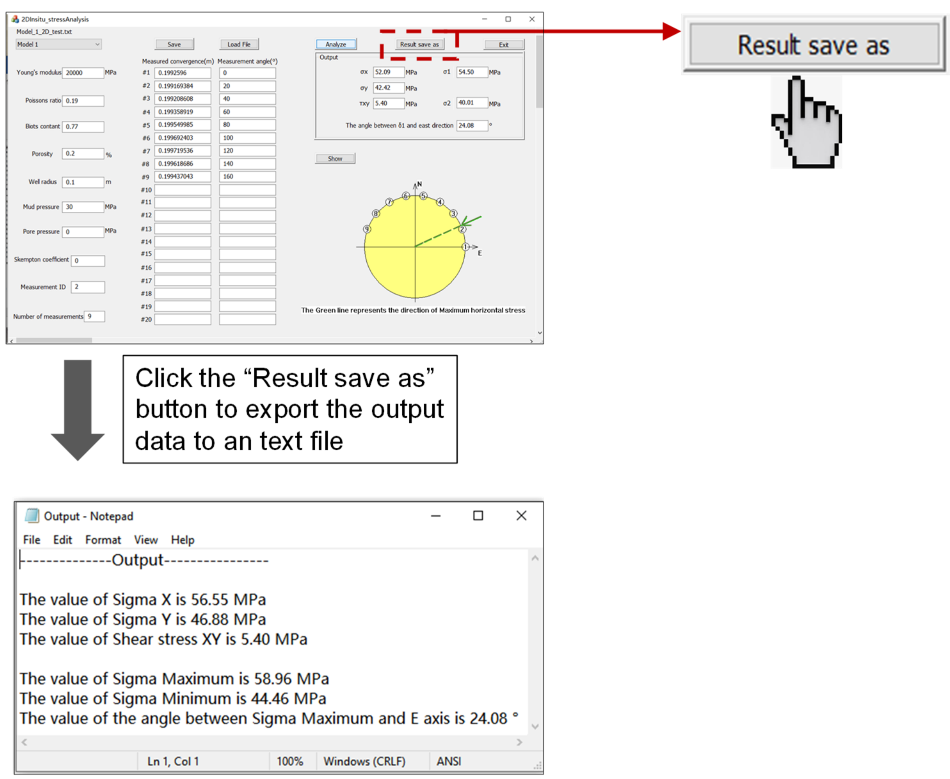

3.7 MFC APPLICATION FOR 3D IN-SITU STRESS ESTIMATION

The MFC application for determining the complete 3D in-situ stress(3D MFC application for short) is also developed through Visual Studio 2013. The structure of the 3D MFC application's solution is similar to that of the 2D application, which consists of header files, source files, resource files, and external dependencies (Figure 3.28). The functions of each file have been illustrated in the former chapter. It should be noted that the source code of the 3D console application's calculation part is completely implanted in the source files of this MFC application.

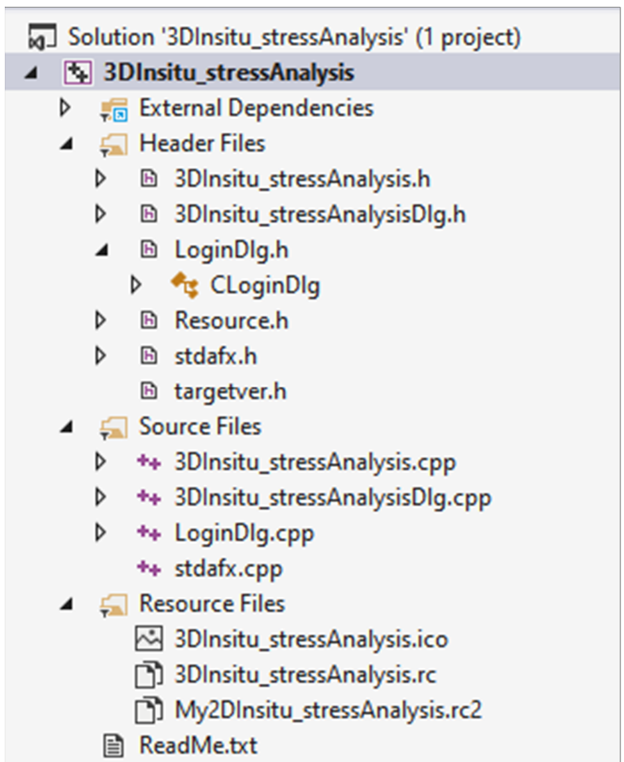

Figure 3.28 The solution of the 3D MFC application

The executable file of the 3D MFC application is depicted in Figure 3.29. As can be seen, the file size is 9.51 megabits, which is close to that of the 2D MFC application.

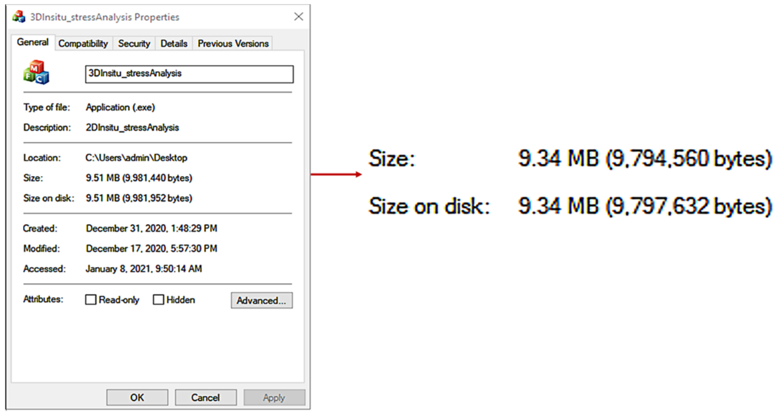

Figure 3.29 The property page of the 3D MFC application

The 3D application is also opened with a log-in interface, which is consistent with the 2D applications'. The user interface will show up when detecting the right combination of the account name and password (Figure 3.30). The primary functions and the related buttons are exactly the same for the 2D application and the 3D application, whereas the user interface is different in several respects. In the input section, the former only required the caliper-logging data from one vertical well, whereas the latter needs the data gathered from three different wellbores, which are indicated by Well A, Well B, Well C in the user interface. For each wellbore, the radius, orientations, number of measurements, caliper-logging data are defined separately. It should be noted that at least three groups of convergence data should be input for each well to fulfill the requirements of the computation.

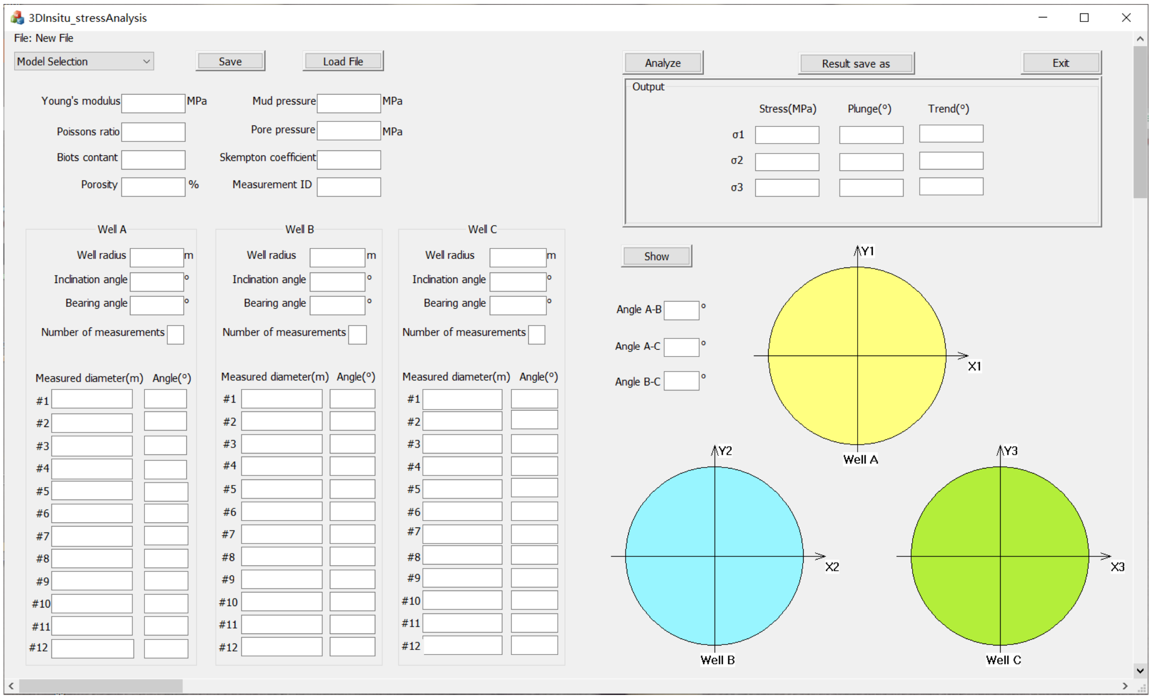

Figure 3.30 The user interface of the 3D MFC application

Three circles filled with yellow, blue, green are drawn in the graphic area to represent the cross-section of well A, B, C, respectively. When activating the show button, the measurement points marked with the corresponding serial number will emerge, as shown in Figure 3.31. In order to reveal the spatial relationship between the three wellbores, the space angles between each two of the three wells are calculated and displayed in the output boxes below the “show” button, named as “Angle A-B,” “Angle A-C,” “Angle B-C.”

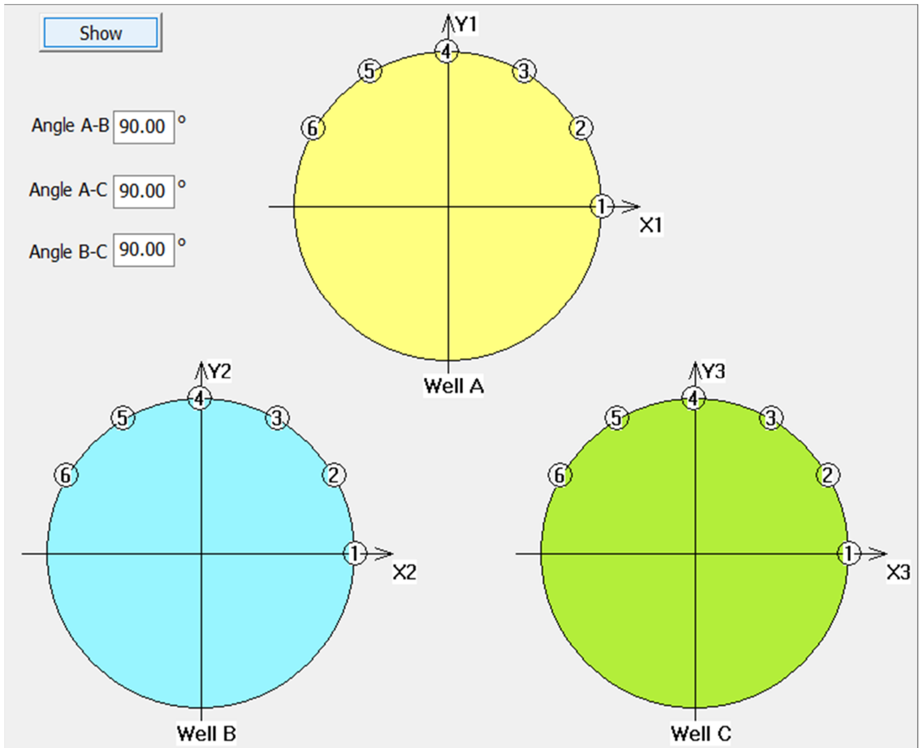

Figure 3.31 The distribution of the measurement points

In the output section of the 3D application, the magnitude and direction of the three principal stress components σ_1, σ_2, σ_3 in the global coordinate system are displayed. The unit of the stress component's magnitude is megapascal, and the orientation is indicated by the plunge and trend angle. Plunge is the angle interval in a vertical plane between the stress and the horizontal plane. Trend is the angle between the horizontal projection of the stress and the North direction counted clockwise. The output text file exported through the "result save as" button is displayed in Figure 3.32.

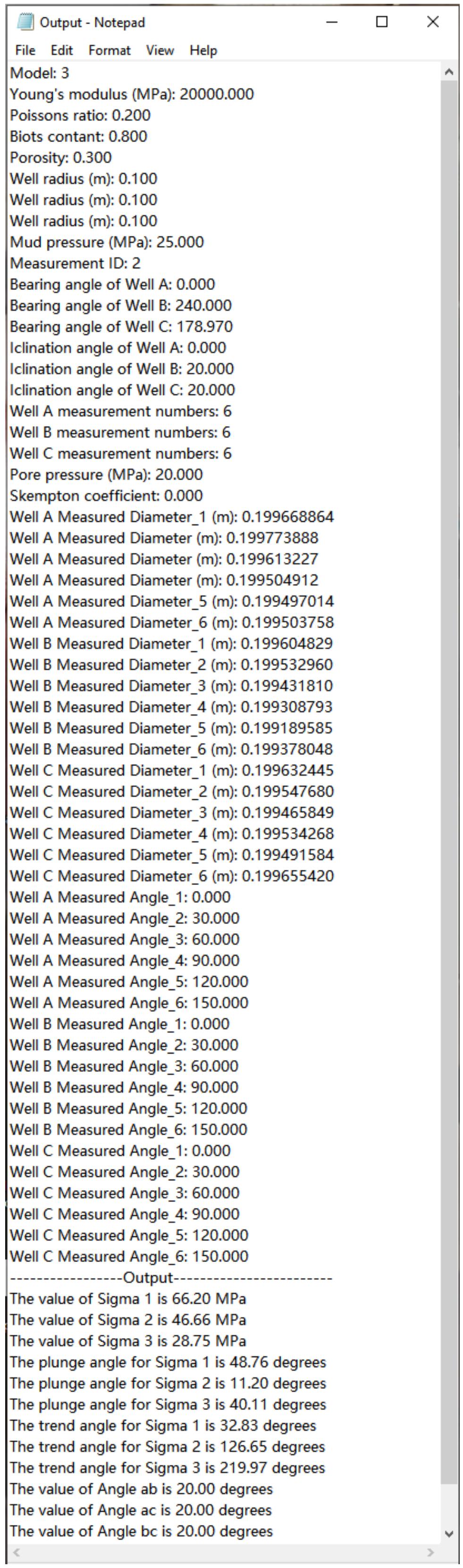

Output - Notepad

File Edit Format View Help

Model: 3
Young's modulus (MPa): 20000.000
Poissons ratio: 0.200
Biots contant: 0.800
Porosity: 0.300
Well radius (m): 0.100
Well radius (m): 0.100
Well radius (m): 0.100
Mud pressure (MPa): 25.000
Measurement ID: 2
Bearing angle of Well A: 0.000
Bearing angle of Well B: 240.000
Bearing angle of Well C: 178.970
Iclination angle of Well A: 0.000
Iclination angle of Well B: 20.000
Iclination angle of Well C: 20.000
Well A measurement numbers: 6
Well B measurement numbers: 6
Well C measurement numbers: 6
Pore pressure (MPa): 20.000
Skempton coefficient: 0.000
Well A Measured Diameter_1 (m): 0.199668864
Well A Measured Diameter (m): 0.199773888
Well A Measured Diameter (m): 0.199613227
Well A Measured Diameter (m): 0.199504912
Well A Measured Diameter_5 (m): 0.199497014
Well A Measured Diameter_6 (m): 0.199503758
Well B Measured Diameter_1 (m): 0.199604829
Well B Measured Diameter_2 (m): 0.199532960
Well B Measured Diameter_3 (m): 0.199431810
Well B Measured Diameter_4 (m): 0.199308793
Well B Measured Diameter_5 (m): 0.199189585
Well B Measured Diameter_6 (m): 0.199378048
Well C Measured Diameter_1 (m): 0.199632445
Well C Measured Diameter_2 (m): 0.199547680
Well C Measured Diameter_3 (m): 0.199465849
Well C Measured Diameter_4 (m): 0.199534268
Well C Measured Diameter_5 (m): 0.199491584
Well C Measured Diameter_6 (m): 0.199655420
Well A Measured Angle_1: 0.000
Well A Measured Angle_2: 30.000
Well A Measured Angle_3: 60.000
Well A Measured Angle_4: 90.000
Well A Measured Angle_5: 120.000
Well A Measured Angle_6: 150.000
Well B Measured Angle_1: 0.000
Well B Measured Angle_2: 30.000
Well B Measured Angle_3: 60.000
Well B Measured Angle_4: 90.000
Well B Measured Angle_5: 120.000
Well B Measured Angle_6: 150.000
Well C Measured Angle_1: 0.000
Well C Measured Angle_2: 30.000
Well C Measured Angle_3: 60.000
Well C Measured Angle_4: 90.000
Well C Measured Angle_5: 120.000
Well C Measured Angle_6: 150.000
----------------Output----------------------
The value of Sigma 1 is 66.20 MPa
The value of Sigma 2 is 46.66 MPa
The value of Sigma 3 is 28.75 MPa
The plunge angle for Sigma 1 is 48.76 degrees
The plunge angle for Sigma 2 is 11.20 degrees
The plunge angle for Sigma 3 is 40.11 degrees
The trend angle for Sigma 1 is 32.83 degrees
The trend angle for Sigma 2 is 126.65 degrees
The trend angle for Sigma 3 is 219.97 degrees
The value of Angle ab is 20.00 degrees
The value of Angle ac is 20.00 degrees
The value of Angle bc is 20.00 degrees

Figure 3.32 Output text file of the 3D MFC application

3.8 OPERATION PROCEDURES OF THE 3D MFC APPLICATION

The user operation procedures for the 3D MFC application can be summarized into the following steps:

a) Download & Decompress

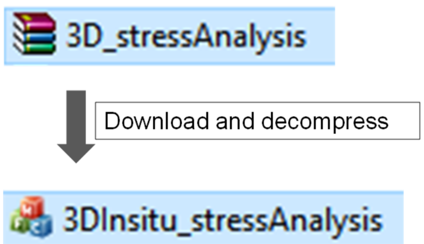

b) Input the required data to the user-interface

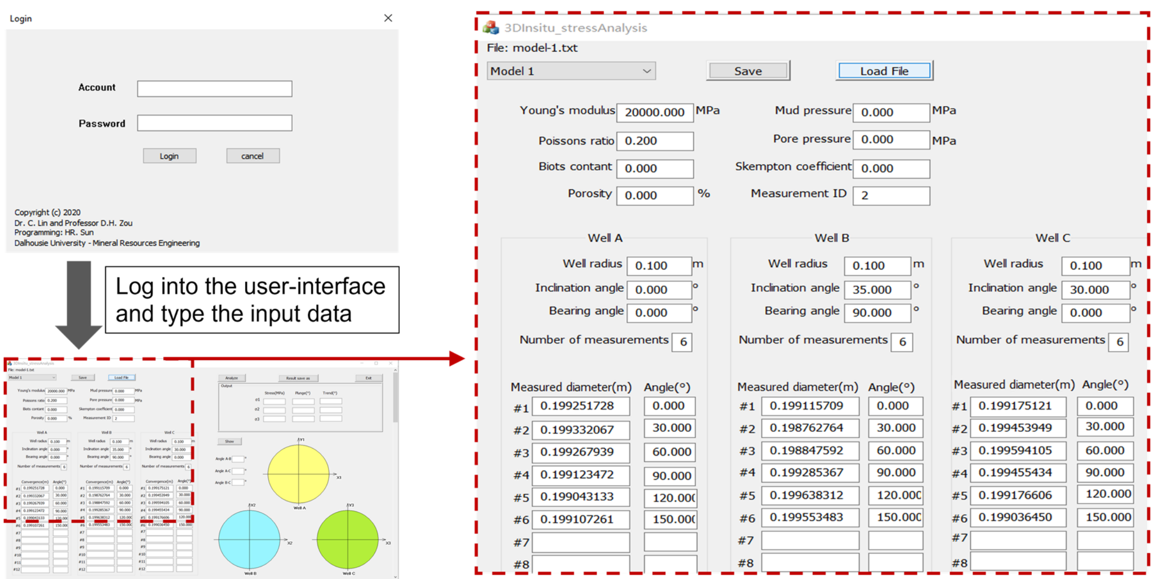

c) Run the application to compute the input data

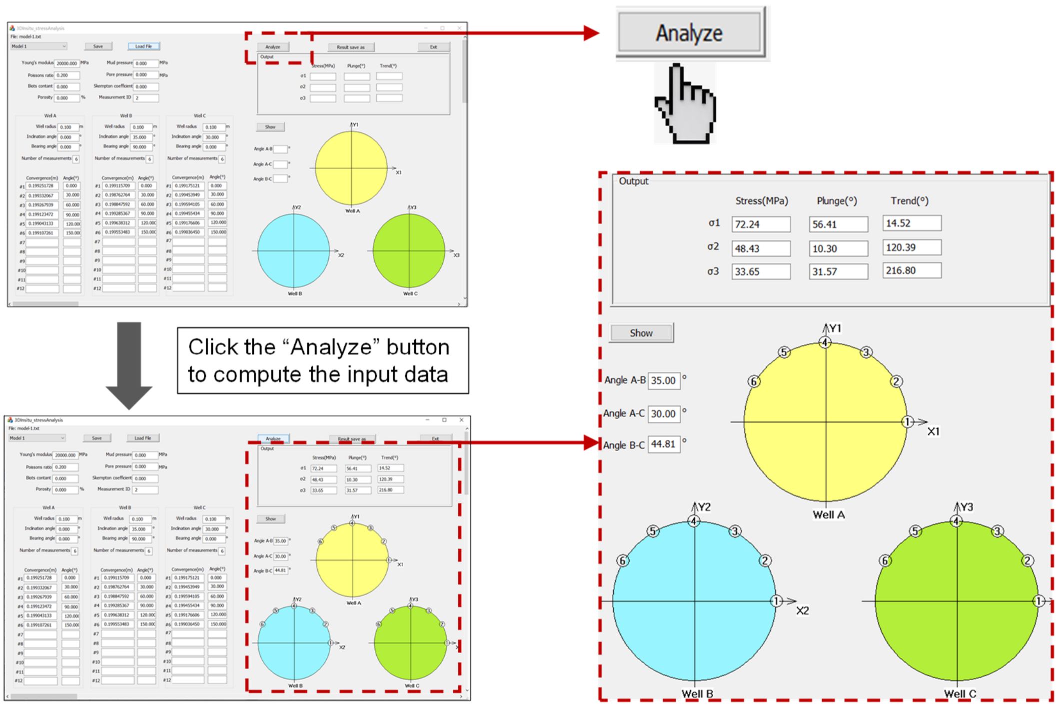

d) Output the results

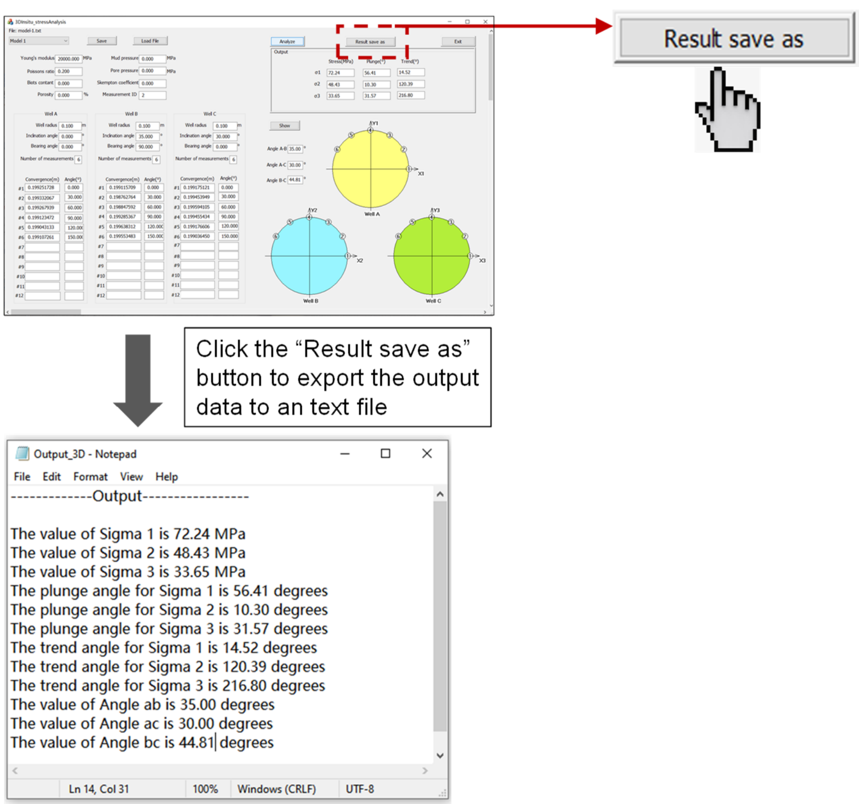

3.9 VERIFICATION OF THE 2D&3D MFC APPLICATIONS

In order to prove the validity of the applications, two test examples are introduced for the 2D and 3D MFC applications, respectively. In these examples, the input data and the output in-situ stress results are referred from Dr. Lin (Lin and Zou 2019). The exact same input data are typed into the MFC applications, and the generated in-situ stress will be compared with the referred output stress.

3.9.1 Verification of the 2D application

Table 3.1 contains the input rock properties, poro-elastic properties and drilling parameters in the five different models, and the caliper-logging data, which are gathered from nine locations in a wellbore's cross-section, are recorded in Table 3.2. The referred in-situ stress and the output stress generated from the MFC application are encompassed in Table 3.3.

- Rock properties
  - Young's modulus E
  - Poisson's ratio ν

- Poro-elastic properties
  - Biot's coefficient α
  - Porosity ϕ
  - Skempton's coefficient s

- Drilling parameters
  - Wellbore size r_o
  - Mud pressure M_m
  - Pore pressure P_P

Table 3.1 Input rock properties, poro-elastic properties and drilling parameters

Input data	Rock properties		Poro-elastic properties			Drilling parameters		
	E[Gpa]	ν	s	α	φ [%]	r_o [m]	P_P [Mpa]	P_m [Mpa]
Model 1	20	0.2	–	–	–	0.1	0	0
Model 2	20	0.2	–	0.8	30	0.1	25	20
Model 3	20	0.2	–	0.8	30	0.1	25	20
Model 4	20	0.2	0.92	0.8	15	0.1	25	20
Model 5	20	0.2	0.92	0.8	15	0.1	25	20

Table 3.2 Borehole diameters in a vertical wellbore

	Location	1	2	3	4	5	6	7	8	9
Model1	Measured diameter [m]	0.19926	0.19916	0.19920	0.19935	0.19955	0.19969	0.19972	0.19961	0.19943
	Measurement angle [°]	0	20	40	60	80	100	120	140	160
Model2	Measured diameter [m]	0.19934	0.19925	0.19929	0.19944	0.19963	0.19977	0.19980	0.19970	0.19952
	Measurement angle [°]	0	20	40	60	80	100	120	140	160
Model3	Measured convergence [m]	0.19956	0.19949	0.19952	0.19964	0.19979	0.19990	0.19992	0.19984	0.19970
	Measurement angle [°]	0	20	40	60	80	100	120	140	160
Model4	Measured diameter [m]	0.19930	0.19921	0.19925	0.19940	0.19959	0.19973	0.19976	0.19966	0.19948
	Measurement angle [°]	0	20	40	60	80	100	120	140	160
Model5	Measured diameter [m]	0.19956	0.19949	0.19952	0.19964	0.19979	0.19990	0.19992	0.19984	0.19970
	Measurement angle [°]	0	20	40	60	80	100	120	140	160

Table 3.3 Referred and back-analyzed 2D in-situ stresses

In-situ stress in 2D		σ_{Hmax} [MPa]	σ_{Hmin} [MPa]	θ_{Hmax} [°]
Model 1	Referred stress	54.5	40	24
	Calculated stress	54.5	40	24
	Differences [%]	0	0	0
Model 2	Referred stress	54.5	40	24
	Calculated stress	54.5	40	24
	Differences [%]	0	0	0
Model 3	Referred stress	54.5	40	24
	Calculated stress	54.5	40	24
	Differences [%]	0	0	0
Model 4	Referred stress	54.5	40	24
	Calculated stress	54.5	40	24
	Differences [%]	0	0	0
Model 5	Referred stress	54.5	40	24
	Calculated stress	54.5	40	24
	Differences [%]	0	0	0

It is apparent from Table 3.3 that there is no difference between the referred and back-analyzed stress results in each model. That means the programming and calculation process of the 2D MFC application are correct.

3.9.2 Verification of the 3D application

As mentioned in Chapter 2.8, caliper-logging data from three different measurement planes are required for determining the three-dimensional in-situ stress field. Measurement planes selected in three different well sections are considered:

- Well section 1: Inclination angle = 0°, Bearing angle = 0°;
- Well section 2: Inclination angle = 25°, Bearing angle = 45°;
- Well section 3: Inclination angle = 50°, Bearing angle = 45°;

The corresponding input rock properties, poro-elastic properties and drilling parameters are recorded in Table 3.4, and the detailed caliper logging data from the three different wellbores are contained in Table 3.5. The r_1, r_2, r_3 indicate the original wellbore size of the three different wellbores.

Table 3.6 demonstrates the results of the three-dimensional principal in-situ stress, which are back-analyzed from those input data. The results were calculated and testified by Dr.Lin through the Excel sheets (Lin and Zou 2019).

Table 3.4 Input rock properties, poro-elastic properties and drilling parameters

Input data	Rock properties		Poro-elastic properties			Drilling parameters				
	E [Gpa]	ν	s	α	φ [%]	r_1 [m]	r_2 [m]	r_3 [m]	P_P [Mpa]	P_m [Mpa]
Model 1	20	0.2	–	–	–	0.1	0.1	0.1	0	0
Model 2	20	0.2	–	0.8	30	0.1	0.1	0.1	25	20
Model 3	20	0.2	–	0.8	30	0.1	0.1	0.1	25	20
Model 4	20	0.2	0.92	0.8	15	0.1	0.1	0.1	25	20
Model 5	20	0.2	0.92	0.8	15	0.1	0.1	0.1	25	20

Table 3.5 Borehole diameters in different wellbores

	Location	1	2	3	4	5	6
Model 1	d_{m1} [m]	0.19925	0.19933	0.19927	0.19912	0.19904	0.19911
	a_{m1} [°]	0	30	60	90	120	150
	d_{m2} [m]	0.19912	0.19876	0.19885	0.19929	0.19964	0.19955
	a_{m2} [°]	0	30	60	90	120	150
	d_{m3} [m]	0.19918	0.19945	0.19959	0.19946	0.19918	0.19904
	a_{m3} [°]	0	30	60	90	120	150
Model 2	d_{m1} [m]	0.19963	0.19971	0.19965	0.19950	0.19942	0.19949
	a_{m1} [°]	0	30	60	90	120	150
	d_{m2} [m]	0.19950	0.19914	0.19923	0.19967	0.20002	0.19993
	a_{m2} [°]	0	30	60	90	120	150
	d_{m3} [m]	0.19956	0.19983	0.19998	0.19984	0.19956	0.19942
	a_{m3} [°]	0	30	60	90	120	150
Model 3	d_{m1} [m]	0.19965	0.19973	0.19966	0.19952	0.19944	0.19950
	a_{m1} [°]	0	30	60	90	120	150
	d_{m2} [m]	0.19951	0.19916	0.19924	0.19968	0.20003	0.19995
	a_{m2} [°]	0	30	60	90	120	150
	d_{m3} [m]	0.19957	0.19985	0.19999	0.19985	0.19957	0.19943
	a_{m3} [°]	0	30	60	90	120	150
Model 4	d_{m1} [m]	0.19962	0.19968	0.19963	0.19951	0.19945	0.19950
	a_{m1} [°]	0	30	60	90	120	150
	d_{m2} [m]	0.19951	0.19922	0.19929	0.19965	0.19993	0.19987
	a_{m2} [°]	0	30	60	90	120	150
	d_{m3} [m]	0.19958	0.19980	0.19992	0.19981	0.19958	0.19946
	a_{m3} [°]	0	30	60	90	120	150
Model 5	d_{m1} [m]	0.19964	0.19970	0.19965	0.19953	0.19947	0.19952
	a_{m1} [°]	0	30	60	90	120	150
	d_{m2} [m]	0.19953	0.19924	0.19931	0.19967	0.19995	0.19988
	a_{m2} [°]	0	30	60	90	120	150
	d_{m3} [m]	0.19960	0.19982	0.19994	0.19983	0.19960	0.19948
	a_{m3} [°]	0	30	60	90	120	150

Table 3.6 Referred 3D in-situ stress

In-situ stress	σ_1	σ_2	σ_3
Magnitude [MPa]	72.24	48.43	33.65
Plunge [°]	56.41	10.30	31.57
Trend [°]	14.52	120.39	216.80

Table 3.7 Back-analyzed results

Output data		σ_1	σ_2	σ_3
Model 1	Magnitude [MPa]	72.24	48.43	33.65
	Plunge [°]	56.41	10.30	31.57
	Trend [°]	14.52	120.39	216.80
Model 2	Magnitude [MPa]	72.24	48.43	33.65
	Plunge [°]	56.41	10.30	31.57
	Trend [°]	14.52	120.39	216.80
Model 3	Magnitude [MPa]	72.24	48.43	33.65
	Plunge [°]	56.41	10.30	31.57
	Trend [°]	14.52	120.39	216.80
Model 4	Magnitude [MPa]	72.24	48.43	33.65
	Plunge [°]	56.41	10.30	31.57
	Trend [°]	14.52	120.39	216.80
Model 5	Magnitude [MPa]	72.24	48.43	33.65
	Plunge [°]	56.41	10.30	31.57
	Trend [°]	14.52	120.39	216.80

The back-analyzed results from the MFC application are given in Table 3.7. As can be seen, the back-analyzed results generated from the 3D MFC application are consistent with the referred in-situ stress. This proves that the application works properly.

To sum up, this chapter illustrates the detailed developing process of the console and MFC applications, the primary functions of the applications, and the user-performing procedure. At present, the 2D and 3D MFC applications successfully realize the automated analysis of the back-analysis method. Their graphic user interfaces and ancillary functions allow users to process input data, generate and export back-analyzed in-situ stress results conveniently.

CHAPTER 4 EXPLORING THE FEASIBLE ORIENTATIONS OF THE THREE WELLBORES IN 3D IN-SITU STRESS ESTIMATION

In the back-analyzed method for the estimation of three-dimensional in-situ stress, caliper-logging data from three non-parallel well sections are required. This can be accomplished through a multi-branch/multilateral well, as mentioned in Chapter 1. A multi-branch well is consists of a main wellbore and several lateral branch wells. In most cases, the main wellbore is a straight vertical well, and the branches could be directional or inclined well (Anon 1999). The application of the multi-branch well enlarges the exploitation range of a single well, dramatically enhances the oil recovery, and has been widely used in the actual field site.

Dr. Lin denoted that the inclination angle intervals between each measurement plane may exert a significant influence on the three-dimensional principal stress results generated from the new back-analyzed method (Lin and Zou 2019). As the inclination angle interval decreases to some extent, the back-analyzed 3D in-situ stress results show a big difference from the real solution. Measurement planes in a directional well must have inclination angle interval greater than 17.5°.

In Lin's research, the three measurement planes have the same bearing angle since they are investigated from a directional well. However, in a multi-branch well, the measurement planes are oriented in different directions. Therefore, instead of the inclination angle, the space angle interval's influence on the accuracy of the 3D in-situ stress results should be investigated in this research.

In the following test example, the three required measurement planes are selected from a multi-branched well as they were three wellbores. The space angle between each wellbore is 10°. The main borehole is a vertical well (well A), and it connects with two inclined brach-wells (well B & C). The combination of the inclination and bearing angle for the three wellbores are:

●Wellbore A: Inclination angle = 0°, Bearing angle = 0°;

●Wellbore B: Inclination angle = 10°, Bearing angle = 70°;

●Wellbore C: Inclination angle = 10°, Bearing angle = 9.75°;

The assumed 3D in-situ stress field, rock formation properties, and the drilling parameters are the same as those in the test of the 3D application, listed in Tables 3.1 and 3.2. Data of exact diametrical convergence caused by drilling at each wellbore's measurement plane are calculated by Equation(2.15). In order to simulate the actual field measurement, up to 20% of random errors are applied to each exact diametrical convergence to generate the hypothetical measured diameters, as given in Table 4.1.

Table 4.1 Up to ±20% of random errors

	Measurement points	Random errors [%]
Wellbore A	1	-6.00%
	2	-16.85%
	3	15.09%
	4	3.03%
	5	-10.32%
	6	-0.10%
Wellbore B	1	-11.73%
	2	15.18%
	3	4.66%
	4	-4.33%
	5	5.98%
	6	-0.85%
Wellbore C	1	2.13%
	2	18.58%
	3	12.92%
	4	-14.24%
	5	-2.51%
	6	-19.85%

Table 4.2 Exact and hypothetical borehole diameters in three wellbores

Measured diameters (m)			1	2	3	4	5	6
Model 1	Exact	Well A	0.19925	0.19933	0.19926	0.19912	0.19940	0.19910
		Well B	0.19921	0.19938	0.19941	0.19928	0.19911	0.19908
		Well C	0.19926	0.19922	0.19915	0.19911	0.19916	0.19923
	Hypothetic	Well A	0.19929	0.19944	0.19915	0.19907	0.19914	0.19910
		Well B	0.19930	0.19928	0.19938	0.19932	0.19906	0.19909
		Well C	0.19924	0.19907	0.19904	0.19924	0.19918	0.19935
Model 2	Exact	Well A	0.19963	0.19971	0.19964	0.19954	0.19942	0.19948
		Well B	0.19959	0.19976	0.19979	0.19962	0.19949	0.199463
		Well C	0.19964	0.19960	0.19953	0.19950	0.19954	0.19961
	Hypothetic	Well A	0.19965	0.19976	0.19959	0.19948	0.19948	0.19948
		Well B	0.19964	0.19972	0.19978	0.19967	0.19946	0.19946
		Well C	0.19963	0.19953	0.19947	0.19957	0.19955	0.19969
Model 3	Exact	Well A	0.19964	0.19972	0.19966	0.19951	0.19943	0.19950
		Well B	0.19961	0.19977	0.19981	0.19967	0.19951	0.19947
		Well C	0.19966	0.19962	0.19954	0.19951	0.19955	0.19962
	Hypothetic	Well A	0.19966	0.19977	0.19961	0.19950	0.19949	0.19950
		Well B	0.19965	0.19974	0.19980	0.19969	0.19948	0.19948
		Well C	0.19965	0.19954	0.19948	0.19958	0.19956	0.19970
Model 4	Exact	Well A	0.19961	0.19968	0.19963	0.19951	0.19944	0.19949
		Well B	0.19959	0.19973	0.19976	0.19965	0.19951	0.19948
		Well C	0.19962	0.19959	0.19953	0.19950	0.19954	0.19960
	Hypothetic	Well A	0.19963	0.19973	0.19957	0.19949	0.19950	0.19949
		Well B	0.19964	0.19969	0.19974	0.19966	0.19948	0.19949
		Well C	0.19962	0.19951	0.19947	0.19957	0.19955	0.19968
Model 5	Exact	Well A	0.19963	0.19970	0.19964	0.19953	0.19946	0.19951
		Well B	0.19961	0.19975	0.19978	0.19967	0.19953	0.19950
		Well C	0.19964	0.19961	0.19955	0.19952	0.19956	0.19962
	Hypothetic	Well A	0.19965	0.19975	0.19959	0.19951	0.19952	0.19951
		Well B	0.199662	0.19971	0.19976	0.19968	0.19950	0.19951
		Well C	0.199640	0.19954	0.19949	0.19959	0.19957	0.19969

The input data are computed by the 3D MFC application, and the correlated output results are given in Table 4.3.

Table 4.3 Back-analyzed result from the MFC application

Output data	In-situ stress	σ_1	σ_2	σ_3
Model 1	Magnitude [MPa]	78.17	-67.02	-74.06
	Plunge [°]	2.86	10.41	11.99
	Trend [°]	93.48	88.09	88.18
Model 2	Magnitude [MPa]	65.39	-20.34	-26.04
	Plunge [°]	4.47	17.37	20.91
	Trend [°]	95.20	88.55	88.97
Model 3	Magnitude [MPa]	64.94	-18.53	-24.16
	Plunge [°]	4.57	17.84	21.51
	Trend [°]	95.28	88.64	89.10
Model 4	Magnitude [MPa]	68.96	-33.47	-39.00
	Plunge [°]	4.03	15.33	18.12
	Trend [°]	94.53	88.27	88.52
Model 5	Magnitude [MPa]	68.18	-30.57	-36.54
	Plunge [°]	4.15	15.85	18.80
	Trend [°]	94.65	88.32	88.61

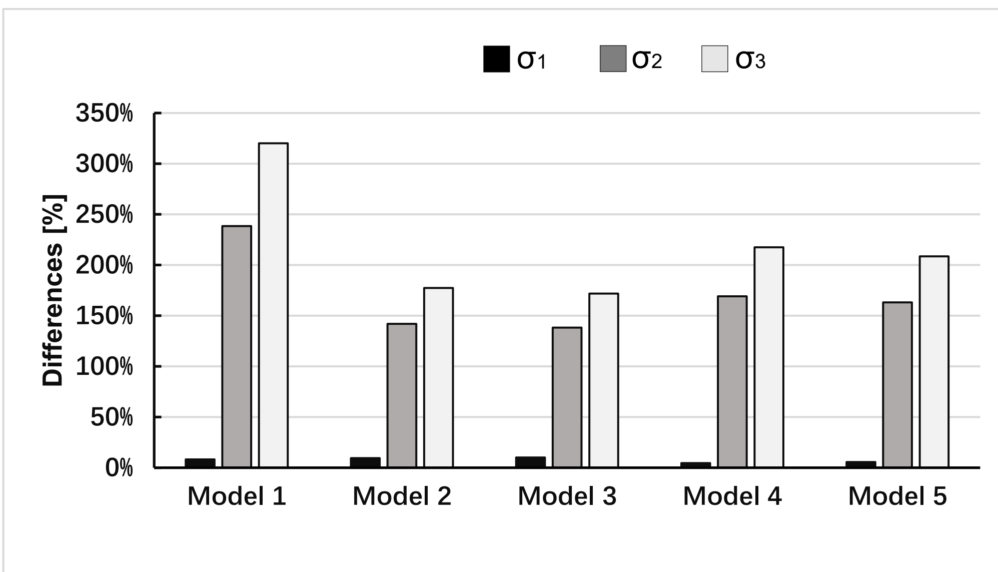

Figure 4.1 Differences between the back-analyzed and the exact principal stress (Space angle between wells: 10°)

As can be seen from Figure 4.1, compared with the exact principal in-situ stress, the back-analyzed in-situ stress results from the five comprehensive models show significant errors.

That means the back-analyzed results are unacceptable when the space angle between each two of the three wellbores is 10 degrees. This phenomenon highly agrees with Dr. Lin's findings (Lin and Zou 2019).

As the space angles between each two wellbores are too small, the measurement planes are almost parallel with each other. In that case, the back-analyzed stress result is not satisfactory. Therefore, the range of the reasonable space angle between each two wellbore needs to be determined for this stress estimation method.

4.1 EFFECTS OF RELATIVE WELLBORE ORIENTATIONS ON IN-SITU STRESS ESTIMATION

4.1.1 The combinations of the inclination and bearing angles

In order to find the reasonable space angle range and explore how the principal stress field effect the back-analyzed result, test examples based on different orientations of the wellbores are analyzed. All calculation procedures are performed with the 3D MFC application.

For all the test examples, a multi-branch well consisted of a vertical main wellbore and two inclined branch wells are considered. Those test examples can be divided into nine scenarios according to the space angle between each two wells. The space angles between each two wellbores are considered at 10°, 20°,30°, 40°, 50°, 60°, 70°, 80°, 90°, for scenario 1 to 9, respectively. For example, in the third scenario, the space angles between wells A and B, wells A and C, wells B and C are the same at 30° (Figure 4.2), and so for the rest scenarios. To maintain a specified space angle, the inclination and bearing angles of wells B and C will change as shown below.

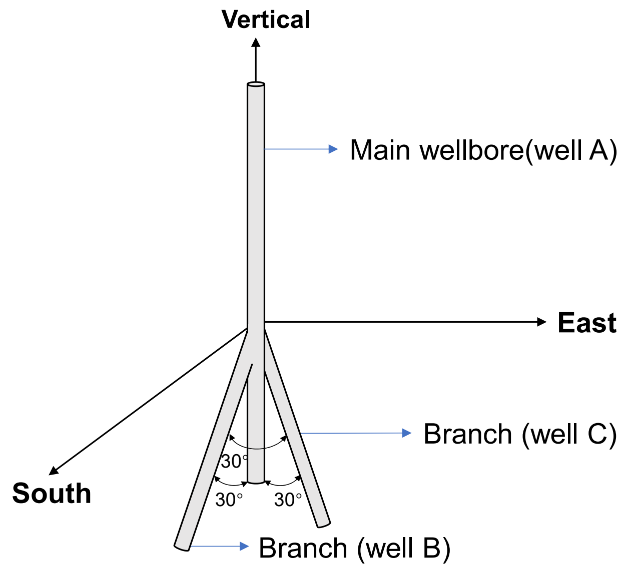

Figure 4.2 Multibranch-well in scenario 3

Assume the well A is vertical, well B and well C are the inclined branch-wells. For the purpose of investigating all possible orientations in three dimensions, thirty-six different combinations of inclination and bearing angle for the wells A, B, C are investigated in each scenario. In Scenario 3, for example, the 36 groups of combinations are:

- 1^{St} combination: $I_A = 0°,\ \beta_A = 0°;\ I_B = 30°,\ \beta_B = 0°;\quad I_C = 30°,\ \beta_C = 297.65°;$
- 2^{nd} combination: $I_A = 0°,\ \beta_A = 0°;\ I_B = 30°,\ \beta_B = 10°;\ I_C = 30°,\ \beta_C = 307.65°;$
- 3^{rd} combination: $I_A = 0°,\ \beta_A = 0°;\ I_B = 30°,\ \beta_B = 20°;\ I_C = 30°,\ \beta_C = 317.65°;$

…

- 36^{th} combination: $I_A = 0°,\ \beta_A = 0°;\ I_B = 30°,\ \beta_B = 350°;\ I_C = 30°,\ \beta_C = 287.65°;$

Where the $I_A,\ I_B,\ I_C$ and $\beta_A,\ \beta_B,\ \beta_C$ represent the inclination and bearing angle for the three wellbores, respectively. The value of those angles in each combination can be calculated by Equation (4.1):

$$si\ n(I_A) \cdot si\ n(I_B) \cdot cos(\beta_A - \beta_B) + cos(I_A) \cdot cos(I_B) = cos(\angle AB) \tag{4.1a}$$

$$si\ n(I_A) \cdot si\ n(I_C) \cdot cos(\beta_A - \beta_C) + cos(I_A) \cdot cos(I_C) = cos(\angle AC) \tag{4.1b}$$

$$si\ n(I_B) \cdot si\ n(I_C) \cdot cos(\beta_B - \beta_C) + cos(I_B) \cdot cos(I_C) = cos(\angle \mathrm{BC}) \tag{4.1c}$$

Where the $\angle AB$, $\angle AC$, $\angle BC$ are the space angles between wells A and B, wells A and C, wells B and C, respectively

The orientation of the wellbore A is fixed because it is the vertical main wellbore, so I_A and β_A are equal to zero. I_B and I_C can be directly determined through the given space angle between each two of the three wellbores. Since the bearing angle of the well B varies from 0° to 350° with 10° interval, the value of β_B is known in each condition. The bearing angle of well C in each combination can be solved through Equation 4.1c.

The variation of the branch wells orientations from the 1^{St} to the 36^{th} the combination is like revolve them around the vertical wellbore with 10° intervals. This is to ensure the test examples in each scenario encompass all of the directions.

Similarly, there are 36 groups of test examples in every other scenario. Detailed information about the inclination and bearing angle combinations in the nine scenarios is given in Appendix D.

4.1.2 Input data of test examples

(1) Rock properties, poro-elastic properties, drilling parameters

The rock properties, poro-elastic properties and corresponding drilling parameters are referred from Dr. Lin's research (Lin and Zou 2019), displayed in Table 4.4. The assumed principal stress field is the same as displayed in Table 3.6.

Table 4.4 Input rock properties, poro-elastic properties and drilling parameters

Input data	Rock properties		Poro-elastic properties			Drilling parameters				
	E [Gpa]	ν	s	α	φ [%]	r_A [m]	r_B [m]	r_C [m]	P_P [Mpa]	P_m [Mpa]
Model 1	20	0.2	–	–	–	0.1	0.1	0.1	0	0
Model 2	20	0.2	–	0.8	30	0.1	0.1	0.1	25	20
Model 3	20	0.2	–	0.8	30	0.1	0.1	0.1	25	20
Model 4	20	0.2	0.92	0.8	15	0.1	0.1	0.1	25	20
Model 5	20	0.2	0.92	0.8	15	0.1	0.1	0.1	25	20

(2) Simulated caliper-logging data

The simulated caliper-logging data include the borehole diameter and the measurement angle obtained from each measurement plane of the three wellbores. For each measurement plane, six measurements of diameter are required to be made at different locations around the well (Figure 4.3). The angles for each measurement point are 0°, 30°, 60°, 90°, 120°, and 150°, respectively.

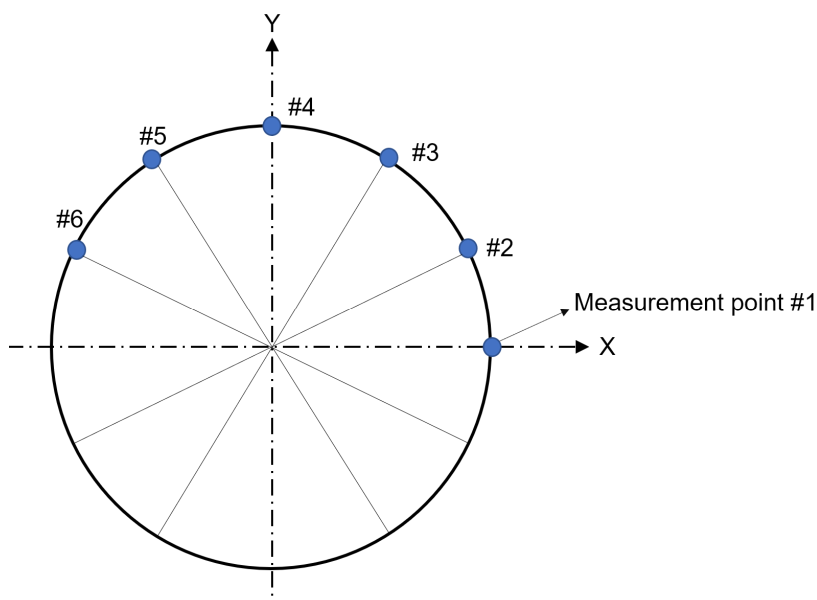

Figure 4.3 Diameter measurements at different locations around the well

The exact diametrical convergence in each measurement plane for all the investigated multi-branch wells are calculated through Equation 2.15. Random errors of up to ±20%

(Table 4.1) are introduced to the exact diametrical convergence to simulate the field condition and generate the hypothetical measured diameters for different scenarios.

4.2 RESULTS AND ANALYSIS OF SPACE ANGLE VARIATION IN BOREHOLES

In the previous section, the combinations of the inclination and bearing angle of the three wellbores, the corresponding simulated caliper-logging data, the rock formation properties, and the drilling parameters have been introduced. Those data are the necessary input data of the 3D MFC application. In the following research, the back-analyzed in-situ stress results calculated based on those input data will be compared and analyzed.

4.2.1 Search for feasible space angle between the three wellbores

The magnitudes of the back-analyzed principal stresses results in the nine scenarios based on different calculation models are presented in Appendix A. Graphs of the difference between the magnitude of the back-analyzed and assumed principal stress for three typical scenarios with space angle at 10°, 50°/60° and 90° in five comprehensive models, are given in figures 4.4 to 4.8 as examples. The rest are listed in Appendix B. The orientations of the back-analyzed and the assumed principal stress in each scenario are drawn on the stereonet, as displayed in Figures 4.9 to 4.13 and Appendix C. It also should be noticed that the inclination angles of the two inclined wells in each scenario are the same, but bearing angles are different. Therefore, Well B's bearing angle is utilized to symbolize each test example on the horizontal axis of those charts.

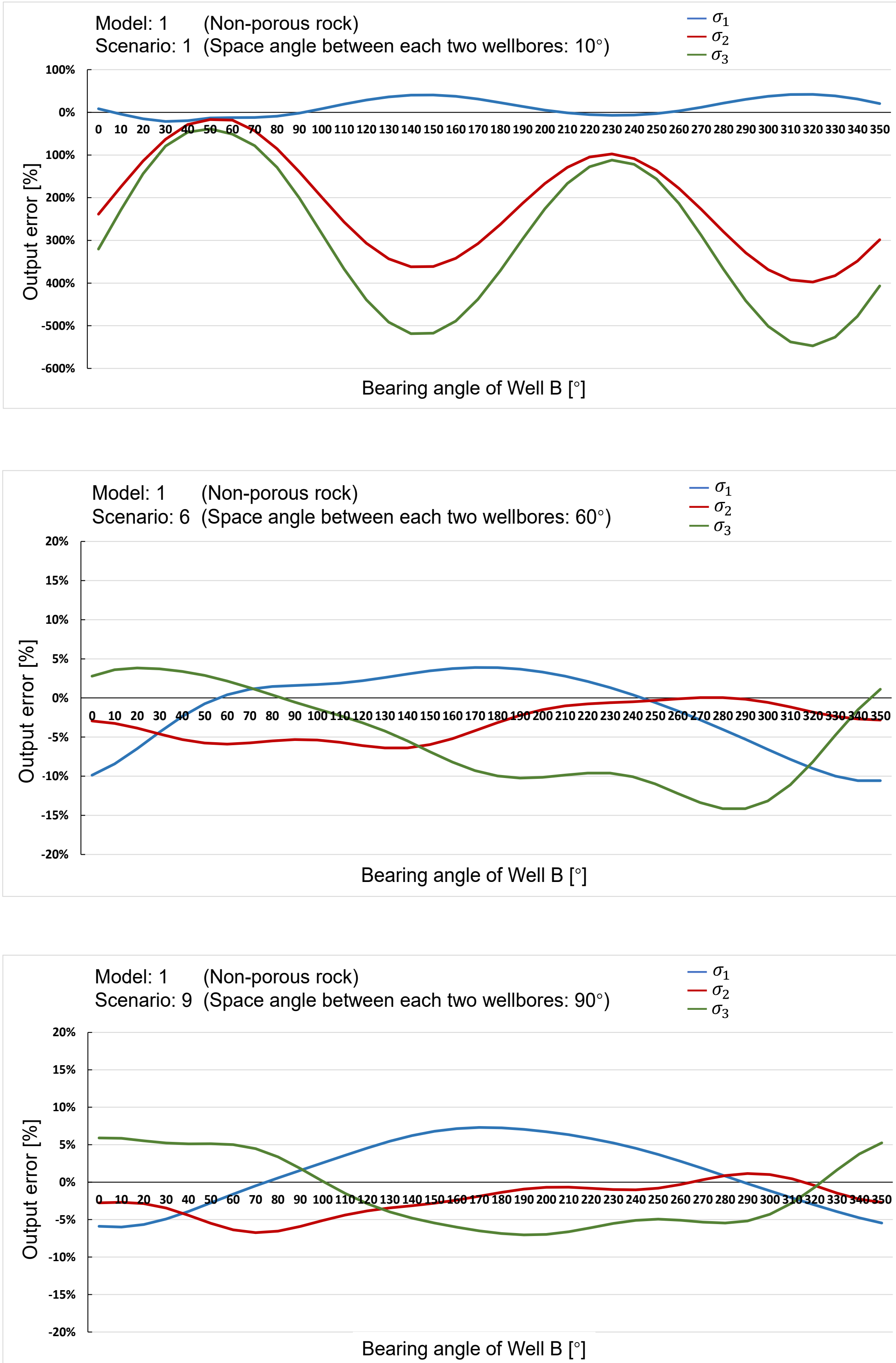

Figure 4.4 Error of the back-analyzed results in model 1, scenarios 1,6,9

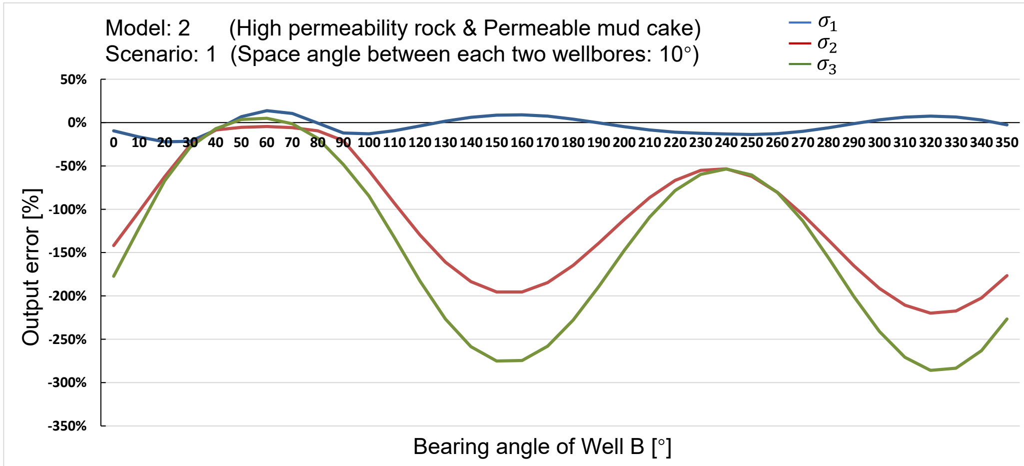

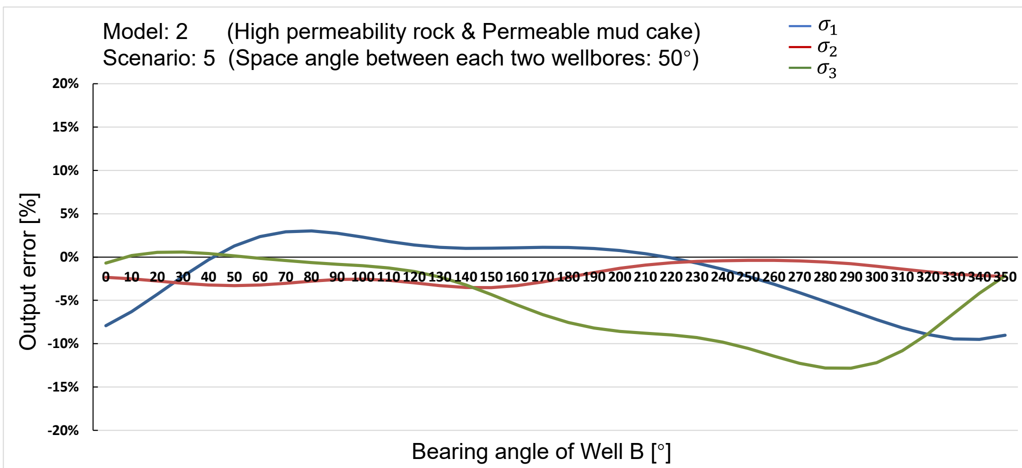

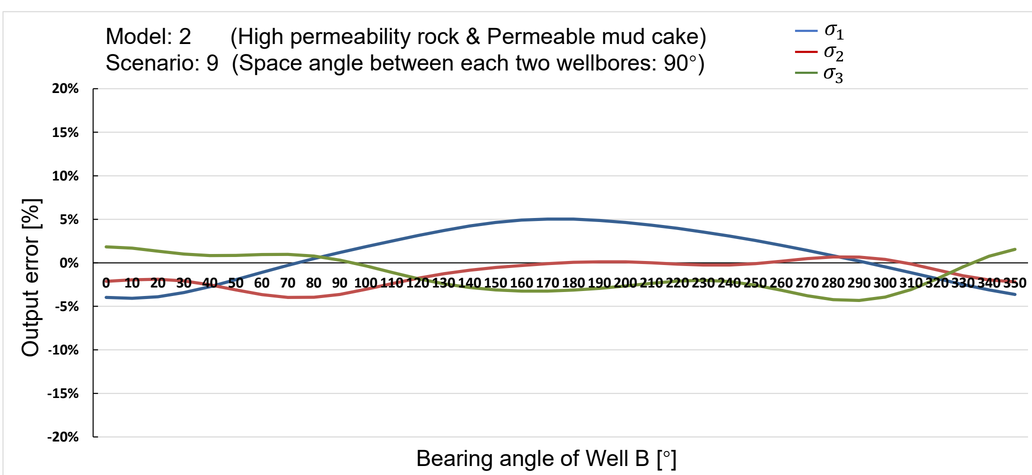

Figure 4.5 Error of the back-analyzed results in model 2, scenarios 1,5,9

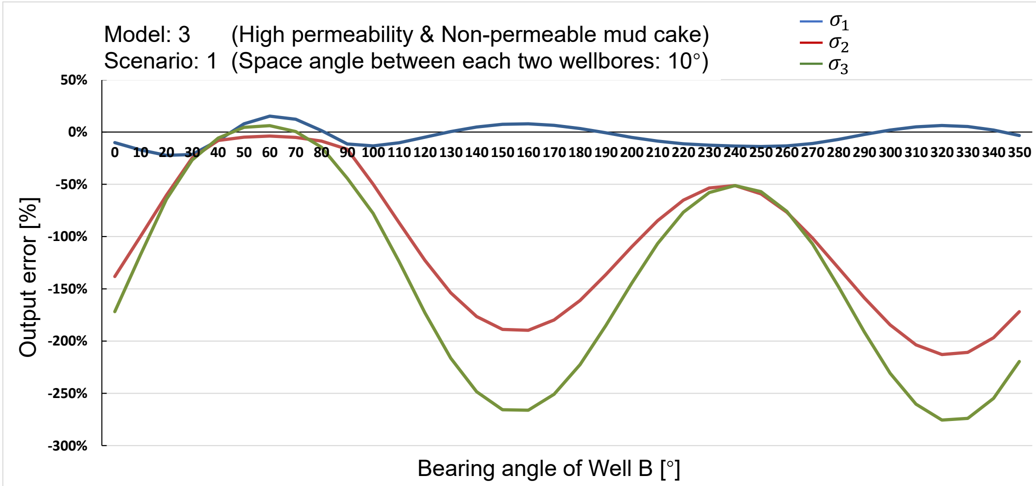

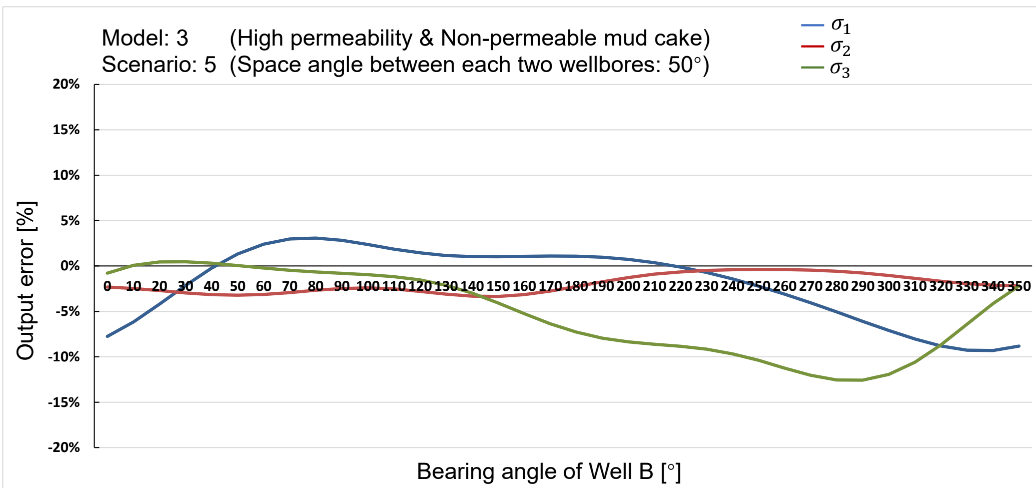

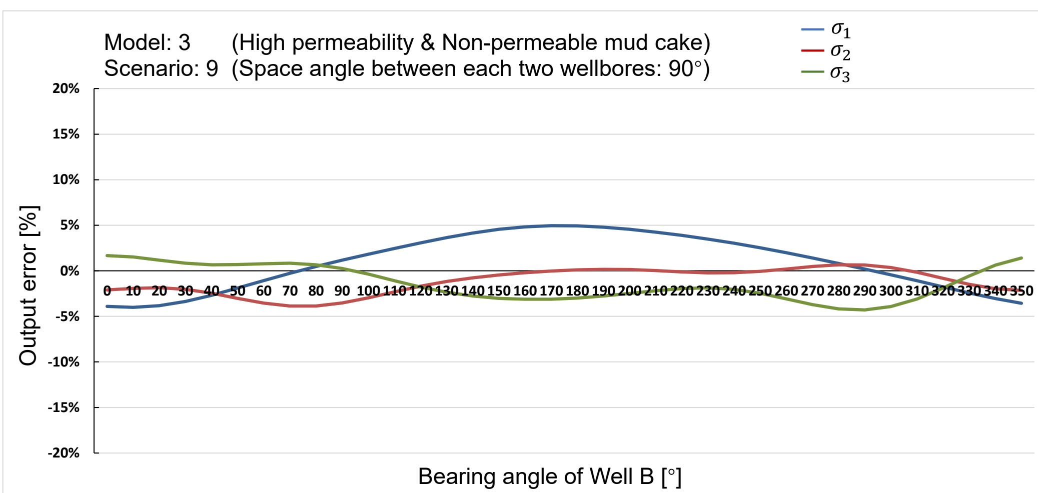

Figure 4.6 Error of the back-analyzed results in model 3, scenarios 1,5,9

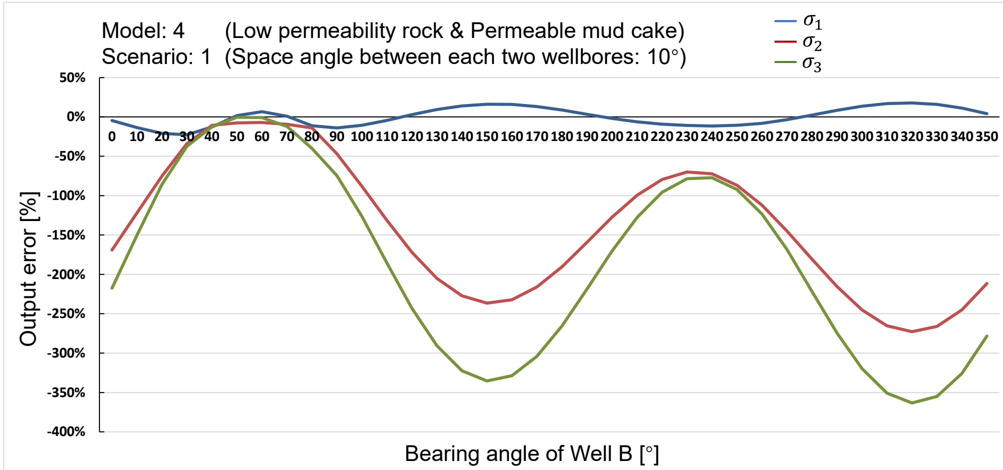

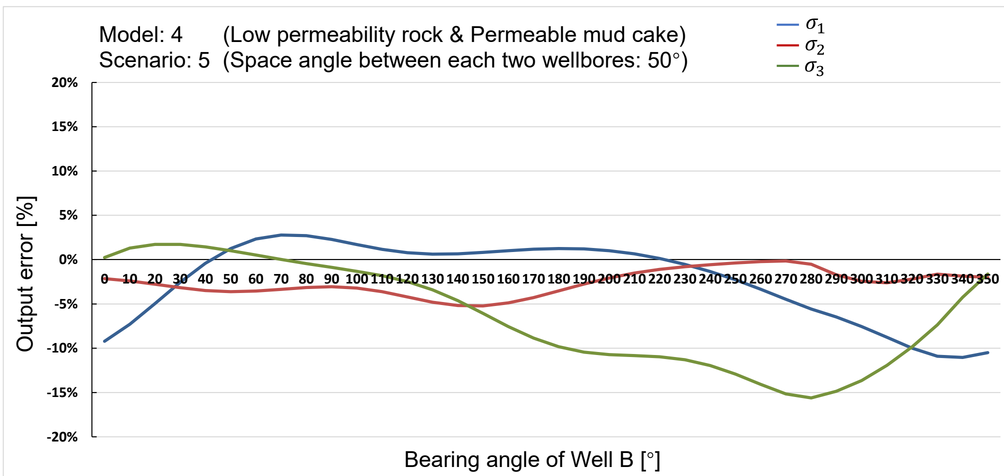

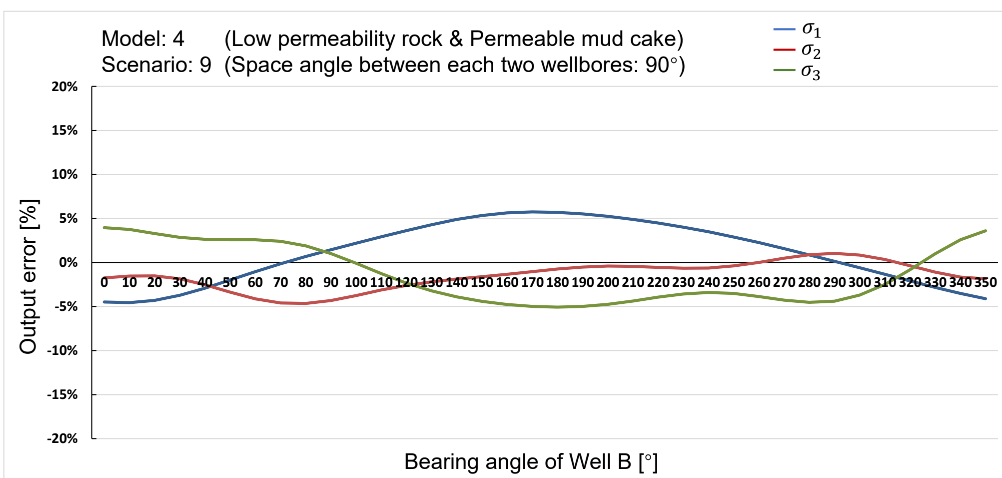

Figure 4.7 Error of the back-analyzed results in model 4, scenarios 1,5,9

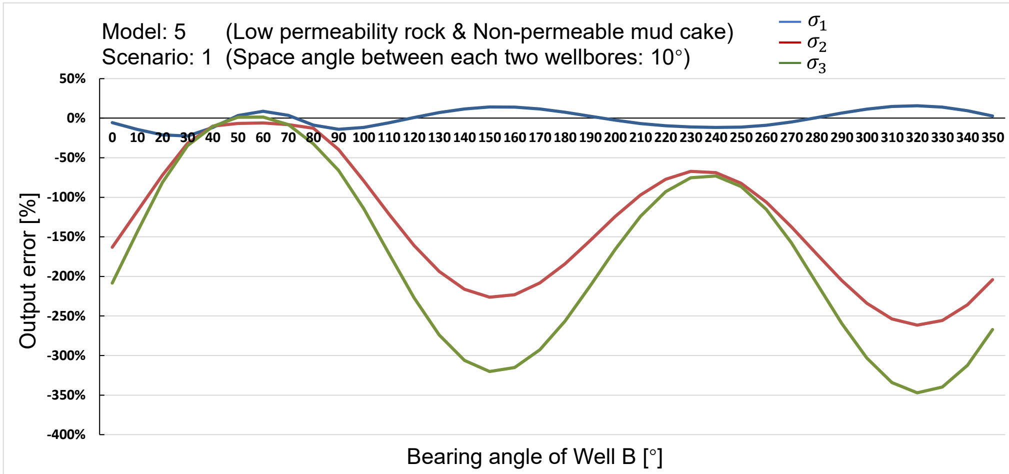

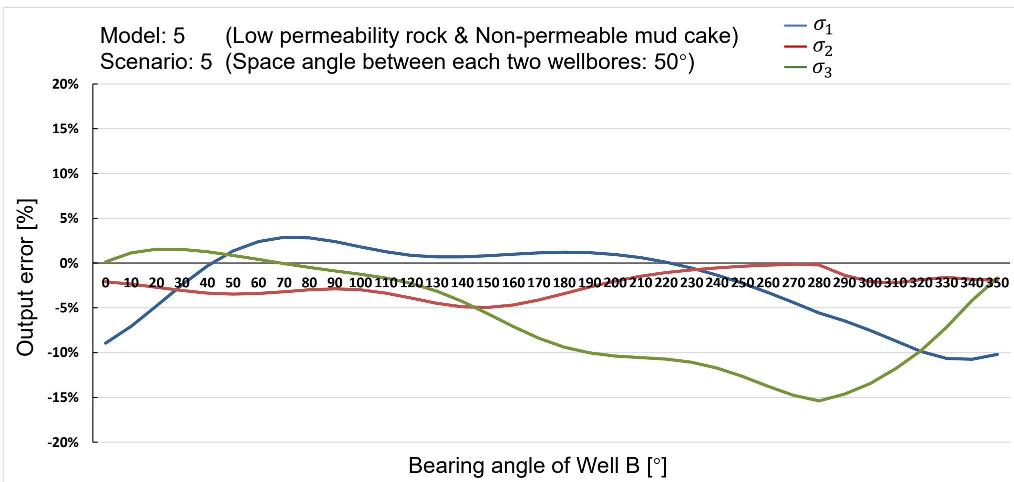

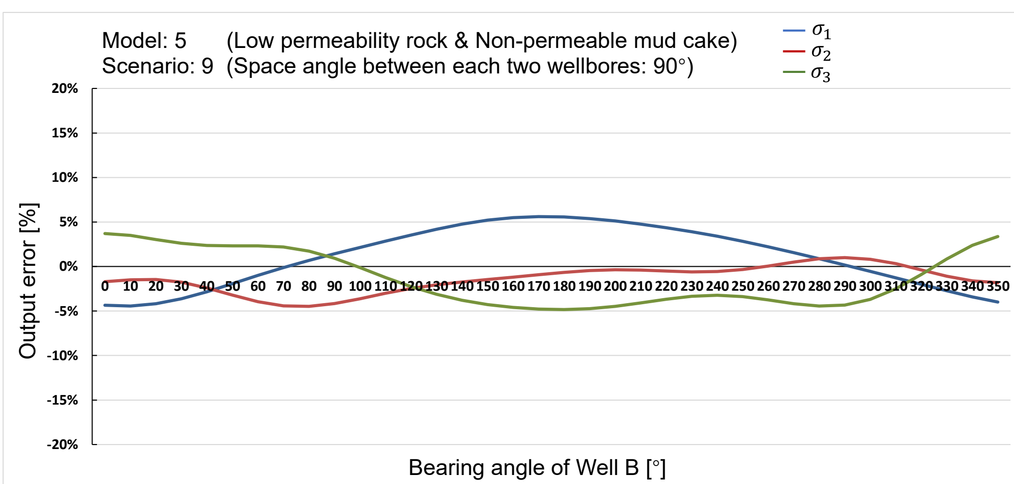

Figure 4.8 Error of the back-analyzed results in model 5, scenarios 1,5,9

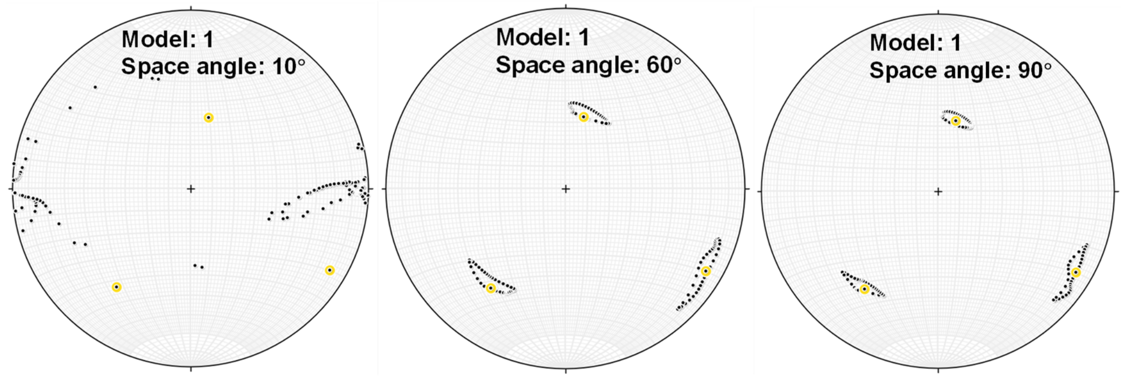

Figure 4.9 Orientations of the back-analyzed and assumed principal stresses in model 1 (Space angle between the three wellbores 10°, 60°, 90°)

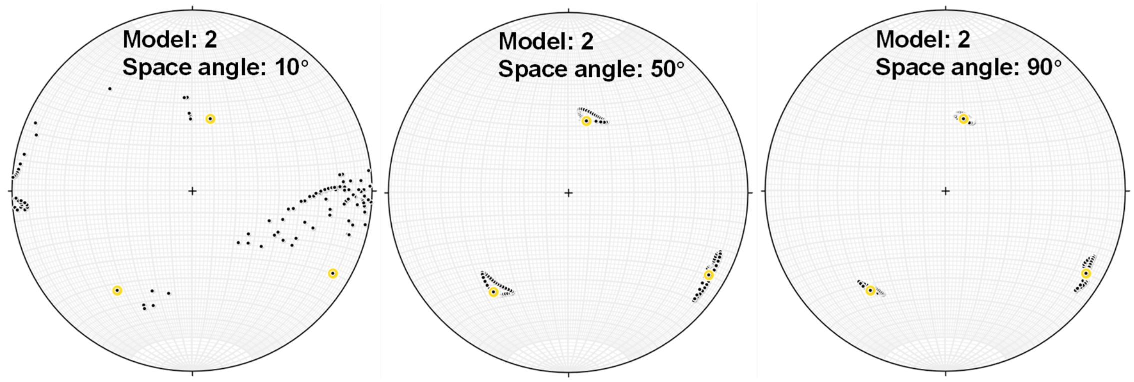

Figure 4.10 Orientations of the back-analyzed and assumed principal stresses in model 2 (Space angle between the three wellbores 10°, 50°, 90°)

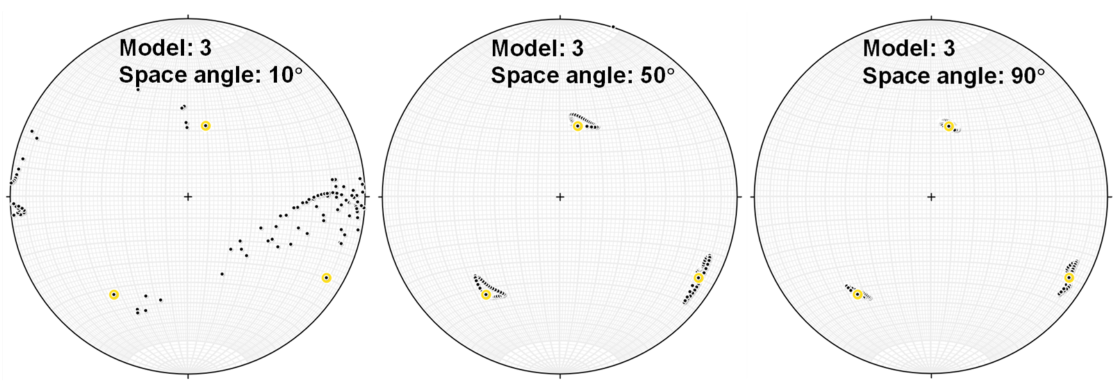

Figure 4.11 Orientations of the back-analyzed and assumed principal stresses in model 3 (Space angle between the three wellbores 10°, 50°, 90°)

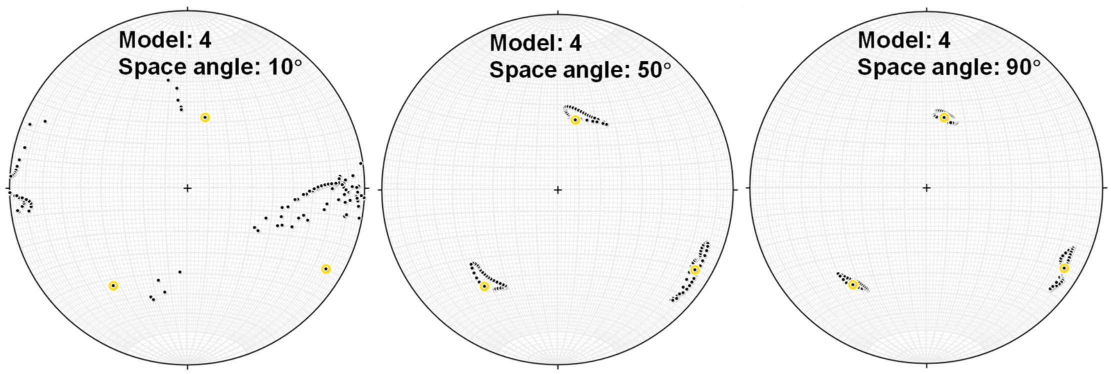

Figure 4.12 Orientations of the back-analyzed and assumed principal stresses in model 4 (Space angle between the three wellbores 10°, 50°, 90°)

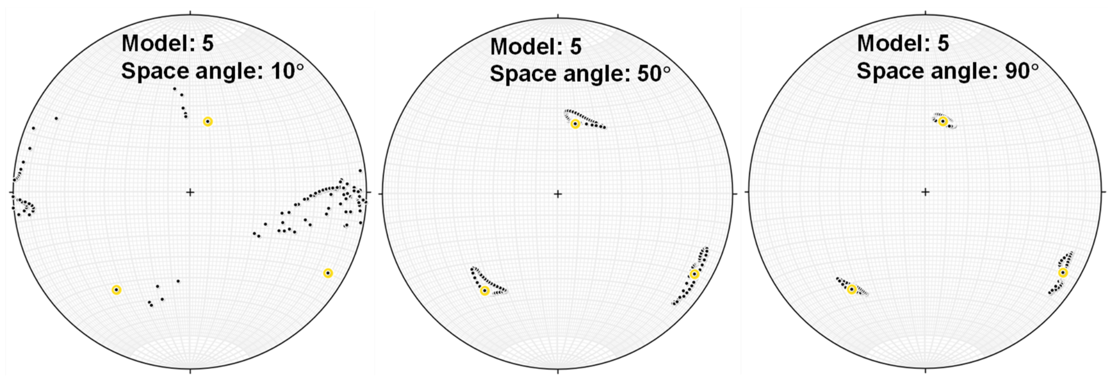

Figure 4.13 Orientations of the back-analyzed and assumed principal stresses in model 5 (Space angle between the three wellbores 10°, 50°, 90°)

It can be seen from the above figures that when the space angle between the three wellbores is 90°, the back-analyzed in-situ stress results are closest to the real solutions in all calculation models. The differences with the real solutions are smaller than 7% despite up to 20% errors in the simulated measurement data. The orientations of the back-analyzed principal stresses converge to three clusters surrounding the actual orientations of the three assumed principal stresses. As the space angle between each two of the three wellbores getting smaller, the output errors increase, which can be seen in Figures 4.4 to 4.8. The method gives large-error results, of which the errors exceed 100%, when the space angles between each two of the three investigated wellbores getting smaller than 20°.

The orientations of the back-analyzed stress also demonstrate the same trend. When the space angle decreases to 10°, the points represented the orientations in the stereonet disperse chaotically.

As the bearing angle of well B varying from 0° to 350° in each scenario, the magnitude and output errors of back-analyzed principal stresses are changed simultaneously, even though the specified space angles between wells are the same. A possible explanation is that, with the variation of the wellbore direction, the space angle interval between the investigated wellbores and the assumed principal stress components are also changed, and this space angle interval may also exert some influence on the accuracy of the back-analyzed results.

Furthermore, an obvious cycle pattern could be observed from the charts of the output errors when the space angles between wells are less than 30°, as displayed in Figure 4.4. This may also suggest some correlation between the accuracy of the back-analyzed results and the orientations of the three wellbores with respect to the in situ stresses. When the wellbores are oriented in various directions, their relations to the principal stresses may be changed. The relationships between the three wellbores and the three principal stresses need further investigation in future studies.

In general, synthetically considering the errors in both magnitude and orientation of the back-analyzes stresses in all cases, the reasonable space angle between each two of the three wellbores for the five calculation models, as illustrated in Figures 4.14 and 4.15, are considered to be:

- Model 1: $\geqslant 60°$;
- Models 2 to 5: $\geqslant 50°$;

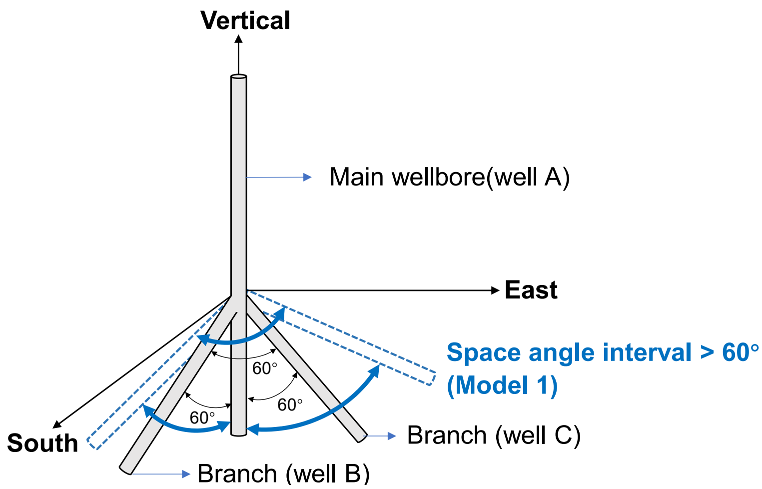

Figure 4.14 Reasonable space angle interval for Model 1

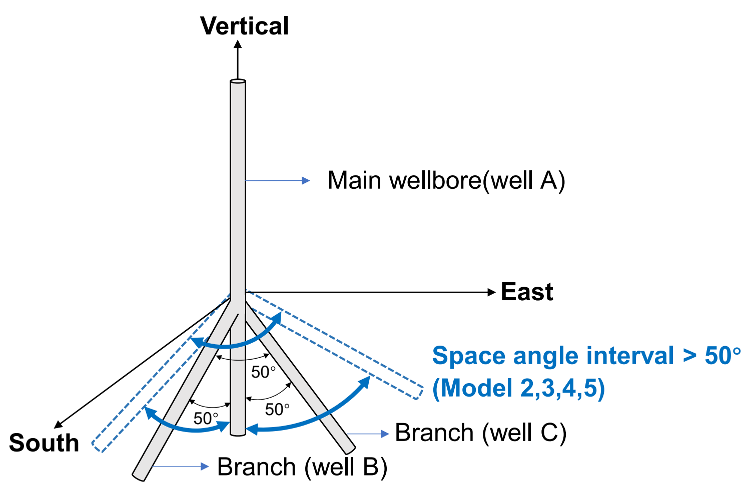

Figure 4.15 Reasonable space angle interval for Model 2,3,4,5

When up to 20% errors are added to the input convergence data, the differences of all the solutions of back-analyzed stresses are lower than 15%, and most are less than 10% in the condition that the space angle between each two of three wellbores is in a reasonable range. Meanwhile, the orientations of the back-analyzed stresses are approximately consistent with the actual ones.

4.2.2 Statistical analysis

In the previous research, only one group of random errors are applied to the exact diametrical convergence in each test example to generate the hypothetical convergence. Considering the results analyzed from only one group of random errors may not be representative and convincible, three test examples using model 2 are selected to perform the statistical analysis with 100 groups of random errors. The combinations of the inclination and bearing angle of the selected examples are:

- Example 1: $I_A = 0°$, $\beta_A = 0°$; $I_B = 10°$, $\beta_B = 0°$; $I_C = 10°$, $\beta_C = 299.75°$;
- Example 2: $I_A = 0°$, $\beta_A = 0°$; $I_B = 50°$, $\beta_B = 0°$; $I_C = 50°$, $\beta_C = 293.04°$;
- Example 3: $I_A = 0°$, $\beta_A = 0°$; $I_B = 90°$, $\beta_B = 0°$; $I_C = 90°$, $\beta_C = 270°$;

Specifically, 100 groups of up to 20% random errors are randomly generated through an Excel sheet and respectively apply to the exact diametrical convergence of the three examples to generate 100 groups of hypothetical diametrical convergence for each example. The back-analyzed in-situ stress results based on those groups of hypothetical convergence are calculated through the 3D MFC application. The range of the errors of the back-analyzed in-situ stresses' magnitude and the correlated frequencies are displayed in Figures 4.16 to 4.18. The distributions of the back-analyzed in-situ stresses' orientations are displayed in Figures 4.19.

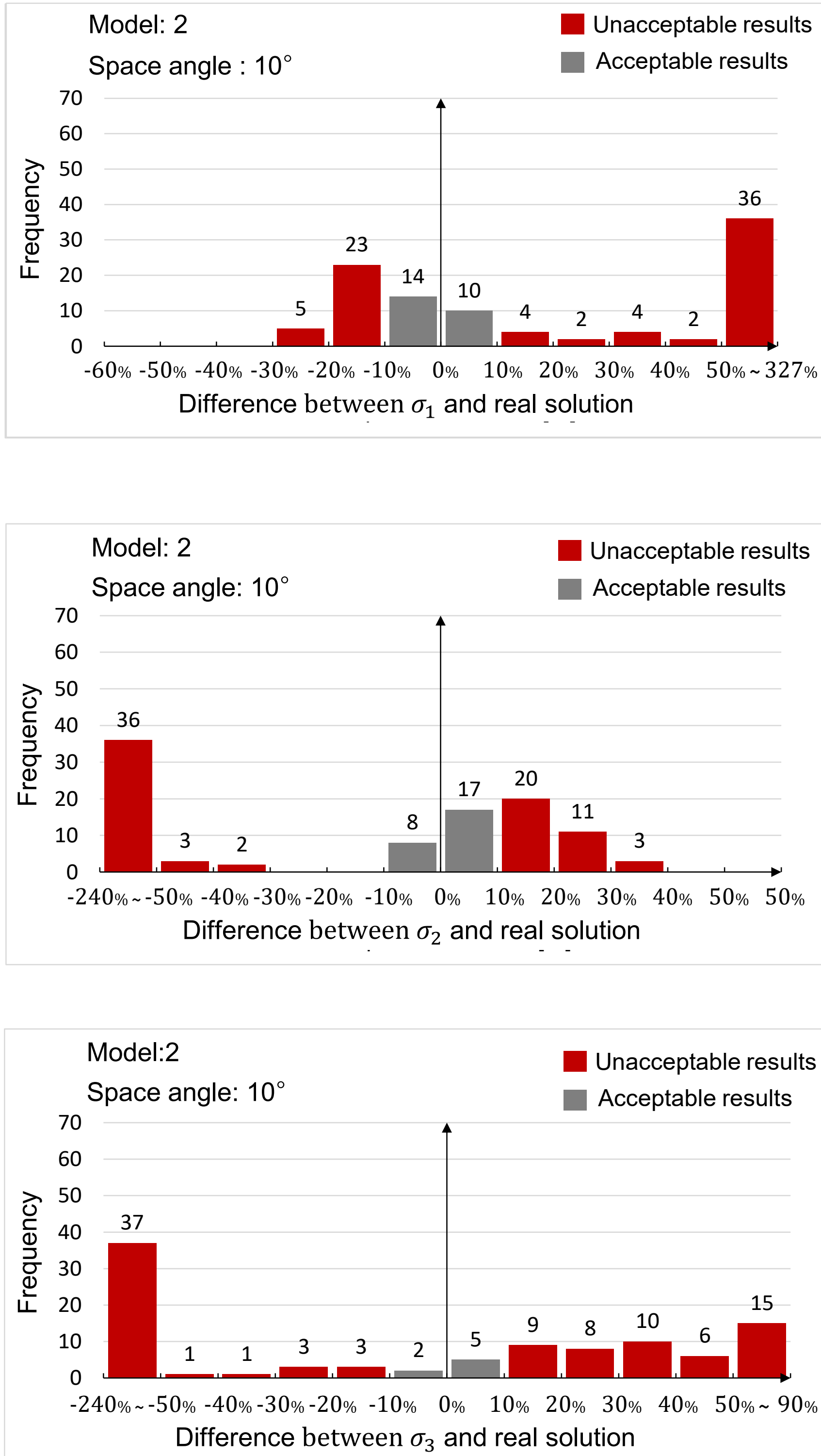

Figure 4.16 Differences between the magnitude of back-analyzed stresses and the real solution of model 2, scenario 1

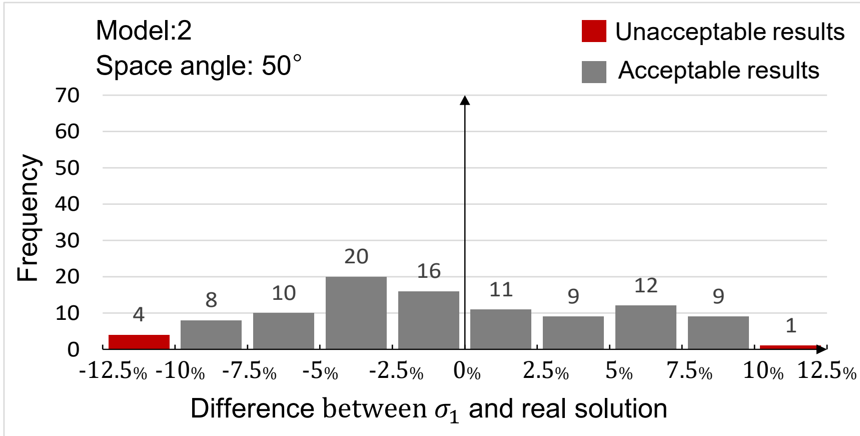

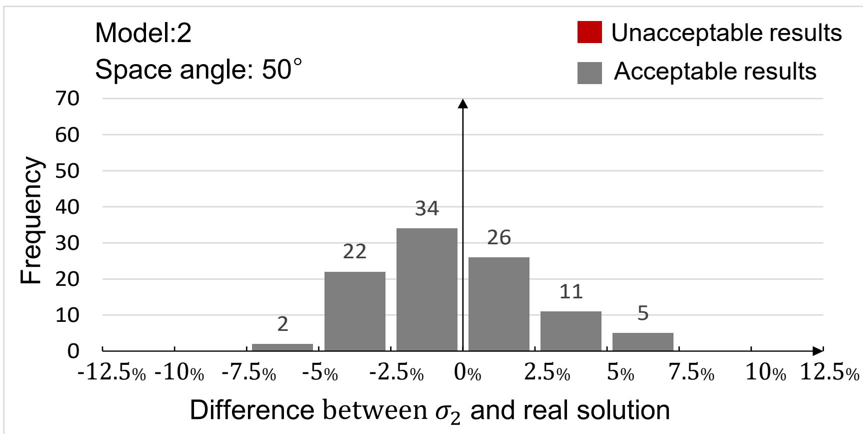

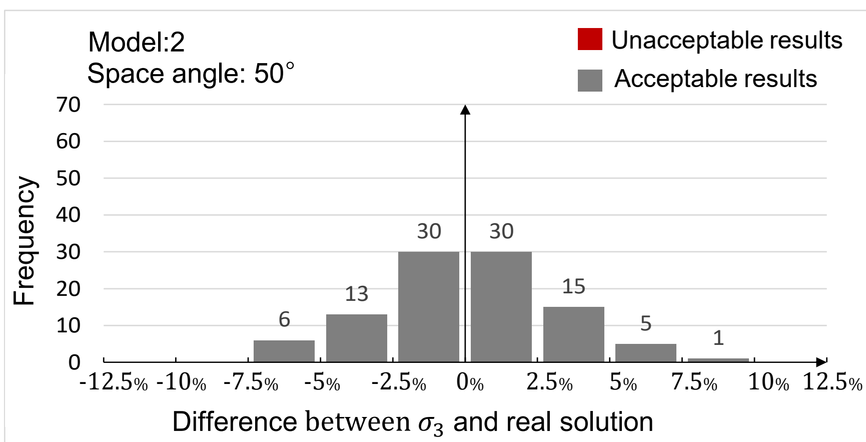

Figure 4.17 Differences between the magnitude of back-analyzed stresses and the real solution of model 2, scenario 5

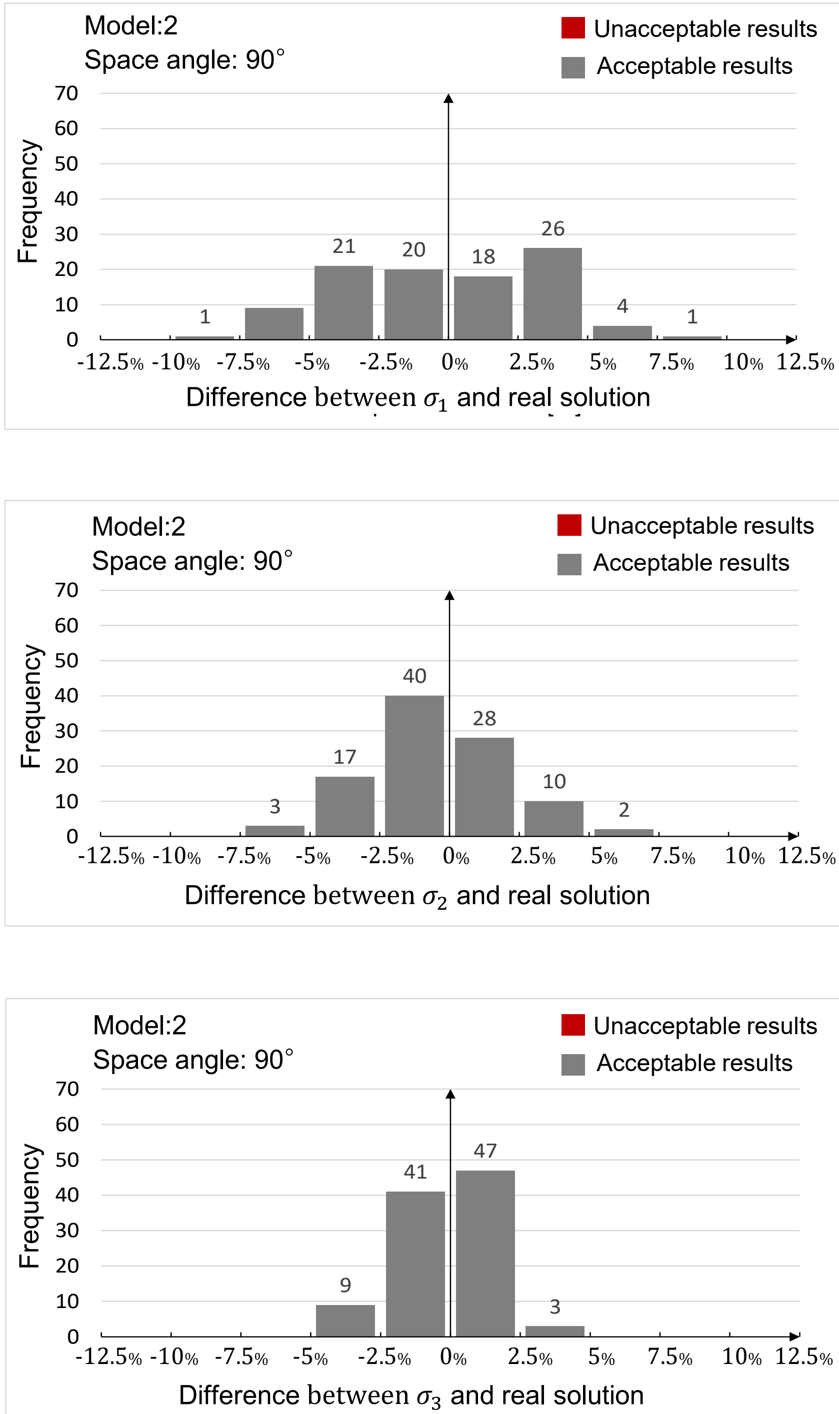

Figure 4.18 Differences between the magnitude of back-analyzed stresses and the real solution of model 2, scenario 9

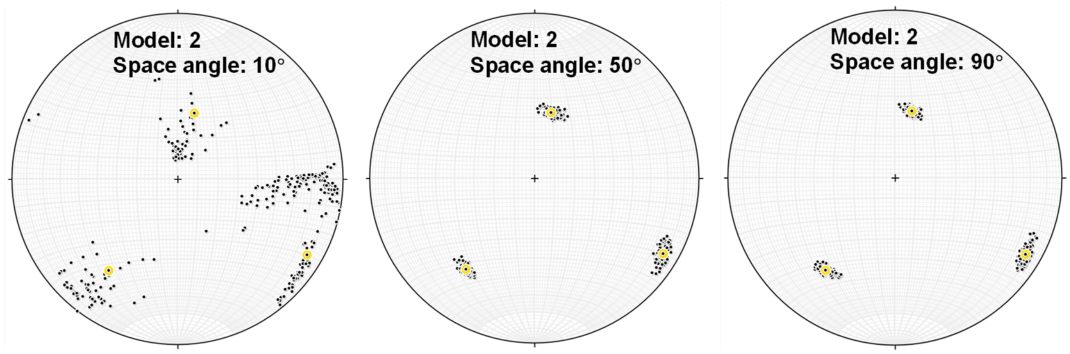

Figure 4.19 Orientations of the back-analyzed and assumed principal stresses in model 2 (Space angle between the three wellbores: 10°, 50°, 90°)

In the statistical analysis, the back-analyzed results would be deemed as unacceptable if its differences with the assumed principal stresses exceed 10%. As can be seen, when the space angle between each well is 10°, more than 70 groups generate unacceptable results. The output errors of 36 groups even reach 50% to 330%. Meanwhile, the back-analyzed stresses' orientations also deviate far away from the real solutions in the stereonet.

As the space angle increases to 50°, approximately all tests can generate satisfied stress results. The differences between the back-analyzed stresses and real solutions are smaller than 12.5%. In the condition of 90°, all the differences are lower than 10% despite up to 20% errors in the input data. The back-analyzed stresses' orientations also distribute in three clusters centered around the actual orientations. Therefore, the principal stress field determined by the back-analysis method will be more accurate when space angles between the selected wellbores enlarge and get closer to 90°.

The results from the statistical analysis highly agree with the findings in the former research and strongly support the reliability of the previous test results.

4.3 ASSESSMENT OF POTENTIAL ERRORS IF A WRONG MODEL IS USED

In the petroleum field, the drilling parameters and borehole convergence data can be measured during the drilling and well-logging process. However, the permeability of the rock formation and mud cake is hard to be determined directly and accurately. Therefore, in the practical application of the back-analysis method in determining the complete 3D stress state, potential errors may exist if users select a wrong model to process the input data. Considering there are five different comprehensive models, five conditions of misusing the model are investigated as follows:

Condition 1: Misuse the input data from model-1 to model-2, model-3, model-4, model-5.

Condition 2: Misuse the input data from model-2 to model-1, model-3, model-4, model-5.

Condition 3: Misuse the input data from model-3 to model-1, model-2, model-4, model-5.

Condition 4: Misuse the input data from model-4 to model-1, model-2, model-3, model-5.

Condition 5: Misuse the input data from model-5 to model-1, model-2, model-3, model-4.

Three different multi-branch wells are investigated in each condition. The combinations of the inclination and bearing angle for the main wellbore and two branch wells are considered as follows:

- 1^{St} Multi-branch well: The space angle between each two of three wellbores is 30°

The sketch of the multi-branch well is displayed in Figure 4.20, and the combinations of the inclination and bearing angle are:

$I_A = 0°$, $\beta_A = 0°$; $I_B = 30°$, $\beta_B = 180°$; $I_C = 30°$, $\beta_C = 117.65°$;

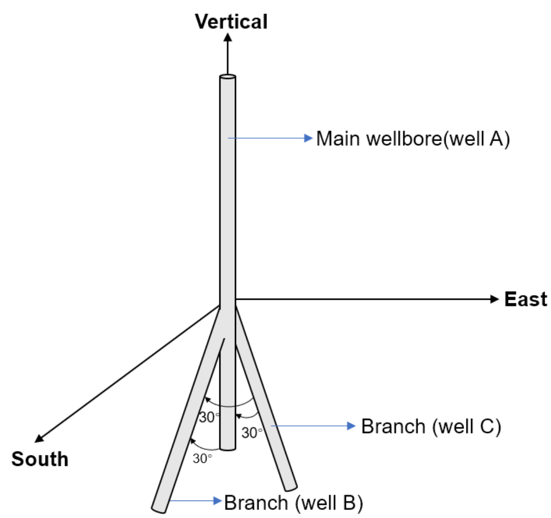

Figure 4.20 1^{St} Multi-branch well

- 2^{nd} Multi-branch well: The space angle between each two of three wellbores is 60°

The sketch of the multi-branch well is displayed in Figure 4.21, and the combinations of the inclination and bearing angle are:

$I_A = 0°$, $\beta_A = 0°$; $I_B = 60°$, $\beta_B = 180°$; $I_C = 60°$, $\beta_C = 109.47°$;

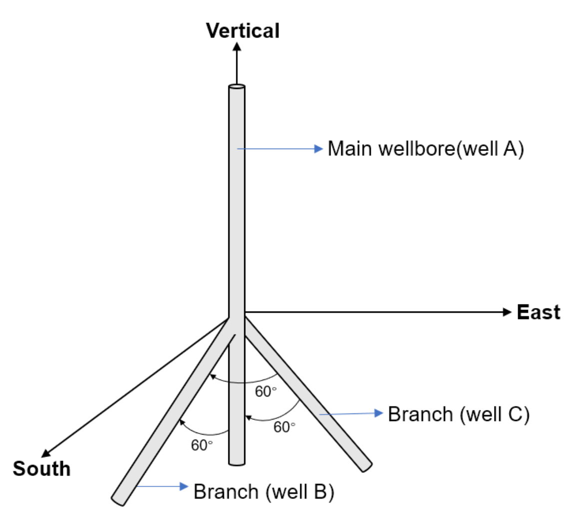

Figure 4.21 2^{nd} Multi-branch well

- 3^{rd} Multi-branch well: The space angle between each two of three wellbores is 90°

The sketch of the multi-branch well is displayed in Figure 4.22, and the combinations of the inclination and bearing angle are:

$I_A = 0°$, $\beta_A = 0°$; $I_B = 90°$, $\beta_B = 180°$; $I_C = 90°$, $\beta_C = 90°$;

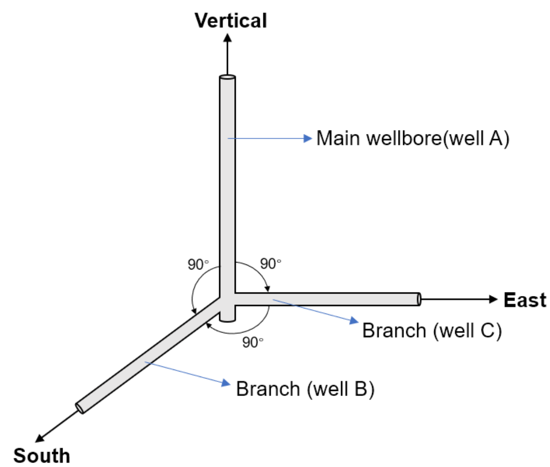

Figure 4.22 3^{rd} Multi-branch well

The Input rock properties, poro-elastic properties and drilling parameters are referred from Table 4.4. Mud pressure in mode-1 is changed from 0 to 25 megapascal to simulate petroleum drilling conditions. The rest simulated input data corresponding to different comprehensive models and the real solution of the in-situ stress results in each condition are listed in the tables below:

Table 4.5 Input borehole diameters for all the models in condition 1

Measured diameter [m]		1	2	3	4	5	6
Space angle between wells: 30°	Well A	0.19957	0.19969	0.19951	0.19912	0.19914	0.19911
	Well B	0.19971	0.19938	0.19922	0.19920	0.19927	0.19861
	Well C	0.19958	0.19897	0.19884	0.19912	0.19945	0.19967
Space angle between wells: 60°	Well A	0.19957	0.19969	0.19951	0.19912	0.19914	0.19911
	Well B	0.19962	0.19968	0.19973	0.19840	0.19879	0.19930
	Well C	0.19929	0.19862	0.19842	0.19887	0.19953	0.19974
Space angle between wells: 90°	Well A	0.19957	0.19969	0.19951	0.19912	0.19914	0.19911
	Well B	0.19982	0.19915	0.19932	0.19872	0.19920	0.19952
	Well C	0.19920	0.19861	0.19840	0.19876	0.19936	0.19958

Table 4.6 Solutions from correct model 1

Correct in-situ stress solution		σ_1	σ_2	σ_3
Space angle between wells: 30°	Magnitude[MPa]	67.71	45.11	23.46
	Plunge[°]	43.76	8.54	44.97
	Trend[°]	6.53	104.80	203.43
Space angle between wells: 60°	Magnitude[MPa]	74.34	47.56	31.78
	Plunge[°]	52.39	9.43	36.01
	Trend[°]	12.49	114.95	211.88
Space angle between wells: 90°	Magnitude[MPa]	76.21	48.31	32.33
	Plunge[°]	53.83	10.25	34.24
	Trend[°]	14.40	118.73	215.80

Table 4.7 Input borehole diameters for all the models in condition 2

Measured diameter [m]		1	2	3	4	5	6
Space angle between wells: 30°	Well A	0.19965	0.19976	0.19959	0.19949	0.19948	0.19949
	Well B	0.19978	0.19948	0.19912	0.19902	0.19914	0.19958
	Well C	0.19966	0.19907	0.19894	0.19945	0.19982	0.19998
Space angle between wells: 60°	Well A	0.19965	0.19976	0.19959	0.19949	0.19948	0.19949
	Well B	0.19982	0.19932	0.19884	0.19883	0.19912	0.19968
	Well C	0.19966	0.19882	0.19864	0.19936	0.19991	0.20001
Space angle between wells: 90°	Well A	0.19965	0.19976	0.19959	0.19948	0.19948	0.19949
	Well B	0.19976	0.19925	0.19899	0.19915	0.19946	0.19980
	Well C	0.19961	0.19878	0.19856	0.19926	0.19979	0.20002

Table 4.8 Solutions from correct model 2

Correct in-situ stress solution		σ_1	σ_2	σ_3
Space angle between wells: 30°	Magnitude[MPa]	67.94	45.44	24.77
	Plunge[°]	44.71	8.79	43.95
	Trend[°]	6.84	105.64	204.21
Space angle between wells: 60°	Magnitude[MPa]	74.16	47.74	32.17
	Plunge[°]	52.73	9.50	35.64
	Trend[°]	12.62	115.32	212.21
Space angle between wells: 90°	Magnitude[MPa]	75.86	48.46	32.60
	Plunge[°]	54.04	10.27	34.02
	Trend[°]	14.43	118.90	215.93

Table 4.9 Input borehole diameters for all the models in condition 3

Measured diameter [m]		1	2	3	4	5	6
Space angle between wells: 30°	Well A	0.19966	0.19977	0.19961	0.19950	0.19949	0.19950
	Well B	0.19979	0.19949	0.19913	0.19903	0.19915	0.19959
	Well C	0.19967	0.19908	0.19895	0.19946	0.19983	0.19999
Space angle between wells: 60°	Well A	0.19966	0.19977	0.19961	0.19950	0.19949	0.19950
	Well B	0.19983	0.19933	0.19886	0.19884	0.19913	0.19969
	Well C	0.19967	0.19883	0.19865	0.19937	0.19992	0.20011
Space angle between wells: 90°	Well A	0.19966	0.19977	0.19961	0.19950	0.19949	0.19950
	Well B	0.19976	0.19927	0.19901	0.19917	0.19947	0.19981
	Well C	0.19962	0.19879	0.19858	0.19927	0.19980	0.20003

Table 4.10 Solutions from correct model 3

Correct in-situ stress solution		σ_1	σ_2	σ_3
Space angle between wells: 30°	Magnitude[MPa]	67.98	45.50	25.01
	Plunge[°]	44.89	8.83	43.76
	Trend[°]	6.90	105.81	204.36
Space angle between wells: 60°	Magnitude[MPa]	74.12	47.77	32.24
	Plunge[°]	52.79	9.51	35.57
	Trend[°]	12.64	115.39	212.27
Space angle between wells: 90°	Magnitude[MPa]	75.80	48.48	32.64
	Plunge[°]	54.07	10.28	33.98
	Trend[°]	14.44	118.93	215.95

Table 4.11 Input borehole diameters for all the models in condition 4

Measured diameter [m]		1	2	3	4	5	6
Space angle between wells: 30°	Well A	0.19964	0.19973	0.19957	0.19949	0.19950	0.19949
	Well B	0.19971	0.19943	0.19915	0.19908	0.19916	0.19953
	Well C	0.19962	0.19913	0.19902	0.19947	0.19976	0.19991
Space angle between wells: 60°	Well A	0.19964	0.19973	0.19957	0.19950	0.19950	0.19949
	Well B	0.19974	0.19929	0.19892	0.19892	0.19914	0.19961
	Well C	0.19962	0.19891	0.19877	0.19938	0.19982	0.19999
Space angle between wells: 90°	Well A	0.19964	0.19974	0.19957	0.19949	0.19950	0.19949
	Well B	0.19970	0.19925	0.19906	0.19920	0.19944	0.19972
	Well C	0.19956	0.19886	0.19869	0.19929	0.19971	0.19992

Table 4.12 Solutions from correct model 4

Correct in-situ stress solution		σ_1	σ_2	σ_3
Space angle between wells: 30°	Magnitude[MPa]	67.67	44.77	23.13
	Plunge[°]	43.60	8.34	45.19
	Trend[°]	6.22	104.25	202.73
Space angle between wells: 60°	Magnitude[MPa]	74.38	47.19	31.50
	Plunge[°]	52.34	9.35	36.09
	Trend[°]	12.47	114.79	211.69
Space angle between wells: 90°	Magnitude[MPa]	76.36	48.07	31.95
	Plunge[°]	53.85	10.09	34.29
	Trend[°]	14.42	118.52	215.49

Table 4.13 Input borehole diameters for all the models in condition 5

Measured diameter [m]		1	2	3	4	5	6
Space angle between wells: 30°	Well A	0.19966	0.19975	0.19959	0.19952	0.19952	0.19951
	Well B	0.19973	0.19946	0.19917	0.19910	0.19919	0.19955
	Well C	0.19965	0.19915	0.19904	0.19949	0.19978	0.19992
Space angle between wells: 60°	Well A	0.19966	0.19975	0.19959	0.19952	0.19952	0.19952
	Well B	0.19975	0.19931	0.19894	0.19894	0.19916	0.19963
	Well C	0.19964	0.19894	0.19879	0.19940	0.19984	0.20001
Space angle between wells: 90°	Well A	0.19966	0.19975	0.19959	0.19951	0.19952	0.19952
	Well B	0.19972	0.19928	0.19901	0.19922	0.19946	0.19974
	Well C	0.19958	0.19988	0.19872	0.19931	0.19973	0.19994

Table 4.14 Solutions from correct model 5

Correct in-situ stress solution		σ_1	σ_2	σ_3
Space angle between wells: 30°	Magnitude[MPa]	67.73	44.87	23.51
	Plunge[°]	43.87	8.42	44.90
	Trend[°]	6.32	104.49	202.97
Space angle between wells: 60°	Magnitude[MPa]	74.32	47.24	31.61
	Plunge[°]	52.43	9.38	35.98
	Trend[°]	12.50	114.90	211.78
Space angle between wells: 90°	Magnitude[MPa]	76.26	48.11	32.02
	Plunge[°]	53.90	10.10	34.23
	Trend[°]	14.43	118.57	215.53

The back-analyzed in-situ stress results when the input data above are used in the wrong models are listed in Appendix E. It can be found that the orientations of back-analyzed in-situ stresses of all conditions are almost consistent with the solutions from correct models. The differences between them are smaller than 2° for all conditions. However, the magnitudes of back-analyzed in-situ stresses in different conditions have some errors.

Figures 4.23 to 4.27 illustrate the difference between the magnitude of back-analyzed stresses and the correct solutions in five conditions, respectively. As can be seen, the errors of σ_1 and σ_2 varies between 1% to 14% in different conditions. The magnitude of σ_3 is more likely to be influenced, and its difference with the correct solution changed from 1% to 28%.

When the space angles between each well are 60° and 90°, the differences between the solutions from a wrong model and the correct one reduce to a value smaller than 10%, 13% and 20% for σ_1, σ_2 and σ_3, respectively.

In general, as wrong models are utilized to process the borehole convergence data, the orientations of back-analyzed in-situ stress components are still reliable and approximately consistent with the correct solutions. The errors of the magnitudes are less than 20% in the condition that the space angles between each well are in the reasonable range (more than 60°).

In future research, well-logging data from the petroleum field are required to be obtained. It can provide assistance and reference for optimizing the model selection in different drilling conditions and improving the D3 stress estimation method furtherly. Meanwhile, the MFC applications will also become a more practical tool for the in-situ stress estimation in the field site.

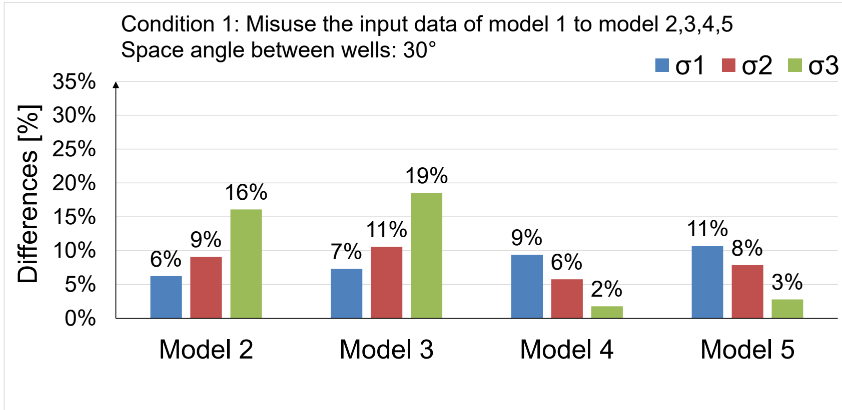

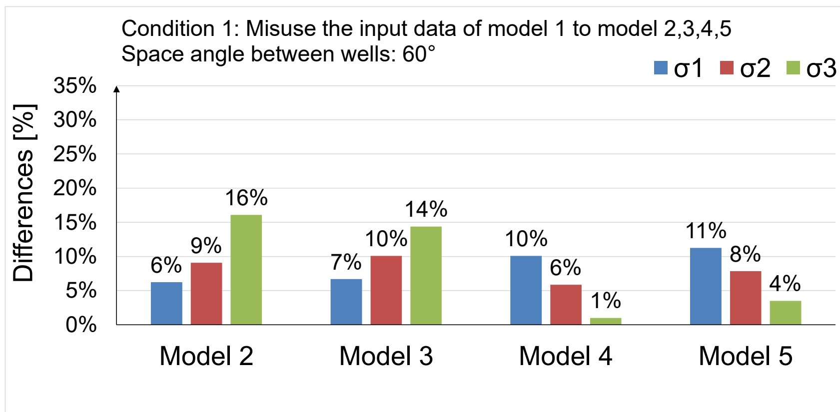

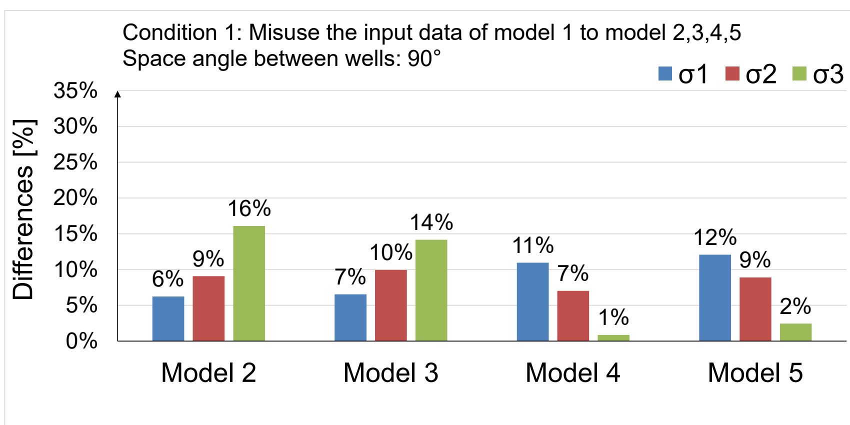

Figure 4.23 Differences between the magnitude of back-analyzed stresses and correct solution of model 1 in condition 1

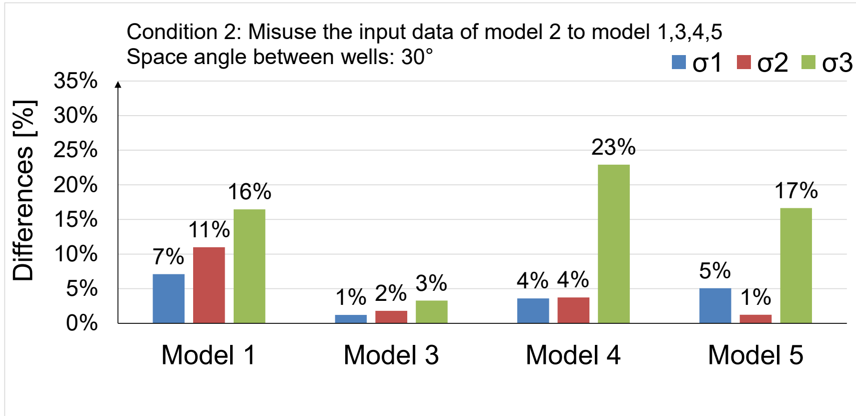

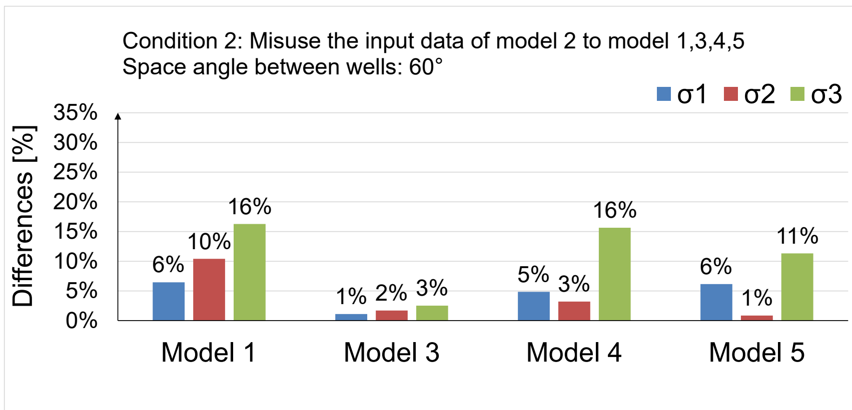

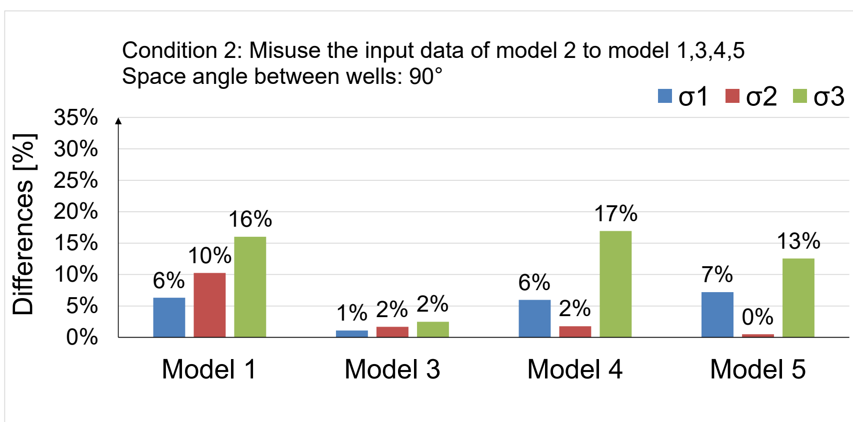

Figure 4.24 Differences between the magnitude of back-analyzed stresses and correct solution of model 2 in condition 2

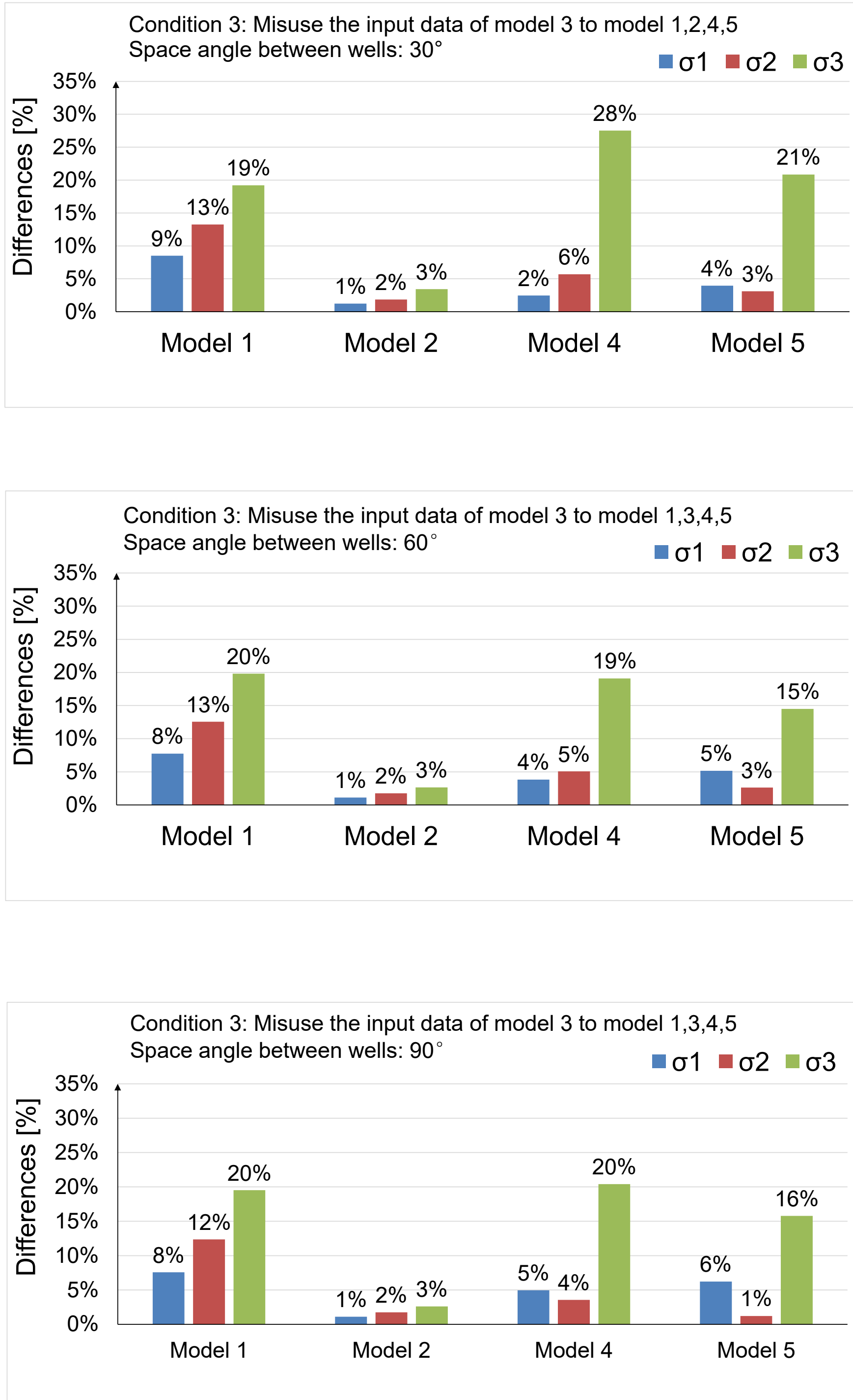

Figure 4.25 Differences between the magnitude of back-analyzed stresses and correct solution of model 3 in condition 3

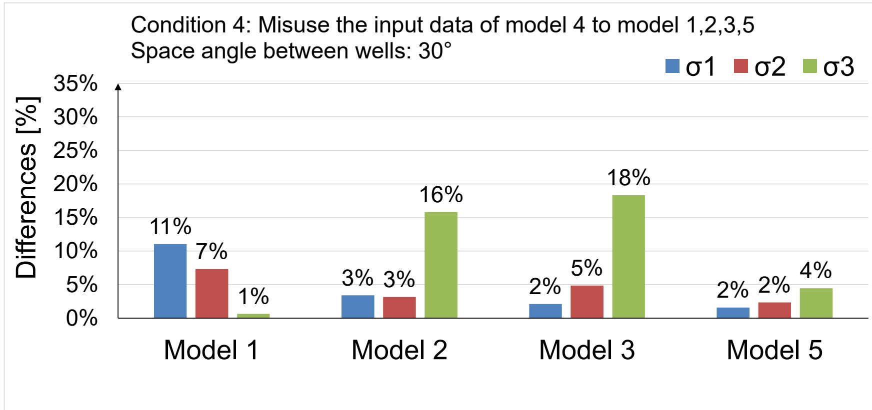

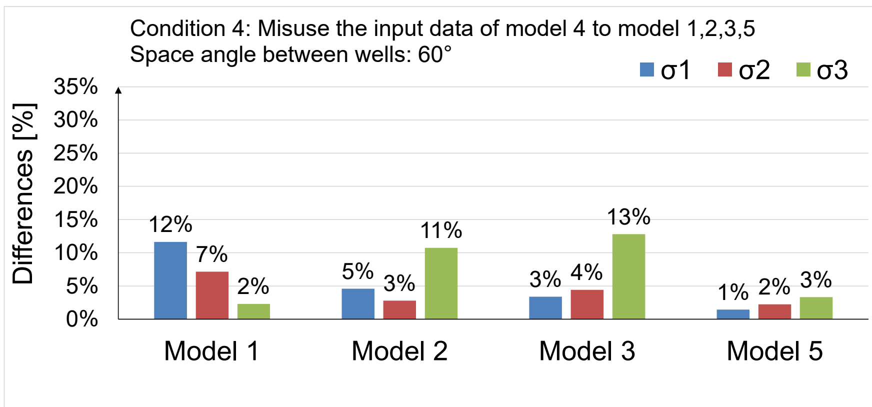

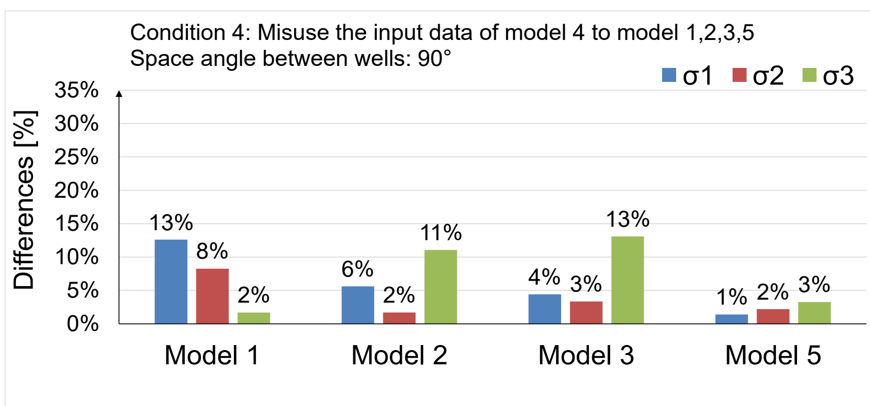

Figure 4.26 Differences between the magnitude of back-analyzed stresses and correct solution of model 4 in condition 4

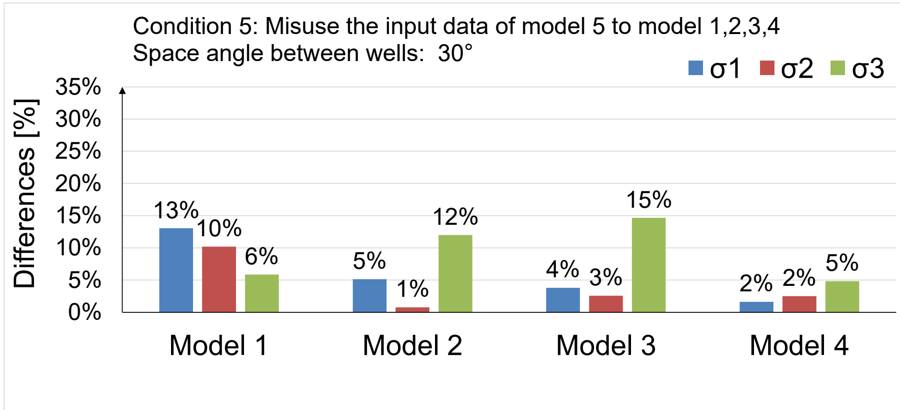

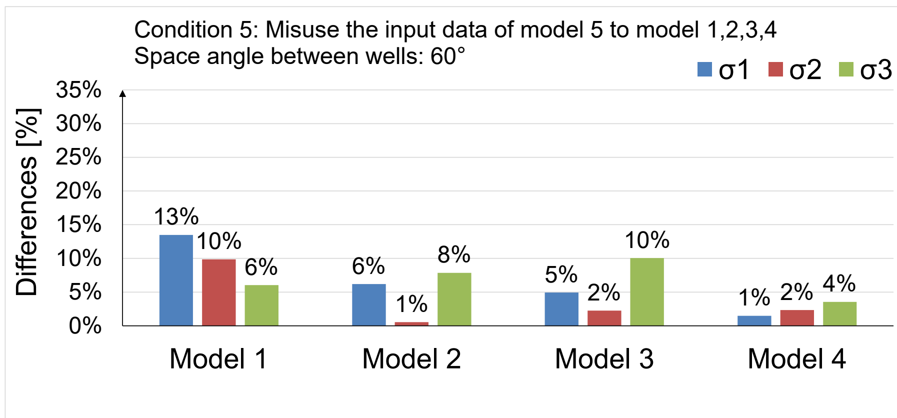

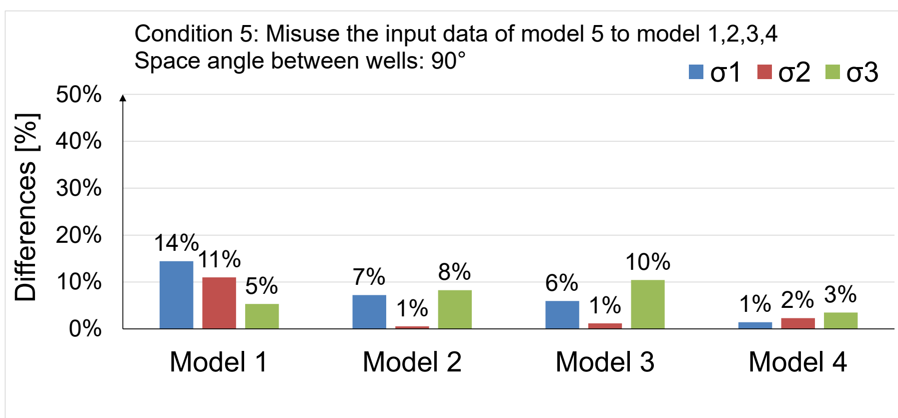

Figure 4.27 Differences between the magnitude of back-analyzed stresses and correct solution of model 5 in condition 5

CHAPTER 5 CONCLUSIONS

In this research, two console applications and two MFC applications have been developed for the automated analysis of the back-analysis method. Test examples according to the simulated field data are processed by the MFC applications, and the relevant back-analyzed results are compared and analyzed. The major works of my research are summarized and important conclusions are given as follows:

(1) Based on the displacement-based back analysis method, two C++-based console applications are developed through Dev C++ for the 2D and 3D in-situ stress estimation at the initial process of my research. The console applications allow users to type in the required input data in a specific text file and obtain the results of the back-analyzed in-situ stresses in an output text file.

(2) Two MFC applications with graphical user interfaces are further developed based on the console applications. The 2D and 3D MFC applications are also compiled in C++ and developed using Visual Studio 2013. The source code from the console applications is fully embedded into the MFC application to perform the calculation process of the back-analysis method.
The MFC application provides two interfaces – log-in interface and user interface. In the log-in interface, users are required to type in the correct combination of the account name and password to step into the user interface. The second interface allows users to input data and view results. The applications have been testified through simulated input data and proved to works properly.

(3) Test results of the 3D in-situ stress estimation show that, even if the input drilling parameters, rock and poro-elastic properties are the same, the accuracy of the back-analyzed results varies when the space angle intervals between each well are changed. The method gives results with large errors exceeding 100%, when

the space angle interval between each well gets smaller than 20°. To ensure the accuracy of the 3D back-analyzed in-situ stresses, the suggested space angle interval between each well should be more than 60° for model 1 and 50° for models 2 to 5. The accuracy of the back-analyzed results increases with the rise of the space angle between wells. As that space angle getting close to 90°, which means the three wellbores are perpendicular to each other, the back-analyzed in-situ stresses are approximately consistent with the real solution.

The space angle interval between the orientations of wellbores and principal stresses may also exert some influence on the accuracy of the back-analyzed results. The correlation between the three wellbores and the three principal stresses needs further investigation.

(4) The results of the statistical analysis also demonstrate the same trend. In the condition that the space angle between each well is merely 10°, the output errors have a high frequency to achieve 50%~330%, with 20% input errors. As the space angle increases to 50° and 90°, the back-analyzed in-situ stresses converge to the actual solution, especially for the 90° condition, of which the output errors are less than 7%.

(5) In practical use of the application, if wrong models are utilized to process the borehole convergence data, the orientations of back-analyzed principal stresses are still reliable and approximately consistent with the correct solutions. The errors of the magnitudes are less than 20% in the condition that the space angles between each well are in the reasonable range (more than 60°).

In future research, well-logging data from the petroleum field are required to be obtained. It can provide assistance and reference for selecting proper comprehensive models in different drilling conditions and improving the D3 stress estimation method furtherly.

REFERENCES

Abé H. and Hayashi K., 1992. Fundamentals of design concept and design methodology for artificial geothermal reservoir systems. Geothermal Resources Council – Bulletin, 21: 149 – 155.

A.Lehtonen and J.W. Cosgrove, 2012. An examination of in situ rock stress estimation using the Kaiser effect. Engineering Geology, 124: 24 – 37.

Anon, 1999. Horizontal and multilateral well: increasing production and reducing overall drilling and completion costs. Journal of Petroleum Technology, 51(7): 20-24

Bock H. and Foruria V., 1983. A recoverable borehole slotting instrument for in-situ stress measurements in rocks. International Symposium on Field Measurements in Geomechanics, Zurich, September 5 – 8, 15 – 29.

Braton C A., Zoback Mark D, 1988. In-situ stress orientation and magnitude at the Fenton geothermal site 'New Mexico' determined from wellbore breakouts. Geophysical Research Letters, 15(5): 467 – 470.

Bruno F., 1966. Determination of in situ stresses using large flat jack tests. Paper presented at the conference of the 6th Asian Rock Mechanics Symposium, New Delhi, India.

Cai.M. and R.L.Blackwood, 1987. Performance of the USBM Borehole Deformation Gage in Different Rock Conditions. Paper presented The 28th U.S. Symposium on Rock Mechanics (USRMS), Tucson, Arizona.

C.D.Martin, P.K.Kaiser, K.R.Chistiansson, 2003. Stress instability and design of underground excavations. International Journal of Rock Mechanics and Mining Sciences, 40(7): 1243 - 1256.

C Fairhurst, 2003. Stress estimation in rock: a brief history and review. International Journal of Rock Mechanics & Mining Sciences, 40(7-8): 957 - 973.

Cui Lin and D.H.Steve Zou, 2016. In-situ stress estimation by back analysis method based on well deformation with consideration of pore pressure. International Journal of Georesources and Environment, 5(1): 1 – 13.

Cui Lin, 2019. Estimation of 2D and 3D In-situ stress using back-analysis of measurement of Well/Borehole deformation. Thesis submitted for the degree of Doctor of Philosophy, Dalhousie University, Canada.

Cui Lin and D.H.Steve Zou, 2021. Formulation and verification of 3D in-situ stress estimation based on differential-direction drilling. International Journal of Rock Mechanics and Mining Sciences, 145 (in press, Sept. 2021, article 104833).

Cui Lin, D.H.Steve Zou, and Sun, H.R., 2019. Exploration of measurement methods of 3D in-situ stresses in rock masses. International Journal of Georesources and Environment, 2019, 5(1): 1 - 13.

DR Hughson., and AM Crawford, 1986. Kaiser effect gauging: A new method for determining the pre-existing in-situ stress from an extracted core by acoustic emissions. Paper presented at the ISRM International Symposium, Stockholm, Sweden, August 1986.

E.R.HOSKINS, 1966. An Investigation of The Flat jack Method of Measuring Rock Stress. International Journal of Rock Mechanics & Mining Sciences & Geomechanics Abstracts, 1966, 3(4): 249

Gough DI, and Bell JS, 1982. Stress orientations from borehole wall fractures with examples from Colorado, east Texas and northern Canada. Canadian Journal of Earth Sciences, 19(7): 1358 – 1370.

Haimson B., 1968. Hydraulic Fracturing in Porous and Non-porous Rock and Its Potential for Determining in-situ Stresses at Great Depth. J Pet Technol 21: 811 – 817.

Hast.N., 1958. The measurement of rock pressure in mines. Arsb. Sver. Geol. Unders, 53p.

Jacques Angelier, 1979. Determination of the mean principal directions of stresses for a given fault population. Tectonophysics, 56(3-4): 17 – 26.

Kaiser E J., 1996. An acoustic emission study of damage development and stress-memory effects in sandstone. International Journal of Rock Mechanics and Mining Sciences & Geomechanics Abstracts, 33(6): 585 – 593.

Kazuo Hayashi, Akira Sato., 1997. In-situ Stress Measurements by Hydraulic Fracturing for a Rock with Many Planes of Weakness. International Journal of Rock Mechanic and Mining Sciences, 34(1): 45 – 58.

Kazuaki Nakamura, 1977. Volcanoes as Possible Indicators of Tectonic Stress Orientation – Principle and Proposal. Journal of Volcanology & Geothermal Research, 2(1):1 – 16.
Leahy T.F., 1984. The Delta-element Reusable Strain Transducer. Experimental Mechanics, 24(3): 191 – 202.

Leeman E.R., 1969. The CSIR “Doorstopper” and Triaxial Rock Stress Measuring Instruments. Rock Mechanics, 3(1): 25 – 50.

Li.C, and Norlund.E, 1993. Experimental Verification of Kaiser Effect in Rocks. Rock Mechanics and Rock Engin, 26(4): 333 – 351.

Li Yong-song and Peng Qian, 2018. Method of Geostress Relieving and Measuring by Borehole Slots: Numerical Analysis and Engineering Application. Journal of the Yangtze Scientific Research Institute, 35(3): 85 – 91. (In Chinese).

Mark D.Zoback., and Daniel Moos, 1985. Well Bore Breakouts and In-situ Stress. Journal of Geophysical Research Atmospheres 90: 5523 – 5530.

Merrill, R.H., 1967. Three-component borehole deformation gauge for determining the stress in Rock. United States Bureau of Mines RI 7015, 38 p.

Paul, B., and Graham, M. E., 2002. Rock Mechanics and Wellbore Stability Analysis While Drilling using LWD Sonic, Density and Caliper Measurements. Proceedings of the SPE/ISRM Rock Mechanics in Petroleum Engineering Conference.

Pawel Gregorczyk, 2000. A Review on Flat-Jack Testing. Eng.Civil, 9: 37 – 50.

P.K. Kaiser, D.H. Zou, P.A. Lang. 1990. Stress Determination by Back-Analysis of Excavation-Induced Stress Changes – a Case Study. Rock Mechanics & Rock Engineering, 23(3): 185 - 200.

Seban, R.R., 1994. An overview of object-oriented design and C++[C]. Paper presented at the Aerospace Applications Conference. IEEE.

S Gaines, MS Diederichs, 2012. Review of borehole in situ stress measurement techniques for various ground conditions and numerical stress estimation considerations. Paper presented at the 46th U.S. Rock Mechanics/Geomechanics Symposium, Chicago.

Tincelin E., 1951. Research on rock pressure in the Iron Mines of Lorraine. Paper presented at the International Conference of Rock Pressure and Support in the Workings, Liege, France.

APPENDIX A THE MAGNITUDE OF THE BACK-ANALYZED 3D IN-SITU STRESSES

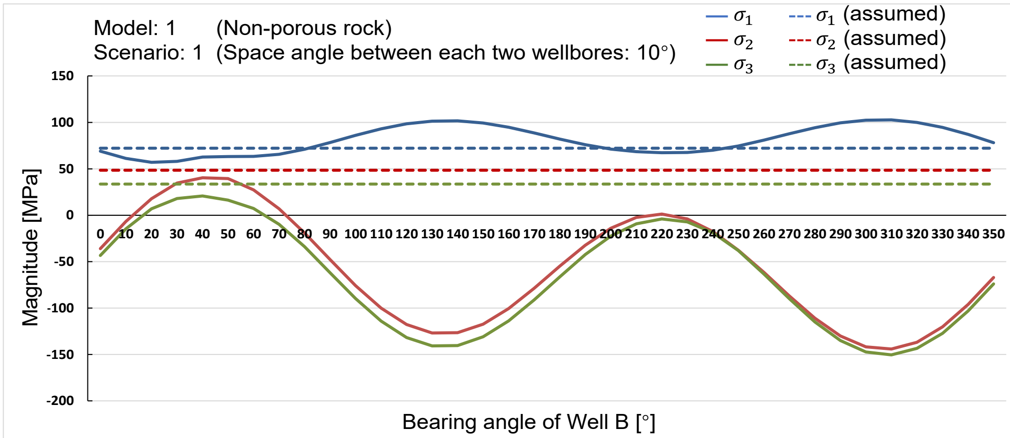

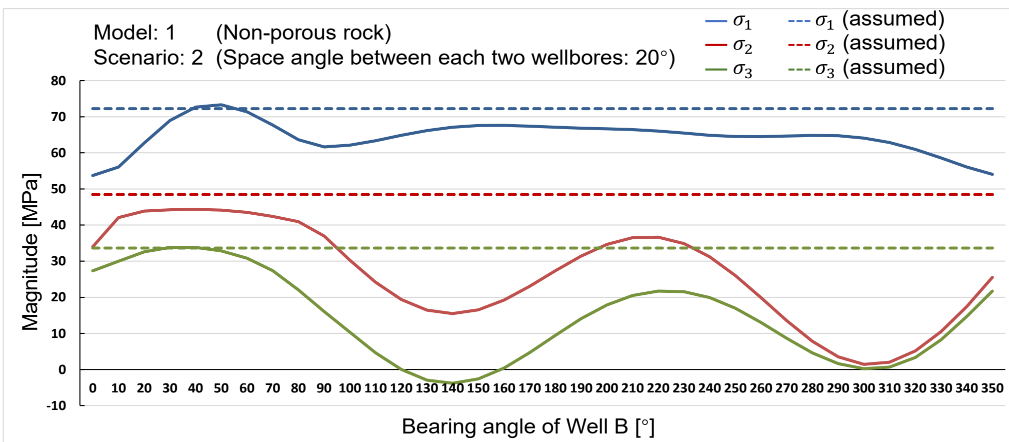

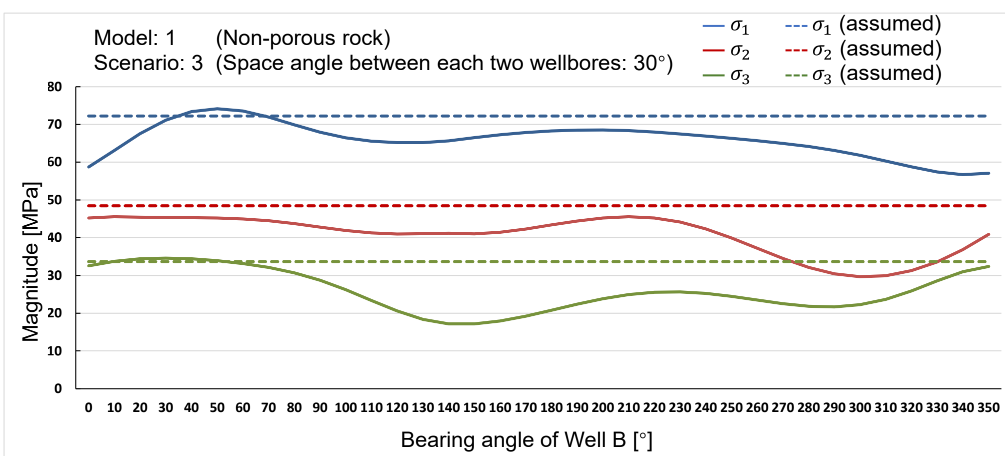

Figure A.1 Back-analyzed result in Model 1, scenarios 1, 2, 3

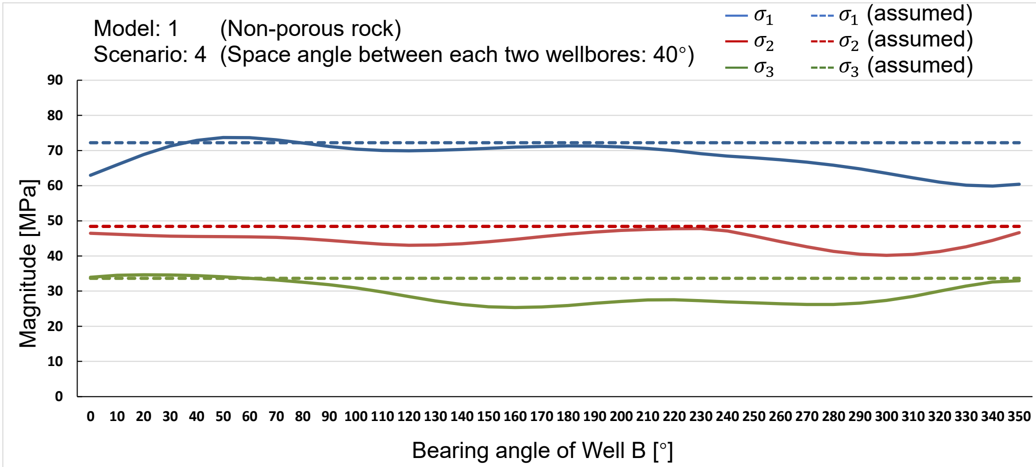

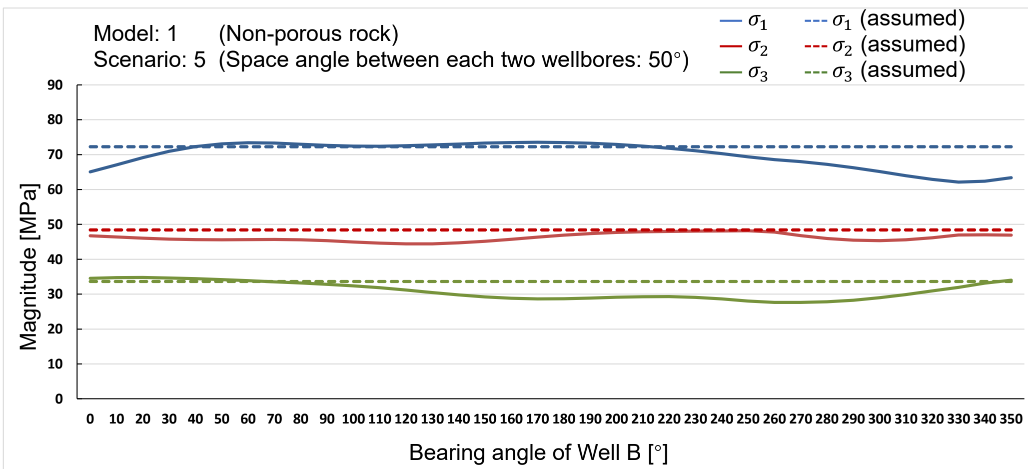

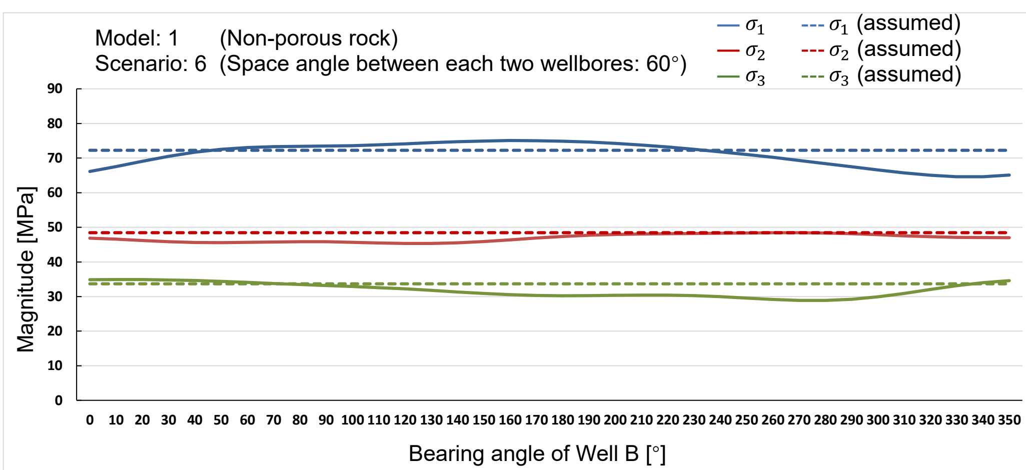

Figure A.2 Back-analyzed result in Model 1, scenarios 4, 5, 6

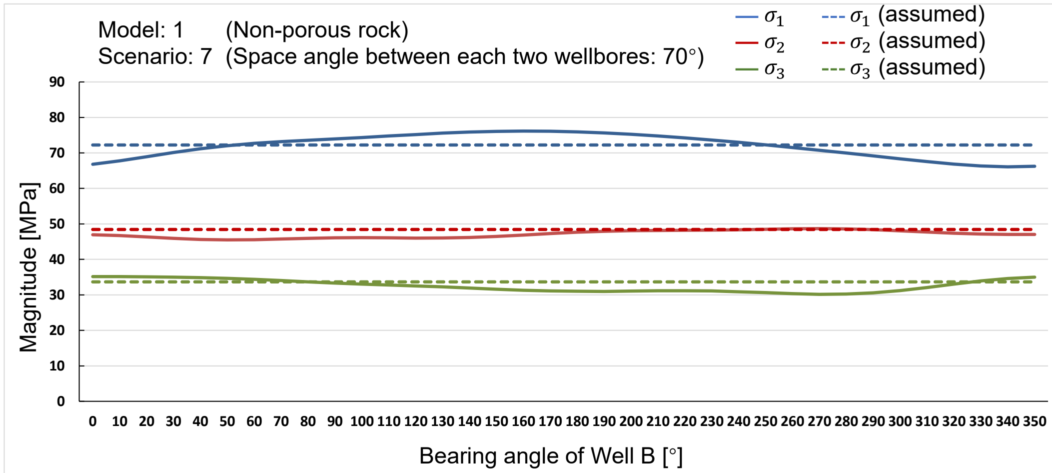

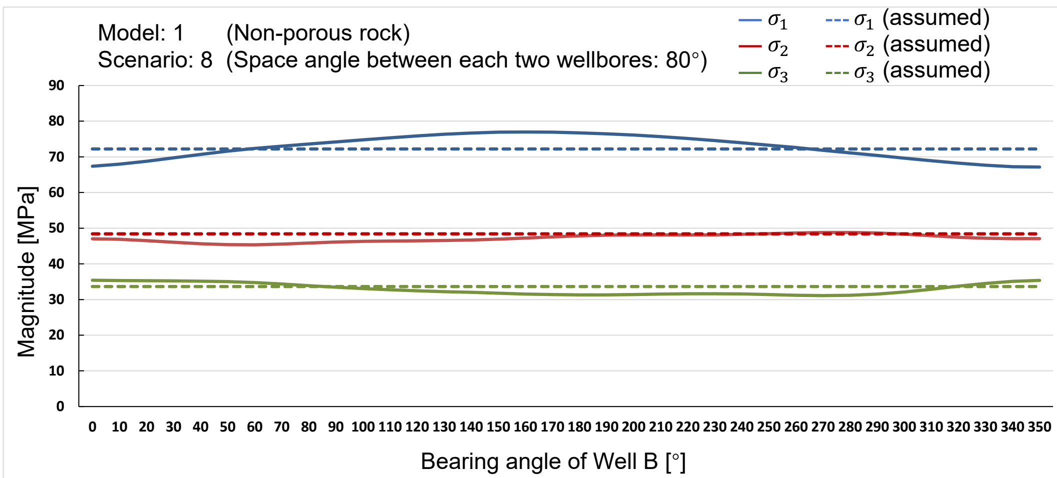

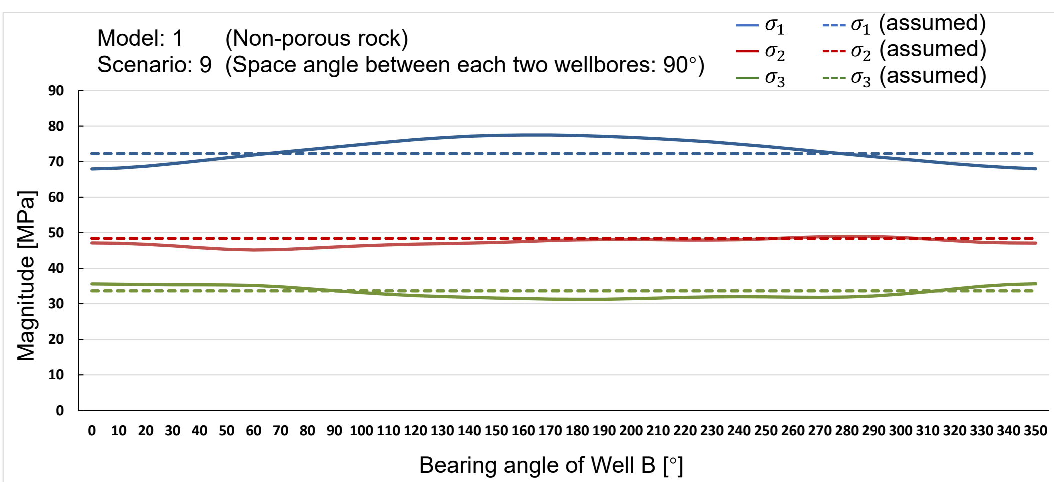

Figure A.3 Back-analyzed result in Model 1, scenarios 7, 8, 9

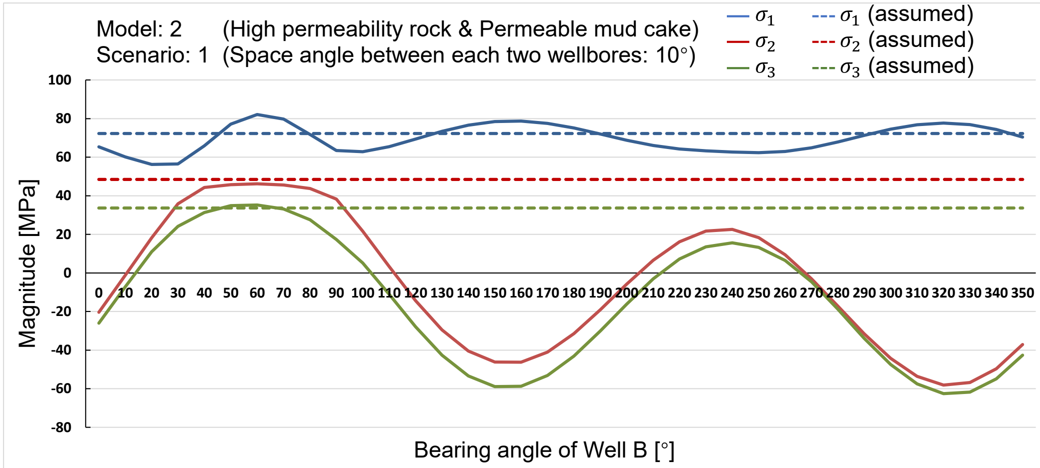

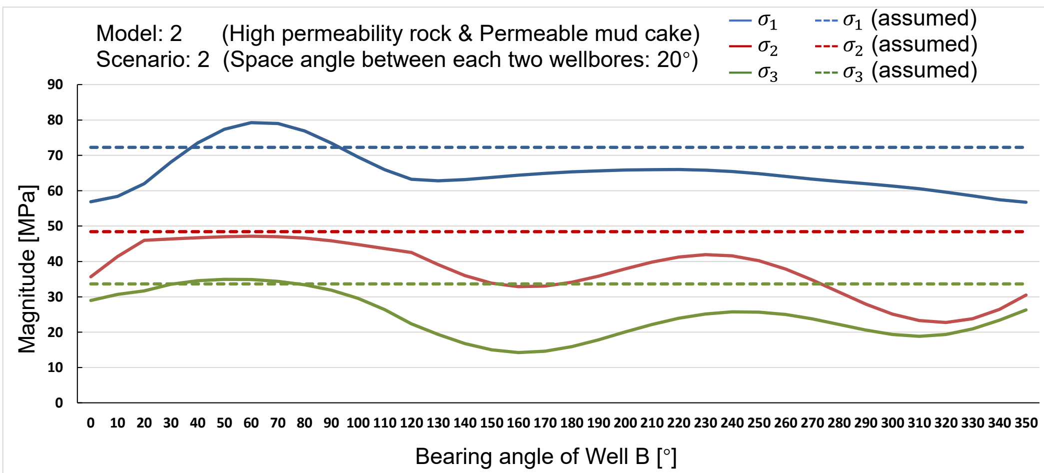

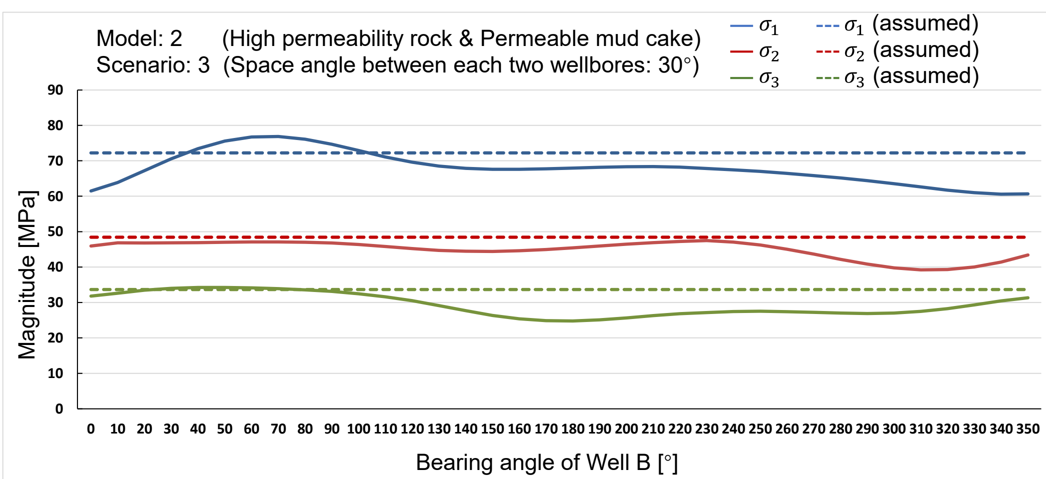

Figure A.4 Back-analyzed result in Model 2, scenarios 1, 2, 3

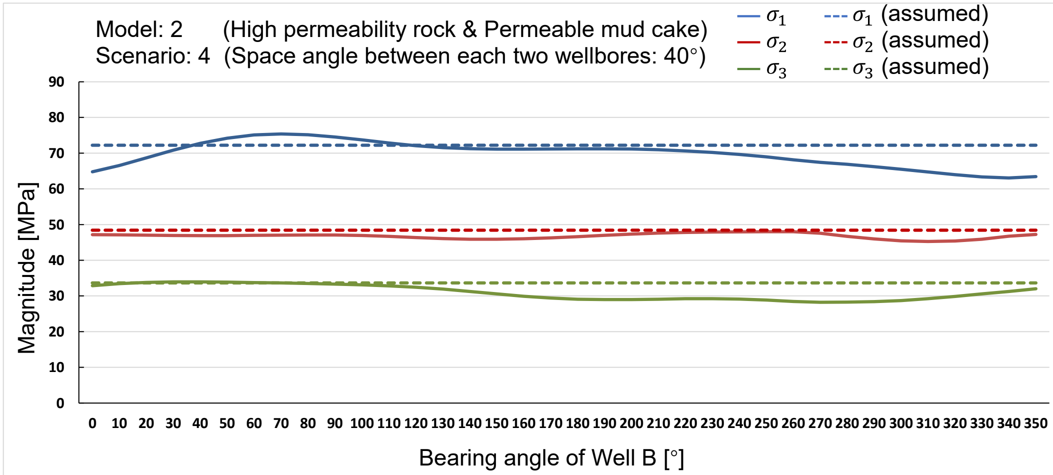

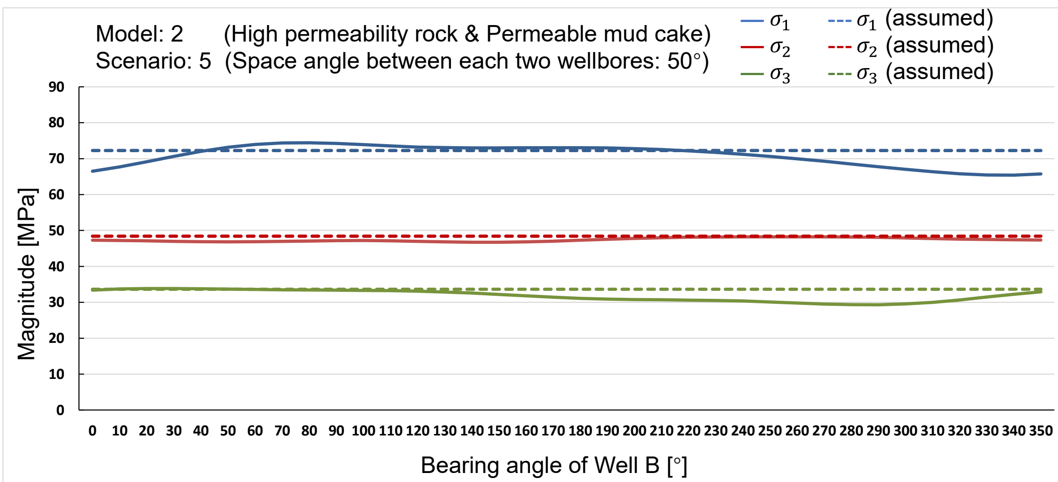

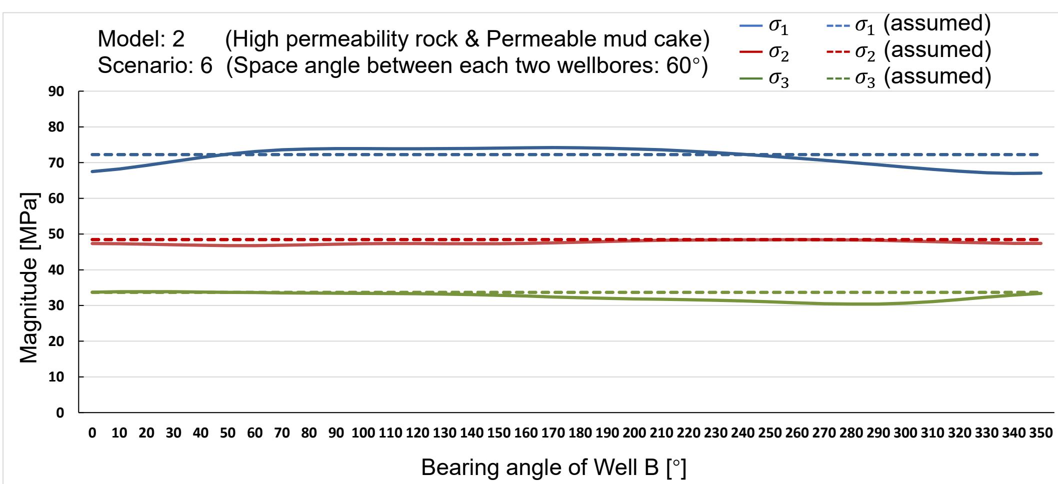

Figure A.5 Back-analyzed result in Model 2, scenarios 4, 5, 6

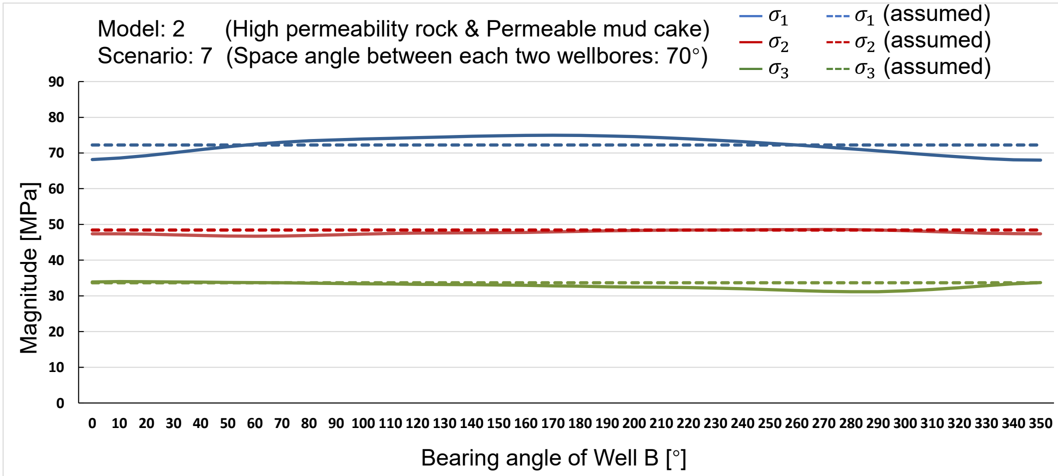

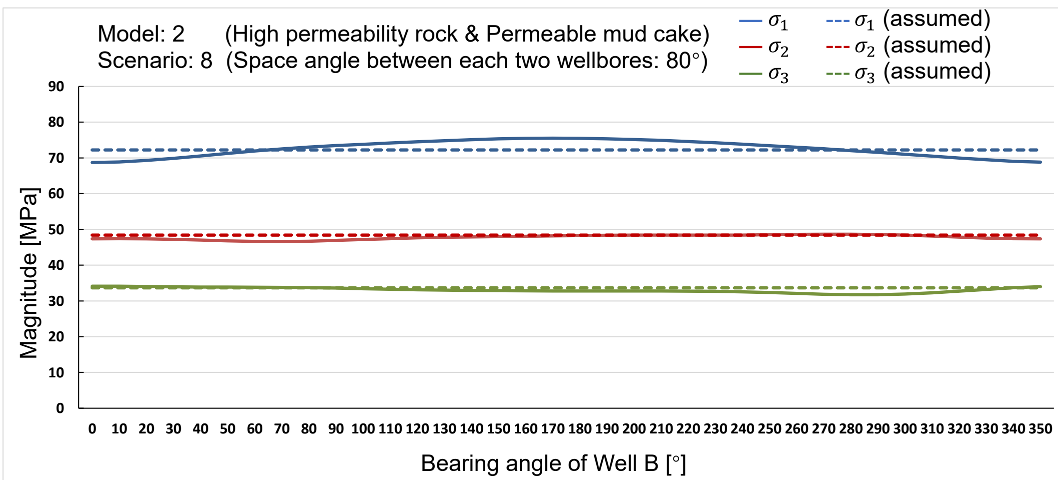

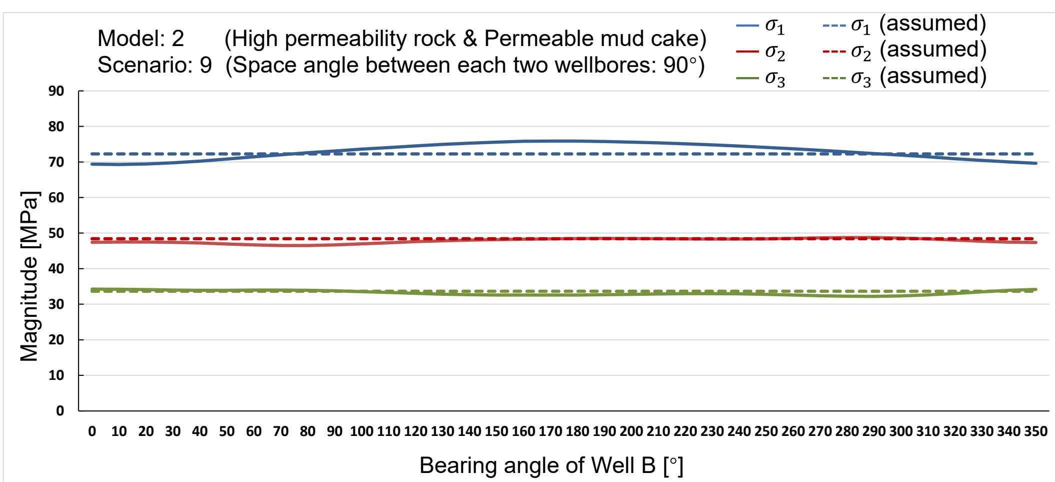

Figure A.6 Back-analyzed result in Model 2, scenarios 7, 8, 9

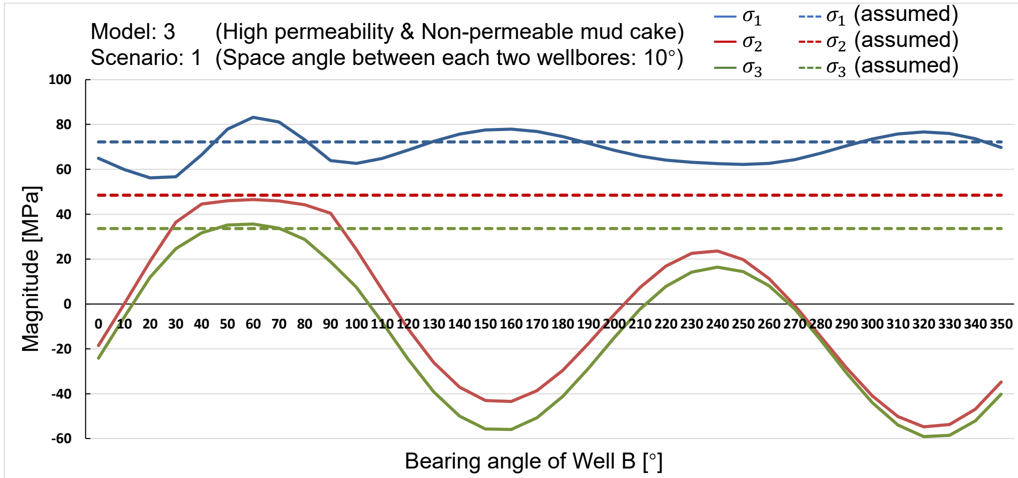

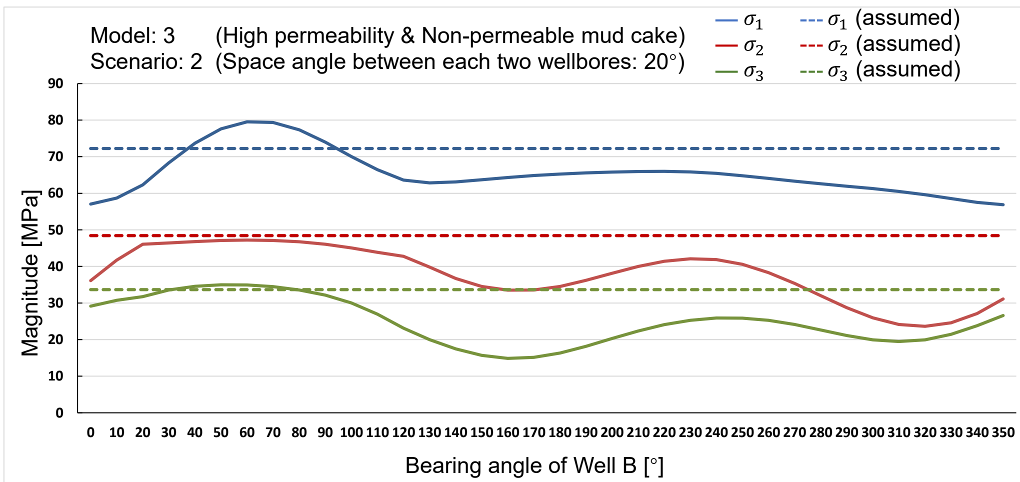

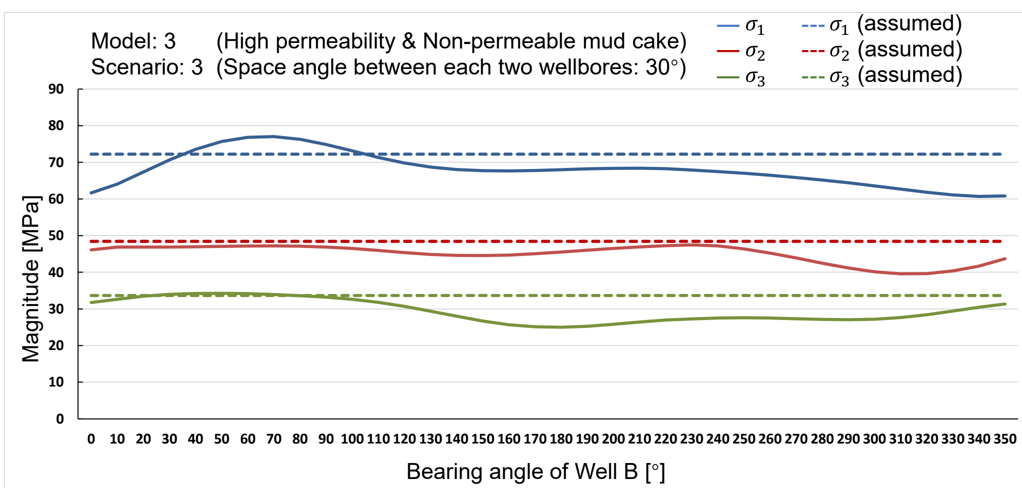

Figure A.7 Back-analyzed result in Model 3, scenarios 1, 2, 3

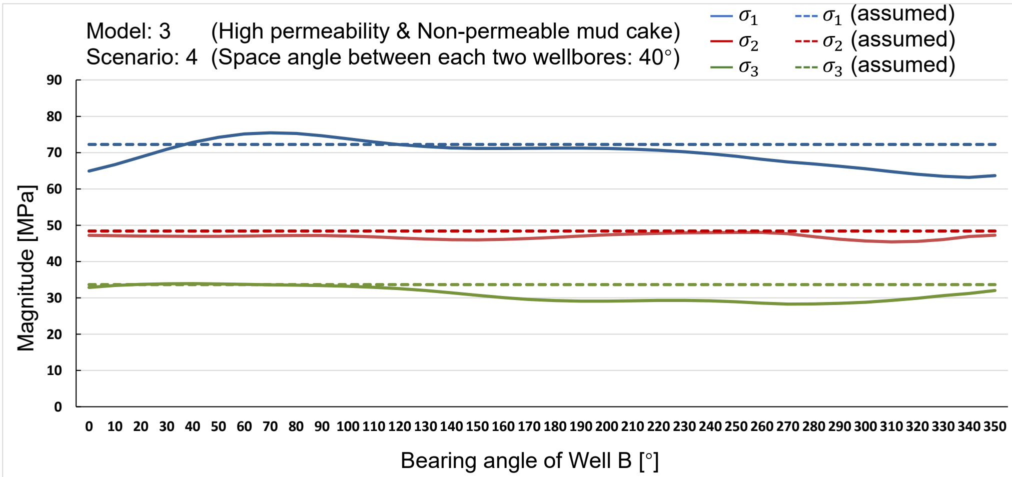

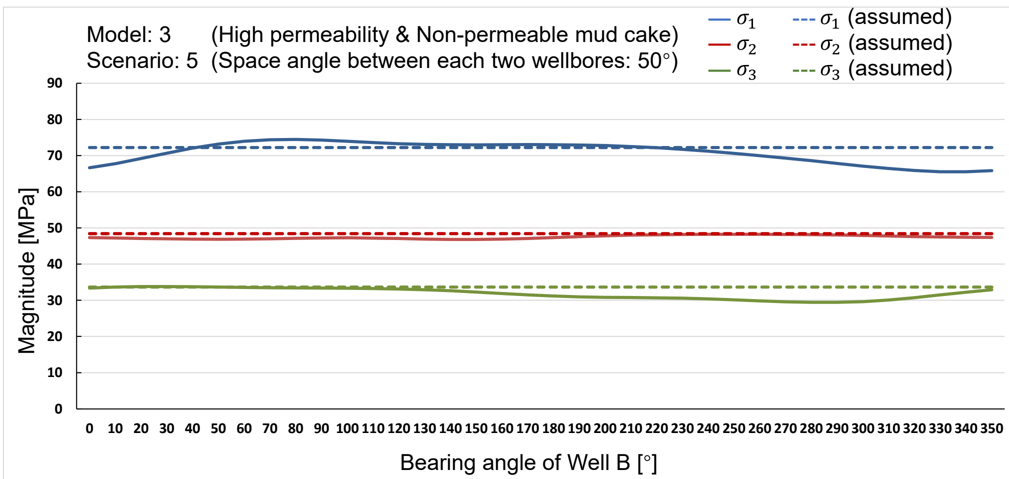

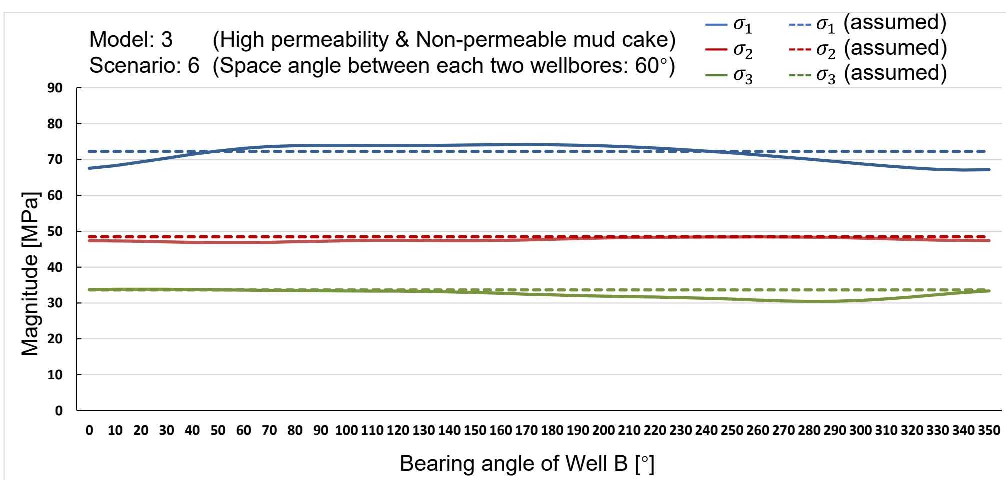

Figure A.8 Back-analyzed result in Model 3, scenarios 4, 5, 6

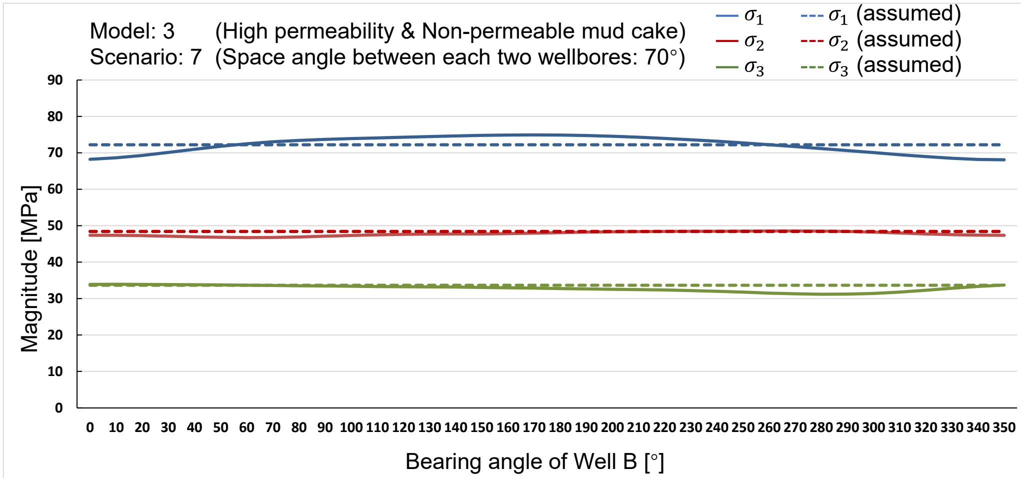

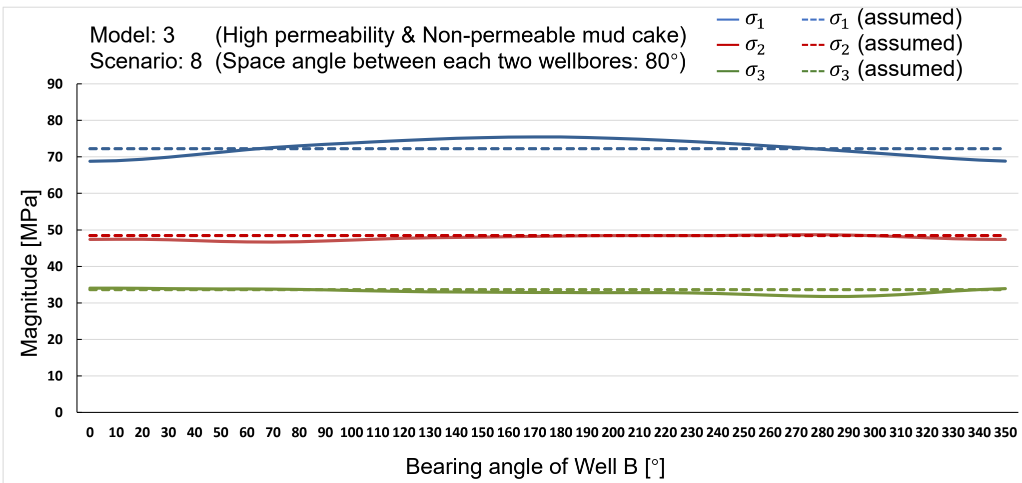

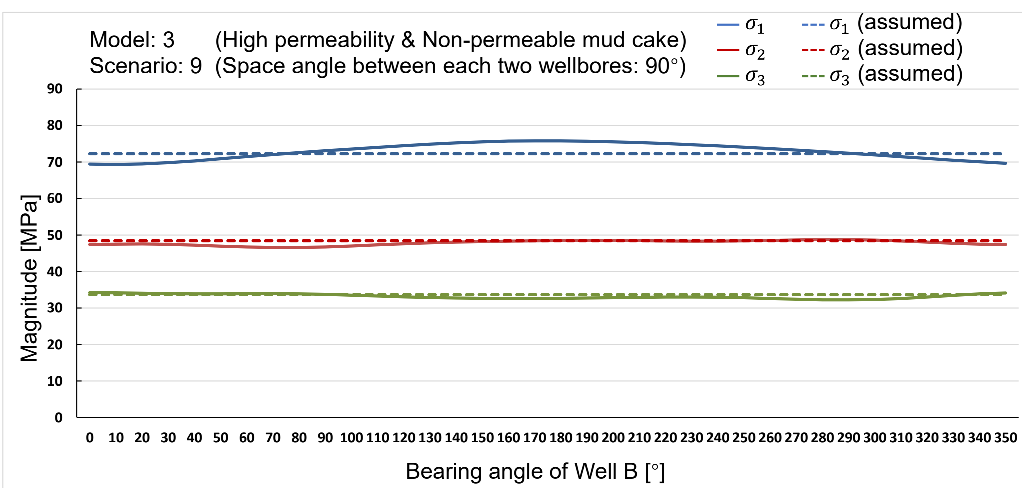

Figure A.9 Back-analyzed result in Model 3, scenarios 7, 8, 9

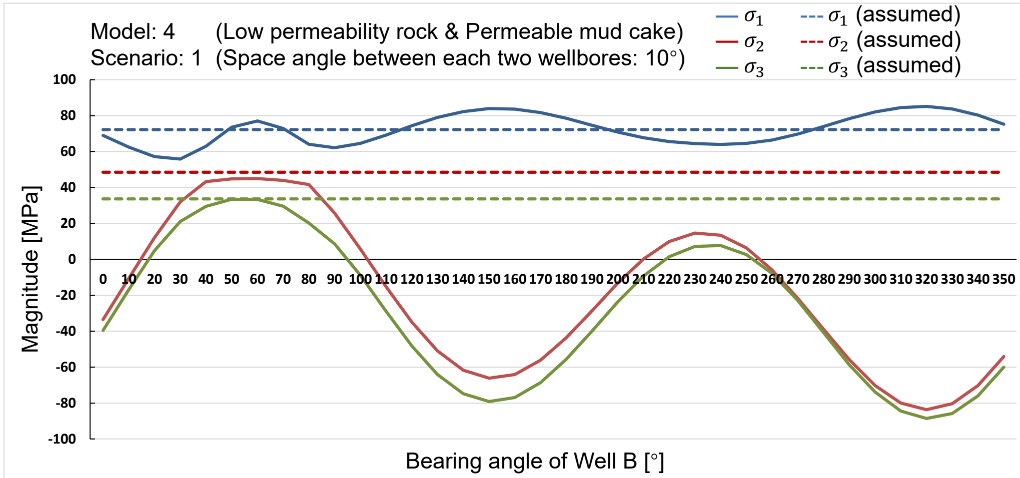

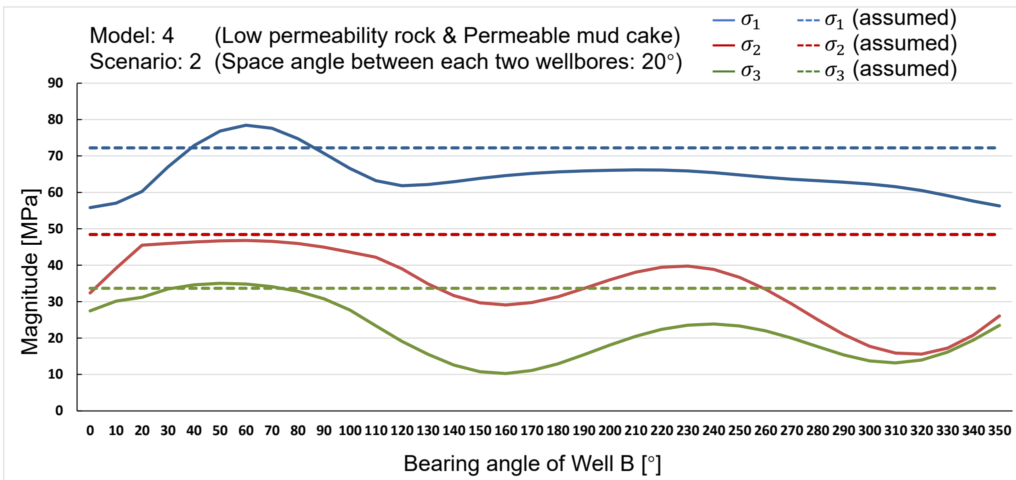

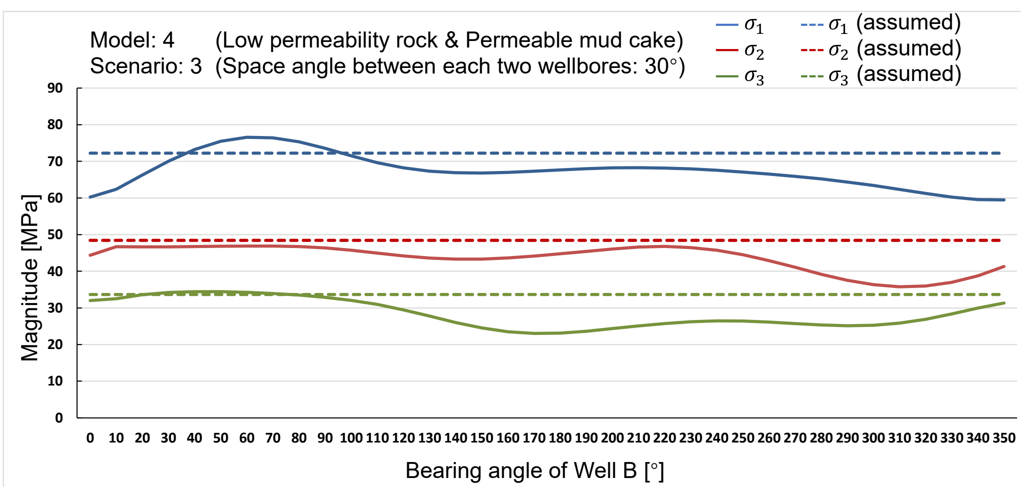

Figure A.10 Back-analyzed result in Model 4, scenarios 1, 2, 3

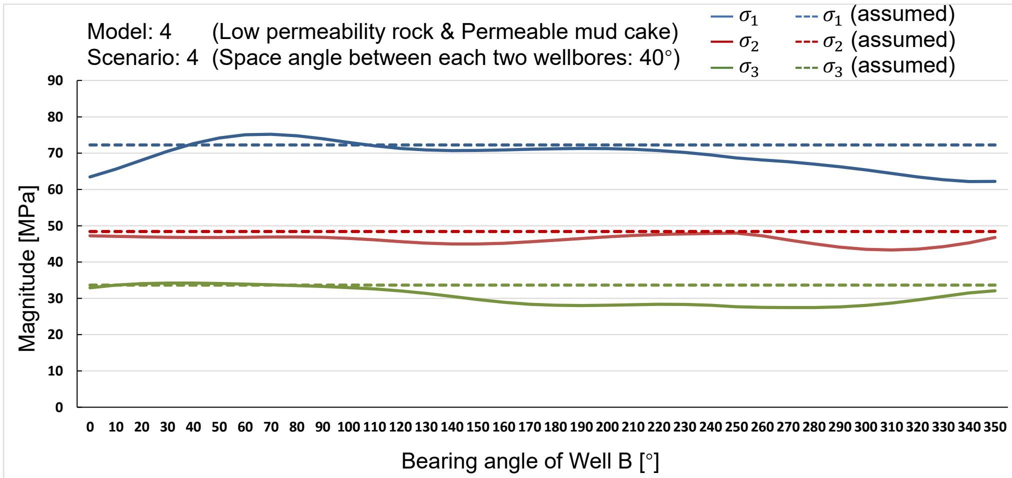

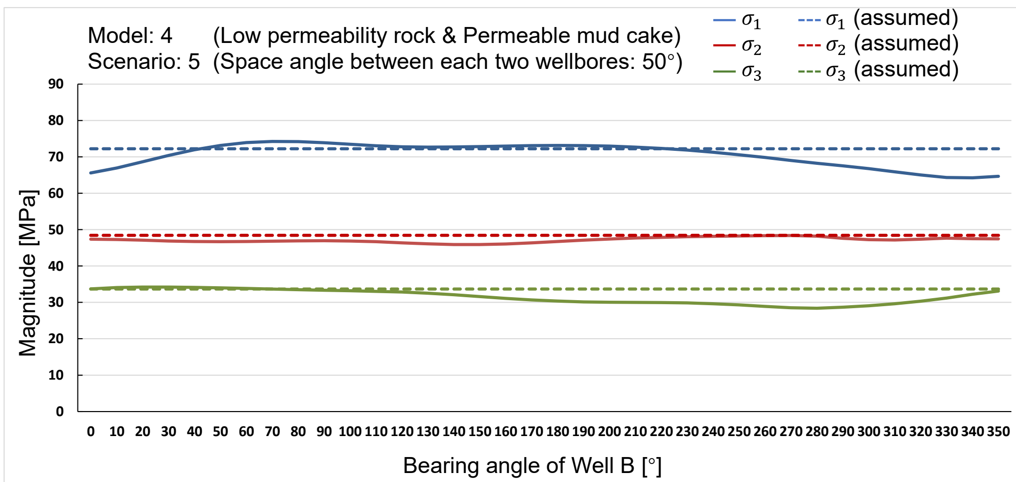

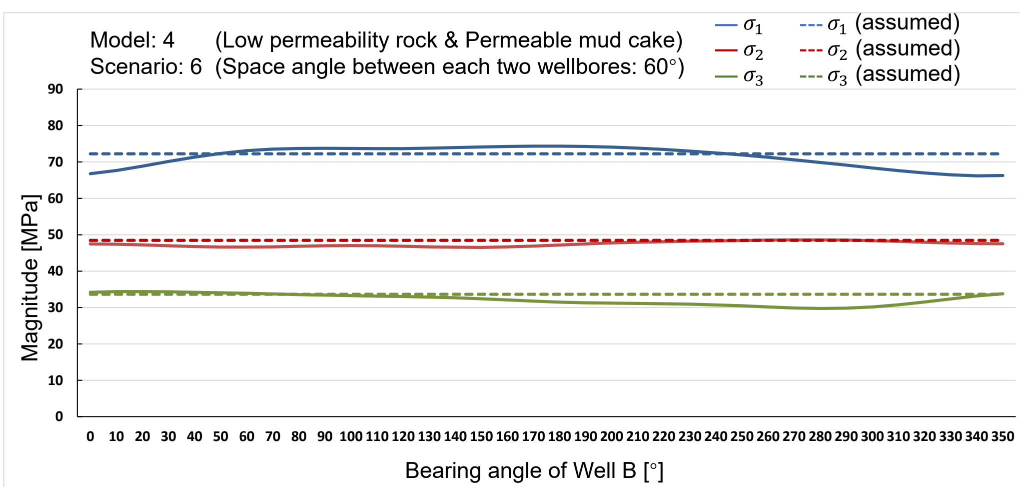

Figure A.11 Back-analyzed result in Model 4, scenarios 4, 5, 6

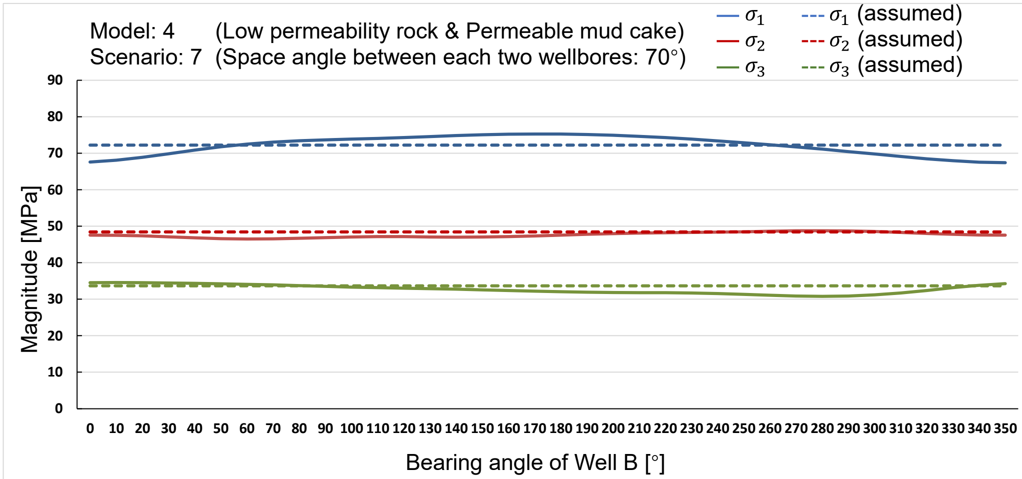

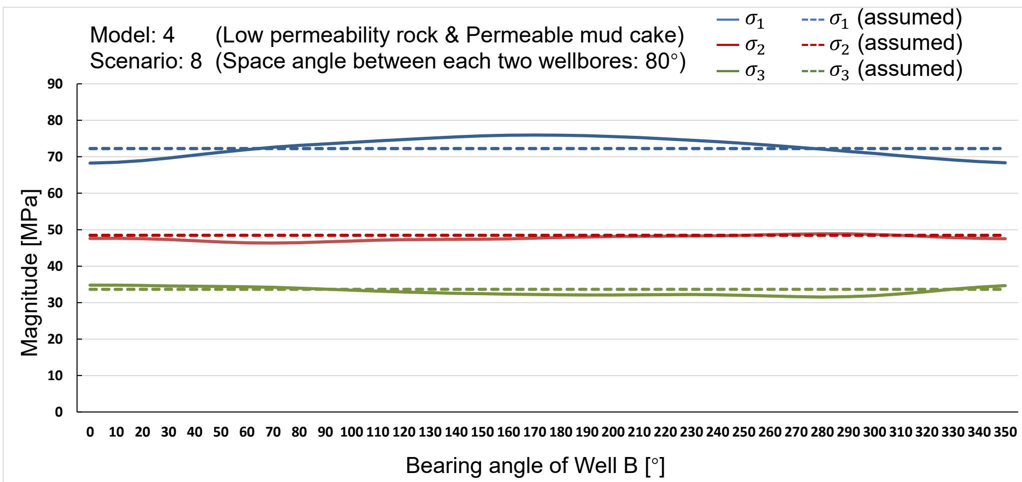

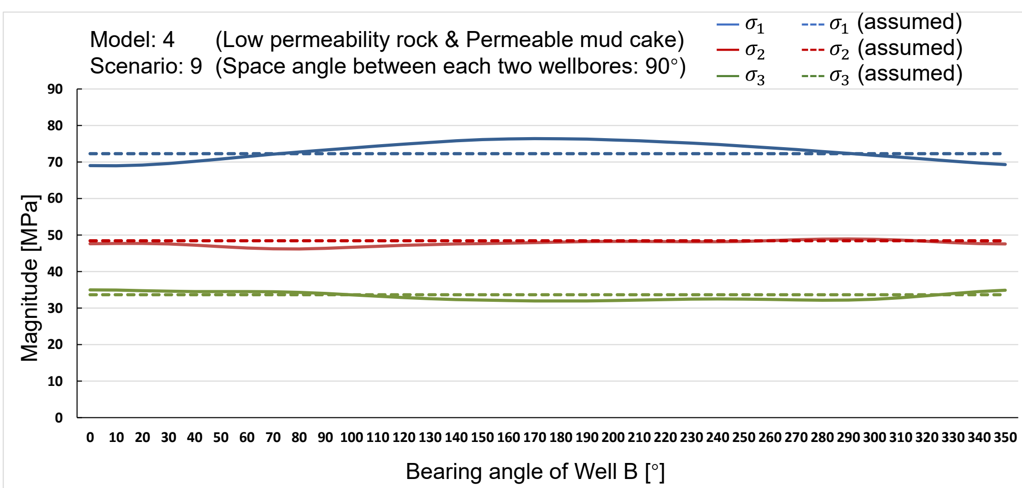

Figure A.12 Back-analyzed result in Model 4, scenarios 7, 8, 9

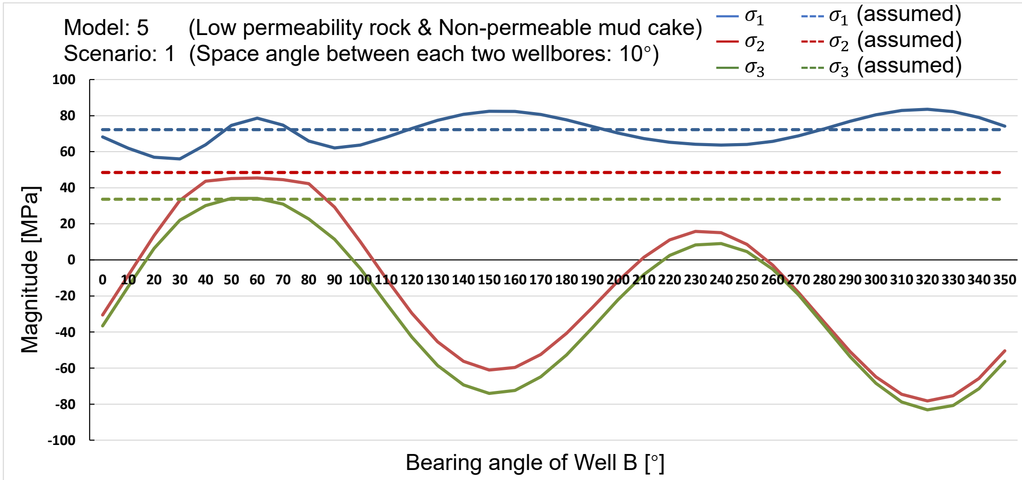

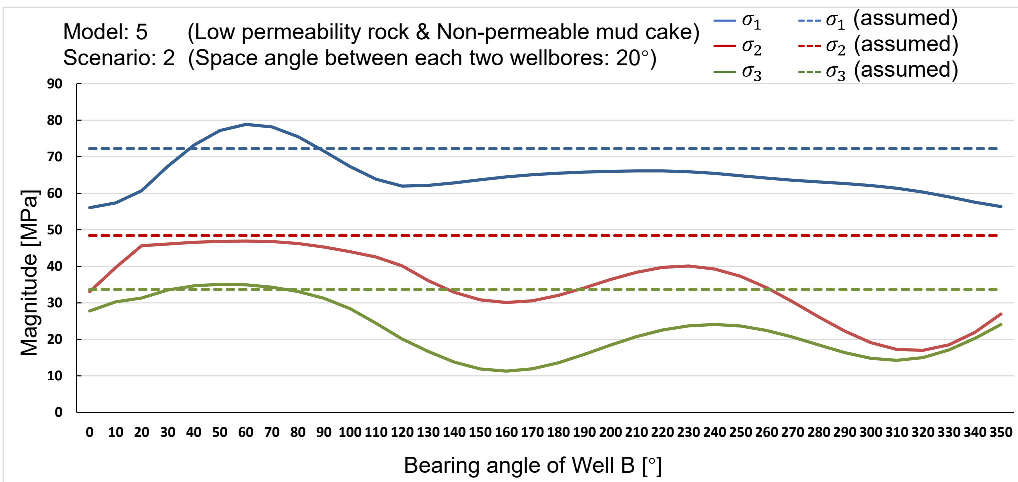

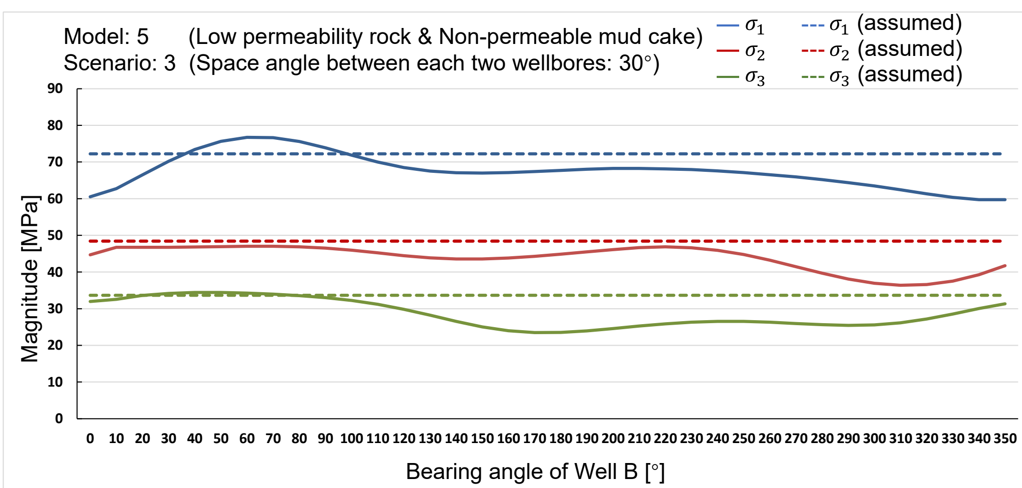

Figure A.13 Back-analyzed result in Model 5, scenarios 1, 2, 3

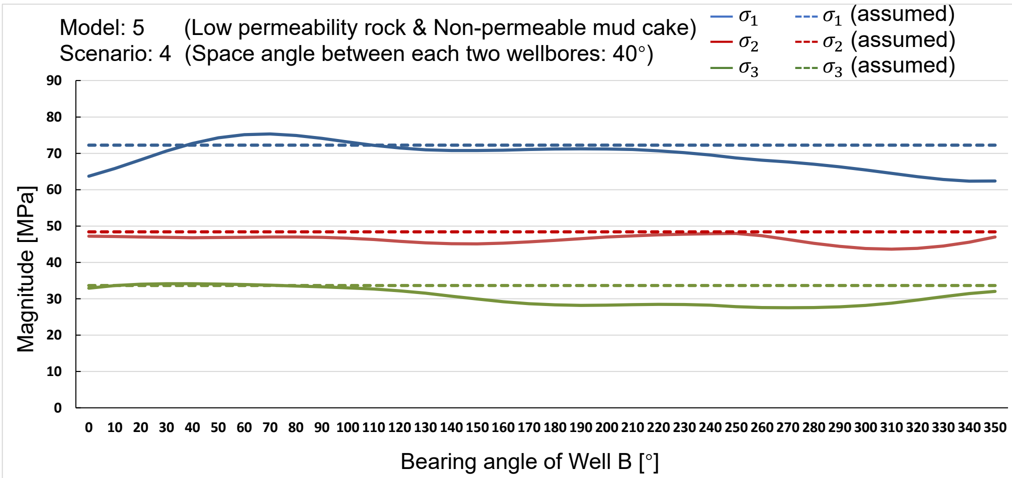

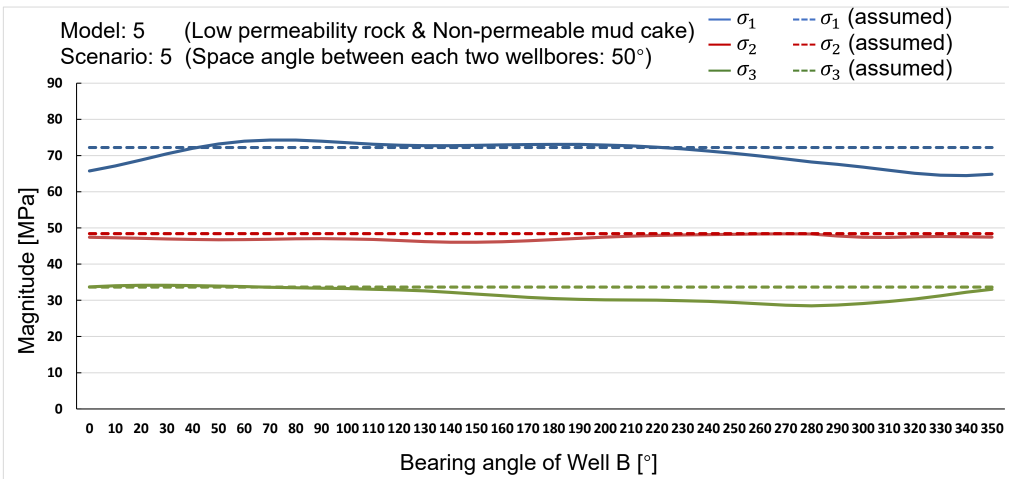

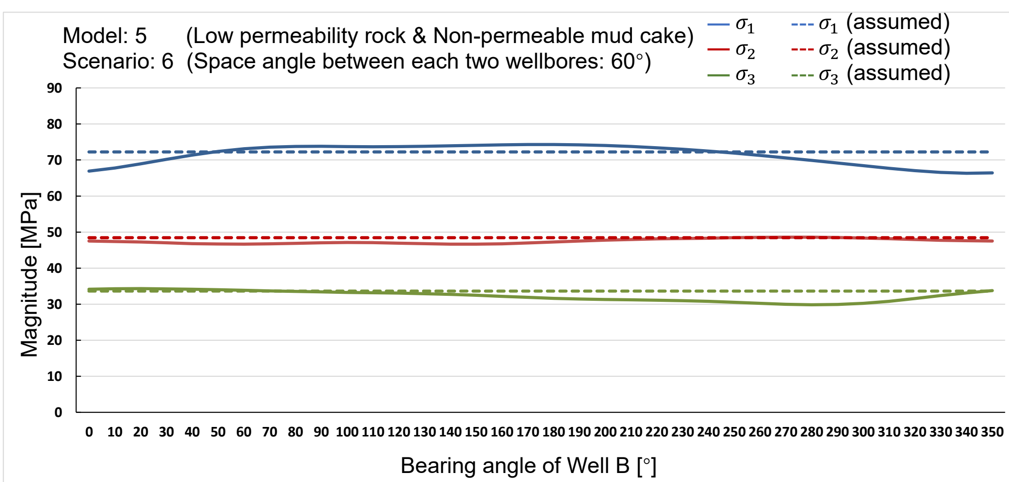

Figure A.14 Back-analyzed result in Model 5, scenarios 4, 5, 6

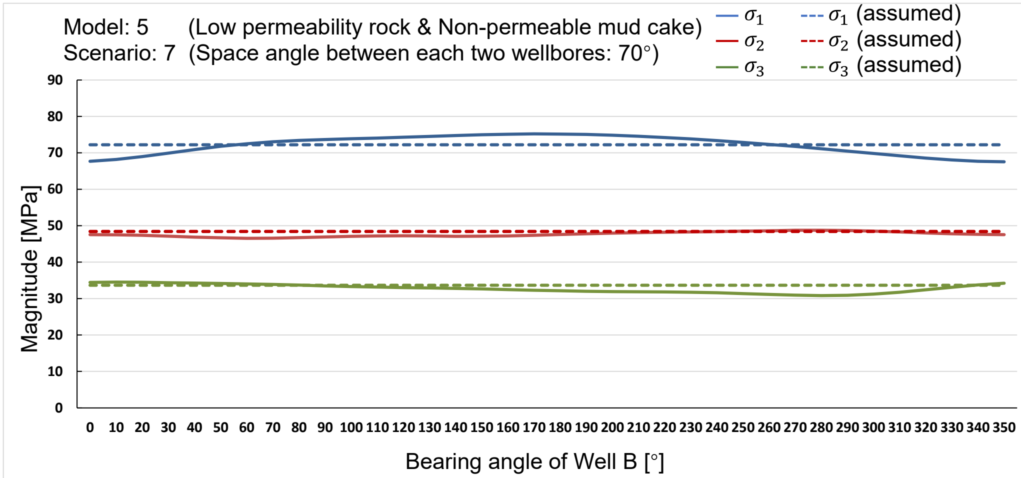

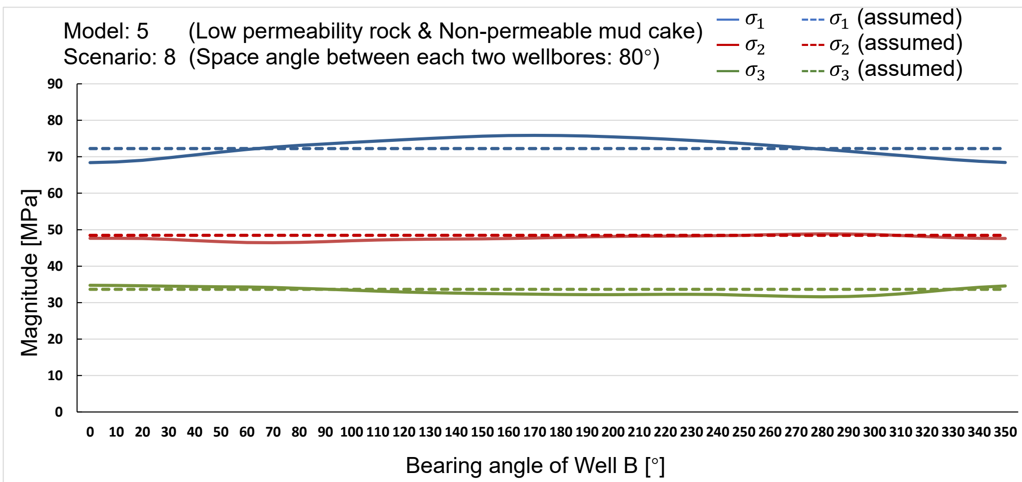

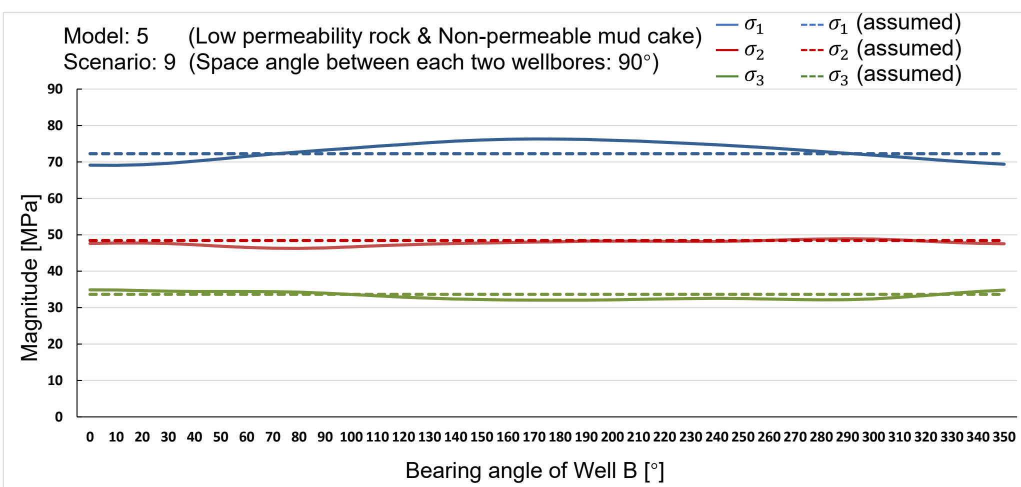

Figure A.15 Back-analyzed result in Model 5, scenarios 7, 8, 9

APPENDIX B THE OUTPUT ERRORS OF THE BACK-ANALYZED 3D IN-SITU STRESSES

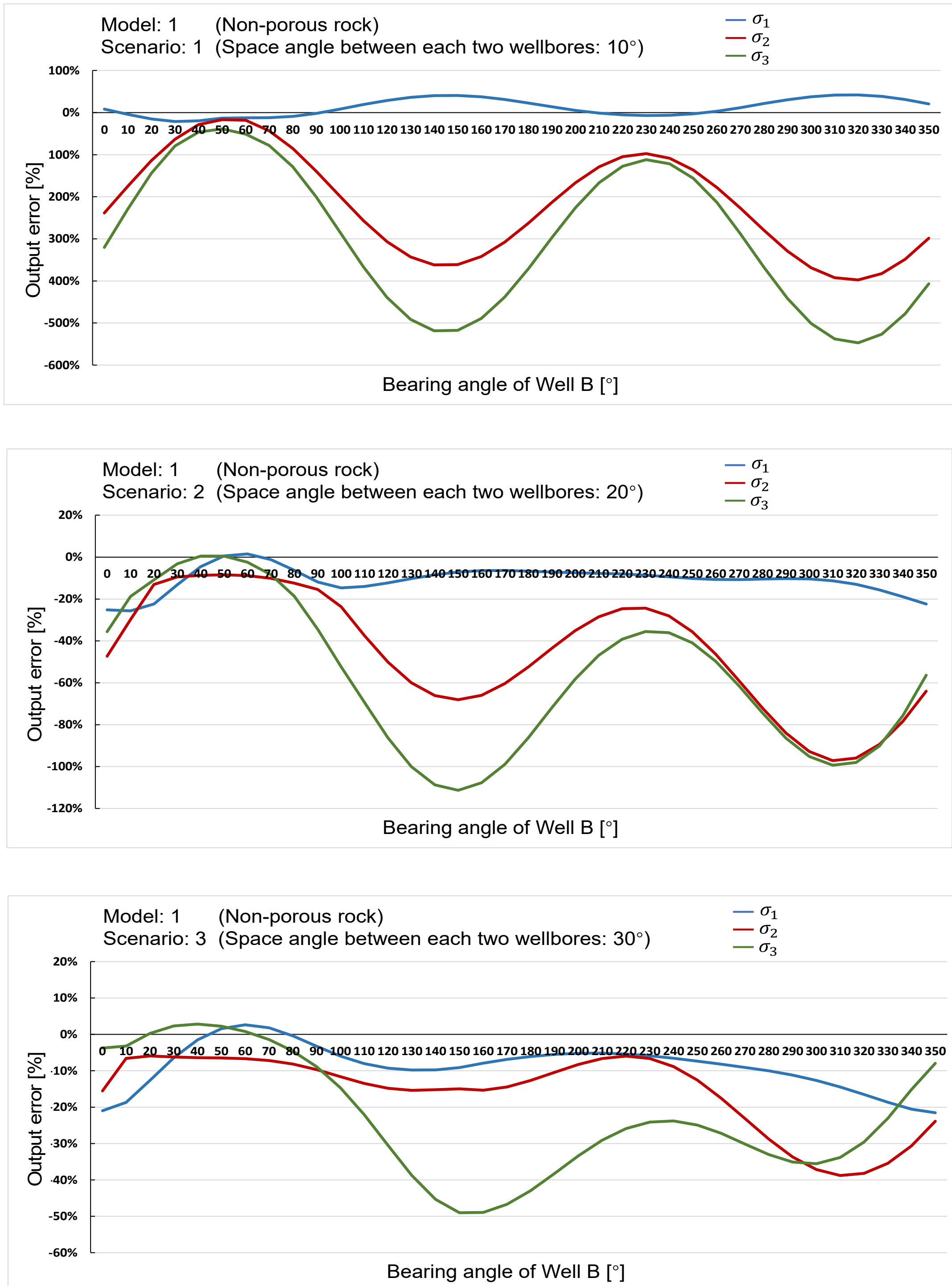

Figure B.1 Output error in model 1, scenarios 1, 2, 3

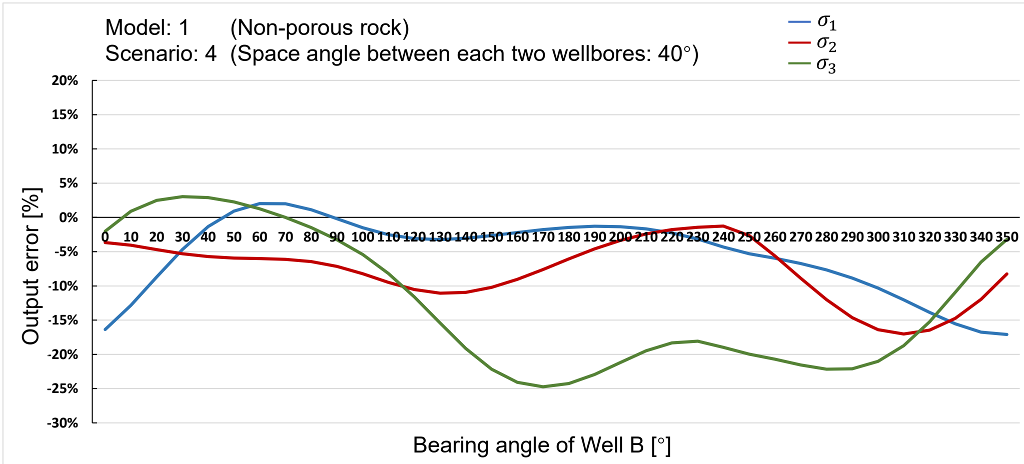

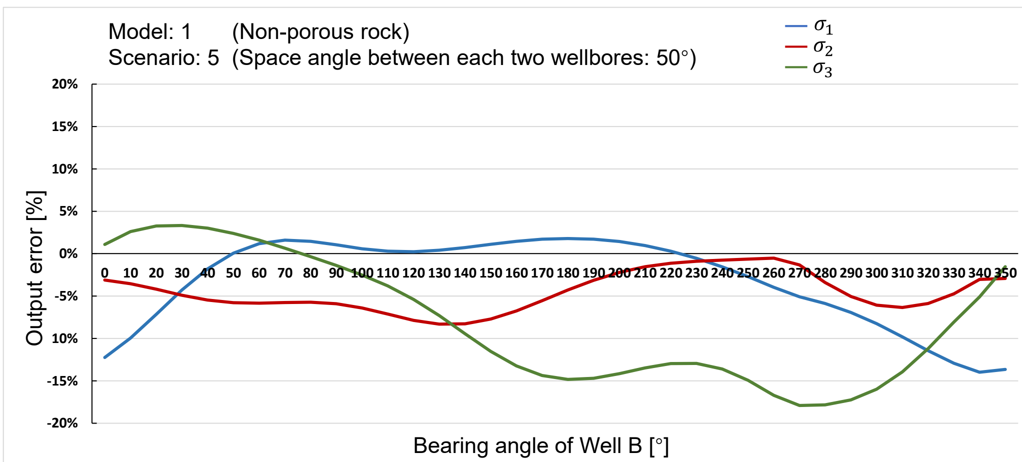

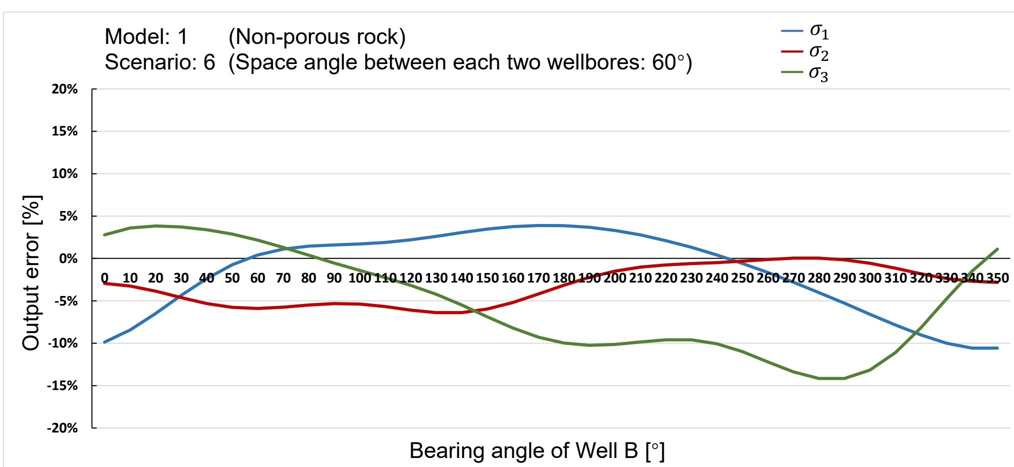

Figure B.2 Output error in model 1, scenarios 4, 5, 6

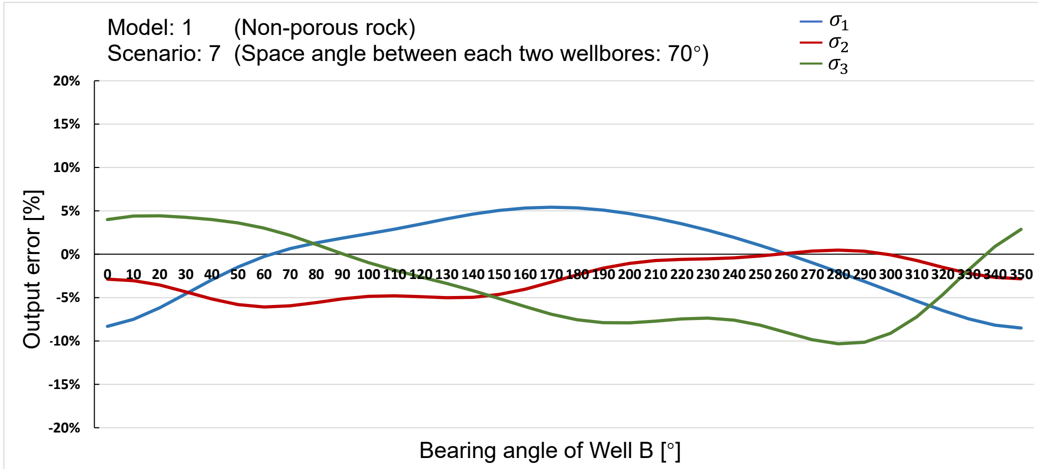

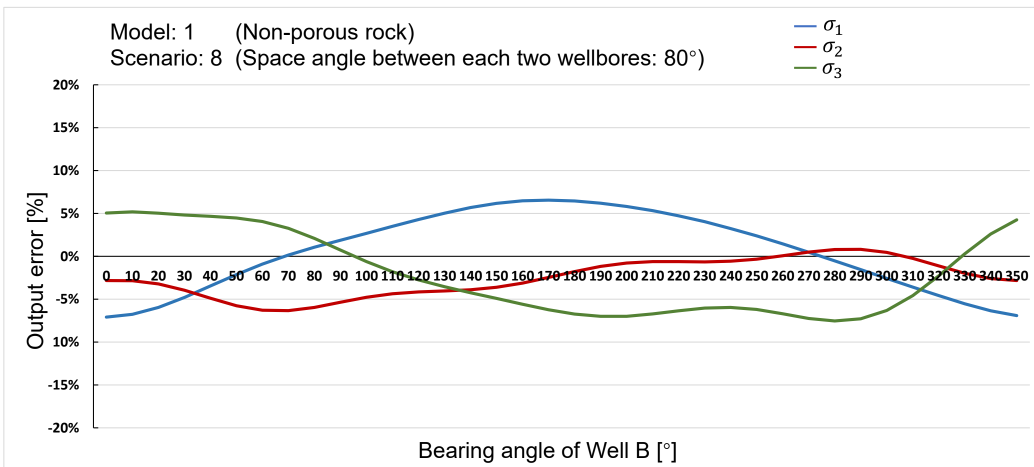

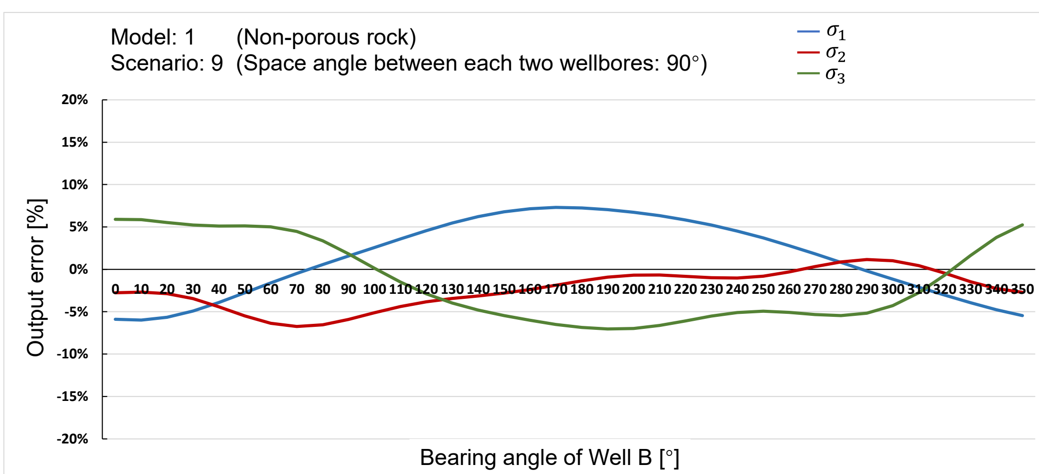

Figure B.3 Output error in model 1, scenarios 7, 8, 9

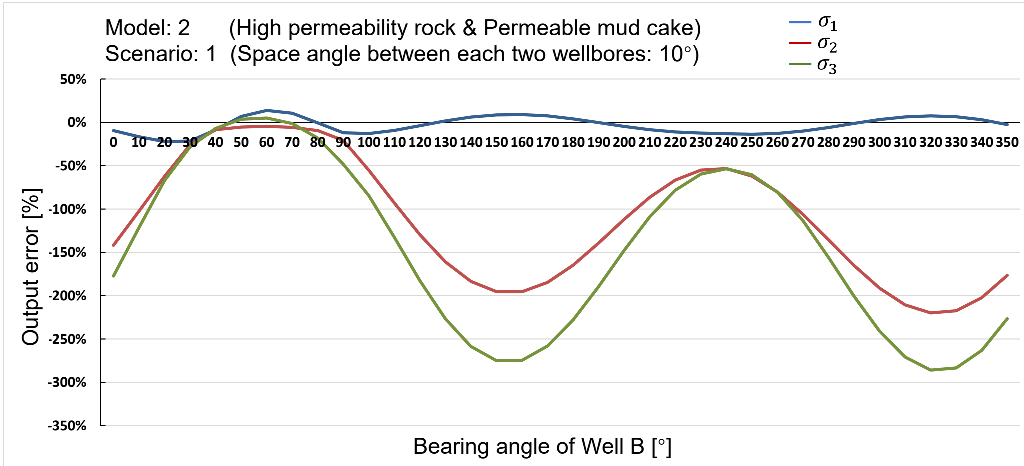

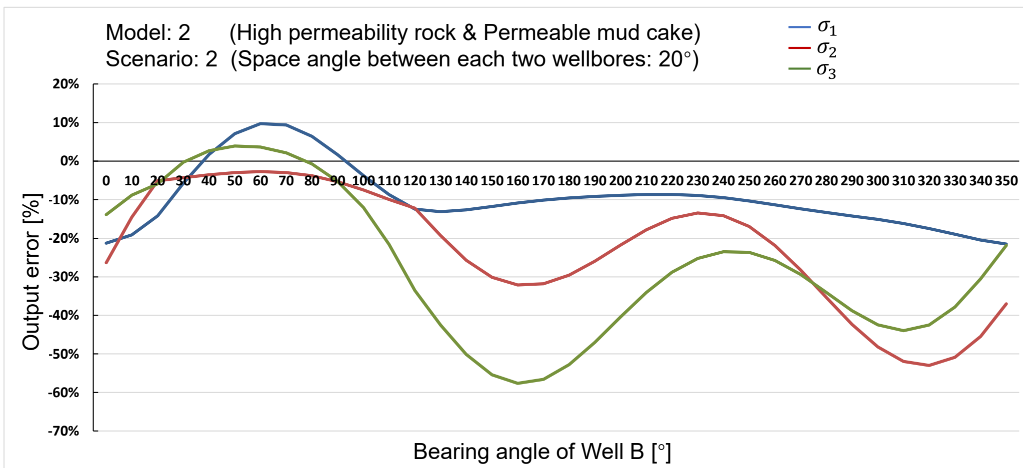

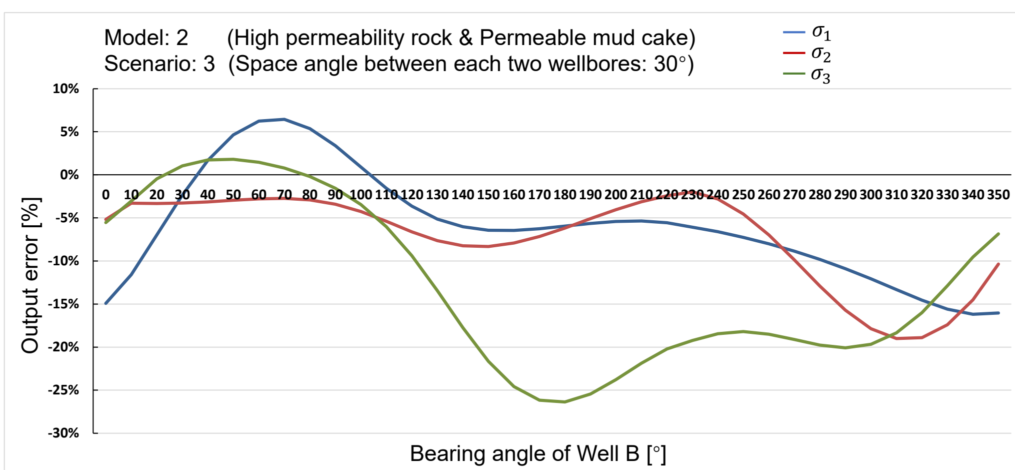

Figure B.4 Output error in model 2, scenarios 1, 2, 3

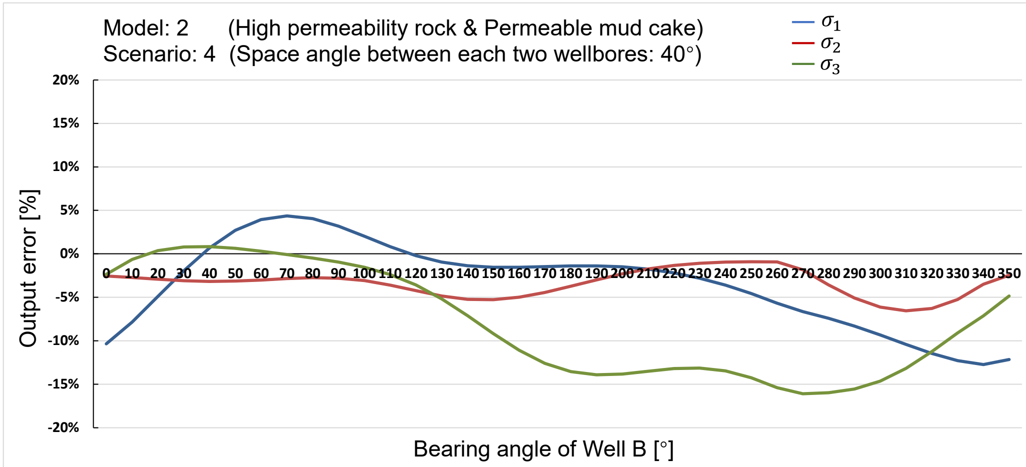

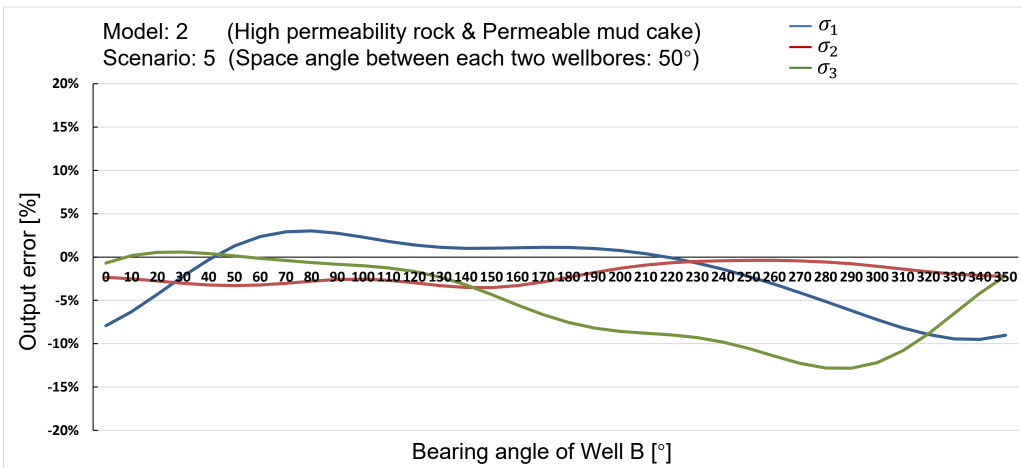

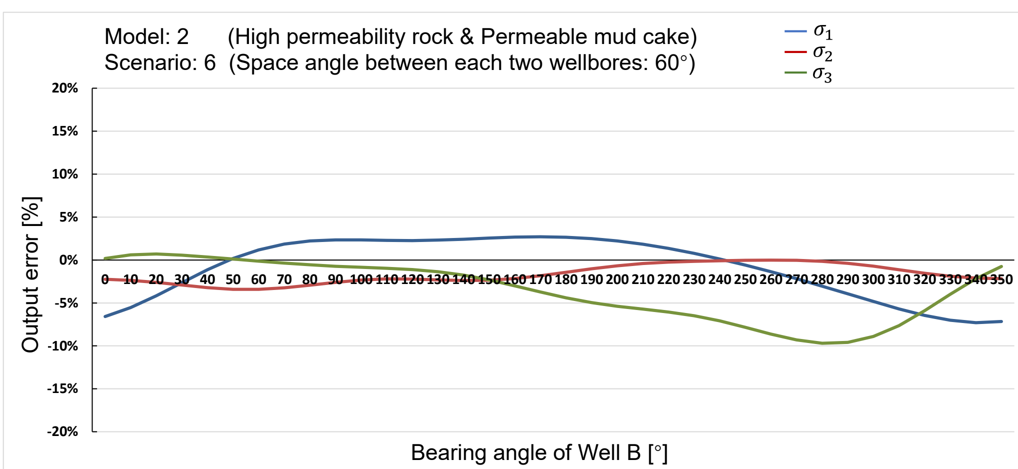

Figure B.5 Output error in model 2, scenarios 4, 5, 6

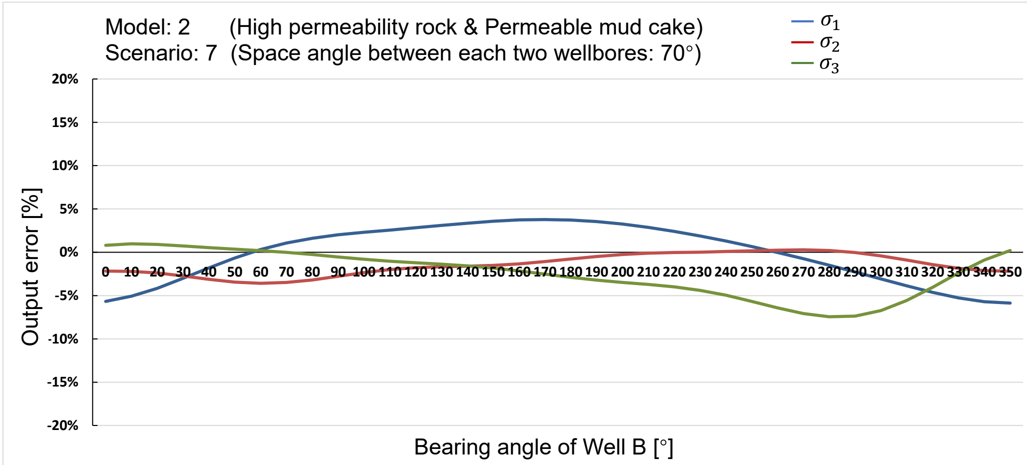

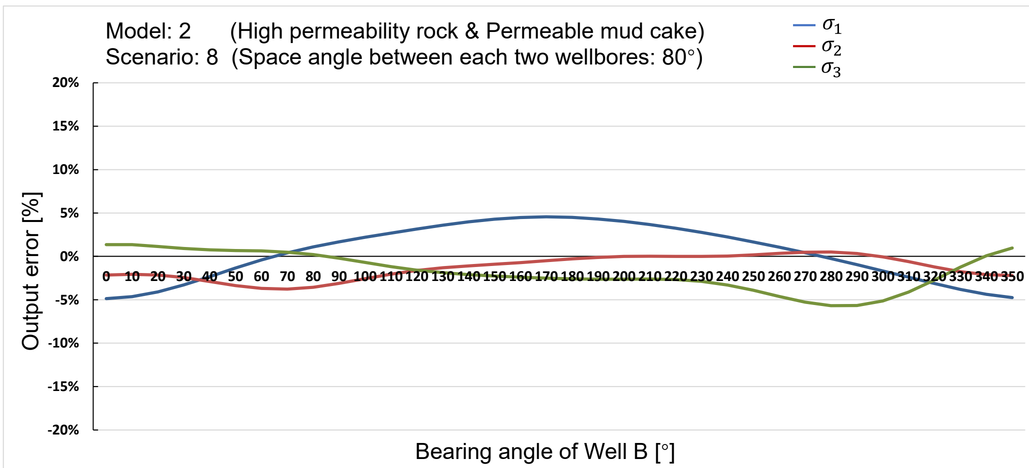

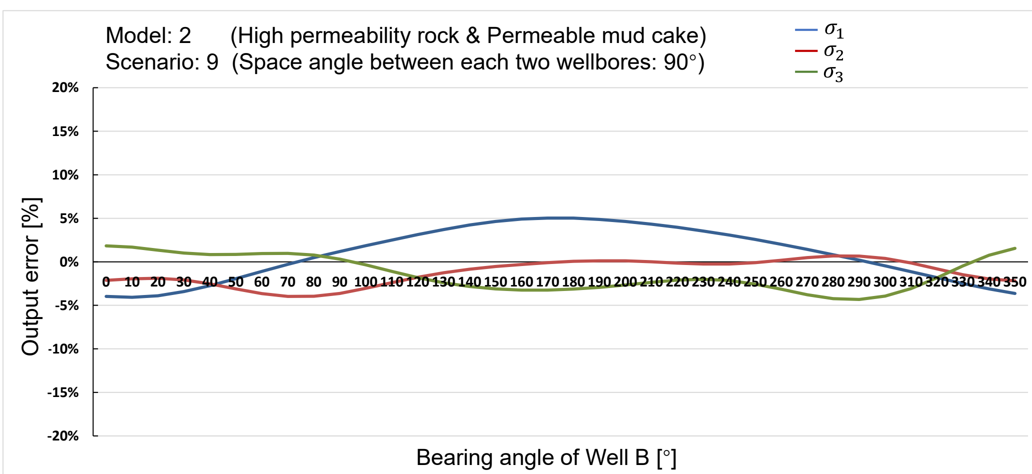

Figure B.6 Output error in model 2, scenarios 7, 8, 9

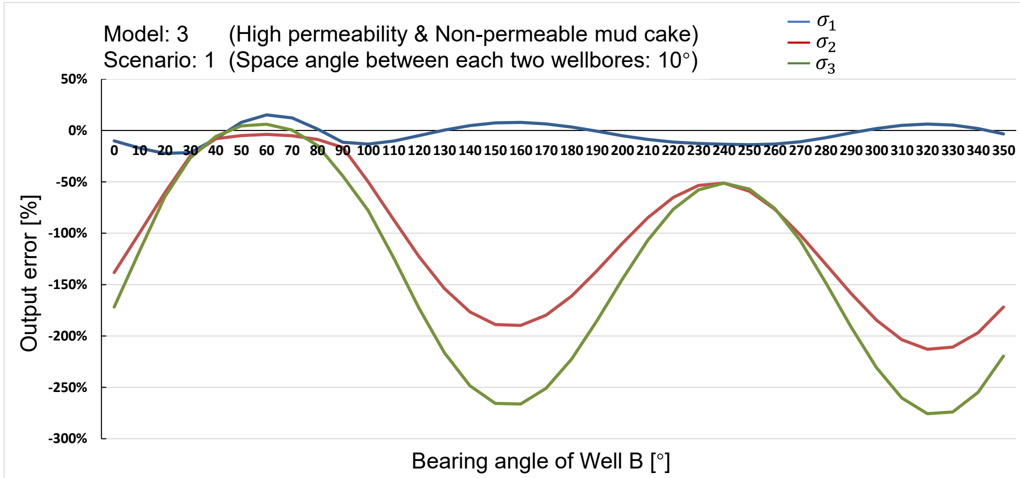

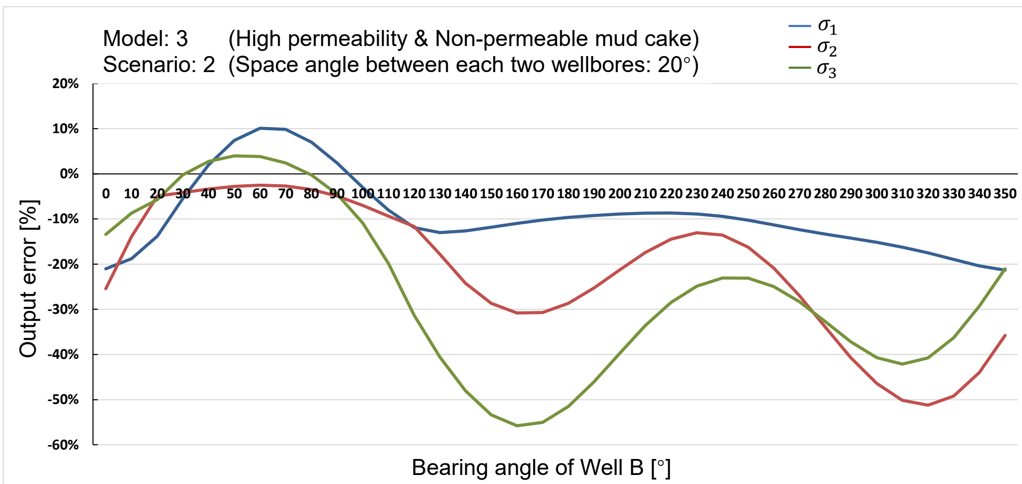

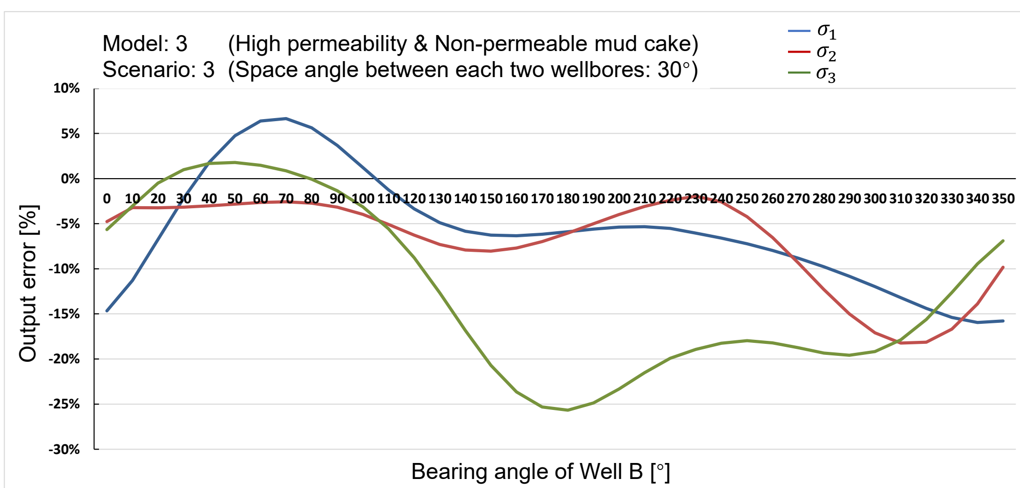

Figure B.7 Output error in model 3, scenarios 1, 2, 3

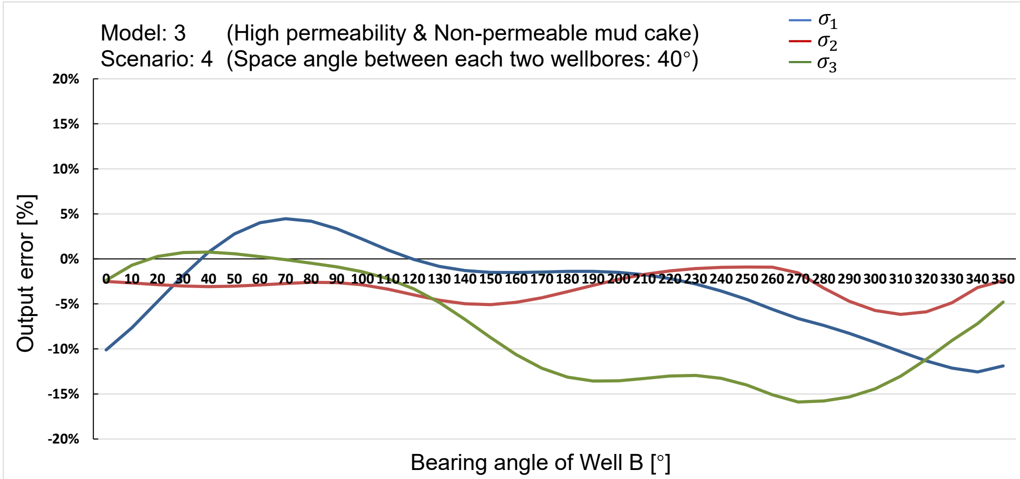

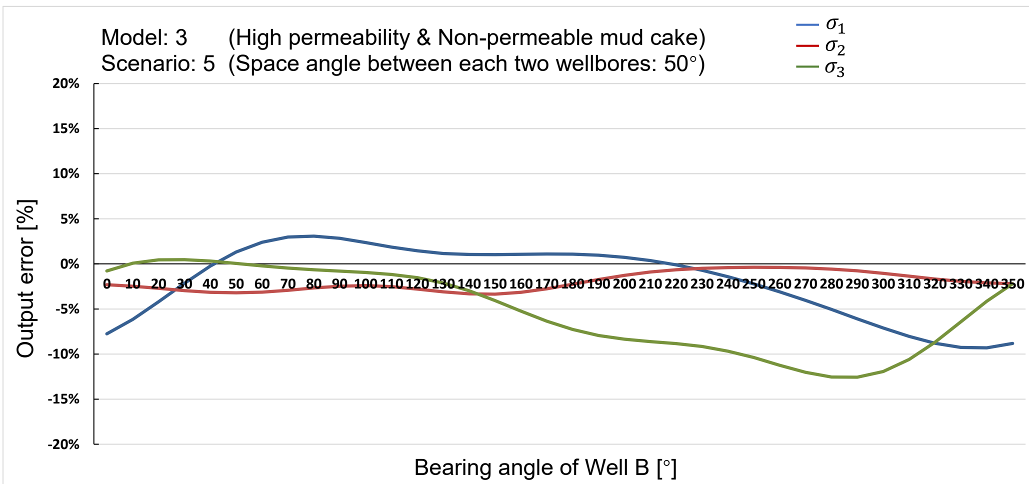

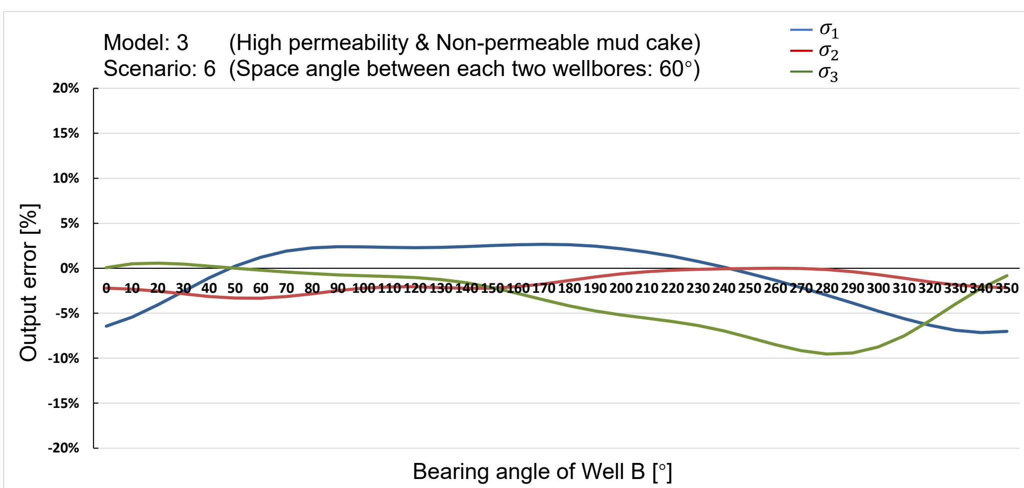

Figure B.8 Output error in model 3, scenarios 4, 5, 6

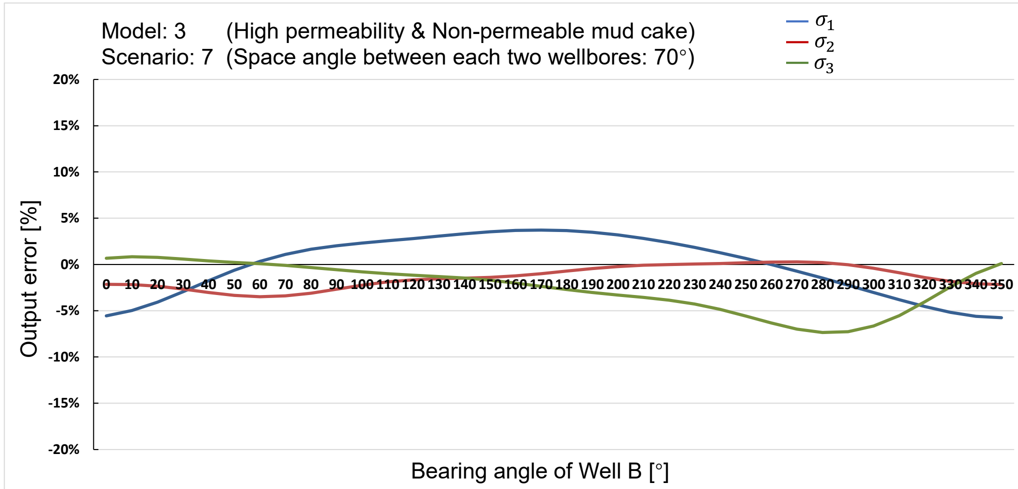

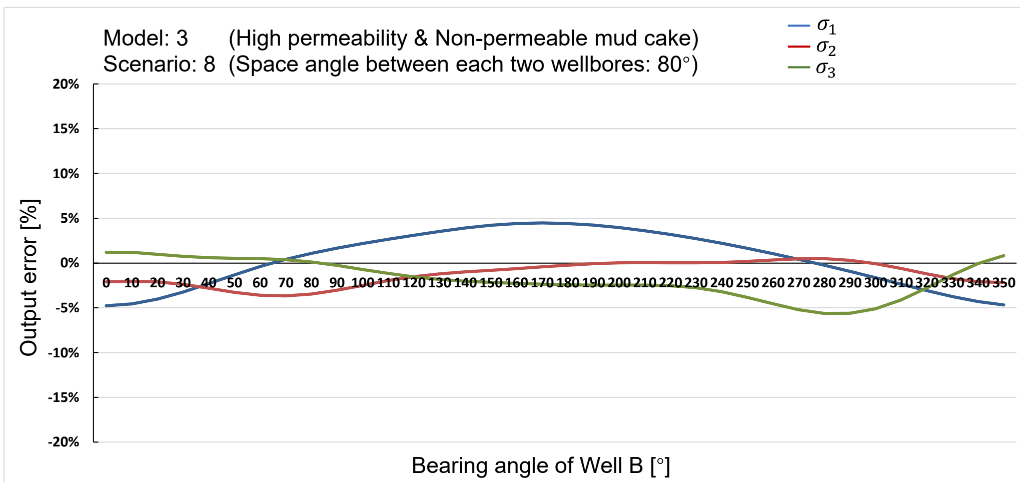

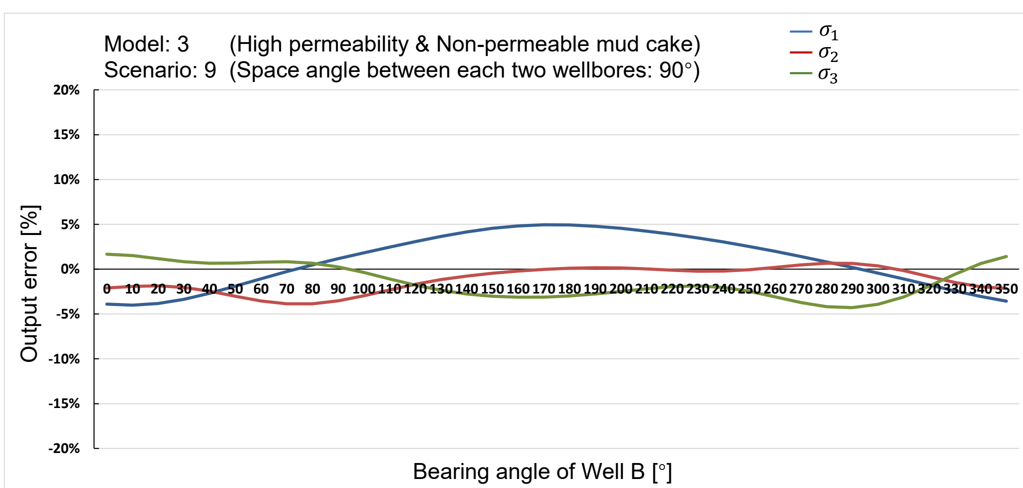

Figure B.9 Output error in model 3, scenarios 7, 8, 9

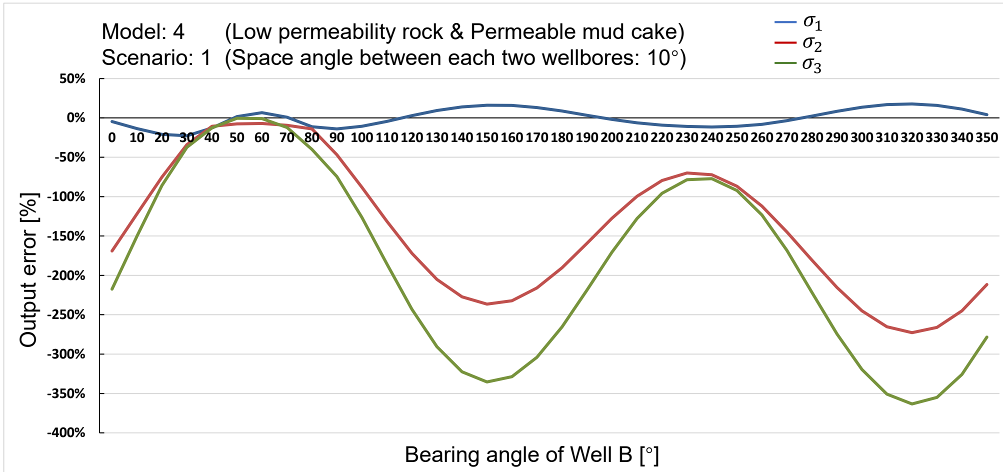

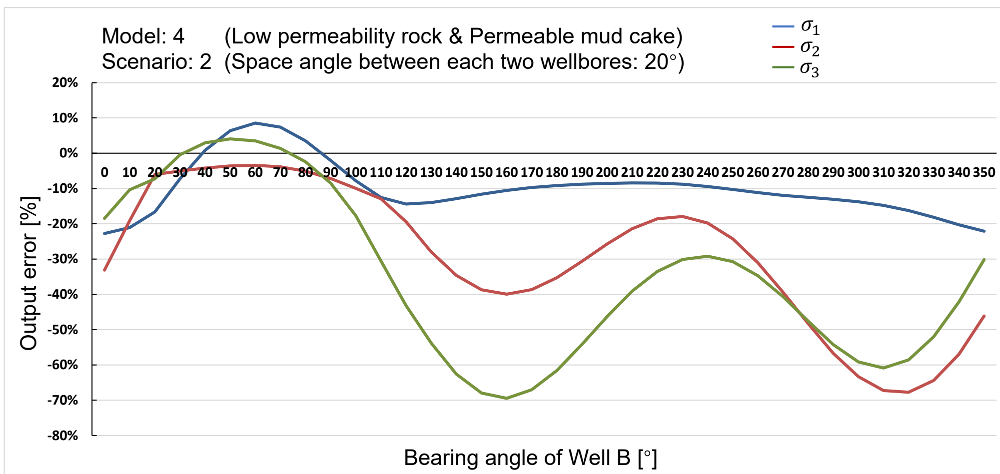

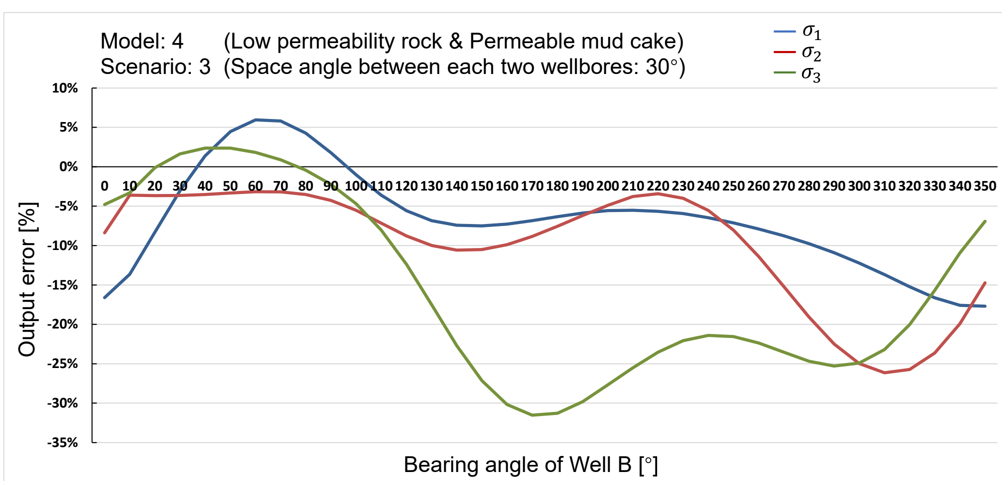

Figure B.10 Output error in model 4, scenarios 1, 2, 3

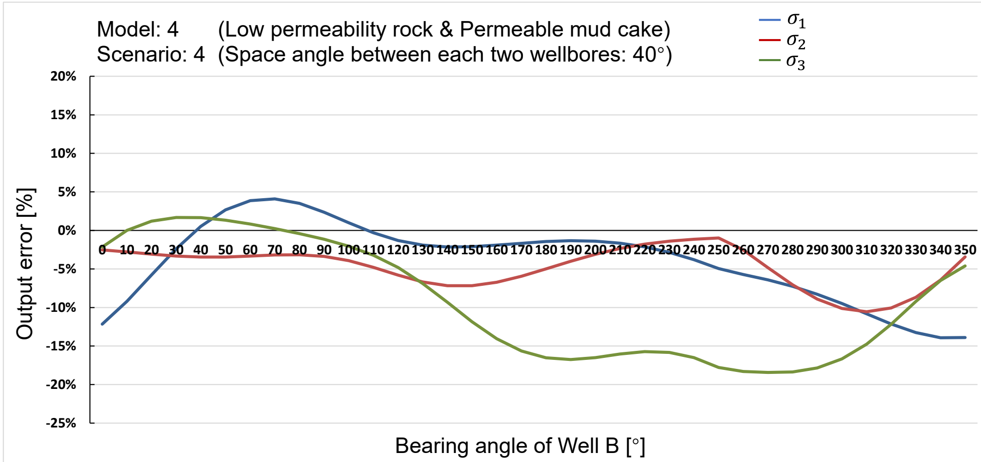

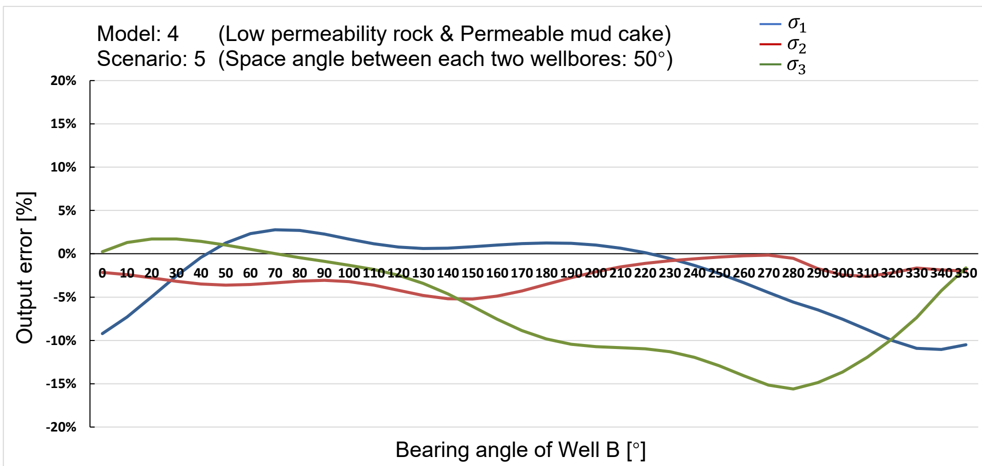

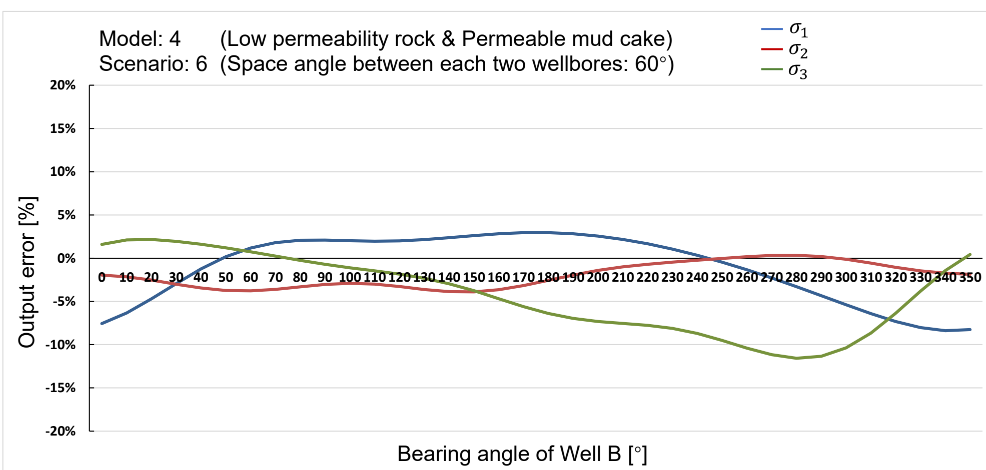

Figure B.11 Output error in model 4, scenarios 4, 5, 6

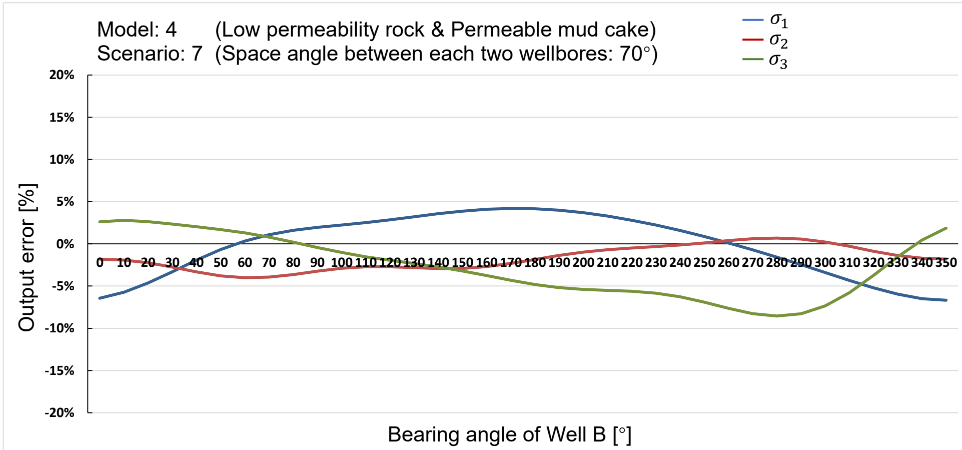

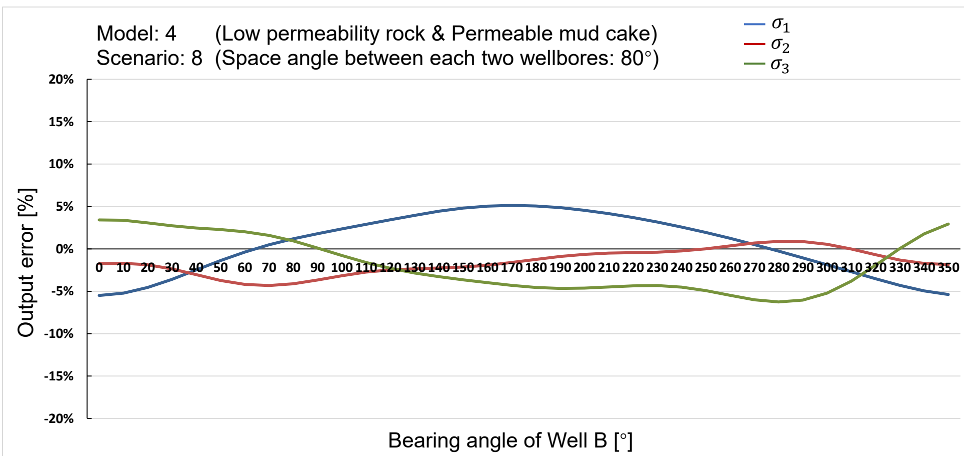

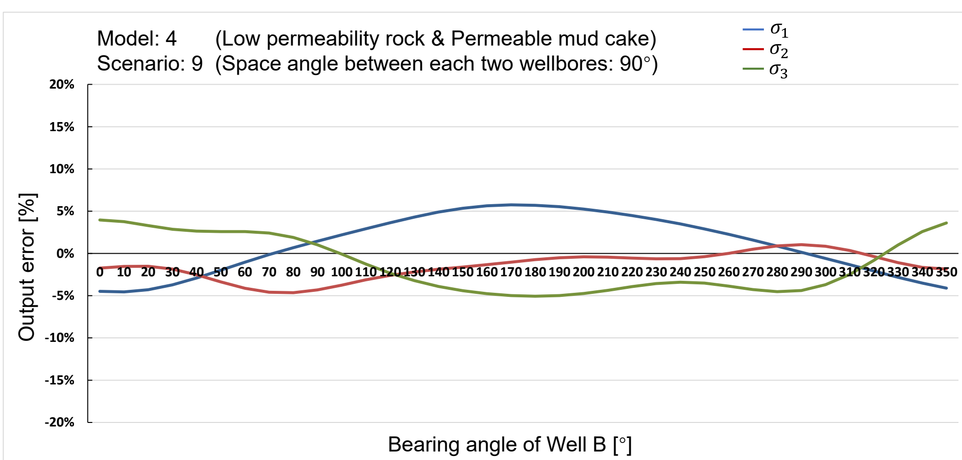

Figure B.12 Output error in model 4, scenarios 7, 8, 9

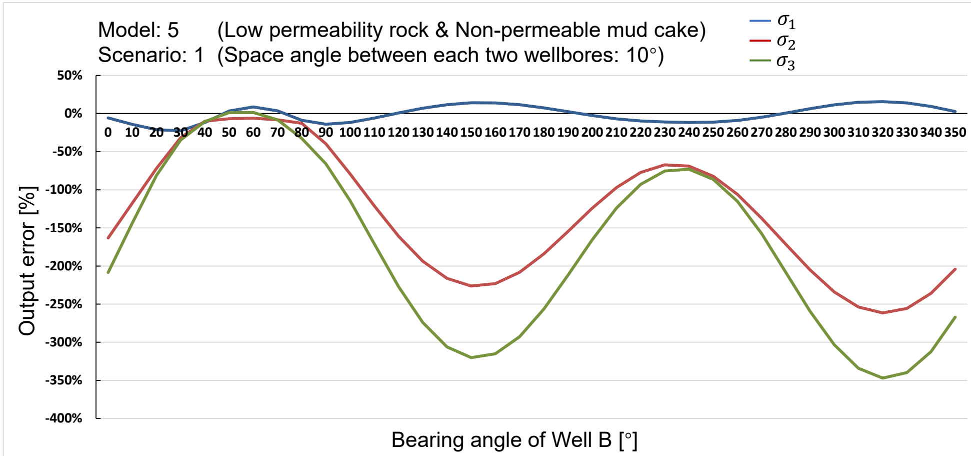

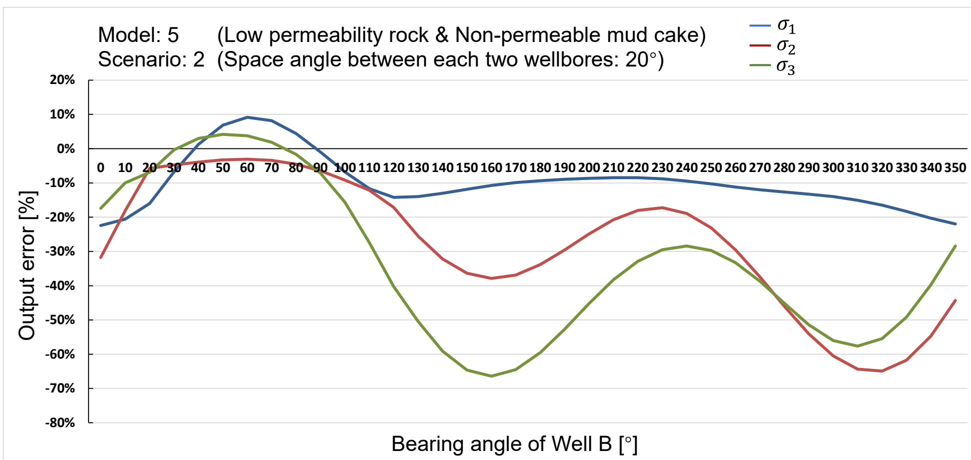

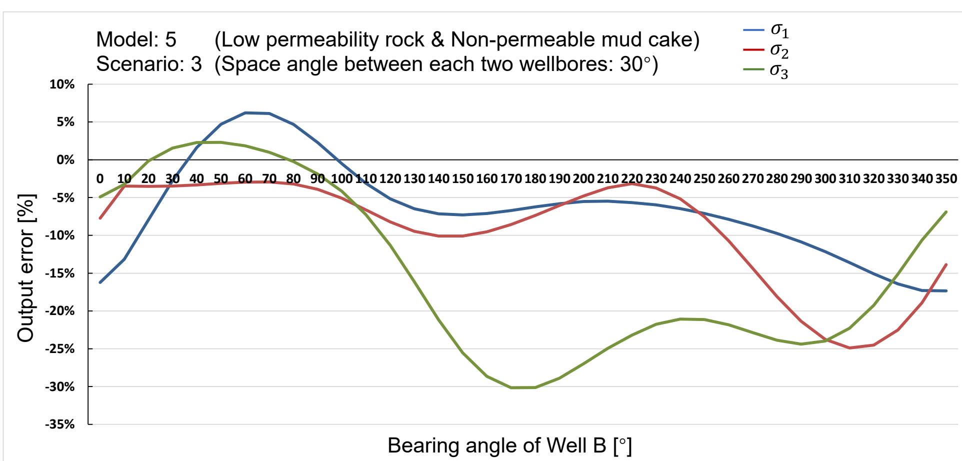

Figure B.13 Output error in model 5, scenarios 1, 2, 3

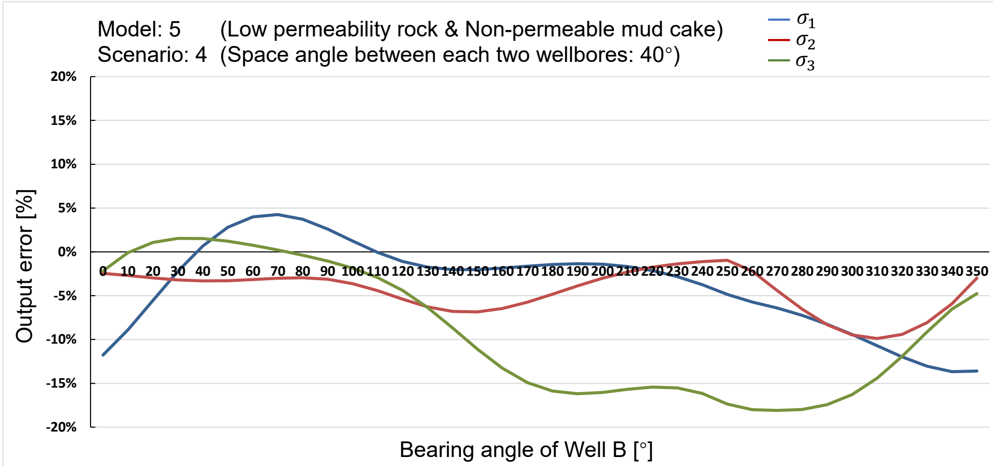

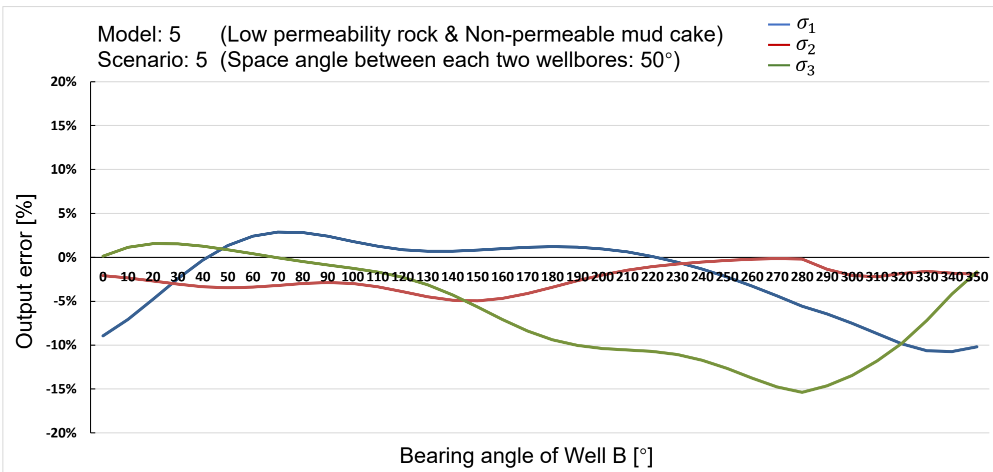

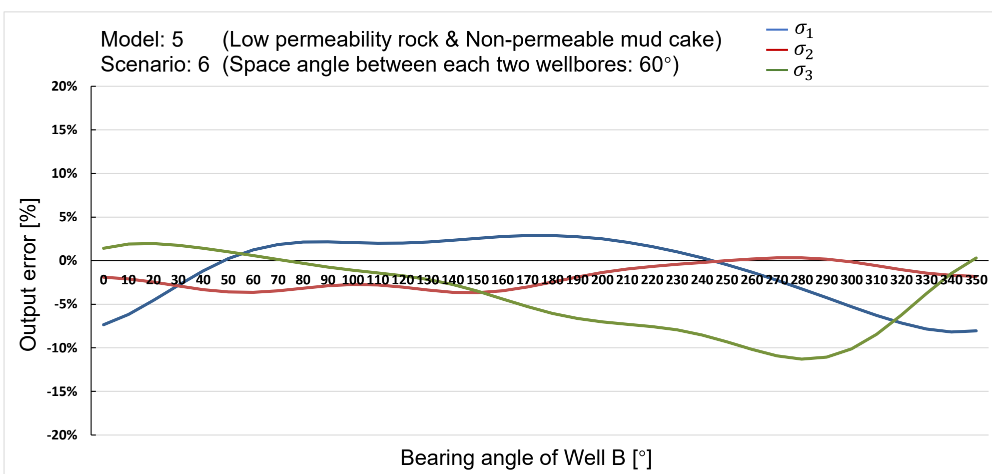

Figure B.14 Output error in model 5, scenarios 4, 5, 6

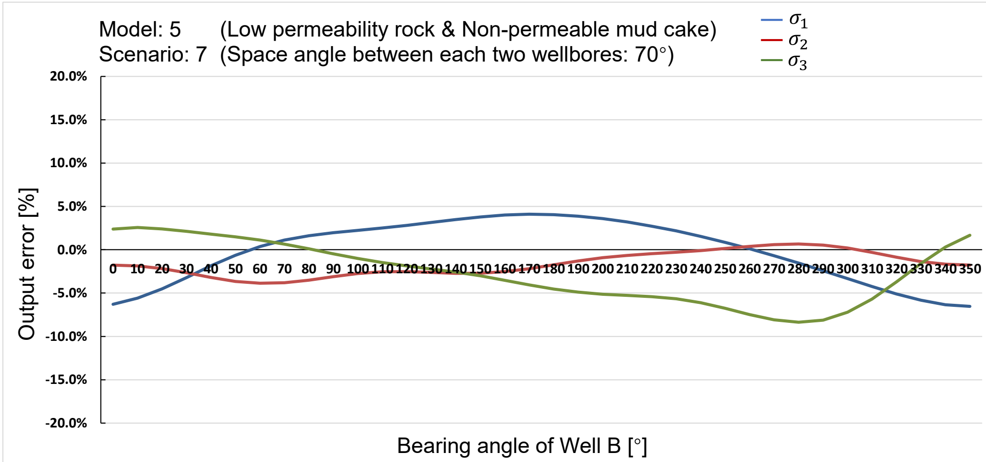

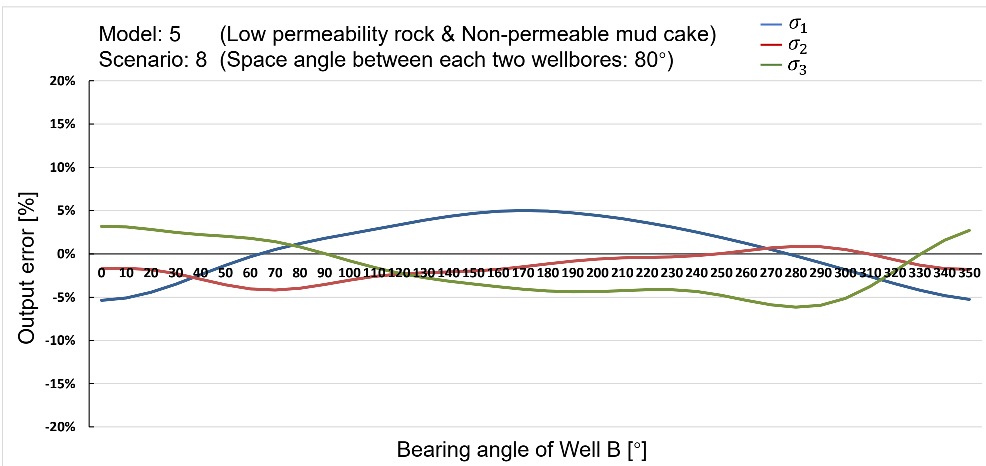

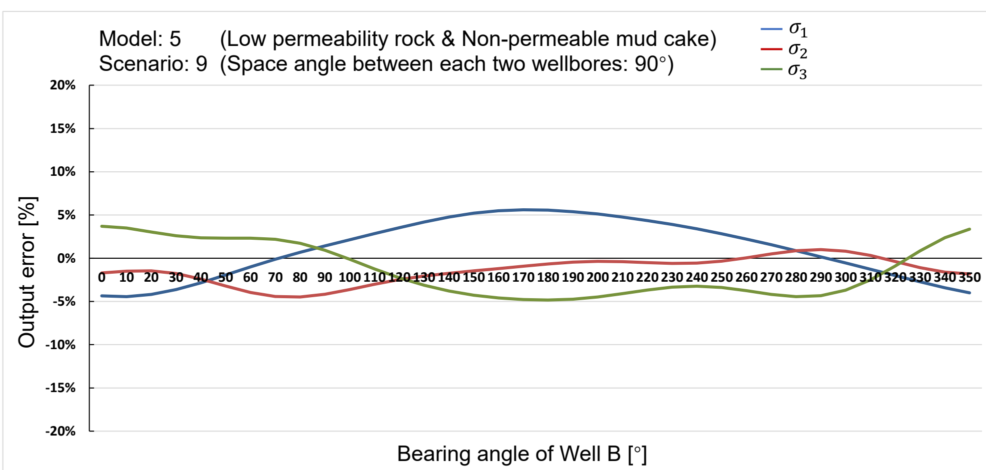

Figure B.15 Output error in model 5, scenarios 7, 8, 9

APPENDIX C THE ORIENTATIONS OF THE BACK-ANALYZED 3D IN-SITU STRESSES

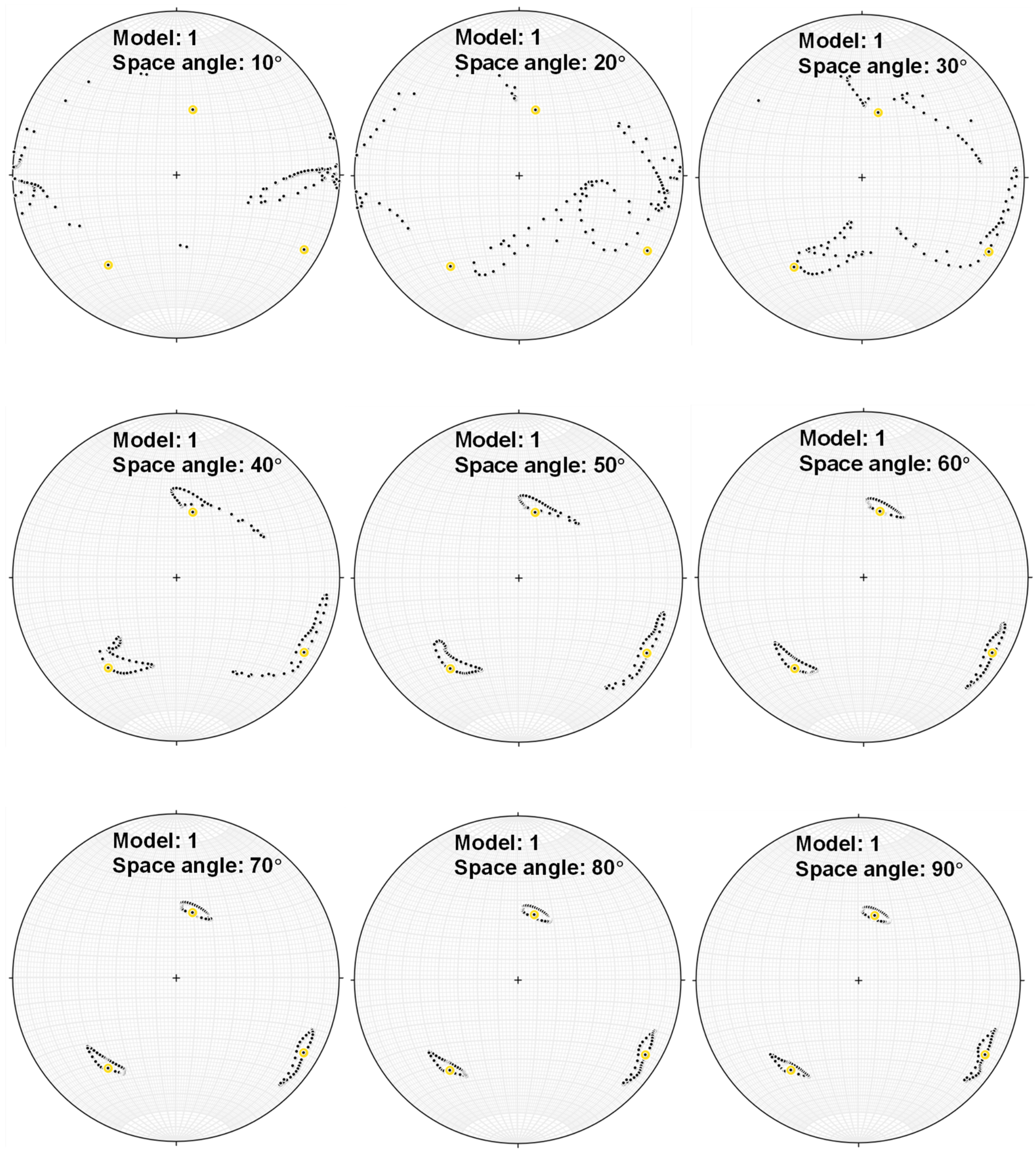

Figure C.1 Orientations of the back-analyzed and assumed principal stresses in model 1 (Space angle between the three wellbores 10°, 20°, 30°, 40°, 50°, 60°, 70°, 80°, 90°)

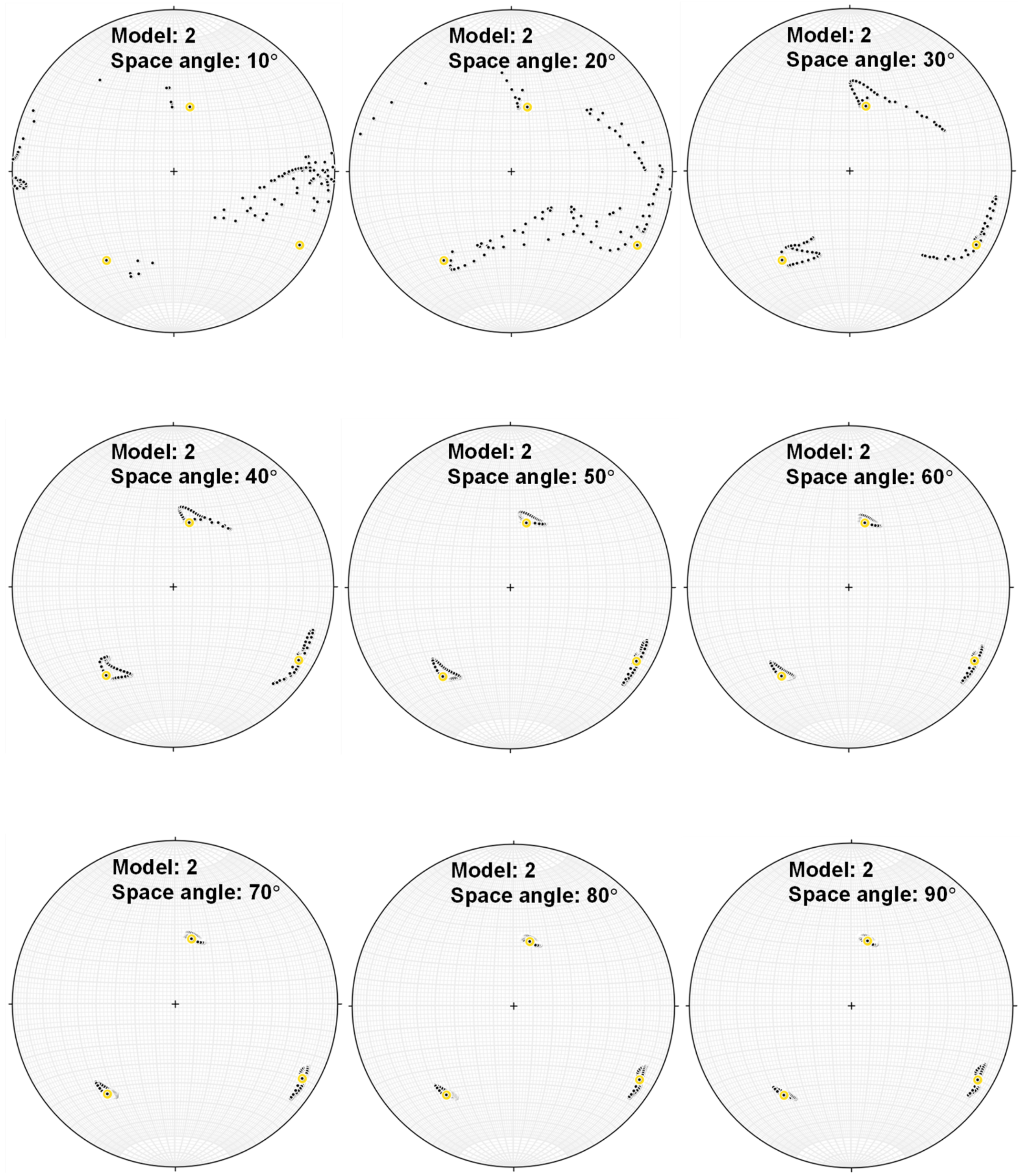

Figure C.2 Orientations of the back-analyzed and assumed principal stresses in model 2 (Space angle between the three wellbores 10°, 20°, 30°, 40°, 50°, 60°, 70°, 80°, 90°)

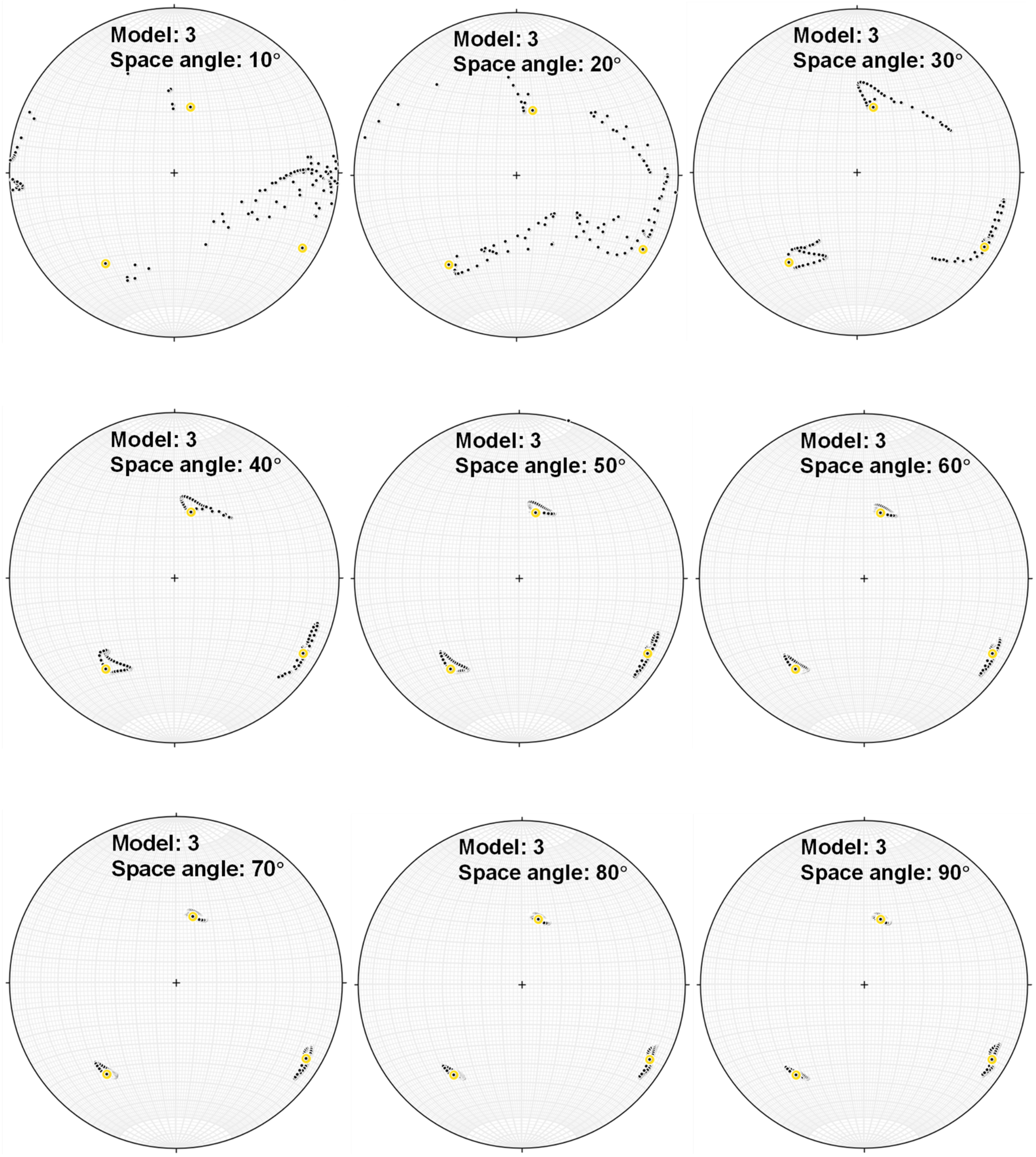

Figure C.3 Orientations of the back-analyzed and assumed principal stresses in model 3 (Space angle between the three wellbores 10°, 20°, 30°, 40°, 50°, 60°, 70°, 80°, 90°)

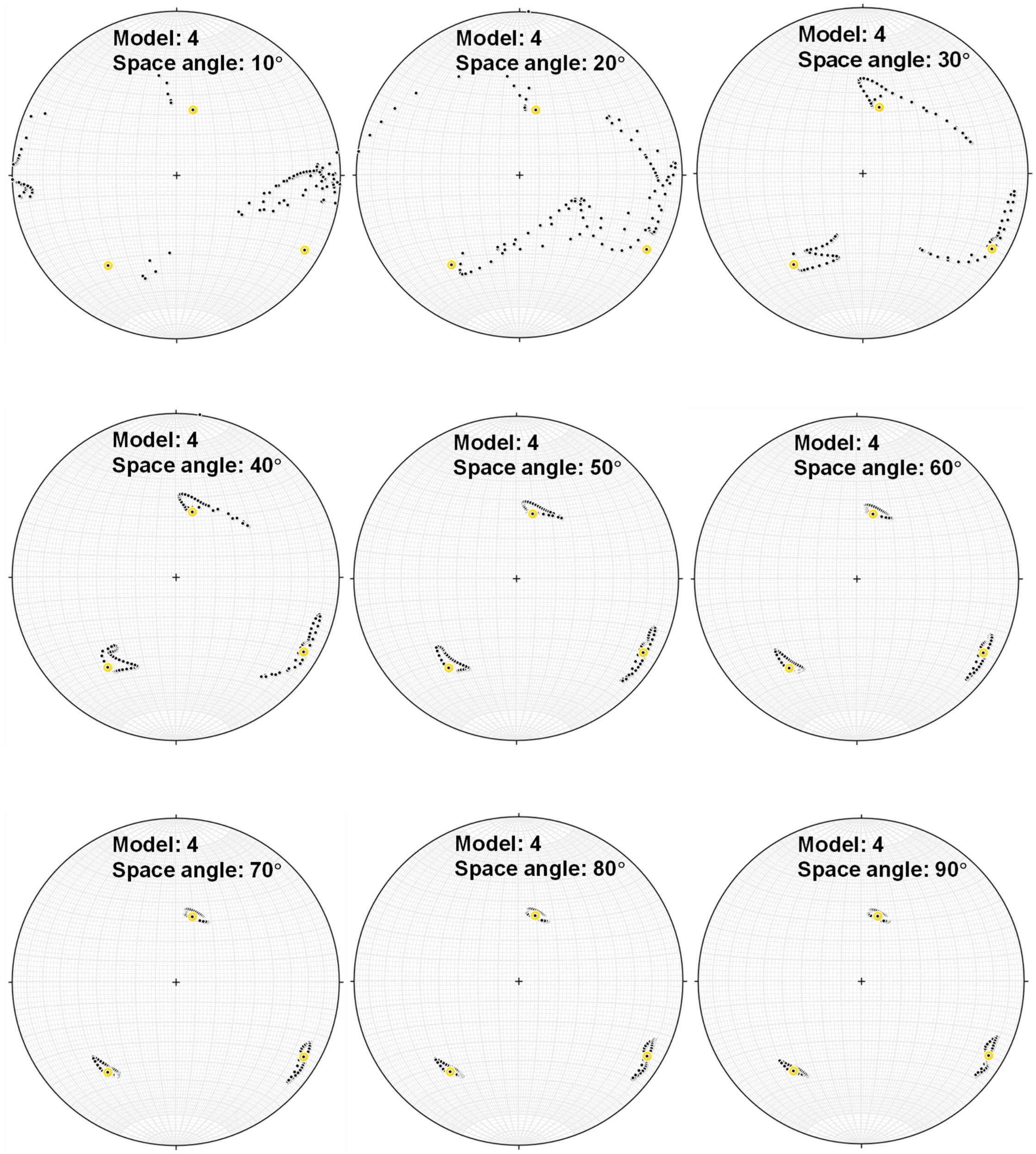

Figure C.4 Orientations of the back-analyzed and assumed principal stresses in model 4 (Space angle between the three wellbores 10°, 20°, 30°, 40°, 50°, 60°, 70°, 80°, 90°)

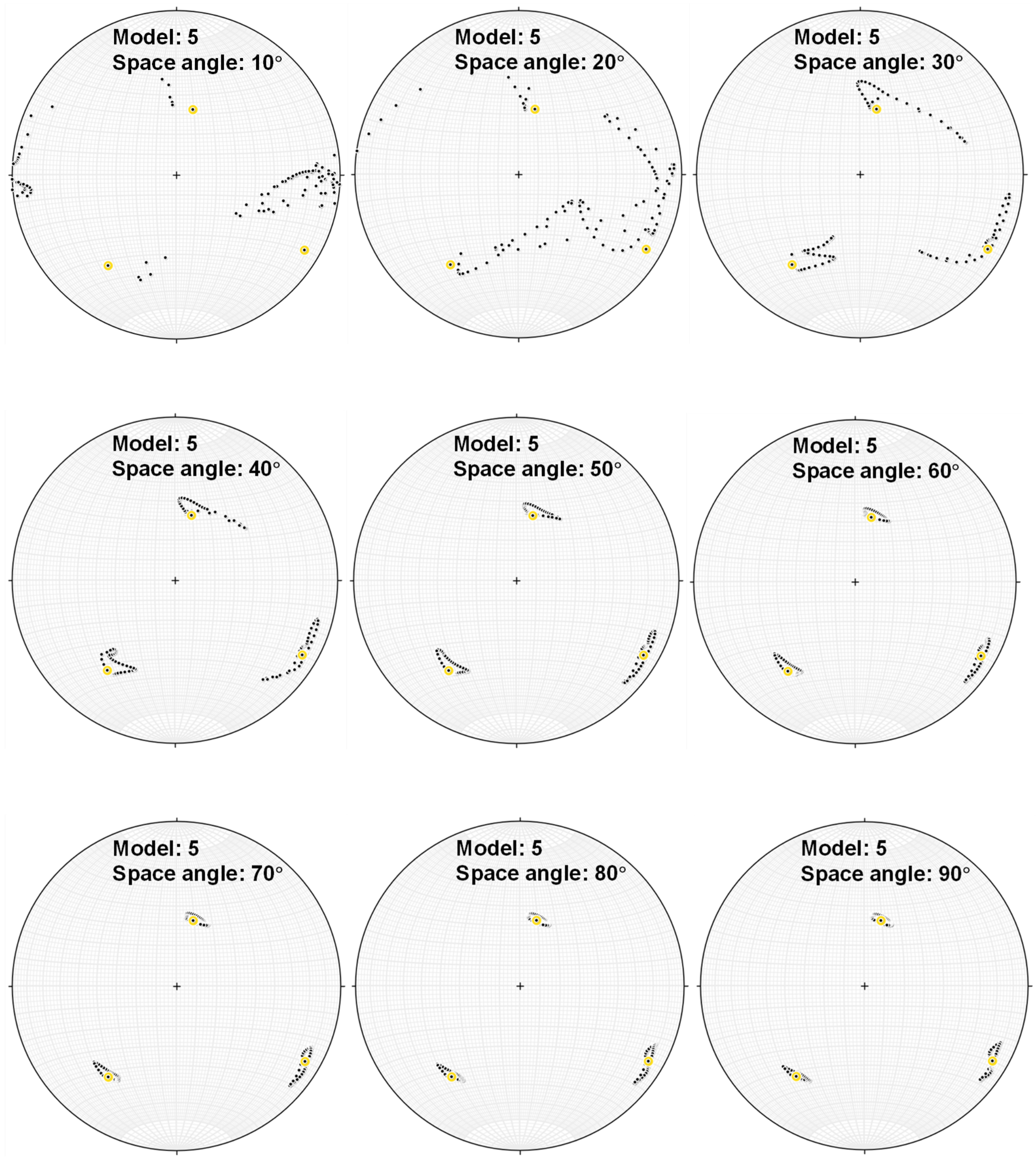

Figure C.5 Orientations of the back-analyzed and assumed principal stresses in model 5 (Space angle between the three wellbores 10°, 20°, 30°, 40°, 50°, 60°, 70°, 80°, 90°)

APPENDIX D COMBINATIONS OF THE INCLINATION AND BEARING ANGLE IN NINE SCENARIOS

Table D.1 Combinations of the inclination and bearing angle in scenario 1 (Space angle=10°)

Group number		Inclination angle [°]	Bearing angle [°]
Group #1	Well A	0	0
	Well B	10	0
	Well C	10	298.97
Group #2	Well A	0	0
	Well B	10	10
	Well C	10	308.97
Group #N	Well A	0	0
	Well B	10	(N-1) * 10
	Well C	10	(N-1) * 10 + 298.97
………			
Group #36	Well A	0	0
	Well B	10	350
	Well C	10	288.97

Table D.2 Combinations of the inclination and bearing angle in scenario 2 (Space angle=20°)

Group number		Inclination angle [°]	Bearing angle [°]
Group #1	Well A	0	0
	Well B	20	0
	Well C	20	299.75
Group #2	Well A	0	0
	Well B	20	10
	Well C	20	309.75
Group #N	Well A	0	0
	Well B	20	(N-1) * 10
	Well C	20	(N-1) * 10 + 299.75
………			
Group #36	Well A	0	0
	Well B	20	350
	Well C	20	288.97

Table D.3 Combinations of the inclination and bearing angle in scenario 3 (Space angle=30°)

Group number		Inclination angle [°]	Bearing angle [°]
Group #1	Well A	0	0
	Well B	30	0
	Well C	30	297.65
Group #2	Well A	0	0
	Well B	30	10
	Well C	30	307.65
Group #N	Well A	0	0
	Well B	30	(N-1) * 10
	Well C	30	(N-1) * 10 + 297.65
………			
Group #36	Well A	0	0
	Well B	30	350
	Well C	30	287.65

Table D.4 Combinations of the inclination and bearing angle in scenario 4 (Space angle=40°)

Group number		Inclination angle [°]	Bearing angle [°]
Group #1	Well A	0	0
	Well B	40	0
	Well C	40	295.7
Group #2	Well A	0	0
	Well B	40	10
	Well C	40	305.7
Group #N	Well A	0	0
	Well B	40	(N-1) * 10
	Well C	40	(N-1) * 10 + 295.7
………			
Group #36	Well A	0	0
	Well B	40	350
	Well C	40	285.7

Table D.5 Combinations of the inclination and bearing angle in scenario 5 (Space angle=50°)

Group number		Inclination angle [°]	Bearing angle [°]
Group #1	Well A	0	0
	Well B	50	0
	Well C	50	293.04
Group #2	Well A	0	0
	Well B	50	10
	Well C	50	303.04
Group #N	Well A	0	0
	Well B	50	(N-1) * 10
	Well C	50	(N-1) * 10 + 293.04
………			
Group #36	Well A	0	0
	Well B	50	350
	Well C	50	283.04

Table D.6 Combinations of the inclination and bearing angle in scenario 6 (Space angle=60°)

Group number		Inclination angle [°]	Bearing angle [°]
Group #1	Well A	0	0
	Well B	60	0
	Well C	60	289.47
Group #2	Well A	0	0
	Well B	60	10
	Well C	60	299.47
Group #N	Well A	0	0
	Well B	60	(N-1) * 10
	Well C	60	(N-1) * 10 + 289.47
………			
Group #36	Well A	0	0
	Well B	60	350
	Well C	60	279.47

Table D.7 Combinations of the inclination and bearing angle in scenario 7 (Space angle=70°)

Group number		Inclination angle [°]	Bearing angle [°]
Group #1	Well A	0	0
	Well B	70	0
	Well C	70	284.76
Group #2	Well A	0	0
	Well B	70	10
	Well C	70	294.76
Group #N	Well A	0	0
	Well B	70	(N-1) * 10
	Well C	70	(N-1) * 10 + 284.76
………			
Group #36	Well A	0	0
	Well B	70	350
	Well C	70	274.76

Table D.8 Combinations of the inclination and bearing angle in scenario 8 (Space angle=80°)

Group number		Inclination angle [°]	Bearing angle [°]
Group #1	Well A	0	0
	Well B	80	0
	Well C	80	278.51
Group #2	Well A	0	0
	Well B	80	10
	Well C	80	288.51
Group #N	Well A	0	0
	Well B	80	(N-1) * 10
	Well C	80	(N-1) * 10 + 278.51
………			
Group #36	Well A	0	0
	Well B	80	350
	Well C	80	268.51

Table D.9 Combinations of the inclination and bearing angle in scenario 9 (Space angle=90°)

Group number		Inclination angle [°]	Bearing angle [°]
Group #1	Well A	0	0
	Well B	90	0
	Well C	90	270
Group #2	Well A	0	0
	Well B	90	10
	Well C	90	280
Group #N	Well A	0	0
	Well B	90	(N-1) * 10
	Well C	90	(N-1) * 10 + 270
………			
Group #36	Well A	0	0
	Well B	90	350
	Well C	90	260

APPENDIX E THE SOLUTION FROM THE WRONG MODELS IN FIVE CONDITIONS

Table E.1 Back-analyzed results in condition 1

Condition 1	Solutions from wrong models							
1^{st} Multi-branch well	Model-2	σ_1	σ_2	σ_3	Model-3	σ_1	σ_2	σ_3
	Magnitude[MPa]	72.21	49.61	27.96	Magnitude[MPa]	73.04	50.45	28.79
	Plunge[°]	43.76	8.54	44.97	Plunge[°]	43.76	8.54	44.97
	Trend[°]	6.53	104.80	203.43	Trend[°]	6.53	104.80	203.43
	Model-4	σ_1	σ_2	σ_3	Model-5	σ_1	σ_2	σ_3
	Magnitude[MPa]	74.72	47.88	23.05	Magnitude[MPa]	75.81	48.96	24.14
	Plunge[°]	42.94	9.43	45.52	Plunge[°]	42.94	9.43	45.52
	Trend[°]	4.99	103.88	203.62	Trend[°]	4.99	103.88	203.62

Condition 1	Solutions from wrong models							
2^{nd}Multi-branch well	Model-2	σ_1	σ_2	σ_3	Model-3	σ_1	σ_2	σ_3
	Magnitude[MPa]	78.84	52.06	36.28	Magnitude[MPa]	79.67	52.89	37.11
	Plunge[°]	52.39	9.43	36.01	Plunge[°]	52.39	9.43	36.01
	Trend[°]	12.49	114.95	211.88	Trend[°]	12.49	114.95	211.88
	Model-4	σ_1	σ_2	σ_3	Model-5	σ_1	σ_2	σ_3
	Magnitude[MPa]	82.68	50.53	31.85	Magnitude[MPa]	83.77	51.61	32.93
	Plunge[°]	51.70	10.73	36.24	Plunge[°]	51.70	10.73	36.24
	Trend[°]	11.39	115.28	213.27	Trend[°]	11.39	115.28	213.27

Condition 1	Solutions from wrong models							
3^{rd} Multi-branch well	Model-2	σ_1	σ_2	σ_3	Model-3	σ_1	σ_2	σ_3
	Magnitude[MPa]	80.71	52.81	36.83	Magnitude[MPa]	81.54	53.64	37.66
	Plunge[°]	53.83	10.25	34.24	Plunge[°]	53.83	10.25	34.24
	Trend[°]	14.40	118.73	215.80	Trend[°]	14.40	118.73	215.80
	Model-4	σ_1	σ_2	σ_3	Model-5	σ_1	σ_2	σ_3
	Magnitude[MPa]	85.59	51.95	32.06	Magnitude[MPa]	86.67	53.03	33.14
	Plunge[°]	53.56	10.00	34.62	Plunge[°]	53.56	10.00	34.62
	Trend[°]	14.45	118.26	215.24	Trend[°]	14.45	118.26	215.24

Table E.2 Back-analyzed results in condition 2

Condition 2	Solutions from wrong models							
1^{st} Multi-branch well	Model-1	σ_1	σ_2	σ_3	Model-3	σ_1	σ_2	σ_3
	Magnitude[MPa]	63.44	40.94	21.27	Magnitude[MPa]	68.77	46.27	25.61
	Plunge[°]	44.71	8.79	43.95	Plunge[°]	44.71	8.79	43.95
	Trend[°]	6.84	105.64	204.21	Trend[°]	6.84	105.64	204.21
	Model-4	σ_1	σ_2	σ_3	Model-5	σ_1	σ_2	σ_3
	Magnitude[MPa]	70.48	43.80	20.15	Magnitude[MPa]	71.56	44.88	21.24
	Plunge[°]	43.91	9.77	44.44	Plunge[°]	43.91	9.77	44.44
	Trend[°]	5.31	104.85	204.57	Trend[°]	5.31	104.85	204.57

Condition 2	Solutions from wrong models							
2^{nd} Multi-branch well	Model-1	σ_1	σ_2	σ_3	Model-3	σ_1	σ_2	σ_3
	Magnitude[MPa]	69.66	43.24	27.67	Magnitude[MPa]	74.99	48.57	33.00
	Plunge[°]	52.73	9.50	35.64	Plunge[°]	52.73	9.49	35.64
	Trend[°]	12.62	115.32	212.21	Trend[°]	12.62	115.32	212.21
	Model-4	σ_1	σ_2	σ_3	Model-5	σ_1	σ_2	σ_3
	Magnitude[MPa]	77.95	46.26	27.82	Magnitude[MPa]	79.03	47.34	28.90
	Plunge[°]	52.04	10.83	35.86	Plunge[°]	52.04	10.83	35.86
	Trend[°]	11.50	115.69	213.64	Trend[°]	11.50	115.69	213.64

Condition 2	Solutions from wrong models							
3^{rd} Multi-branch well	Model-1	σ_1	σ_2	σ_3	Model-3	σ_1	σ_2	σ_3
	Magnitude[MPa]	71.36	43.96	28.10	Magnitude[MPa]	76.70	49.29	33.43
	Plunge[°]	54.04	10.27	34.02	Plunge[°]	54.04	10.27	34.02
	Trend[°]	14.43	118.90	215.93	Trend[°]	14.43	118.90	215.93
	Model-4	σ_1	σ_2	σ_3	Model-5	σ_1	σ_2	σ_3
	Magnitude[MPa]	80.67	47.62	27.88	Magnitude[MPa]	81.75	48.70	28.96
	Plunge[°]	53.75	10.04	34.41	Plunge[°]	53.75	10.04	34.41
	Trend[°]	14.47	118.44	215.40	Trend[°]	14.47	118.44	215.40

Table E.3 Back-analyzed results in condition 3

Condition 3	Solutions from wrong models							
1^{st} Multi-branch well	Model-1	σ_1	σ_2	σ_3	Model-2	σ_1	σ_2	σ_3
	Magnitude[MPa]	62.65	40.17	20.98	Magnitude[MPa]	67.15	44.67	24.18
	Plunge[°]	44.89	8.83	43.76	Plunge[°]	44.89	8.83	43.76
	Trend[°]	6.90	105.81	204.36	Trend[°]	6.90	105.81	204.36
	Model-4	σ_1	σ_2	σ_3	Model-5	σ_1	σ_2	σ_3
	Magnitude[MPa]	69.69	43.05	19.61	Magnitude[MPa]	70.78	44.13	20.69
	Plunge[°]	44.10	9.83	44.23	Plunge[°]	44.10	9.83	44.23
	Trend[°]	5.37	105.04	204.75	Trend[°]	5.37	105.04	204.75

Condition 3	Solutions from wrong models							
2^{nd} Multi-branch well	Model-1	σ_1	σ_2	σ_3	Model-2	σ_1	σ_2	σ_3
	Magnitude[MPa]	68.79	42.44	26.91	Magnitude[MPa]	73.29	46.94	31.41
	Plunge[°]	52.79	9.51	35.57	Plunge[°]	52.79	9.51	35.57
	Trend[°]	12.64	115.39	212.27	Trend[°]	12.64	115.39	212.27
	Model-4	σ_1	σ_2	σ_3	Model-5	σ_1	σ_2	σ_3
	Magnitude[MPa]	77.07	45.47	27.07	Magnitude[MPa]	78.15	46.55	28.16
	Plunge[°]	52.10	10.84	35.79	Plunge[°]	52.10	10.84	35.79
	Trend[°]	11.52	115.77	213.70	Trend[°]	11.52	115.77	213.70

Condition 3	Solutions from wrong models							
3^{rd} Multi-branch well	Model-1	σ_1	σ_2	σ_3	Model-2	σ_1	σ_2	σ_3
	Magnitude[MPa]	70.47	43.15	27.31	Magnitude[MPa]	74.97	47.65	31.81
	Plunge[°]	54.07	10.28	33.98	Plunge[°]	54.07	10.28	33.98
	Trend[°]	14.44	118.93	215.95	Trend[°]	14.44	118.93	215.95
	Model-4	σ_1	σ_2	σ_3	Model-5	σ_1	σ_2	σ_3
	Magnitude[MPa]	79.75	46.81	27.11	Magnitude[MPa]	80.84	47.90	28.19
	Plunge[°]	53.78	10.05	34.37	Plunge[°]	53.78	10.05	34.37
	Trend[°]	14.47	118.47	215.43	Trend[°]	14.47	118.47	215.43

Table E.4 Back-analyzed results in condition 4

Condition 4	Solutions from wrong models							
1^{st} Multi-branch well	Model-1	σ_1	σ_2	σ_3	Model-2	σ_1	σ_2	σ_3
	Magnitude[MPa]	60.94	41.72	22.98	Magnitude[MPa]	65.44	46.22	27.48
	Plunge[°]	44.29	7.57	44.71	Plunge[°]	44.29	7.57	44.71
	Trend[°]	7.64	105.09	202.66	Trend[°]	7.64	105.09	202.66
	Model-3	σ_1	σ_2	σ_3	Model-5	σ_1	σ_2	σ_3
	Magnitude[MPa]	66.28	47.06	28.31	Magnitude[MPa]	68.75	45.85	24.21
	Plunge[°]	44.29	7.57	44.71	Plunge[°]	43.60	8.34	45.19
	Trend[°]	7.64	105.09	202.66	Trend[°]	6.22	104.25	202.73

Condition 4	Solutions from wrong models							
2^{nd} Multi-branch well	Model-1	σ_1	σ_2	σ_3	Model-2	σ_1	σ_2	σ_3
	Magnitude[MPa]	66.62	44.04	30.79	Magnitude[MPa]	71.12	48.54	35.29
	Plunge[°]	52.91	8.23	35.86	Plunge[°]	52.91	8.23	35.83
	Trend[°]	13.46	114.49	210.49	Trend[°]	13.46	114.49	210.49
	Model-3	σ_1	σ_2	σ_3	Model-5	σ_1	σ_2	σ_3
	Magnitude[MPa]	71.95	49.37	36.13	Magnitude[MPa]	75.46	48.27	32.58
	Plunge[°]	52.91	8.23	35.83	Plunge[°]	52.34	9.35	36.09
	Trend[°]	13.46	114.49	210.49	Trend[°]	12.47	114.79	211.69

Condition 4	Solutions from wrong models							
3^{rd} Multi-branch well	Model-1	σ_1	σ_2	σ_3	Model-2	σ_1	σ_2	σ_3
	Magnitude[MPa]	67.81	44.40	31.42	Magnitude[MPa]	72.31	48.90	35.92
	Plunge[°]	54.07	10.34	33.96	Plunge[°]	54.07	10.34	33.96
	Trend[°]	14.37	118.95	216.02	Trend[°]	14.37	118.95	216.02
	Model-3	σ_1	σ_2	σ_3	Model-5	σ_1	σ_2	σ_3
	Magnitude[MPa]	73.14	49.73	36.76	Magnitude[MPa]	77.45	49.15	33.03
	Plunge[°]	54.07	10.34	33.96	Plunge[°]	53.85	10.09	34.29
	Trend[°]	14.37	118.95	216.02	Trend[°]	14.42	118.52	215.49

Table E.5 Back-analyzed results in condition 5

Condition 5	Solutions from wrong models							
1^{st} Multi-branch well	Model-1	σ_1	σ_2	σ_3	Model-2	σ_1	σ_2	σ_3
	Magnitude[MPa]	59.92	40.72	22.21	Magnitude[MPa]	64.42	45.22	26.71
	Plunge[°]	44.55	7.63	44.44	Plunge[°]	44.55	7.63	44.44
	Trend[°]	7.73	105.31	202.86	Trend[°]	7.73	105.31	202.86
	Model-3	σ_1	σ_2	σ_3	Model-4	σ_1	σ_2	σ_3
	Magnitude[MPa]	65.25	46.05	27.55	Magnitude[MPa]	66.65	43.78	22.43
	Plunge[°]	44.55	7.63	44.44	Plunge[°]	43.87	8.41	44.90
	Trend[°]	7.73	105.31	202.86	Trend[°]	6.32	104.49	202.97

Condition 5	Solutions from wrong models							
2^{nd} Multi-branch well	Model-1	σ_1	σ_2	σ_3	Model-2	σ_1	σ_2	σ_3
	Magnitude[MPa]	65.49	43.00	29.81	Magnitude[MPa]	69.99	47.50	34.31
	Plunge[°]	53.01	8.24	.35.76	Plunge[°]	53.01	8.24	.35.76
	Trend[°]	13.50	114.59	210.57	Trend[°]	13.50	114.59	210.57
	Model-3	σ_1	σ_2	σ_3	Model-4	σ_1	σ_2	σ_3
	Magnitude[MPa]	70.83	48.33	35.14	Magnitude[MPa]	73.24	46.16	30.53
	Plunge[°]	53.01	8.24	.35.76	Plunge[°]	52.43	9.38	35.98
	Trend[°]	13.50	114.59	210.57	Trend[°]	12.50	114.90	211.78

Condition 5	Solutions from wrong models							
3^{rd} Multi-branch well	Model-1	σ_1	σ_2	σ_3	Model-2	σ_1	σ_2	σ_3
	Magnitude[MPa]	66.64	43.35	30.40	Magnitude[MPa]	71.14	47.85	34.90
	Plunge[°]	54.13	10.35	33.90	Plunge[°]	54.13	10.35	33.90
	Trend[°]	14.38	119.00	216.05	Trend[°]	14.38	119.00	216.05
	Model-3	σ_1	σ_2	σ_3	Model-4	σ_1	σ_2	σ_3
	Magnitude[MPa]	71.97	48.68	35.74	Magnitude[MPa]	75.18	47.03	30.94
	Plunge[°]	54.13	10.35	33.90	Plunge[°]	53.90	10.10	34.23
	Trend[°]	14.38	119.00	216.05	Trend[°]	14.43	118.57	215.53